Active optical waveguides for lightwave applications

Robert Roderick Thomson

A dissertation submitted for the degree of Doctor of Philosophy

Heriot-Watt University

School of Engineering and Physical Sciences

July 2006

HERIOT WATT UNIVERSITY

ACADEMIC REGISTRY
Research Thesis Submission

Name:	Robert Roderick Thomson		
School/PGI:	Engineering and Physical Sciences		
Version: *(i.e. First, Resubmission, Final)*	Final	Degree Sought:	PhD

Declaration

In accordance with the appropriate regulations I hereby submit my thesis and I declare that:

1) the thesis embodies the results of my own work and has been composed by myself
2) where appropriate, I have made acknowledgement of the work of others and have made reference to work carried out in collaboration with other persons
3) the thesis is the correct version of the thesis for submission*.
4) my thesis for the award referred to, deposited in the Heriot-Watt University Library, should be made available for loan or photocopying, subject to such conditions as the Librarian may require
5) I understand that as a student of the University I am required to abide by the Regulations of the University and to conform to its discipline.

* *Please note that it is the responsibility of the candidate to ensure that the correct version of the thesis is submitted.*

Signature of Candidate:		Date:	28/9/06

Submission

Submitted By *(name in capitals)*:	ROBERT RODERICK THOMSON JANICE SUTTIE
Signature of Individual Submitting:	Janice Suttie
Date Submitted:	4 OCTOBER 2006

For Completion in Academic Registry

Received in the Academic Registry by *(name in capitals)*:	KATRINA WALLACE		
Method of Submission *(Handed in to Academic Registry; posted through internal/external mail)*:	BY HAND		
Signature:	K Wallace	Date:	4/10/06

March 2005

Abstract

The majority of work described in this thesis is concerned with the development of Er-doped waveguides for telecommunications amplifier applications. Through the course of this work, the sol-gel, pulse laser deposition (PLD) and femtosecond waveguide inscription (FWI) routes have all been used to fabricate such waveguides.

As a result of the sol-gel work, Er-doped waveguides exhibiting excellent passive performance were fabricated using only a single sol-gel deposition for each of the core and cladding layers. It was found however that it was not possible to induce a population inversion in these waveguides by optical pumping, and it is concluded that the most probable reason for this is clustering of the Er^{3+} ions.

As a result of the PLD work, optically active Er-doped oxyfluoride-silicate glass films were fabricated using PLD. Through a number of experimental studies it is concluded that although the stoichiometry of the PLD film and target material are very similar, the Er^{3+} ion environment in each is significantly different. In particular, time resolved studies of the $^4I_{13/2} \rightarrow {}^4I_{15/2}$ transition fluorescence indicate the presence of significant quenching mechanisms in the PLD film.

As a result of the FWI studies, embedded waveguide structures were fabricated in Er-doped oxyfluoride-silicate glass and crystalline $LiNbO_3$ using FWI. Of particular significance is the demonstration of a 1.9 cm long Er-doped waveguide that exhibits an internal gain of 1.7 dB at 1537 nm when optically pumped. As a result of the $LiNbO_3$ work, high confinement guiding at 1550 nm is demonstrated in a $LiNbO_3$ waveguide fabricated using FWI for the first time.

To my grandparents

Acknowledgements

Firstly, I would like to thank my academic supervisor Dr. Ajoy Kar for his support, both as a supervisor and as a friend. Without Ajoy, this would not have been possible.

I would also like to thank the various members of the NLO group. In particular, I would like to thank Dr. Henry Bookey, Dr. Ian Blewett and Dr. Graeme Brown for their assistance in many aspects of both theoretical and experimental physics.

I would also like to thank Professor Derryck Reid and Stuart Campbell of the ultrafast optics group for allowing me to use their femtosecond laser. Without this facility, none of the femtosecond waveguide inscription work would have been possible.

I would also like to thank Professor Animesh Jha and Dr. Shaoxiong Shen from the University of Leeds, Professor Maurizio Martino and co-workers at the University of Lecce, Professor Costos Fotakis and co-workers at ULF-FORTH and Dr. Navin Suyal and co-workers at Exxelis LtD. All of these groups of people have made me feel exceptionally welcome during my visits, and without these collaborations none of the work described in this thesis would have been possible.

I would also like to thank all the technical staff in the physics department at Heriot-Watt University. In particular, I would like to thank Neil Ross for performing the photolithography and reactive ion etching, and Peter Heron for his patience with my poor technical drawings.

I would also like to thank my office mates, Ray Fulton, Peter Harrison and Srinu Kumpatla. Their friendship has made the last four years a great experience.

I would also like to thank my mum and Kenny for their support (both financially and motivationally) and encouragement over the last 28 years, without them none of this would have been possible (literally).

Finally, I would like to thank my Fiancée, Claire, for her friendship, support and incredible patience. I have no doubt, I owe this to her.

Table of Contents

Lists of Figures

List of Tables

List of abbreviations

AFM	Atomic Force Microscope
AON	All Optical Network
ASE	Amplified Spontaneous Emission
BL	Bit-rate Length
CWDM	Course Wavelength Division Multiplexing
DFB	Distributed Feedback
DWDM	Dense Wavelength Division Multiplexing
EDFA	Erbium Doped Fibre Amplifier
EDWA	Erbium Doped Waveguide Amplifier
EDX	Energy Dispersive X-ray
ESA	Excited State Absorption
FBG	Fibre Bragg Grating
FHD	Flame Hydrolysis Deposition
FTTH	Fibre To The Home
FWHM	Full Width Half Maximum
FWI	Femtosecond Waveguide Inscription
HCU	Homogeneous Cooperative Upconversion
HRR	High Repetition Rate
ITU	International Telecommunications Union
LAN	Local Area Network
LRR	Low Repetition Rate
LW	Longitudinal Writing
MAN	Metropolitan Area Network
MFD	Mode Field Diameter
PDG	Polarisation Dependent Gain
PDL	Polarisation Dependent Loss
PECVD	Plasma Enhanced Chemical Vapour Deposition
PLC	Planar Lightwave Circuit
PLD	Pulsed Laser Deposition
QD-SOA	Quantum-Dot Semiconductor Optical Amplifier
R	Pumping rate
RIE	Reactive Ion Etching
SBS	Stimulated Brillouin Scattering

SC-RTA	Spin Coating – Rapid Thermal Anneal
S/N	Signal to Noise ratio
SOA	Semiconductor Optical Amplifier
SRS	Stimulated Raman Scattering
TE	Transverse Electric
TEOS	Tetraethoxysilane
TM	Transverse Magnetic
TW	Transverse Writing
WAN	Wide Area Network
WDM	Wavelength Division Multiplexing

List of symbols

Abs	Absorption
at. %	Atomic %
α	Loss coefficient
b	Confocal parameter
C	Cooperative upconversion / energy transfer coefficient
c	Speed of light in a vacuum
D	Total dispersion
$\mathrm{D_w}$	Waveguide dispersion
$\mathrm{D_M}$	Material dispersion
∇	Del operator
E	Electric field vector
ε	Material permittivity
g	Waveguide gain function
Γ	Mode-waveguide overlap factor
Γ_p	Pump-waveguide overlap factor
Γ_s	Signal-waveguide overlap factor
G_{Rel}	Relative gain
H	Magnetizing field vector
h	Plank's constant
k	Laser material gain function
I_p	Pump light intensity
I_s	Signal light intensity
L	Waveguide length
mol %	Molar %
N	Ion population density
n	Either refractive index or fractional population of $^4\mathrm{I}_{13/2}$ state, depending on context
$\mathrm{P_{out}}$	Signal power after device
$\mathrm{P_{in}}$	Signal power before device
p_o	Intensity distribution of propagating mode
R	Pumping rate
ρ_{Er}	Concentration of Er^{3+} ions

s	Normalised signal intensity
σ_p^a	Absorption cross section for the pump wavelength
σ_s^a	Absorption cross section for the signal wavelength
σ_s^e	Emission cross section for the signal wavelength
t	Time
τ	1/e lifetime of state
μ	Material permeability
υ_p	Pump light frequency
υ_s	Signal light frequency
ω_0	Beam waist
wt. %	Weight %
W_a	Stimulated absorption rate at signal wavelength
W_e	Stimulated emission rate at signal wavelength
λ	Free space wavelength
λ_{ZD}	Zero dispersion wavelength
z	Distance
z_R	Rayleigh range

List of Publications by the Candidate

Journal papers

[1] R. R. Thomson, S. Campbell, I. J. Blewett, A. K. Kar, D. T. Reid, S. Shen and A. Jha, "Active waveguide fabrication in erbium-doped oxyfluoride silicate glass using femtosecond pulses," *Appl. Phys. Lett.*, vol. 87, no. 12, Art. 121102, Sept.2005.

[2] R. R. Thomson, H. T. Bookey, H. Ur-Rehman, S. Liu, N. Suyal, and A. K. Kar, "Optically active erbium-doped waveguides fabricated using a single-sol-gel deposition technique," *J. Lightwave Technol.*, vol. 23, no. 12, pp. 4249-4256, Dec. 2005.

[3] R. R. Thomson, H. T. Bookey, A. K. Kar, M. R. Taghizadeh, A. Klini, C. Fotakis, F. Romano, A. P. Caricato, M. Martino, S. Shen, and A. Jha, "Erbium-doped waveguide fabrication via reactive pulsed laser deposition of erbium-doped oxyfluoride-silicate glass," *Electron. Lett.*, vol. 41, no. 25, pp. 1376-1377, Dec. 2005.

[4] R. R. Thomson, S. Campbell, I. J. Blewett, A. K. Kar, and D. T. Reid, "Optical waveguide fabrication in z-cut lithium niobate ($LiNbO_3$) using femtosecond pulses in the low repetition rate regime," *Appl. Phys. Lett.*, vol. 88, no. 11, Art. No. 111109, Mar. 2006.

[5] R. R. Thomson, H. T. Bookey, N. Psaila, S. Campbell, D. T. Reid, S. Shen, A. Jha, and A. K. Kar, "Internal gain from an erbium-doped oxyfluoride-silicate glass waveguide fabricated using femtosecond waveguide inscription" *IEEE Photonic. Tech. L.* vol. 18, no. 14, pp. 1515-1517. Jul. 2006.

[6] R. R. Thomson, H. T. Bookey, N. Suyal, A. K. Kar, "Homogeneous cooperative upconversion in sol-gel fabricated erbium doped channel waveguides," *Appl. Phys. Lett.*, (In press)

[7] A. P. Caricato, A. Fazzi, A. Jha, A. K. Kar, G. Leggieri, A. Luches, M. Martino, F. Romano, S. Shen, M. Taghizadeh, R. R. Thomson, T. Tunno, "Er-doped oxyfluoride silicate thin films prepared by pulsed laser deposition," *Opt. Mater.*, (In press)

Conference papers

[8] R. R. Thomson, H. T. Bookey, S. Campbell, D. T. Reid, A. K. Kar, S. Shen and A. Jha, "Erbium doped waveguide amplifiers (EDWAs) fabricated in novel bulk glasses using femtosecond pulses," presented at the Optical Fiber Communication conference (OFC), Anaheim, California, 2005, (Oral presentation), Paper OThL6.

[9] R. R. Thomson, H.T.Bookey, A.K.Kar, H.Ur-Rehman, S.Liu, and N.Suyal, "Erbium doped waveguide amplifiers (EDWAs) fabricated via a single sol-gel deposition technique," presented at the Conference on Lasers and Electro-Optics (CLEO), Baltimore, Maryland, 2005, (Oral presentation), Paper CThI4.

[10] R. R. Thomson, S. Campbell, G. Brown, I. J. Blewett, A. K. Kar, D. T. Reid, "Femtosecond waveguide fabrication in bulk $LiNbO_3$," presented at the Conference on Lasers and Electro-Optics (CLEO), Baltimore, Maryland, 2005, (Oral presentation), Paper CThV5.

[11] R. R. Thomson, G. Brown, I. J. Blewett, S. Campbell, D. T. Reid, A. K. Kar, S. Shen and A. Jha, "Active waveguide fabrication in novel erbium-doped glasses using focussed femtosecond pulses," presented at the Conference on Lasers and Electro-Optics (CLEO), Baltimore, Maryland, 2005, (Oral presentation), Paper CFH4.

[12] R. R. Thomson, S. Shen, A. Jha, F. Romano, A. P. Caricato, M. Martino, A. K. Kar, "Optically active erbium doped waveguides fabricated using reactive pulsed laser deposition (RPLD)," presented at the annual meeting of the IEEE Lasers and Electro-Optics Society (IEEE-LEOS), Sydney, Australia, 2005, (Oral presentation), Paper ThJ3.

[13] R. R. Thomson, S. Campbell, S. Shen, A. Jha, A. K. Kar and D.T. Reid, "Active waveguide fabrication in erbium-doped oxyfluoride silicate glass using femtosecond pulses," presented at the annual meeting of the IEEE Lasers and Electro-Optics Society (IEEE-LEOS), Sydney, Australia, 2005, (Oral presentation), Paper WBB4.

[14] R. R. Thomson, H. T. Bookey, N. Psaila, S. Campbell, D. T. Reid, A. K. Kar, S. Shen, A. Jha, "Active waveguide fabrication in erbium doped oxyfluoride-silicate glass using femtosecond pulses," presented at the Conference on Lasers and Electro-Optics (CLEO) Long-beach, California, 2006, (Oral presentation), Paper CWD5.

Chapter 1– Introduction

1.1 Research motivation

As the demand for high bandwidth applications in the home increases, so too does the demand for suitable network devices to meet the demands of metropolitan area and local area networks (MAN / LANs). Suitable devices must minimise power and size requirements. The motivation behind this research is to develop new techniques for the fabrication of such devices. In particular, much of the research is aimed at developing novel erbium doped waveguide amplifiers (EDWAs) for MAN / LAN networks employing wavelength division multiplexing (WDM).

1.1.1 Evolution of optical fibre communications

Electromagnetic waves have long been used for communications applications. Marconi was first to transmit information using electromagnetic radio waves in 1895. Unfortunately, the long wavelengths of radio signals mean that their information carrying capacity (or bandwidth) is much lower than that of radiation in the optical region of the spectrum. Unlike radio waves however, optical waves do not diffract nearly as much as radio signals and as a result free space optical communications are limited to line-of-sight applications.

In order for optical communications not limited to line-of-sight applications to become a reality, it was necessary to invent a transmission medium that could guide light from the information source to the destination. In 1870, John Tyndall demonstrated that light could be contained and guided along a thin stream of water, but it wasn't until the 1950's that work began on the development of fibre optic bundles for transporting images. With the advent of the laser in the 1960's, research interest in fibre optic communications was stimulated. By the 1970's researchers at Corning Glass Works had fabricated a glass fibre with an attenuation of $\approx$ 20 dB.km^{-1} at 633 nm, thus proving the feasibility of optical fibre communications. Over the next two decades, low-loss single mode fibres with propagation losses of $\approx$ 0.2 dB.km^{-1} at 1550 nm were developed and in 1988, the first transatlantic telecommunications line (TAT-8) was laid with an information carrying capacity of 4000 telephone calls. In the previous year (1987), the erbium doped fibre amplifier (EDFA) was invented at the University of Southampton allowing the all optical amplification of many channels at different wavelengths in one device. As a result, the age of WDM was born allowing all-optical networks and increased capacity.

Optical fibre communications can in general be separated into five generations, each generation with an improved information capacity due to a series of technological advancements. The first generation was developed in the latter half of the 1970's and operated at 800 nm using multi-mode fibre. They operated at a bit-rate of 45 $Mb.s^{-1}$ with a maximum repeater separation of 10 km. The capacity of first generation systems was limited by inter-modal dispersion and fibre loss. The second generation was developed from 1977 - 1985 and used the reduced loss and reduced dispersion of single mode fibre operating at 1.3 μm. By 1987, second generation systems were operating at bit-rates up to 1.7 $Gb.s^{-1}$ with a repeater station of $\approx$ 50 km. Third generation systems were developed from 1980-1991 and used reduced loss, dispersion shifted single mode fibre and single longitudinal mode lasers operating at 1.5 μm. Third generation systems were able to transmit at 10 $Gb.s^{-1}$ with a repeater separation of 100 km. The fourth generation was developed from 1989 onwards and makes use of optical amplifiers, in particular the EDFA. By 2001, a single transpacific system could transmit > 1$Tb.s^{-1}$ over a distance of 10,000 km. The fifth generation aims to solve the dispersion problem in Dense WDM systems (DWDM) through the use of techniques such as soliton propagation to allow multi $Tb.s^{-1}$ capacity long haul links. Fifth generation systems are not yet commercially available.

1.1.2 The general optical fibre communication system

The purpose of any communications system is to transmit *information* reliably from a source to a destination. Figure 1-1 shows a schematic diagram of a general optical fibre communication system. First, an information source provides information that is encoded on an electrical signal by an electrical encoder. The electrical encoder then drives an optical source that produces a modulated optical signal. The amplitude, frequency, phase and polarisation of the optical carrier wave can all be used to encode the information. The optical signal is then transmitted via the optical fibre transmission medium to the destination end. At the destination end the optical signal is detected by an optical detector which converts the optical signal to an electrical signal. The electrical signal is then decoded by an electrical decoder for processing at the destination.

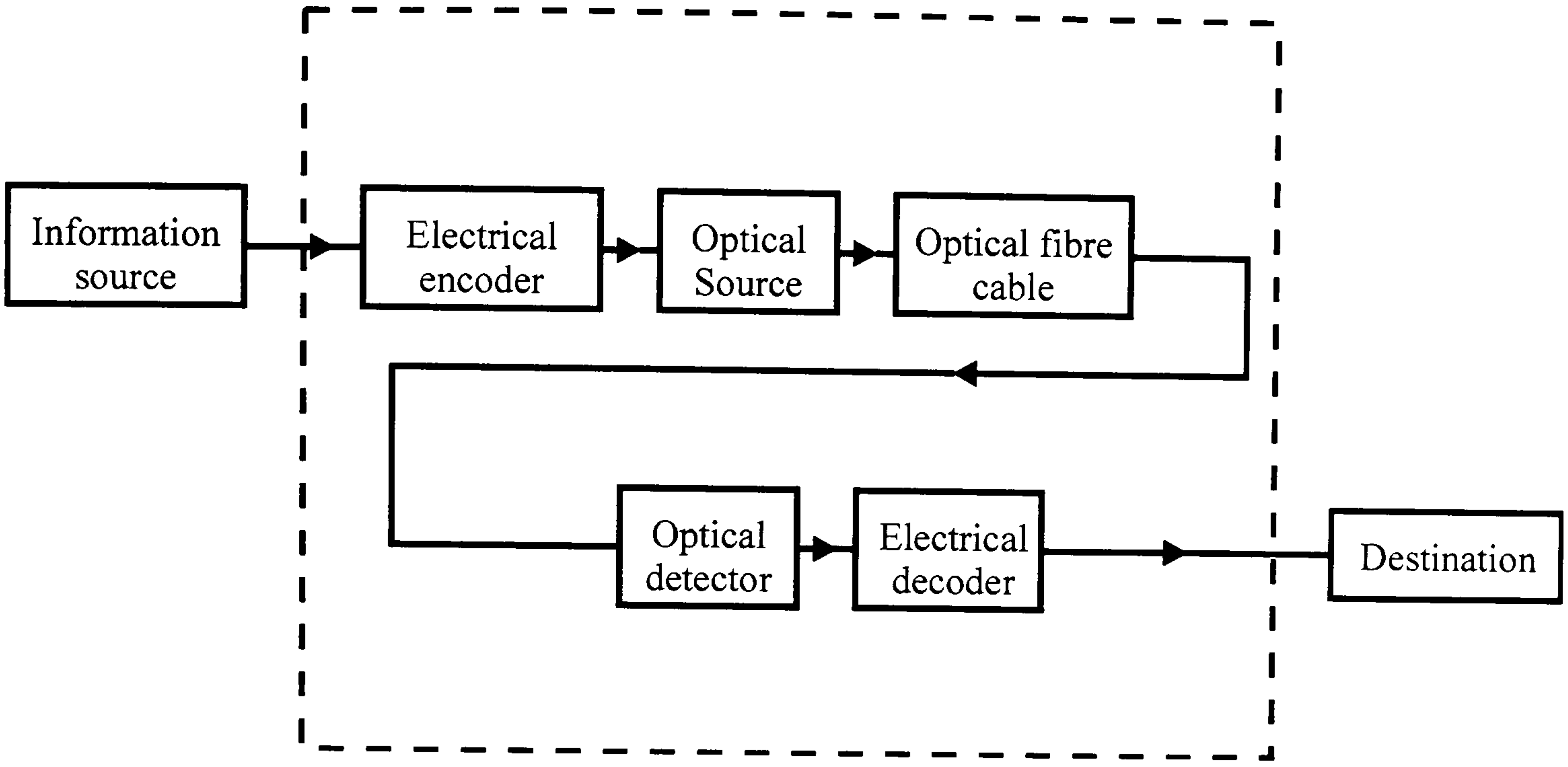

Figure 1-1 Block diagram of an optical fibre communications system

Although all optical fibre communications systems have the same basic structure shown in Figure 1-1, the differences between practical systems are vast.

1.1.3 Transmission line capacity

The optical carrier frequency is of the order of 100 THz. As a result, the information transfer capacity is potentially of the order of 1Tb.s^{-1} for a single wavelength. In practice however, the capacity of a lightwave connection is limited by degradation in the signal to noise (S/N) ratio of the information as it is transmitted along the fibre. An important figure of merit for any lightwave connection is its bit-rate-length product (BL), where B is the transmission bit-rate and L is the maximum length the transmission line can be without the need for regeneration. In practice, the BL product of a transmission line is either loss limited or dispersion limited.

If the BL product of a transmission line is loss limited, it is the sensitivity of the detector, the power of the signal source and the loss of the transmission line that determine how long the link may be without the need for signal regeneration. Figure 1-2 shows a sketch of fibre loss as a function of wavelength for standard low loss single mode silica fibre [1].

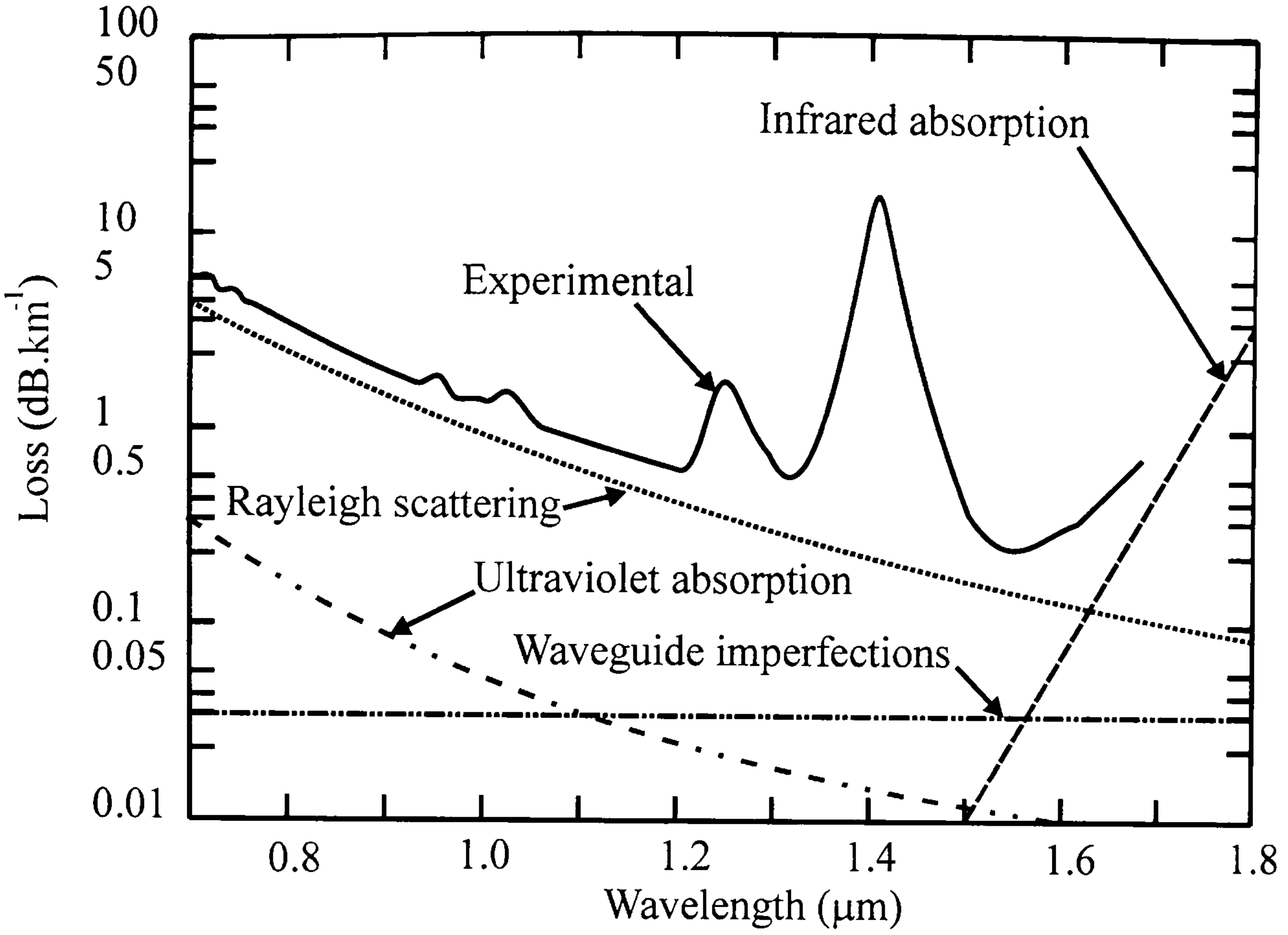

Figure 1-2 Sketch of fibre loss as a function of wavelength for some standard single mode silica fibre

From Figure 1-2 it can be seen that due to a combination of scattering and absorption losses, two windows centred at 1.3 and 1.55 μm exist for low loss transmission in silica fibre. The international telecommunications union (ITU) has designated six spectral bands within the 1260 -1675 nm region. These are the O-band (1260 -1360 nm), the E-band (1360 – 1460 nm), the S-band (1460-1530 nm), the C-band (1530 to 1565 nm), the L-band (1565 -1625 nm) and the U-band (1625 – 1675 nm) [2].

The BL product of a loss limited connection can be increased through the use of optical amplifiers that amplify the signal periodically without the necessity for signal regeneration. EDFAs operating in the C and L-bands are now at a stage whereby loss is no longer a significant factor in long distance telecommunications. EDFAs are not well suited to LAN and MAN applications however since they are large, expensive and have large power requirements.

If the BL product of a lightwave connection is not loss limited, it is dispersion limited. As an optical pulse propagates along a single mode fibre it spreads in time due to dispersion, reducing the S/N ratio of the transmitted data. The total dispersion it experiences is due to a combination of both the fibre material dispersion and the waveguide dispersion. Figure 1-3 shows a sketch of the total dispersion (D), and the relative contributions of material dispersion (D_M) and waveguide dispersion (D_W) for a standard single mode silica fibre [3].

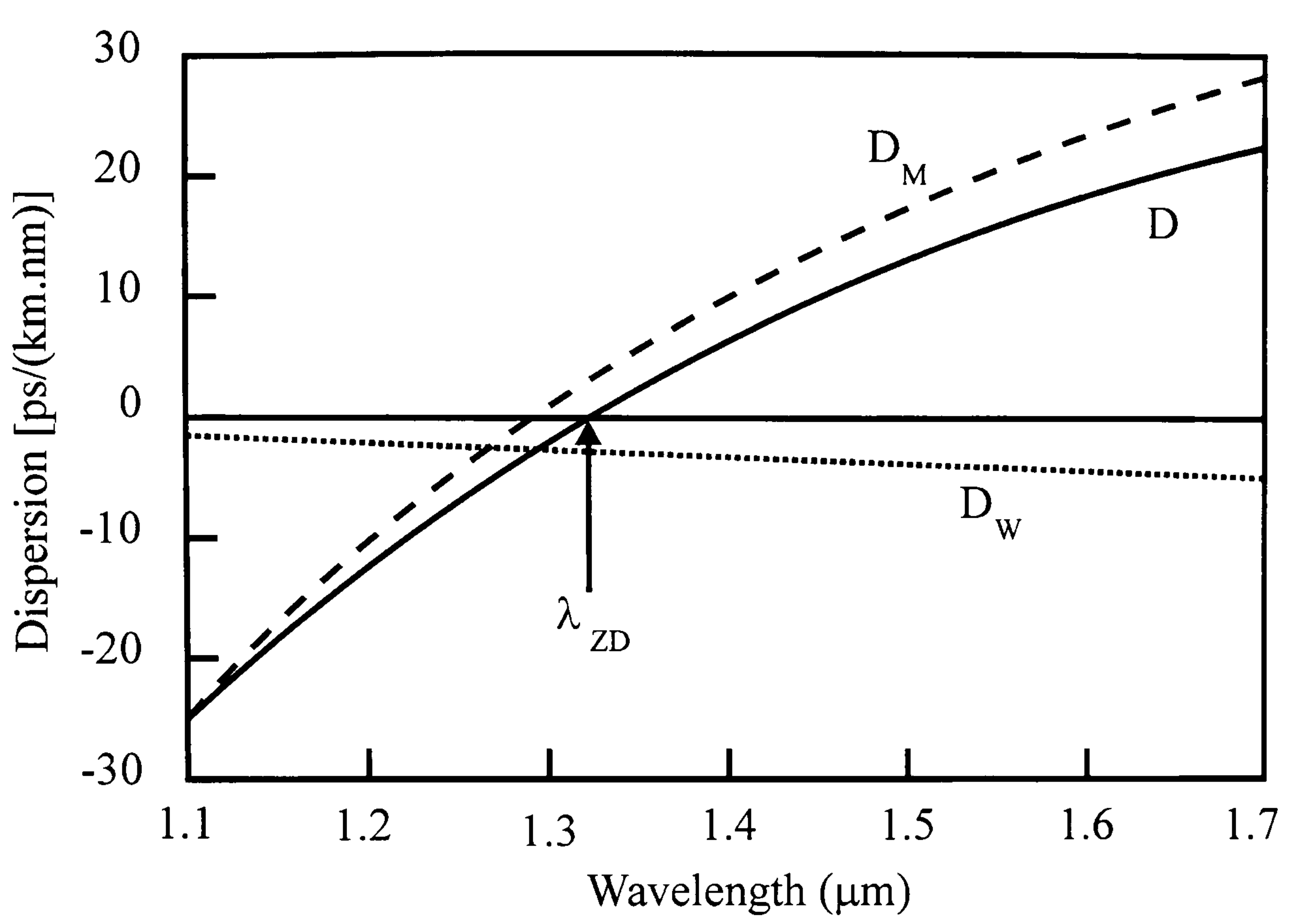

Figure 1-3 Sketch of the total dispersion (D) and the relative contributions of material dispersion (D_M) and waveguide dispersion (D_W) for a standard single mode silica fibre.

The BL product of a dispersion limited connection can be increased by operating near the zero dispersion wavelength of the fibre and using a narrow line width laser and / or, inserting a piece of dispersion compensating fibre in the transmission line that has a total dispersion equal in magnitude but opposite in sign to the previous part of the transmission line.

1.1.4 Optical fibre communications networks

Although point-to-point links of the kind shown in Figure 1-1 do have practical uses, the most important uses of optical fibre communications involve interconnecting many different users within a given area using an optical fibre communications network. Optical fibre communications networks can be divided into three broad categories, LANs, MANs and wide area networks (WANs). LANs generally extend up to a few kilometres and interconnect users in a localised area such as a neighbourhood or campus. MANs may extend up to ≈ 100 km and provide interconnections between

LANs within the MAN area. WANs extend over a large geographic area and interconnect MANs within that area.

The physical structure of LAN and MAN networks depend entirely on their function. For example, some network applications (e.g. cable TV) require only the distribution of a signal to many different users *without* the requirement for a two-way connection. Other networks applications (e.g. a university campus network) require any user on the network to be able to communicate bi-directionally with any other user on the network. At present, the majority of fibre-optic communications systems have been developed for telecommunications network applications that transmit not only voice data but computer and fax data also. The entire telecommunications network is made up of a series of long-haul, high capacity point-to-point lines that effectively form the world wide telecommunications WAN, and numerous short haul MAN and LAN networks.

At present, the vast majority of telecommunications LANs do not reach the user premises, with the last stretch from the user to the LAN being covered by conventional coaxial cable. Due to the growth in high bandwidth applications in the home, the last stretch of coaxial cable is gradually being replaced by an optical fibre link in a development known *as fibre-to-the-home* (FTTH).

1.1.5 Wavelength division multiplexing (WDM)

WDM is the name given to the scheme whereby a number of separate channels at different wavelengths are used to transmit information on a single fibre. The role of WDM in telecommunications applications is two fold. The first is to increase the information carrying capacity of point-to-point transmission links, the second is to allow all optical routing in networks without the need for electronic routers.

If one channel at a certain wavelength is able to transmit 10 $Gb.s^{-1}$, then N channels at N different wavelengths can transmit $N \times 10$ $Gb.s^{-1}$. As such, WDM allows a linear increase in the capacity of a transmission line. Figure 1-4 shows schematically how N channels can be combined together in a multiplexer, transmitted along an optical fibre and separated at the other end using a de-multiplexer.

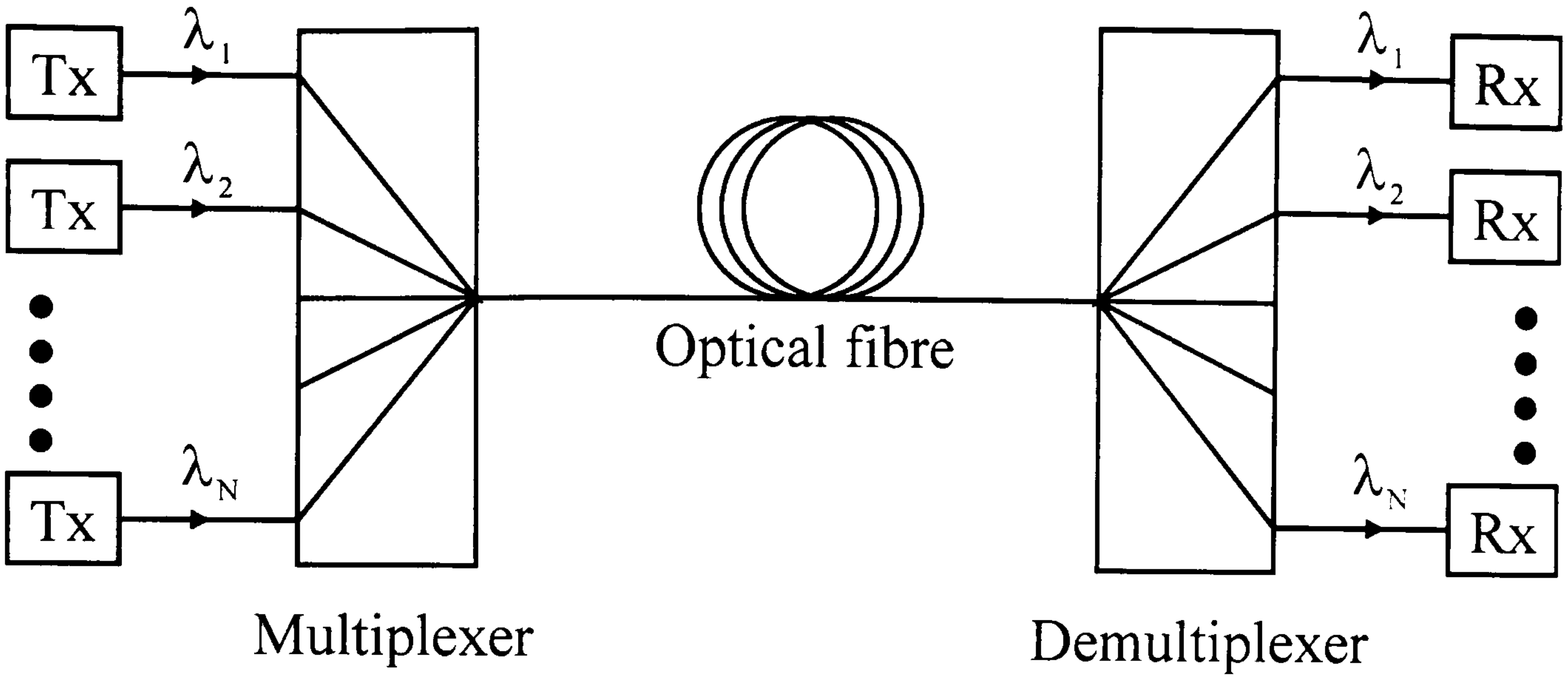

Figure 1-4 Schematic diagram of the construction of a point-to-point connection using wavelength division multiplexing

The number of possible WDM channels is determined by the range of the optical spectrum which can be practically used, as well the inter-channel spacing. An examination of Figure 1-2 shows that low loss guiding (< 0.5 dB.km^{-1} loss) in silica fibre would be possible from about 1.25– 1.65 μm (400 nm) if it weren't for O-H impurities in the fibre. As a result of O-H impurities however, two low loss windows centred near 1.3 and 1.55 μm exist. Additional constraints on the possible transmission wavelengths are the availability of suitable optical amplifiers and distributed feedback (DFB) lasers. Once the regions of the spectrum suitable for transmission are identified, the number of possible channels is limited by the inter-channel spacing. This parameter is reliant on issues regarding inter-channel cross-talk which exists due to both linear (e.g. coupler imperfections) and non-linear (e.g. stimulated Brillouin scattering (SBS), stimulated Raman scattering (SRS), amplifier spectra hole burning) mechanisms [4].

For long haul point-to-point links where system capacity is the primary concern, DWDM schemes can be employed. State of the art commercial DWDM systems can carry up to 160 channels separated by 50 GHz across both the C and L telecommunications bands. Each channel can carry up to 10 Gb.s^{-1} giving a total link capacity of 1.6 Tb.s^{-1} [5]. Recent laboratory experiments have however demonstrated the possibility for point-to-point links carrying 373 channels over an 11,000 km long link resulting in an BL product of over 41 (Pb.s^{-1}).km [6].

In addition to increasing the information capacity, WDM can also be used to route information from one place to another using wavelength dependent couplers. As a result, all optical networks (AONs) or nearly AONs can be constructed that reduce the need for electrical routers that reduce bandwidth and increase costs. Figure 1-5 shows how a number of users can be connected using a metro access ring and 8-channel coarse WDM (CWDM) routing via a series of hubs. The hubs are connected by means of a bi-directional ring loop. For short haul MAN / LAN applications where cost is a primary concern, 8-channel CWDM or 16-channel WDM routing techniques are widely used which relax the tolerances on the performance specifications of the network components compared to DWDM systems [7].

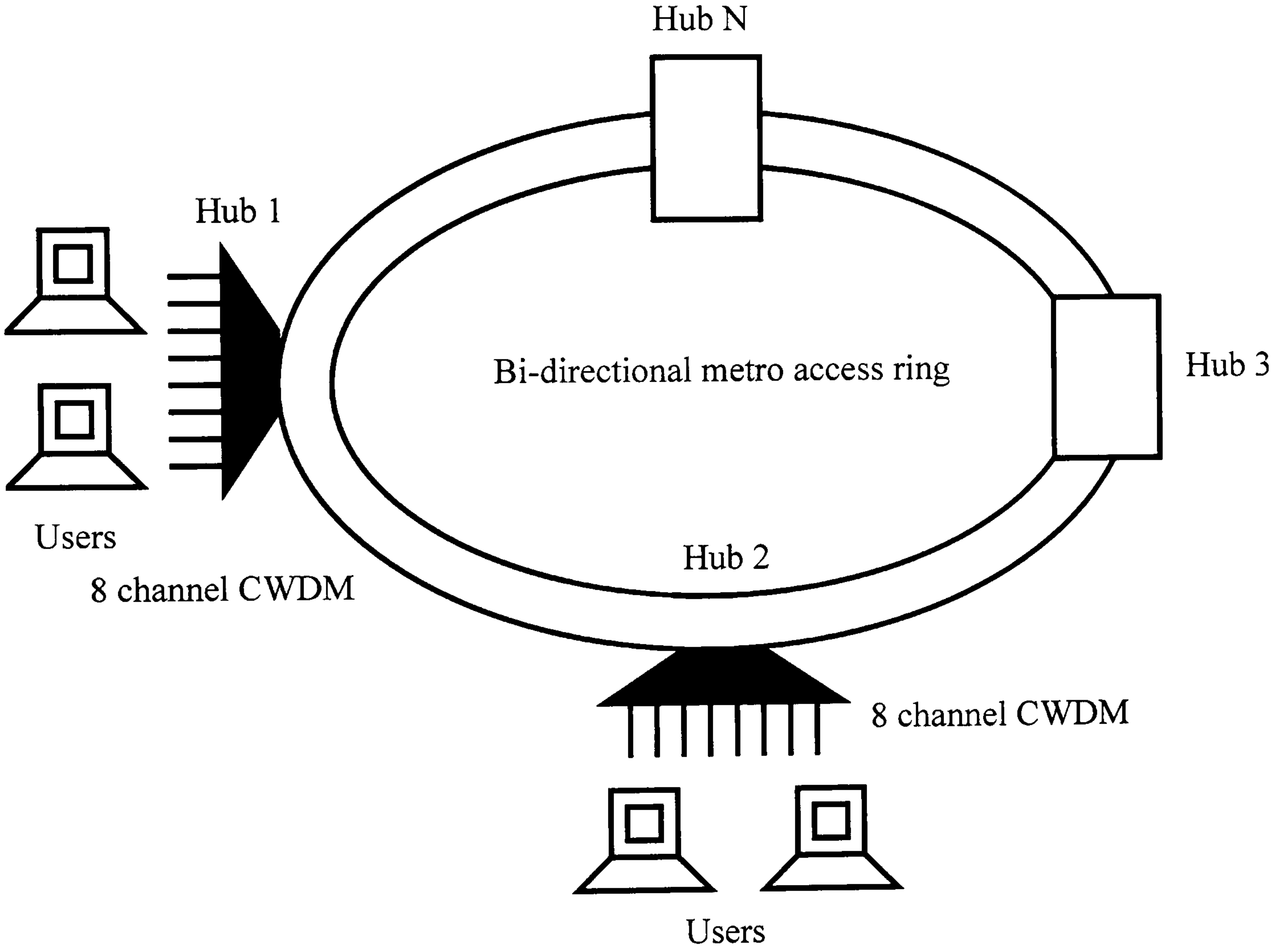

Figure 1-5 Example of a LAN / MAN network using CWDM for an AON

1.2 Optical amplifiers for fibre optic communications

In the previous section, the role of optical amplifiers in telecommunications systems was described. In this section, the various types of fibre and integrated optical amplifiers will be discussed. In particular, the advantages and disadvantages of each for telecommunications applications will be described.

1.2.1 Fibre amplifiers

At present, three types of fibre amplifier, Raman, Brillouin and doped fibre, are used in optical fibre communications. The following will briefly review the operation of each of these.

Raman and Brillouin amplifiers use SRS and SBS respectively to provide amplification at the signal wavelength. In contrast to other types of optical amplifier, these amplifiers use inelastic scattering of a higher energy pump photon to provide gain for a lower energy signal photon. The difference between the pump and signal photons is known as the Stokes shift (approximately 80 → 100 nm in silica fibre). Raman and Brillouin amplifiers have the advantage that they use the transmission line fibre itself as the gain medium. Both types of amplifier have been shown to allow substantial gains of 30 dB or greater, but due to the narrow gain bandwidth of these amplifiers compared to doped fibre amplifiers, they are rarely used for 1.5 μm telecommunications applications.

In contrast to either Raman or Brillouin fibre amplifiers, doped fibre amplifiers use the electronic energy level structures of various ions to facilitate amplification at the signal wavelength. Optical amplifiers are fabricated by doping the core region of the fibre with a suitable concentration of the active element. Many different elements can be used as a dopant to obtain amplification at different wavelengths. To date, erbium (Er), holmium (Ho), ytterbium (Yb), neodymium (Nd), samarium (Sm) and thulium (Tm) have all been investigated for amplifier potential with each element providing the potential for amplification in a different region of the spectrum [8].

The EDFA is easily the most successful of all fibre amplifiers. As show in Figure 1-6, EDFAs utilise the broadband ${}^4I_{13/2} \rightarrow {}^4I_{15/2}$ electronic transition in the Er^{3+} erbium ion to amplify signals in the 1525 → 1610 nm region (C and L telecommunications bands). As shown in Figure 1-6, pumping is achieved optically using either 980 or 1480 nm pump light.

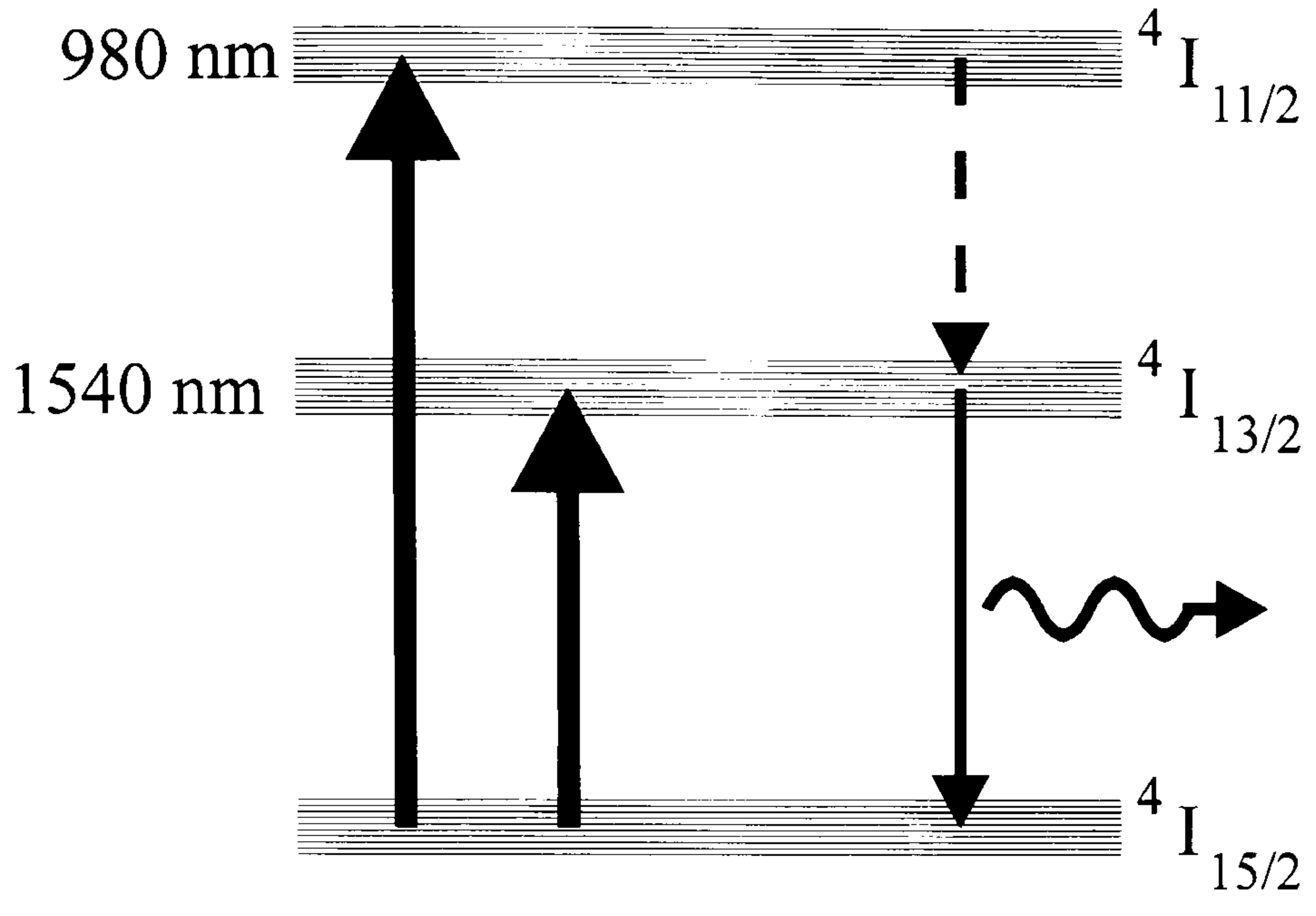

Figure 1-6 Schematic diagram of the first three energy levels of the Er^{3+} ion dissolved in a glass host.

Due to the amorphous nature of the glass host and the circular geometry of the doped core, EDFAs do not exhibit the polarisation dependent loss (PDL) or polarisation dependent gain (PDG) problems that other amplifiers suffer from. Furthermore, the exceptionally long lifetime of upper lasing level (≈ 10 ms) means that EDFAs are immune to interchannel cross talk due to transient gain modulation effects. It is this property in particular that makes EDFAs so suitable for WDM network applications. EDFAs can be designed with negligible PDL and PDG, net gains of over 50 dB, noise figures close to 3 dB and gain flattened bandwidths of ≈ 100 nm. In practice, it is not possible to design a generic cost effective EDFA to exhibit all these properties simultaneously and the performance of a particular EDFA depends entirely on the job which it is designed to do.

1.2.2 Integrated optical amplifiers

The demand for optical amplifiers suitable for LAN and MAN applications is increasing. The performance of suitable amplifiers must be comparable to EDFAs, but importantly they must be small and integrateable with other functions such as splitters, filters and couplers. To meet these demands, a number of integrated optical amplifiers have been developed. The following section will briefly review the properties of three different types of integrated optical amplifier, the semiconductor optical amplifier, the quantum-dot semiconductor optical amplifier and the doped waveguide amplifier.

Semiconductor optical amplifiers (SOAs) are effectively semiconductor lasers that have an input and output signal, and have been designed to prevent feedback oscillation. SOAs for amplification at 1.5 μm are heterostructure semiconductor devices fabricated on an InP base material. The gain material is fabricated from the quaternary compound InGaAsP. By a suitable choice of the gain material composition, the bandgap can be tuned to between 1.24 and 0.75 eV (1.0 and 1.65 μm). SOAs can be particularly useful as pre-amplifiers as they allow monolithic integration with the detector. SOAs do suffer from a number of drawbacks however such as relatively large noise figure (> 6 dB), polarisation sensitivity due to the crystal structure of the gain material and interchannel cross-talk due to cross gain saturation and four wave mixing effects [9]. The latter of these drawbacks makes SOAs unsuitable for WDM applications.

Quantum-dot semiconductor optical amplifiers (QD-SOAs) are fast becoming a possible future competitor to doped waveguide and doped fibre optical amplifier technologies. In a QD-SOA, nano-sized semiconductor particles known as quantum-dots provide the stimulated emission at the signal wavelength. Because the size of an individual quantum-dot is of the order of 10 nm, quantum confinement effects are significant which reduce the allowed energy levels for the holes and electrons within the dot. As a result of these quantum effects, the gain spectrum of a QD-SOA is determined not only by the material bandgap, but also by the size distribution of the dots. In contrast to standard SOAs therefore, QD-SOAs can be inhomogeneously broadened (> 300 nm) by increasing the size distribution of the dots. Because the gain spectrum of a QD-SOA is inhomogeneously broadened, QD-SOAs do not suffer to the same degree as standard SOAs from inter-channel cross talk [10]. In addition, QD-SOAs have also been shown to exhibit high saturation output powers and low noise figures [11]. As yet however, QD-SOAs are not commercially available.

Doped waveguide amplifiers operate in exactly the same way as doped fibre amplifiers. In contrast to fibre amplifiers however, waveguide amplifiers are generally fabricated in a planar format using techniques reliant on photolithography. Due to the smaller interaction length in doped waveguide amplifiers they require substantially higher concentrations of the active ions when compared to fibre amplifiers. The most important advantages of doped waveguide amplifiers are their size and the possibility of combining other functions such as splitters or interleavers on the same device. At present, only the EDWA has attracted substantial research attention. EDWA devices are currently commercially available, these devices will be reviewed in the following section.

1.3 State of the art in erbium doped waveguide amplifiers (EDWAs)

Integrated EDWAs and lasers have been the subject of great research attention since the start of the 1990s. Thus far, devices showing optical gain have been fabricated using many different routes including sol-gel [12], femtosecond waveguide inscription (FWI) [13], plasma enhanced chemical vapour deposition (PECVD) [14], flame hydrolysis deposition (FHD) [15], RF-sputtering [16], ion indiffusion / exchange [17], ion implantation [18], e-beam evaporation [19], and doped polymer routes to name a few. Other routes such as pulsed laser deposition (PLD) are also currently under investigation but have not yet resulted in operational devices. In addition to the various fabrication routes, a number of different host materials have been investigated. These materials include both crystalline hosts such as $LiNbO_3$ as well as amorphous hosts such as phosphate and tellurite glasses.

In the following section, brief descriptions of the state of the art in both commercially available EDWA devices and EDWA research will be given. In addition, a more detailed review of the state of the art in each of the EDWA fabrication routes of particular interest to this thesis will also be given.

1.3.1 Commercially available devices

To the best of the author's knowledge, EDWA devices are currently only commercially available from Teem Photonics [20]. Teem Photonics offer a number of EDWA based devices including an amplifier-splitter / combiner series, an amplifier array series and a single amplifier only series. The amplifier-splitter / combiner series combine multiplexer or de-multiplexer functions with an amplifier in one package. They can combine or separate up to eight different wavelengths for CWDM networks while providing up to 10 dB of amplification for signals between 1530 and 1560 nm. The device exhibits noise figures of < 7dB, PDL and PDG values of < 0.5 dB and a gain uniformity of < 0.5 dB. The functions are carried out on single package with dimensions 13 × 2.7 × 1.3 cm, which includes a 980 nm pump laser with a thermoelectric cooler. The amplifier array series offered by Teem Photonics combines four EDWAs in a single package. Each amplifier can deliver small signal net gains of > 15 dB for signals in the 1530 - 1560 nm range with a 7 dB noise figure. The packaged device is 9.5 × 5.5 × 1.2 cm in size and incorporates un-cooled pump laser diodes. Finally, the amplifier-only series can supply small signal net gains of up to 27 dB for signals in the 1530-1560 nm range, with noise figures of < 7 dB. The packaged device is 8.1 × 3.5 × 1.2 cm in size and incorporates an uncooled laser diode pump.

Although the specifications and range of functionality of the devices available from Teem Photonics is impressive, there is still scope to improve the function of EDWA devices and develop new fabrication routes to reduce costs. As a result, EDWAs are still the subject of great research interest. The following section will review the state-of-the-art in current EDWA research, highlighting the achievements of each fabrication route.

1.3.2 General overview of EDWA research

EDWAs are still currently the subject of great research interest with research being driven by the need for smaller and cheaper amplifiers with improved functionality. With this in mind, the specifications of the commercially available EDWAs given in section 1.3.1 do give a good idea of the level of functionality and performance that any EDWA in the research stage should at least aim to provide.

To date, EDWAs have been fabricated using numerous different routes. To compare the achievements of each fabrication route, Table 1-1 lists the highest net gains reported to date from EDWA devices fabricated using each of the most significant routes.

Fabrication method	Core material	Erbium concentration	Propagation loss ($dB.cm^{-1}$)	Net gain @ pump power (dB@mW)	Transparency pump power	Waveguide length (cm)	Gain / unit length ($dB.cm^{-1}$)	Noise Figure (dB)	Pump wavelength (nm)	Ref.
Sol-gel	ErYb: aluminophosphosilicate	0.25 mol. %	0.1	5.4@175	25	5.0	1.08	-	980	[12]
PECVD	phosphosilicate glass	0.48 wt.%	0.17	5.0 @ 420	23	7.5	0.67		980	[14]
FHD	Silicate	0.45 wt. %	-	27@264	55	47.7	0.56		980	[15]
RF-sputtering	Bismuthate glass	6250 ppm	0.13	18@280	-	24	0.75	5.5	1480	[21]
FWI	ErYb:Phosphate	2.0 wt. %	0.4	7.3@460	≈200	3.7	1.97	<5	975	[13]
Ion-indiffusion / exchange	Er:Yb:Phosphate	2.0 wt. %	< 0.1	11.6@120	NA	4.5	2.58	<4.5	975	[17]
Ion-implantation	$Er:Al_2O_3$	2.7×10^{20} $ions.cm^{-3}$	0.35	2.3@9	3	4.0	0.58	-	1480	[22]
Doped polymer	ErYb doped organic polymer	0.33×10^{20} $ions.cm^{-3}$	-	13@110 (Relative)	-	1.8	-	-	980	[23]

Table 1-1 Highest net gains reported to date from EDWA devices

As can be seen from Table 1-1, the achievements of each of the fabrication routes are wide ranging. Although fabrication routes such as FHD have resulted in devices exhibiting very high net gains, the ability to homogeneously dope the core layer at high doping concentrations is limited. As a result, long waveguide lengths are required to provide the necessary gain, increasing the device size on the wafer and increasing fabrication costs. One approach to fabricating smaller amplifiers is to use materials that allow large net gains / unit length. At present, the highest net gain / unit length was reported by Patel et al who fabricated a 3 mm long waveguide in an ErYb-doped phosphate glass using ion-exchange technology [24]. The device exhibited a net gain of 4.1 dB giving a net gain / unit length of 13.7 $dB.cm^{-1}$. Another approach to reducing the device size is to use materials that allow waveguides with high refractive index contrasts and therefore small bend radii to be fabricated. Using RF-sputtering, Kondo et al fabricated a 24 cm long Er-doped bismuthate EDWA on a chip only 1 cm^2 in area using a spiral waveguide path. As detailed in Table 1-1, the device exhibited an impressive peak net gain of 18 dB.

In addition to fabricating smaller amplifiers with higher net gains, much of the present research is focussed on fabricating low cost amplifiers using routes such as sol-gel and doped polymer waveguides that do not require expensive fabrication facilities. In one recent demonstration, Wong et al reported the direct UV printing of Er-doped polymer waveguide arrays on thermally oxidised silicon [25], a proof-of-concept demonstration that certainly shows the feasibility of fabricating very low cost EDWA devices.

Clearly, many different approaches to fabricating EDWA devices are currently under investigation and the EDWA area as a whole is still very much at the research stage. Each of the fabrication routes exhibits potential benefits such as scalability or cost. The following section will review more thoroughly the areas of EDWA fabrication that are of particular interest to this thesis.

1.3.3 EDWA fabrication via sol-gel

The sol-gel method provides a simple, low cost route for fabricating dense smooth glass layers. The first step in the sol-gel method is to produce a suspension (sol) which contains all the elements required to form the final glass matrix. This is done by adding precursors to a solvent such as alcohol in the correct quantities, followed by an hydrolysis step using water. The second step is to spin coat the sol onto the desired substrate. This step produces a thin gel layer consisting of all the elements that will form the glass and a substantial amount of the solvent. The solvent is then removed from the gel layer by heating in an oven. In practice only a fume cupboard, spin coater and oven are required to produce sol-gel glass films.

The first attempt to fabricate erbium doped planar waveguides using a sol-gel route was reported by Bahat et al in 1994 using a TiO_2 host material [26]. Since then, various groups have explored other host materials such as, SiO_2 [27], Al_2O_3-SiO_2 [28], GeO [29], Al_2O_3 [30]. $BaTiO_3$ [31], multicomponent silcate [32] and Y_2O_3 [33] to name a few. Few groups have however fabricated channel waveguides from these films.

The first reported attempt to fabricate erbium doped channel waveguide devices using the sol-gel route was published by Orignac et al in 1999 using a predominantly SiO_2-TiO_2 host material [34]. The group used a strip loaded waveguide structure and an Er-Yb doped core layer doped with ≈ 0.2 at.% Er. Although the device structure was not optimum, the group reported a relative gain (signal enhancement) of 2.7 dB for a 5.7 cm long device (0.5 $dB.cm^{-1}$) under 100 mW of 980 nm pumping, and estimated the fraction of excited ions to be about 25 %. Later on that year Yeatman et al reported a slightly higher relative gain coefficient of 1 $dB.cm^{-1}$, but with only a slightly higher fraction of the ions excited (≈ 30%) [35]. Over the next 3 years little work was reported in this area until in 2002, Huang et al reported the first fibre-device-fibre net gain from a sol-gel fabricated EDWA. The device exhibited a net gain of 5.75 dB for a 5 cm long device and was fabricated using a hybrid sol-gel / PECVD fabrication route whereby the multicomponent silicate core material, doped with 0.25 mol% Er_2O_3 and 0.25 mol% Yb_2O_3, was deposited using the sol-gel route, but the upper cladding material was deposited using PECVD. Clearly the results reported by Huang et al demonstrate the potential for the fabrication of low cost EDWA devices using the sol-gel route. In a later paper published by the same group [36], it was reported that the advancement in the fabrication was moving to a material host with lower process temperatures than the SiO_2-TiO_2 host previously investigated. As a result, high doping concentrations were possible while maintaining a high degree of doping homogeneity.

Although the results reported by Huang et al are impressive, the fabrication of the device was time consuming and therefore not cost-effective in a commercial environment. The core layer required the use of 20 iterative spin coating cycles to overcome problems with stress induced cracking in thick films, and the cladding layer was fabricated using PECVD, an expensive technology that would negate the commercial benefits of using the sol-gel route. As a result, there is undoubtedly scope for improvement in both the device operation and fabrication. With this in mind, we published the first report of erbium doped waveguide fabrication using a novel single sol-gel deposition route [37]. In comparison to other reported devices, our devices were fabricated using only a single sol-gel deposition for each of the core and cladding layers. At present, the results published, both by us and by Huang et al represent the state of the art in sol-gel EDWA fabrication.

1.3.4 EDWA fabrication via pulsed laser deposition (PLD)

Pulsed laser deposition (PLD) is an extremely versatile route for fabricating thin films. Thin films of almost any material can be fabricated by ablating a target material / materials using a pulsed laser, and depositing the plume of ablated material onto a substrate. Although the technique of PLD is well researched, its application to the fabrication of erbium doped integrated optical devices is much less so.

The first report of Er-doped film production using PLD was by Afonso et al in 1996 who reported the fabrication of an ErYb-doped phosphate glass planar waveguide by ablating an ErYb-doped phosphate glass target [38]. The same group later reported that the Er^{3+} ions were optically active in these films, but that the $^4I_{13/2} \rightarrow {}^4I_{15/2}$ transition fluorescence lifetime was approximately 200 μs, significantly shorter than has been reported for bulk materials of the same composition [39]. Serna et al, of the same group later reported that same year the fabrication of $Er:Al_2O_3$ films using PLD. In this work they used separate Al_2O_3 and Er ablation targets to build up a 200 nm Er-doped Al_2O_3 film. The advantage of this technique was the ability to control the Er doping profile by varying the number and frequency of ablations from the Er target throughout the deposition. The films were doped with 1 at. % erbium and exhibited a $^4I_{13/2} \rightarrow {}^4I_{15/2}$ transition fluorescence lifetime of 4.4 ms after annealing [40]. The same group later reported on the importance of the erbium ion-ion spacing on the fluorescence lifetime in similar films and were able to show an increase in the $^4I_{13/2} \rightarrow {}^4I_{15/2}$ transition fluorescence lifetime from 6 → 7 ms by increasing the ion-ion separation from 3-9 nm [41,42]. Suarez-Garcia et al, again of the same group, later reported the incorporation of Yb into similar films using a multi-target technique and reported an increase in the fluorescence yield at 1.5 μm of over two orders of magnitude due to efficient energy transfer to the Er ions from the Yb ions [43]. Lanzerstorfer et al was the first to report the fabrication of Er:SiO_2 and Er-doped soda lime silicate glass films using PLD in 1999 and found that the Er-doped soda lime glass films exhibited much higher luminescence yield due to the higher solubility of erbium in the multi-component silicate host [44]. In 2003, Martino et al reported the fabrication of optically active Er-doped tellurite planar waveguides using PLD [45,46]. These waveguides were found however to have high propagation losses in the region of 20 dB.cm^{-1} at 633 nm. No mention was made to the $^4I_{13/2} \rightarrow {}^4I_{15/2}$ transition fluorescence lifetime in these films. Recently, in 2005, Martino et al reported the first fabrication of Er-doped oxyfluoride silicate glass planar waveguide films using PLD [47]. Again, no mention was made to the magnitude of the $^4I_{13/2} \rightarrow {}^4I_{15/2}$ transition fluorescence lifetime in these films or the propagation losses.

The majority of work thus far on fabricating Er-doped devices using PLD has centred on optimising the fabrication of thin film planar waveguides. Chapter 4 of this thesis describes the development of the first Er-doped channel waveguides using PLD [48]. The films used for this study were fabricated by Martino et al in work similar to that described in [47]. As described in [48], planar waveguide films with propagation losses in the region of 1 dB.cm^{-1} at 633 nm were fabricated. It was found however that the $^4I_{13/2} \rightarrow {}^4I_{15/2}$ transition fluorescence lifetime was very short (< 0.1 ms) indicating the presence of significant quenching mechanisms.

1.3.5 EDWA fabrication using femtosecond waveguide inscription (FWI)

Recently it has been demonstrated that under the correct fabrication conditions, optical waveguides may be fabricated by translating a transparent dielectric material through the focus of a focussed femtosecond pulse train [49]. Since this first demonstration, FWI has been applied to numerous active materials and glasses.

The first report of femtosecond inscripted waveguides supporting a 1550 nm mode was by Coric et al in 2002 [50]. Since then, this technique has been applied to a number of Er-doped and ErYb-doped materials. The first report of waveguide writing in an Er-doped material was in 2002 by Osellame et al [51] who fabricated a low insertion loss, active waveguide in an ErYb-doped phosphate glass. Although unable to demonstrate net gain, an internal gain of 0.2 dB at 1565 nm was demonstrated for the 25 mm long device. An operational amplifier device was not demonstrated until 2004 when Osellame et al reported the fabrication of an ErYb-doped waveguide amplifier using FWI. The 12 mm long device was fabricated in an ErYb-doped phosphate glass, had a total insertion loss of ≈ 1.5 dB and was able to supply a maximum net gain of up to 1.2 dB at 1533 nm under 250 mW of bi-directional 980 nm pumping [52]. The highest net gain from a femtosecond inscripted waveguide amplifier was again reported by the same group in 2005 by Della Valle et al [13]. The 37 mm long waveguide device was again fabricated in the same ErYb-doped phosphate glass and had a total background insertion loss of ≈ 1.9 dB. When pumped with 460 mW of bi-directional 980 nm pumping the device exhibited net gain across the whole of the C-band with a minimum net gain of 3.6 dB at 1565 nm and a maximum net gain of 7.3 dB at 1535 nm. The minimum saturation output power was measured to be 8.4 dBm at 1535 nm and the maximum noise figure was measured to be approximately 5 dB at 1535 nm. Although the operation of this device is not quite at the stage of commercially available devices, it certainly proves the feasibility of this waveguide fabrication technique for optical amplifier applications.

As outlined above, all operational devices have been fabricated in Er-doped phosphate glasses. In addition to this work, other work is ongoing to fabricate optical amplifiers using FWI in different Er-doped glasses. One particularly promising candidate is Er-doped oxyfluoride-silicate glass which has been shown in previous work to combine the structural properties of a silica based glass with the spectroscopic properties of a fluoride based glass [53]. Recent results published by us [54,55] indicate that Er-doped oxyfluoride silicate glass is a promising candidate for amplifier fabrication using FWI.

1.4 Thesis outline

The work described in this thesis is aimed at developing novel fabrication techniques for telecommunications LAN and MAN components. The majority of the work is centred on developing novel EDWAs using sol-gel, PLD and FWI. In addition to these primary research areas, some additional research carried out by the author on the femtosecond inscription of optical waveguides in crystalline $LiNbO_3$ is also described in this thesis. The outline of the thesis is as follows.

In Chapter 2, the physical operation of an EDWA is described. In particular, the physics and role of both the Er^{3+} ion and the waveguide structure itself is outlined. To understand the significance of each physical property in the EDWA operation, a mathematical model is developed to model the EDWA operation.

Chapters 3, 4 and 5, describe studies of Er-doped waveguide fabrication using the sol-gel, PLD and FWI routes respectively. Additional work carried out by the author on FWI in crystalline $LiNbO_3$ is also described in Chapter 5.

Finally, Chapter 6 draws conclusions from the studies presented in Chapters 3, 4 and 5 and suggests possible future work in each area.

1.5 References

[1] J. M. Senior, "Transmission characteristics of optical fibers," in *Optical fiber communications: Principles and Practice*, 2nd ed., Prentice hall, 1992, pp. 91.

[2] G. Keiser, "Basic concepts of communications systems," in *Optical communications essentials,* McGraw-Hill, 2003, pp. 10.

[3] G. P. Agrawal, "Optical fibers," in *Fiber-optic communications systems*, 2nd ed., John Wiley & Sons, 1997, pp. 44.

[4] G. P. Agrawal, "Multichannel lightwave systems," in *Fiber-optic communications systems*, 2nd ed., John Wiley & Sons, 1997, pp. 318-329.

[5] G. P. Agrawal, "WDM Systems" in *Lightwave technology-Telecommunications systems,* John Wiley & Sons, 2005, pp. 350.

[6] J. X. Cai, D. G. Foursa, C. R. Davidson, Y. Cai, G. Domagala, H. Li, L. Liu, W. W. Patterson, A. N. Pilipetskii, M. Nissov, and N. S. Bergano, "A DWDM Demonstration of 3.73 Tb/s over 11,000 km using 373 RZ-DPSK Channels at 10 Gb/s," *Proc. Optical fiber Communications Conf.*, Optical Society of America, Washington, DC, 2004, Paper PD22-1.

[7] G. Keiser, "Connecting the WDM netwrok puzzle," in *Optical communications essentials,* McGraw-Hill, 2003, pp. 230.

[8] M. Dejneka and B. Samson, "Rare-Earth-Doped Fibres for Telecommunications Applications," *MRS Bulletin*, vol 24, no. 9 pp. 39-45, Sep. 2005.

[9] G.P.Agrawal, "Lightwave technology-components and devices," New Jersey: John Wiley & Sons, 2004, pp. 214-215.

[10] D. Bimberg, N. Kirstaedter, N. N. Ledentsov, Z. I. Alferov, P. S. Kop'ev, and V. M. Ustinov, "InGaAs-GaAs quantum-dot lasers," *IEEE J. Sel. Top. Quant.*, vol. 3, no. 2, pp. 196-205, Apr. 1997.

[11] T. Akiyama, K. Kawaguchi, M. Sugawara, M. Ekewa, H. Ebe, and Y. Arakawa, "Quantum-dot semiconductor optical amplifiers," *IEEE-LEOS newsletter,* vol. 20, no. 1, pp. 11-13. Feb. 2006.

[12] W. Huang, R. R. A.Syms, E. M. Yeatman, M. M. Ahmad, V. T. Clapp., and S. M. Ojha, "Fiber-device-fiber gain from a sol-gel erbium-doped waveguide amplifier," *IEEE Photon. Technol. Lett.*, vol 14, no. 7, 959-961, Jul 2002.

[13] G. Della Valle, R. Osellame, N. Chiodo, S. Taccheo, G. Cerullo, P. Laporta, A. Killi, U. Morgner, M. Lederer, and D. Kopf, "C-band waveguide amplifier produced by femtosecond laser writing," *Opt. Express*, vol. 13, no. 16, pp. 5976-5982, Aug. 2005.

[14] K. Shuto, K. Hattori, T. Kitagawa, Y. Ohmori, and M. Horiguchi, "Erbium doped phosphosilicate glass waveguide amplifier fabricated by PECVD," *Electron. Lett.*, vol 29, no. 2, pp. 139-141, Jan. 1993.

[15] K. Hattori, T. Kitagawa, M. Oguma, Y. Ohmori, and M. Horiguchi, "Erbium-doped silica-based waveguide amplifier integrated with a 980/1530 nm WDM Coupler," *Electron. Lett.*, vol. 30, no. 11, pp. 856-857, May 1994.

[16] Y. C. Yan, A. J. Faber, H .de Waal, P. G. Kik, and A. Polman, "Erbium-doped phosphate glass waveguide on silicon with 4.1 dB/cm gain at 1.535 μm," *Appl. Phys. Lett.*, vol. 71, no. 20, pp. 2922-2924, Nov. 1997.

[17] D. Barbier, M. Rattay, F. Saint Andre, G. Clauss, M. Trouillon, A. Kevorkian, J. M. P. Delavaux, and E. Murphy, "Amplifying four-wavelength combiner, based on erbium / ytterbium - doped waveguide amplifiers and integrated splitters," *IEEE Photon. Technol. Lett.*, vol. 9, no. 3, pp. 315-317, Mar. 1997.

[18] P. G. Kik and A. Polman, "Cooperative upconversion as the gain-limiting factor in Er doped miniature Al_2O_3 optical waveguide amplifiers," *J. Appl. Phys.*, vol. 93, no. 9, pp. 5008-5012, May. 2003.

[19] M. Nakazawa and Y. Kimura, "Electron-beam vapour-deposited erbium-doped glass waveguide laser at 1.53μm," *Electron. Lett.*, vol. 28, no. 22, pp. 2054-2056, Oct. 1992.

[20] Teem Photonics. (2002, Oct), "Optical amplifier products". [Online]. Available: http://www.teemphotonics.com/documents/product/edwa/metro.pdf

[21] Y. Kondo, M. Ono, J. Kageyama, M. Reyes, H. Hayashi, and N. Sugimoto, "1-cm^2-size Er-doped waveguide based on bismuthate glass for compact amplifier with > 15 dB gain at whole C-band," *Proc. Optical fiber Communications Conf.*, Optical Society of America, Washington, DC, 2005, Paper PDP2.

[22] G. N. van den Hoven, R. J. I. M. Koper, A. Polman, C. van Dam, J. W. M. van Uffelen, and M. K. Smit, "Net optical gain at 1.53 μm in Er-doped Al_2O_3 waveguides on silicon," *Appl. Phys. Lett.*, vol. 68, no. 14, pp. 1886-1888, Apr. 1996.

[23] W. H. Wong, E. Y. B. Pun, and K. S. Chan, "Er^{3+}-Yb^{3+} codoped polymeric optical waveguide amplifiers," *Appl. Phys. Lett.*, vol. 84, no. 2, pp. 176-178, Jan. 2004.

[24] F. D. Patel, S. DiCarolis, P. Lum, S. Venkatesh, and J. N. Miller, "A compact high-performance optical waveguide amplifier," *IEEE Photonic. Tech. L.*, vol. 16, no. 12, pp. 2607-2609, Dec. 2004.

[25] W. H. Wong, K. S. Chan, and E. Y. B. Pun, "Ultraviolet direct printing of rare-earth-doped polymer waveguide amplifiers," *Appl. Phys. Lett.*, vol. 87, Art. 011103, Jul. 2005.

[26] A. Bahtat, M. Bouazaoui, M. Bahtat, and J. Mugnier, "Fluorescence of Er^{3+} ions in TiO_2 planar waveguides prepared by a sol-gel process," *Opt. Commun.*, vol. 111, no. 1-2, pp. 55-60, Sept. 1994.

[27] C. K. Ryu, H. Choi, and K. Kim, "Fabrication of highly concentrated Er^{3+} doped aluminosilicate films via sol-gel processing," *Appl. Phys. Lett.*, vol. 66, no. 19, pp. 2496-2498, May 1995.

[28] M. Benatsou, B. Capoen, M. Bouazaoui, W. Tchana, and J. P. Vilcot, "Preparation and characterization of sol-gel derived Er^{3+}:Al_2O_3-SiO_2 planar waveguides," *Appl. Phys. Lett.*, vol. 71, no. 4, pp. 428-430, Jul. 1997.

[29] G. Brusatin, M. Guglielmi, and A. Martucci, "GeO_2-based sol-gel films," *J. Am. Ceram. Soc.*, vol. 80, no. 12, pp. 3139-3144, Dec. 1997.

[30] Y. Kurokawa, T. Ishizaka, T. Ikoma, and S. Tero-Kubota, "Photo-properties of rare earth ion (Er^{3+}, Eu^{3+} and Sm^{3+}) - doped alumina films prepared by the sol-gel method," *Chem. Phys. Lett.*, vol. 287, no. 5-6, pp. 737-741, May 1998.

[31] H. X. Zhang, C. H. Kam, Y. Zhou, X. Q. Han, S. Buddhudu, Q. Xiang, Y. L. Lam, and Y. C. Chan, "Green upconversion luminescence in Er^{3+}: $BaTiO_3$ films," *Appl. Phys. Lett.*, vol. 77, no. 5, pp. 609-611, 2000.

[32] A. Biswas, G. S. Maciel, R. Kapoor, C. S. Friend, and P. N. Prasad, "Er^{3+}-doped multicomponent sol-gel-processed silica glass for optical signal amplification at 1.5 μm," *Appl. Phys. Lett.*, vol. 82, no. 15, pp. 2389-2391, Apr. 2003.

[33] H. Guo, W. Zhang, L. Lou, A. Brioude, and J. Mugnier, "Structure and optical properties of rare earth doped Y_2O_3 waveguide films derived by sol-gel process," *Thin Solid Films*, vol. 458, no. 1-2, pp. 274-280, Jun. 2004.

[34] X. Orignac, D. Barbier, X. M. Du, R. M. Almeida, O. McCarthy, and E. Yeatman, "Sol-gel silica/titania-on-silicon Er/Yb-doped waveguides for optical amplification at 1.5 μm," *Opt. Mater.*, vol. 12, no. 1, pp. 1-18, May 1999.

[35] E. M. Yeatman, M. M. Ahmad, O. McCarthy, A. Vannucci, P. Gastaldo, D. Barbier, D. Mongardien, and C. Moronvalle, "Optical gain in Er-doped SiO_2-TiO_2 waveguides fabricated by the sol-gel technique," *Opt. Commun.*, vol. 164, no. 1-3, pp. 19-25, Jun. 1999.

[36] A. Laliotis, E. M. Yeatman, M. M. Ahmad, and W. Huang, "Molecular homogeneity in erbium-doped sol-gel waveguide amplifiers," *IEEE J. Quantum Electron.*, vol 40, no. 6, pp. 805-814, Jun 2004.

[37] R. R. Thomson, H. T. Bookey, H. Ur-Rehman, S. Liu, N. Suyal, and A. K. Kar, "Optically active erbium doped waveguides fabricated using a single-sol-gel deposition technique," *J. Lightwave Technol.*, vol. 23, no. 12, pp. 4249-4256, Dec. 2005.

[38] C .N. Afonso, J. M. Ballesteros, J. Gonzalo, G. C. Righini, and S. Pelli, "Rare-earth doped glass waveguides prepared by pulsed laser deposition," *Appl. Surf. Sci.*, vol. 96-98 pp. 760-763, Apr. 1996.

[39] R. Serna, J. M. Ballesteros, M. Jiménez de Castro, J. Solis, and C. N. Afonso, "Optically active Er-Yb doped glass films prepared by pulsed laser deposition," *J. Appl. Phys.*, vol. 84, no. 4, pp. 2352-2354, Aug. 1998.

[40] R. Serna and C. N. Afonso, "In situ growth of optically active erbium doped Al_2O_3 thin films by pulsed laser deposition," *Appl. Phys. Lett.*, vol. 69, no. 11, pp. 1541-1543, Sep. 1996.

[41] R. Serna, M. Jiménez de Castro, J. A. Chaos, C. N. Afonso, and I. Vickridge, "The role of Er^{3+}-Er^{3+} separation on the luminescence of Er-doped Al_2O_3 films prepared by pulsed laser deposition," *Appl. Phys. Lett.*, vol. 75, no. 26, pp. 4073-4075, Dec. 1999.

[42] R. Serna, M. Jiménez de Castro, J. A. Chaos, A. Suárez-Garcia, C. N. Afonso, M. Fernández, and I. Vickridge, "Photoluminescence performance of pulsed-laser deposited Al_2O_3 thin films with large erbium concentrations," *J. Appl. Phys.*, vol. 90, no. 10, pp. 5120-5125, Nov. 2001.

[43] A. Suarez-Garcia, R. Serna, M. Jiménez de Castro, C. N. Afonso, and I. Vickridge, "Nanostructuring the Er-Yb distribution to improve the photoluminescence response of thin films," *Appl. Phys. Lett.*, vol. 84, no. 12, pp. 2151-2153, Mar. 2004.

[44] S. Lanzerstorfer, J. D. Pedarnig, R. A. Gunasekaran, D. Bäuerle, and W. Jantsch, "1.54 μm emission of pulsed-laser deposited Er-doped films on Si," *J. Lumin.*, vol. 80, no. 1-4, pp. 353-356, Dec. 1998.

[45] M. Martino, A. P. Caricato, M. Fernández, G. Leggieri, A. Jha, M. Ferrari, and M. Mattarelli, "Pulsed laser deposition of active waveguides," *Thin Solid Films* vol. 433, no. 1-2, pp. 39-44, Jun. 2003.

[46] A. P. Caricato, M. Fernández, M. Ferrari, G. Leggieri, M. Martino, M. Mattarelli, M. Montagna, V. Resta, L. Zampedri, and R. M. Almeida. "Er^{3+} doped tellurite waveguides deposited by excimer laser ablation," *Mat. Sci. Eng. B-Solid*, vol. 105, no. 1-3, pp. 65-69, Dec. 2003.

[47] M. Martino, A. P. Caricato, A. Fazzi, F. Romano, V. K. Tikhomirov, A. B. Seddon, M. Mattarelli, A. Chiappini, and K. C. Vishnubhatla, "Pulsed laser deposition of Er^{3+}-doped oxyfluoride thin films," *J. Non-Cryst. Solids*, vol. 351, no. 21-23, pp. 1810-1813, Jul. 2005.

[48] R. R. Thomson, H. T. Bookey, A. K. Kar, M. R. Taghizadeh, A. Klini, C. Fotakis, F. Romano, A. P. Caricato, M. Martino, S. Shen, and A. Jha, "Erbium-doped waveguide fabrication via reactive pulsed laser deposition of erbium-doped oxyfluoride-silicate glass," *Electron. Lett.*, vol. 41, no. 25, pp. 1376-1377, Dec. 2005.

[49] K. M. Davis, K. Miura, N. Sugimoto, and K. Hirao, "Writing waveguides in glass with a femtosecond laser," *Opt. Lett.*, vol. 21, no. 21, pp. 1729-1731, Nov. 1996.

[50] D. Ćorić, P. R. Herman, R. Dhardwaj, P. B. Corkum, and D. M. Rayner, "Prospects for ultrafast-laser writing of three-dimensional photonic devices for telecom applications," *Proc. Optical fiber Communications Conf.*, Optical Society of America, Washington, DC, 2002, Paper ThGG52

[51] R. Osellame, S. Taccheo, G. Cerullo, M. Marangoni, D. Polli, R. Ramponi, P. Laporta, and S. De Silvestri, "Optical gain in Er-Yb doped waveguides fabricated by femtosecond laser pulses," *Electron. Lett.*, vol. 38, no. 17, pp. 964-965, Aug. 2002.

[52] R. Osellame, N. Chiodo, G. Della Valle, S. Taccheo, R. Ramponi, G. Cerullo, A. Killi, U. Morgner, M. Lederer, and D. Kopf, "Optical waveguide writing with a diode-pumped femtosecond oscillator," *Opt. Lett.*, vol. 29, no. 16, pp. 1900-1902, Aug. 2004.

[53] S. X. Shen and A. Jha, "The influence of F^--ion doping on the fluorescence ($^4I_{13/2} \rightarrow {}^4I_{15/2}$) line shape broadening in Er^{3+}-doped oxyfluoride silicate glasses," *Opt. Mater.*, vol. 25, no. 3, pp. 321-333, Apr. 2004.

[54] R. R. Thomson, S. Campbell, I. J. Blewett, A. K. Kar, D. T. Reid, S. Shen and A. Jha, "Active waveguide fabrication in erbium doped oxyfluoride silicate glass using femtosecond pulses," *Appl. Phys. Lett.*, vol. 87, Art. 121102, Sept. 2005.

[55] R. R. Thomson, H. T. Bookey, N. Psaila, S. Campbell, D. T. Reid, S. Shen, A. Jha, and A. K. Kar, "Internal gain from an erbium-doped oxyfluoride-silicate glass waveguide fabricated using femtosecond waveguide inscription," *IEEE Photonic. Tech. L.,* vol. 18, no. 14, pp. 1515-1517, Jul. 2006.

Chapter 2-The physics of an erbium-doped waveguide amplifier (EDWA)

2.1 Introduction

EDWA devices have been fabricated using many different routes and materials, but the physical principles behind the operation of all EDWAs are the same. This chapter aims to describe these principles to the reader, with the aim of identifying the physical parameters that affect the operation of an EDWA. To understand the significance of each of these parameters, a simple model is used to quantitatively investigate their effect on the gain vs. pump power characteristics of a theoretical EDWA.

2.2 The basic operation of an EDWA

The operation of an EDWA can be summarised as follows. Continuous wave pump light is coupled into an Er-doped waveguide at either one or both ends. As the pump light travels along the waveguide, it excites Er^{3+} ions to a higher energy level and induces a population inversion. Signal light from a fibre optic transmission line is coupled into the Er-doped waveguide via a pump / signal multiplexer and is amplified by stimulated emission processes associated with the excited Er^{3+} ions as it travels along the waveguide. At the output end of the waveguide the amplified signal is de-multiplexed from any unabsorbed pump light using a second pump / signal multiplexer, and coupled back into the fibre optic transmission line. Strictly speaking, the entire EDWA device consists of pump lasers, multiplexers, electronics and the Er-doped waveguide itself. Since all of these technologies are common to all EDWAs, with the exception of the Er-doped waveguide, we will consider only the physics and operation of the Er-doped waveguide.

Figure 2-1 is a diagram of one of many possible Er-doped waveguide constructions. The waveguide shown in Figure 2-1 consists of an Er-doped dielectric core region of refractive index n_2, surrounded on all sides by an undoped dielectric cladding material of refractive index n_1. The compositions of the core and cladding materials are chosen such that $n_2 > n_1$ to achieve guiding at both the signal and pump wavelengths.

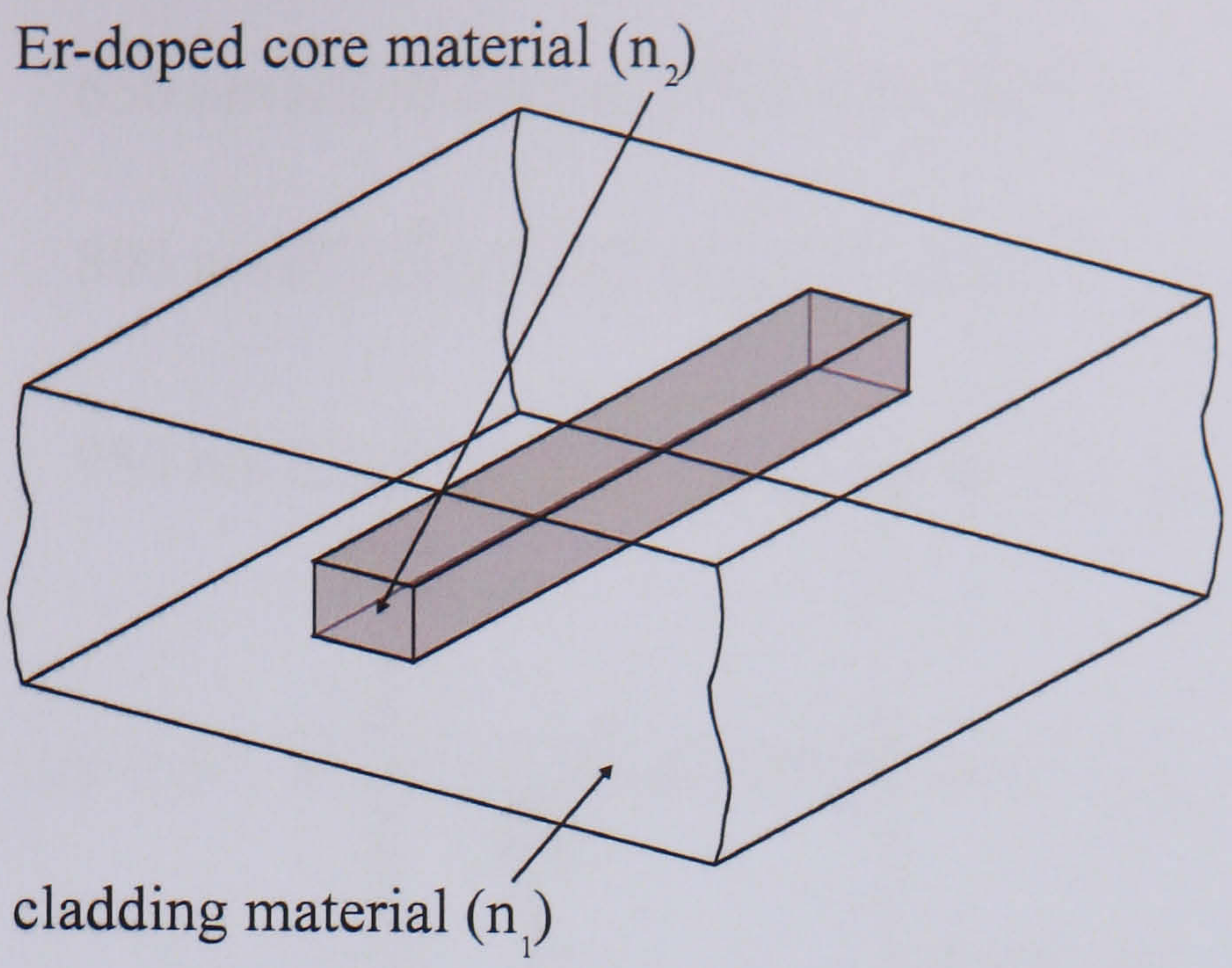

Figure 2-1 Typical Er-doped waveguide construction

The operation of an EDWA relies on two separate sets of physical properties associated with the Er-doped waveguide. The first set of properties are associated with the Er-doped laser material, the second set of properties are associated with the waveguide structure. The following sections will describe and discuss the role and physics of each.

2.3 The physics and role of the Er^{3+} ion

2.3.1 Er^{3+} ion energy level structure

At the heart of EDWA operation are the Er^{3+} ions themselves. The erbium atom has the electronic configuration [Xe] $4f^{12}$ $6s^2$, where [Xe] represents the close shell electronic configuration of xenon. When the erbium atom is doped into a dielectric host material such as a glass, a number of important phenomena occur. Firstly, the erbium atoms form ionic bonds with the surrounding host lattice by removing two electrons from the *6s* level and one electron from the *4f* level. The dopant Er atoms therefore become trivalent Er^{3+} ions with the electronic structure [Xe] $4f^{11}$ $5s^2$ $5p^6$ $6s^0$. It is the intra *4f* -*4f* transitions within the Er^{3+} ion that allow amplification of 1550 nm signals [1]. A further effect of the host material is that the degeneracy of the Er^{3+} ion energy levels is lifted by the interaction of the surrounding crystal field with the Er^{3+} ion electron orbitals via the Stark effect. Since the exact form of the crystal field surrounding each Er^{3+} ion is site dependent within the material, when viewing the ion population as a whole, the width of each energy level increases due to inhomogeneous broadening [2]. Figure 2-2 is a schematic representation of the first five intra *4f* energy levels of the Er^{3+} ion.

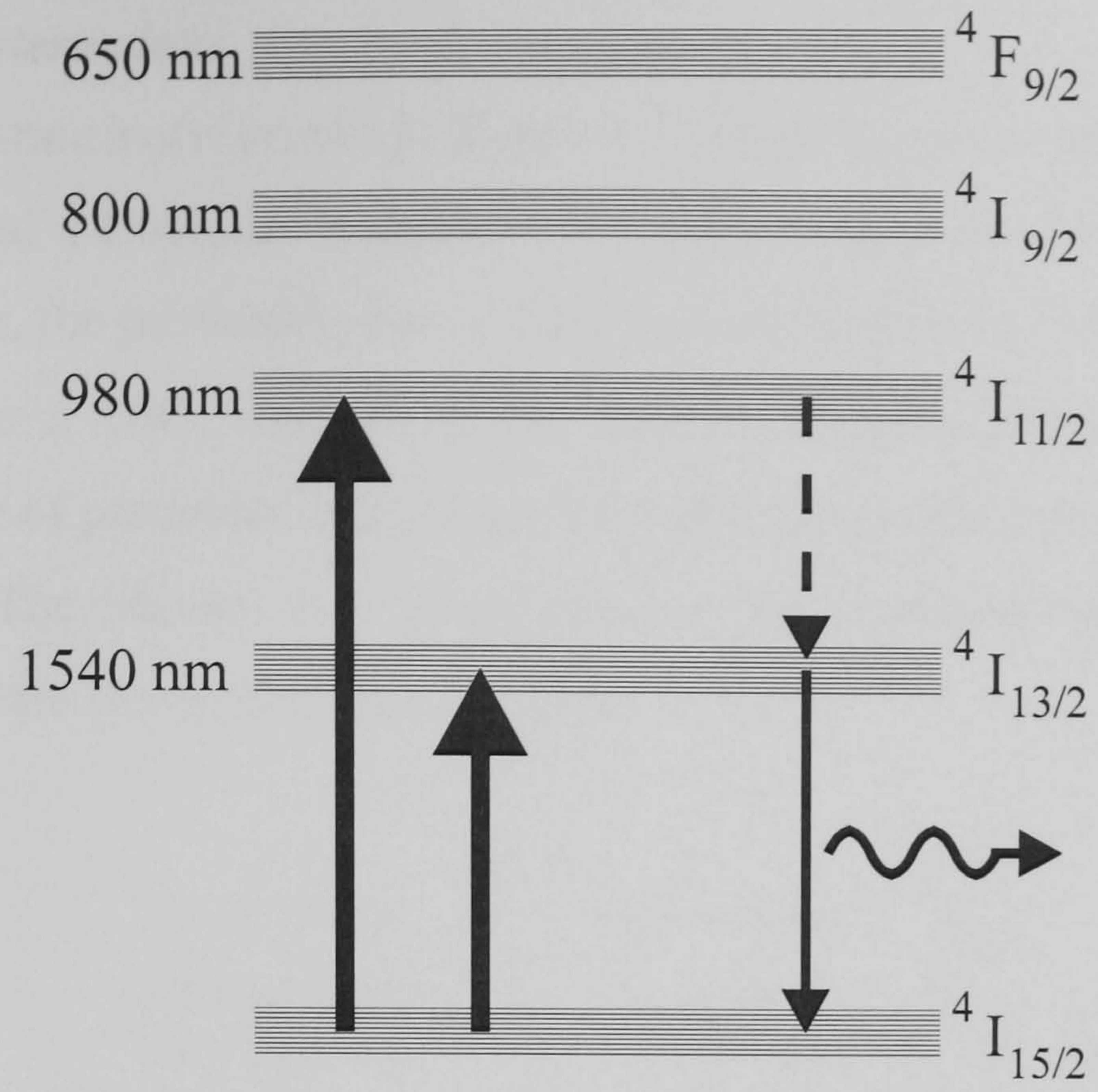

Figure 2-2 Schematic representation of the first five intra *4f* energy levels of the Er^{3+} ion in a dielectric host material.

As shown on the right of Figure 2-2, stimulated emission at around 1550 nm is obtained from the $^4I_{13/2} \rightarrow {}^4I_{15/2}$ transition. The necessary population inversion between the $^4I_{13/2}$ and $^4I_{15/2}$ states is obtained by optical pumping to either the short lived $^4I_{11/2}$ state using 980 nm light, or by pumping directly to the top of the $^4I_{13/2}$ state using 1480 nm light, these transitions are shown in the left of Figure 2-2. Also shown on the right of Figure 2-2 is the non-radiative transition from the $^4I_{11/2}$ level to the $^4I_{13/2}$ level necessary for 980 nm pumping.

Due to partial shielding of the *4f* levels by the outer lying *s* and *p* orbitals, both the pump absorption and signal emission cross sections are relatively small, of the order of $\approx 10^{-21}$ cm^2. As a result, substantial doping concentrations ($\approx 10^{20}$ ions.cm^{-3}) are required to achieve significant gains after a short interaction length. An additional consequence of the small transition cross sections is that high pump intensities are required to induce the necessary population inversion. These high pump intensities may only be produced and sustained over the interaction length by confining both the pump and signal together in a waveguide structure.

2.3.2 *Ion-ion interactions*

In addition to the transitions shown in Figure 2-2, spatially close ions may also transfer energy by means of a Coulomb interaction [3]. According to the Förster-Dexter theory for energy transfer, the probability that energy transfer will occur between any two ions increases at a rate $\propto 1/R^6$, where R is the inter-ion spacing [4]. As a result, energy transfer effects are of particular importance for highly doped devices where the inter-ion spacing is small. The relevant cross relaxation and upconversion transitions that occur between Er^{3+} ions are shown in Figure 2-3 [5].

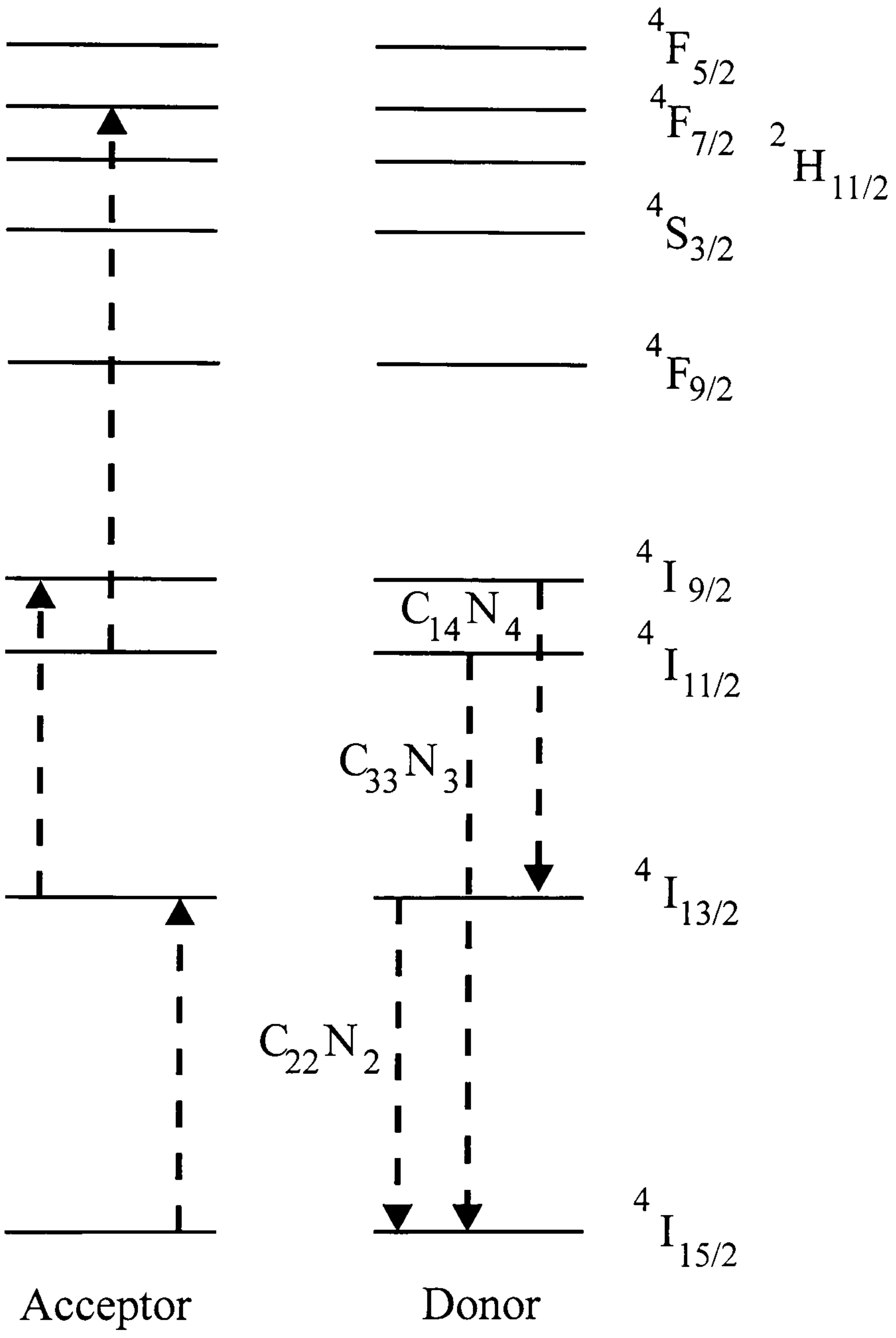

Figure 2-3 Schematic representation of the relevant cross relaxation and upconversion transitions that occur between Er^{3+} ions.

As shown in Figure 2-3, each energy transfer mechanism is characterised by a coupling coefficient (C) in units of $cm^3.s^{-1}$, such that the total rate of transitions is $N^2 \times C$, where N is the density of the interacting ions ($ions.cm^{-3}$).

Although all energy transfer mechanisms between Er^{3+} ions are detrimental to the gain operation of an EDWA, energy transfer mechanisms can also be used to improve EDWA operation. One example of this is the nearly resonant transfer of energy between Yb^{3+} ions in the $^2F_{5/2}$ level to Er^{3+} ions in the $^4I_{11/2}$ level. Since the 980 nm absorption cross section of the Yb^{3+} ion is approximately ten times that of the Er^{3+} ion, pump radiation can be efficiently absorbed by the Yb^{3+} ions and then transferred to the Er^{3+} ions [6]. Co-doping Er-doped materials with Yb is now commonplace to increase the 980 nm pumping efficiency.

2.3.3 Excited state absorption

One final mechanism that can influence the dynamics of the Er^{3+} population is excited state absorption (ESA). In the effect of ESA, light at frequency υ is not absorbed by an ion in the ground level (1), but by an ion residing in a higher lying energy level (2) due to the existence of a third level (3) whose energy gap $\Delta E = E_3 - E_2$ with level 2 happens to closely match the incident photon energy. ESA can occur from any state with a finite population, but is most likely to occur from the $^4I_{13/2}$ state due to its long lifetime [7]. ESA can occur at both the pump and signal wavelengths but in both cases results in reduced device gain.

For silica glass hosts, where all energy levels are characterised by short lifetimes except for the $^4I_{13/2}$ level, the effect of ESA has been shown to result in only an increase in the pump absorption and that the $^4I_{15/2}$ and $^4I_{13/2}$ level populations remain unchanged. Due to the short lifetime of the $^4I_{11/2}$ state, ESA under 980 nm pumping is negligible in silica based materials [8].

2.3.4 Rate equations

The four mechanisms that can affect the Er^{3+} ion energy level populations are stimulated emission, stimulated absorption, ion-ion energy transfer and ESA. Now that these mechanisms have been identified and discussed, a set of rate equations that describe the Er^{3+} ion population dynamics in a predominantly silica glass host can be constructed. All Er-doped waveguides discussed in this thesis were fabricated using predominantly silica glass hosts.

As shown in Figure 2-2, pumping at 980 nm involves pumping to the short lived ${}^4I_{11/2}$ level, resulting in a three level laser system, whereas pumping at pumping at 1480 nm involves pumping directly to the top of the long lived ${}^4I_{13/2}$ level, resulting in a quasi-two-level laser system. Since the ratio of the absorption to emission cross sections at 1480 nm for the ${}^4I_{13/2} \rightarrow {}^4I_{15/2}$ and ${}^4I_{15/2} \rightarrow {}^4I_{13/2}$ transitions is approximately 0.3 [9], pumping at 1480 nm also induces a substantial amount of stimulated emission and the maximum population inversion under 1480 nm pumping is limited to approximately 70 % [10]. Consequently, pumping at 980 nm is usually preferred to maximise the overall performance of the amplifier.

By considering only 980 nm pumping, the following rate equations that describe the Er^{3+} population dynamics in a silica glass host can be constructed (Equation 2-1 to Equation 2-4) [5]. Due to the short lifetime of the ${}^4I_{11/2}$ level in silicate host materials, the effect of ESA and pump induced stimulated emission is negligible when pumping at 980 nm. As a result, these effects are not included in the rate equations given below.

$$\frac{dN_1}{dt} = -(R+W_a).N_1 + \left(W_e + 1/\tau_{21}\right).N_2 + C_{22}.N_2^2 - C_{14}.N_1.N_4 + C_{33}.N_3^2$$

Equation 2-1

$$\frac{dN_2}{dt} = W_a.N_1 - \left(W_e + 1/\tau_{21}\right).N_2 + \frac{N_3}{\tau_{32}} - 2C_{22}.N_2^2 + 2C_{14}.N_1.N_4$$

Equation 2-2

$$\frac{dN_3}{dt} = R.N_1 - \frac{N_3}{\tau_{32}} + \frac{N_4}{\tau_{43}} - 2C_{33}.N_3^2$$

Equation 2-3

$$\frac{dN_4}{dt} = -\frac{N_4}{\tau_{43}} + C_{22}.N_2^2 - C_{14}.N_1.N_4 + C_{33}.N_3^2$$

Equation 2-4

where, N_1, N_2, N_3, N_4 are the ion populations of the ${}^4I_{15/2}$, ${}^4I_{13/2}$, ${}^4I_{11/2}$, ${}^4I_{9/2}$ levels respectively (ions.cm^{-3}), R, W_a, W_e are the pumping, stimulated absorption and stimulated emission transition rates respectively (s^{-1}), C_{22} is the cooperative upconversion coefficient for a population of ions in the ${}^4I_{13/2}$ state (cm^3.s^{-1}), C_{33} is the cooperative upconversion coefficient for a population of ions in the ${}^4I_{11/2}$ state (cm^3.s^{-1}),

C_{14} is the cross relaxation coefficient for two ion populations, one in the $^4I_{15/2}$ state, the other in the $^4I_{9/2}$ state (cm^3.s^{-1}).

The pumping, stimulated absorption and stimulated emission transition rates are in turn defined as Equation 2-5, Equation 2-6 and Equation 2-7 respectively.

$$R = \frac{\sigma_p^a . I_p}{h.\upsilon_p}$$

Equation 2-5

$$W_a = \frac{\sigma_s^a . I_s}{h.\upsilon_s}$$

Equation 2-6

$$W_e = \frac{\sigma_s^e . I_s}{h.\upsilon_s}$$

Equation 2-7

where, I_p, I_s are the pump and signal intensities respectively (W.cm^{-2}), υ_p, υ_s are the pump and signal frequencies respectively (Hz), σ_p^a is the pump absorption cross section for the $^4I_{15/2} \rightarrow {}^4I_{11/2}$ transition (cm^2), σ_s^a, σ_s^e are the signal absorption and emission cross sections for the $^4I_{15/2} \rightarrow {}^4I_{13/2}$ and $^4I_{13/2} \rightarrow {}^4I_{15/2}$ transitions respectively (cm^2).

These rate equations are applicable throughout the doped region wherever the signal and pump fields are present. Because the pump light not only varies along the length of the waveguide, but also across the waveguide cross section, the population of the $^4I_{13/2}$ state is variable in all directions.

These rate equations can however be substantially simplified through the following approximations:

1. The decay rates from the higher lying levels to the $^4I_{13/2}$ level are high compared to the decay rate from the $^4I_{13/2}$ level to the ground level.

2. The amplifier is operating in the low signal regime. As a result the signal intensity does not significantly affect the ion populations.

By applying these approximations a much simpler "quasi-two-level" system described by Equation 2-8 and Equation 2-9 may be obtained.

$$\frac{dN_1}{dt} = -R.N_1 + \frac{N_2}{\tau_{21}} + C_{22}.N_2^2$$

Equation 2-8

$$\frac{dN_2}{dt} = R.N_1 - \frac{N_2}{\tau_{21}} - C_{22}.N_2^2$$

Equation 2-9

It is important to note that due to these approximations, $N_1 + N_2 = N_{Total}$.

By making the following two substitutions, $N_2 = \rho_{Er}.n_2$ and $N_1 = (1-n_2)\rho_{Er}$, where ρ_{Er} is the doping concentration of Er^{3+} ions and n_2 is the fraction of ions in the $^4I_{13/2}$ level, Equation 2-9 may be expressed in terms of the fraction of total ions in the $^4I_{13/2}$ metastable to give Equation 2-10.

$$\frac{dn_2}{dt} = R.(1-n_2) - \frac{n_2}{\tau_{21}} - \rho_{Er}.C_{22}.n_2^2$$

Equation 2-10

Under continuous wave pumping, $\frac{dn_2}{dt} = 0$ and Equation 2-11 is a solution to Equation 2-10.

$$n_2 = \frac{R + \frac{1}{\tau_{21}}}{2.\rho_{Er}.C_{22}}\left(\sqrt{1 + \frac{4.\rho_{Er}.C_{22}.R}{\left(R + \frac{1}{\tau_{21}}\right)^2}} - 1\right)$$

Equation 2-11

Equation 2-10 and Equation 2-11 were first proposed by Snoeks et al to describe the Er^{3+} ion population dynamics in an Er-doped silica glass waveguide [11].

Although Equation 2-10 is clearly reliant on a number of assumptions, a comparison of theoretical modelling results and experimental measurements published by other groups indicate that it adequately describes the population dynamics of homogeneously Er-doped silica materials [11,12].

2.4 The physics and role of the waveguide structure

As outlined previously, the small transition cross sections of the Er^{3+} ion require for the pump and signal light to be confined together in a waveguide structure. The following sections will describe the physical principles that govern the guiding of light in a waveguide structure and, in particular, relate how the various properties of the waveguide affect the operation of an EDWA.

2.4.1 Optical waveguide modes

Light in an optical waveguide must propagate in certain distinct optical modes, analogous to the vibration modes of a string. Each mode has a particular spatial distribution of energy. From the rate equation analysis presented in the previous section it is clear that the population inversion at any point is dependent on the pumping intensity at that point. Consequently, careful consideration must be given to the spatial distribution of both the pump and signal fields to achieve efficient pumping.

Although the ray-optic model approach to describing the propagation of light in a waveguide structure is useful [13], it can only go so far in describing waveguide phenomena. To understand the physics behind waveguide propagation at a deeper level, a more in depth analysis using Maxwell's equations must be considered. Since all Er-doped waveguides are fabricated using either glass or crystal dielectric materials, Maxwell's equations (Equation 2-12 → Equation 2-15) for a linear, non-magnetic dielectric medium where no free charges are present are applicable [14].

$$\nabla.(\varepsilon E) = 0$$

Equation 2-12

$$\nabla.(\mu H) = 0$$

Equation 2-13

$$\nabla \times E = -\mu \frac{\partial H}{\partial t}$$

Equation 2-14

$$\nabla \times H = \varepsilon \frac{\partial E}{\partial t}$$

Equation 2-15

Where, E is the electric field vector, H is the magnetizing field vector, μ is the material permeability, ε is the material permittivity and t is time.

From Maxwell's equations, the vector wave equation, Equation 2-16, for a material of this kind can be derived. The derivation of the vector wave equation from Maxwell's equations is given in many text books [14,15].

$$\nabla^2 E - \frac{n^2}{c^2} \frac{\partial^2 E}{\partial t^2} = 0$$

Equation 2-16

Where, c is the velocity of light in a vacuum and n is the refractive index of the material.

The vector wave equation has solutions of the form $E(x, y, z, t) = \mathrm{Re}[E(x, y, z)e^{i\varpi t}]$ and allows the form of the electric field to be considered independently of the magnetic field. If E has only one dominant component, E_x for example, then the above equation is a scalar equation for E_x. Since most Er-doped waveguides intended for EDWA applications are either single mode or close to single mode at both the pump and signal wavelengths, the assumption that $E_z = 0$ is valid.

To find the allowed propagation modes for a given waveguide structure, the problem is to find the solutions to the scalar wave equation given certain boundary conditions.

These boundary conditions are the continuity of E and the normal derivative of E across any dielectric boundaries and, for well confined modes, the magnitude of E must also decay exponentially outside the core region also. Finding these solutions is normally not possible using an analytical approach and Equation 2-16 is usually solved using an iterative numerical approach.

2.4.2 Waveguide structures

Many possible waveguide structures exist. The guiding properties of many of these structures can only be understood from the point of the scalar wave equation. Thus far, Er-doped waveguides have been fabricated using channel, ridge, strip loaded, and indiffused waveguides. In all cases however, the pump and signal propagate together within the erbium doped core region. Figure 2-4 shows schematic diagrams of the various waveguide structures that have been used for fabricating Er-doped waveguides.

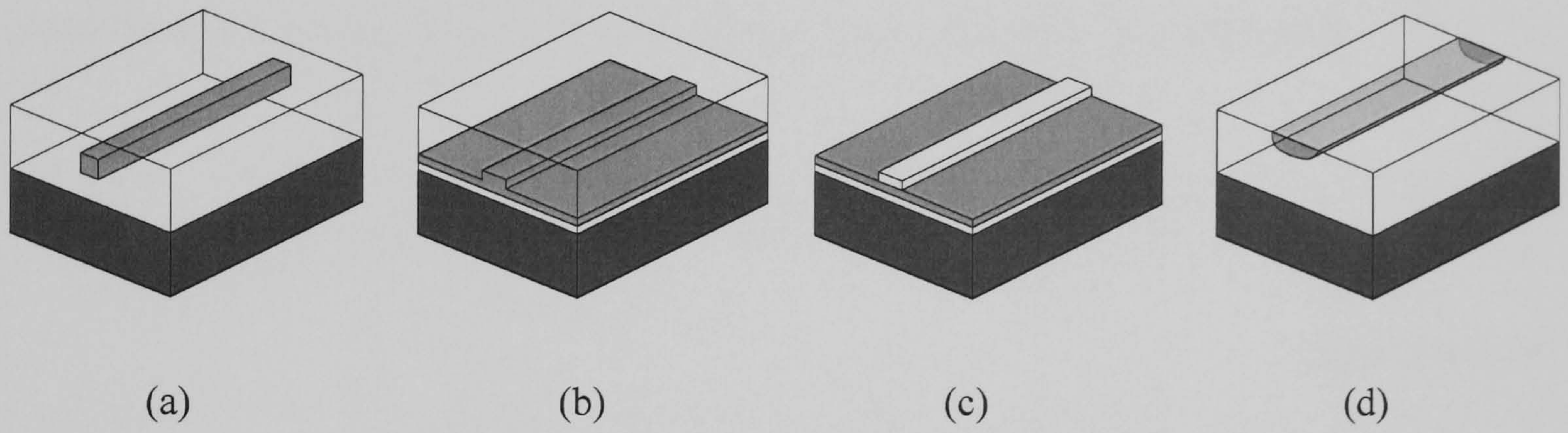

Figure 2-4 Schematic diagrams of the various waveguide structures that have been used to fabricate Er-doped waveguides. Shown in the figure are (a) a channel waveguide (b) a ridge waveguide (c) a strip loaded waveguide and (d) an in-diffused waveguide.

In each of the diagrams shown in Figure 2-4, the pump and signal light is confined in the Er-doped material coloured light grey in each diagram.

2.4.3 Describing the propagation of the pump and signal along an Er-doped waveguide

As light travels down an optical waveguide it is attenuated by extrinsic loss mechanisms, such as radiation losses at bends, and intrinsic loss mechanism, such as Rayleigh scattering. These loss mechanisms will be referred to as "background" loss mechanisms since they occur in all waveguides. In an Er-doped waveguide however, the light may also experience amplification and absorption associated with the dopant Er^{3+} ions. These "loss" mechanisms will be referred to as "doping" loss mechanisms.

The evolution of the intensity of guided light as it travels along a passive un-doped waveguide is described by an exponential decay law of the form given by Equation 2-17 [16].

$$I(z) = I_0 \exp(-\alpha . z)$$

Equation 2-17

where, $I(z)$ is the signal intensity at some point z, I_0 is the signal intensity at $z = 0$ and α is the waveguide loss coefficient (cm^{-1}).

By differentiating Equation 2-17 with respect to z, Equation 2-18 is obtained.

$$\frac{dI(z)}{dz} = -\alpha . I_0 \exp(-\alpha . z) = -\alpha . I(z)$$

Equation 2-18

Equation 2-18 gives the rate of change of the intensity of the guided light due to background loss mechanisms at any point along the waveguide.

As light propagates through a pumped Er-doped material it may experience a certain amount of gain due to stimulated emission and a certain amount of absorption due to ground state absorption. For a signal of intensity I at a frequency υ travelling through a gain medium, the signal changes in intensity after a length dx by an amount dI given by Equation 2-19 [17].

$$\frac{dI_\upsilon}{dx} = I_\upsilon . N . \sigma_\upsilon$$

Equation 2-19

where, N is the density of ions in the 1st state of the transition (ions.cm^{-3}) and σ_{υ} is the transition cross section at the frequency of the propagating light (cm^2).

Equation 2-19 can be extended to the case of Er-doped waveguides as follows. As light travels down the Er-doped waveguide, a certain fraction of the propagating mode travels outside the doped waveguide. Consequently, it is necessary to introduce an overlap factor to account for this which effectively reduces the magnitude of the transition cross section by its magnitude. The magnitude of the overlap factor (Γ) is given by Equation 2-20.

$$\Gamma = \int_{-x}^{+x} \int_{-y}^{+y} p_0(x,y)\, dxdy$$

Equation 2-20

where, $+x$, $-x$, $+y$, $-y$ are the dimensions of the Er-doped core region and $p_o(x,y)$ is the intensity distribution of the propagating mode, normalised such that $\int_{-\infty}^{+\infty} \int_{-\infty}^{+\infty} p_0(x,y)\, dxdy = 1$.

The rate of change of signal intensity due to doping loss mechanisms in Er-doped waveguides is therefore given by Equation 2-21:

$$\frac{dI_v}{dx} = I_v.N.\sigma_v.\Gamma_v$$

Equation 2-21

It is important to note that since N can vary across the waveguide, N in Equation 2-21 is the average population of the 1st state of the transition.

Equation 2-21 gives the rate of change of the intensity of the guided light due to doping loss mechanisms at any point along the waveguide.

By combining the background and doping loss mechanisms the evolution of both the pump and signal intensities along the waveguide can be represented mathematically.

For the case of the 980 nm pump light, the stimulated emission cross section is assumed to be zero due to the short lifetime of the $^4I_{11/2}$ level. The evolution of the pump light intensity is therefore given by Equation 2-22.

$$\frac{dI_p(z)}{dz} = -\alpha_p.I_p(z) - I_p(z).(1-n_2).\sigma_p^a.\Gamma_p.\rho_{Er}$$

Equation 2-22

where, I_p is the pump light intensity, α_p is the loss coefficient of the waveguide for 980 nm light, n_2 is the fraction of ions in the $^4I_{13/2}$ level, σ_p^a is the $^4I_{15/2} \rightarrow {}^4I_{11/2}$ transition absorption cross section at 980 nm, Γ_s is the pump-waveguide overlap factor and ρ_{Er} is the doping concentration of Er^{3+} ions.

For the signal wavelength, since both stimulated emission and absorption take place Equation 2-23 applies.

$$\frac{dI_s(z)}{dz} = -\alpha_s.I_s(z) - I_s(z).(1-n_2).\sigma_s^a.\Gamma_s.\rho_{Er} + I_s(z).n_2.\sigma_s^e.\Gamma_s.\rho_{Er}$$

Equation 2-23

Where, I_s is the signal intensity, α_s is the loss coefficient of the waveguide at the signal wavelength, n_2 is the fraction of ions in the $^4I_{13/2}$ level, σ_s^a, σ_s^e are the $^4I_{15/2} \rightarrow {}^4I_{13/2}$ and $^4I_{13/2} \rightarrow {}^4I_{15/2}$ transition cross sections at the signal wavelength respectively, Γ_s is the signal-waveguide overlap factor and ρ_{Er} is the doping concentration of Er^{3+} ions.

Finally, since Equation 2-23 can be expressed in terms of the normalised signal intensity, $s(z)$, where $s(z) = \frac{I(z)}{I(z=0)}$, the gain function $g(z) \equiv \ln[s(z)]$ along the waveguide can be expressed as Equation 2-24.

$$\frac{dg(z)}{dz} = -\alpha - (1-n_2).\sigma_s^a.\Gamma_s.\rho_{Er} + n_2.\sigma_s^e.\Gamma_s.\rho_{Er}$$

Equation 2-24

Again, Equation 2-22, Equation 2-23 and Equation 2-24 were first proposed by Snoeks et al to describe the evolution of the pump and signal intensities and gain function along an Er-doped silica waveguide [12].

2.5 Modelling the gain of a Er-doped silica waveguide

To investigate quantitatively how the various parameters affect the gain operation of an EDWA, the gain vs. 980 nm pump power characteristics for a uni-directionally pumped Er-doped waveguide were modelled using the model proposed by Snoeks et al [12]. In this model, the steady state population of the $^4I_{13/2}$ level along the length of the waveguide is found by numerically solving Equation 2-11 and Equation 2-22 simultaneously as the pump light propagates along the waveguide. Once the distribution of the $^4I_{13/2}$ level population along the waveguide is found, Equation 2-24 is solved numerically to find the gain of the waveguide. In this model a number of assumptions are made. Firstly, it is assumed the amplifier is operating in the small signal regime. Secondly, the variation in the pump and signal intensities across the waveguide cross section are neglected, with the pump and signal intensities simplified to $I = P/A$, where I is the intensity, P is the optical power and A is the waveguide cross section. Thirdly, it is assumed that the Er^{3+} ions are distributed homogeneously throughout the host material and as a result, interact according to one homogeneous C_{22} cooperative upconversion coefficient.

To perform the calculations, Equation 2-11 and Equation 2-22 were solved simultaneously using the "ode15s" differential equation solver function in Matlab v.6. By doing so, a vector of values representing the fraction of ions in the $^4I_{13/2}$ level along the waveguide was obtained. This vector of values was then used to calculate the gain of the waveguide by numerically integrating Equation 2-24 along the length of the waveguide. The Matlab code written to perform these functions is given in Appendix A.

Unless otherwise stated, the parameters used in the model are given in Table 2-1.

Parameter	Magnitude	Unit	Ref.
Doped waveguide core dimensions	5 × 5	μm	[18]
Pump light wavelength	980	nm	[12]
Signal light wavelength	1535	nm	[12]
Erbium concentration (ρ_{Er})	1×10^{20}	ions.cm^{-3}	[18]
Pump light $^4I_{15/2} \rightarrow {}^4I_{11/2}$ transition cross section (σ_p^a)	2.58×10^{-21}	cm^2	[19]
Signal light $^4I_{15/2} \rightarrow {}^4I_{13/2}$ transition cross section (σ_s^a)	5.36×10^{-21}	cm^2	[19]
Signal light $^4I_{13/2} \rightarrow {}^4I_{15/2}$ transition cross section (σ_s^e)	5.41×10^{-21}	cm^2	[19]
Homogeneous cooperative upconversion constant (C_{22})	3×10^{-18}	cm^3.s^{-1}	[11]
$^4I_{13/2}$ level lifetime (τ_{21})	10	ms	[20]
Waveguide length	10	cm	[18]
Pump-waveguide overlap factor (Γ_p)	0.9	Dimensionless	[18]
Signal-waveguide overlap factor (Γ_s)	0.7	Dimensionless	[18]
Waveguide propagation loss at both the pump and signal wavelengths	1.0	dB.cm^{-1}	[12]

Table 2-1 Parameter values used to model the EDWA operation

Using the parameters defined in Table 2-1, Figure 2-5, Figure 2-6, Figure 2-7, Figure 2-8, Figure 2-9 and Figure 2-10 show the effect of the doped waveguide core area, erbium concentration, homogeneous C_{22} cooperative upconversion constant, $^4I_{13/2}$ level lifetime, waveguide length and waveguide propagation loss respectively on the modelled net gain vs. 980 nm pump power characteristics. The effect of the transition cross sections were not modelled since their magnitudes are only slightly dependent on the host material. The effect of the overlap factors were also not modelled since they effectively only reduce the magnitudes of the transition cross sections. It is important to note that the modelled net gain does not take into consideration coupling losses to and from the waveguide for either the pump or signal light.

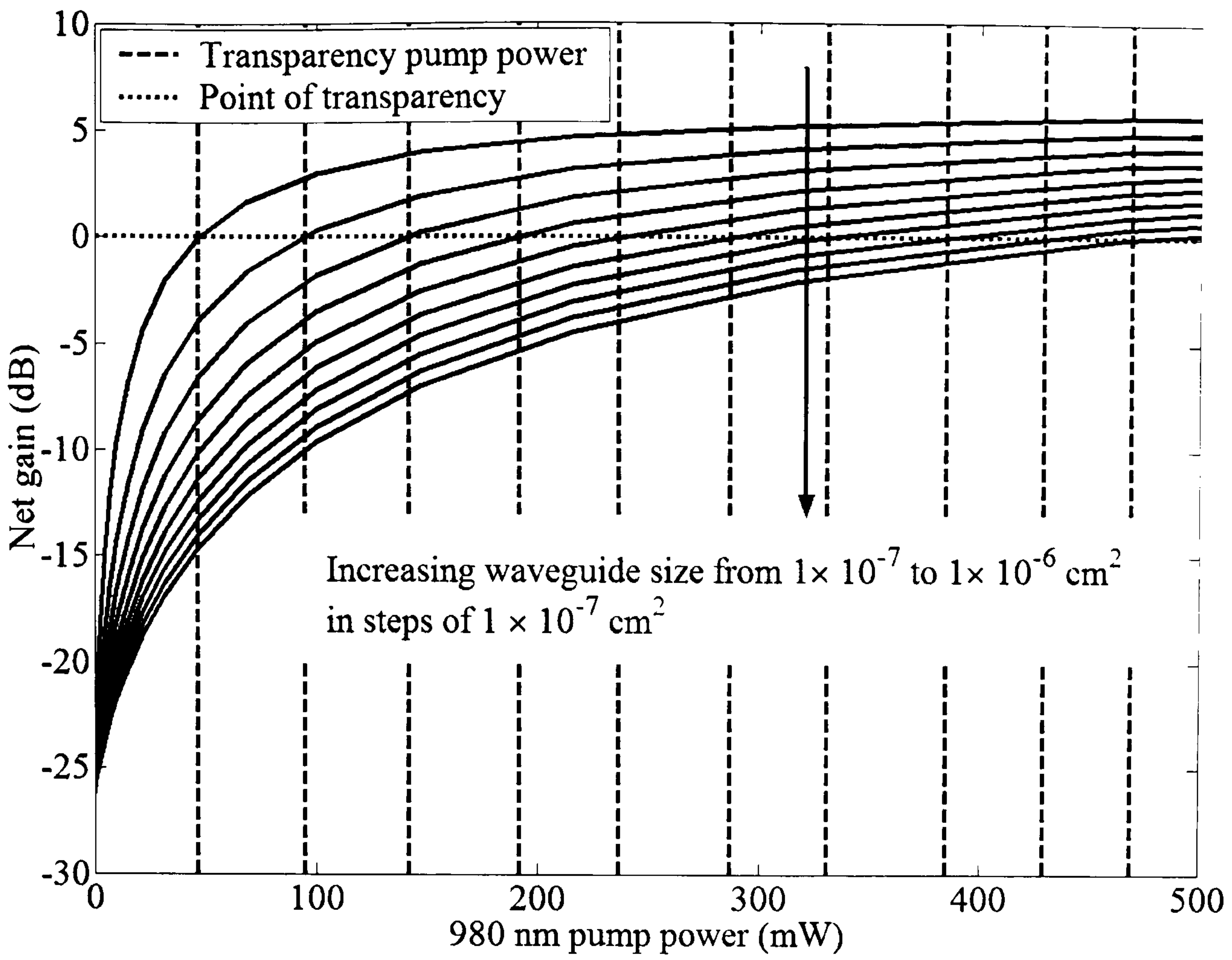

Figure 2-5 Modelled net gain vs. 980 nm pump power characteristics for the same waveguide with different doped waveguide core areas.

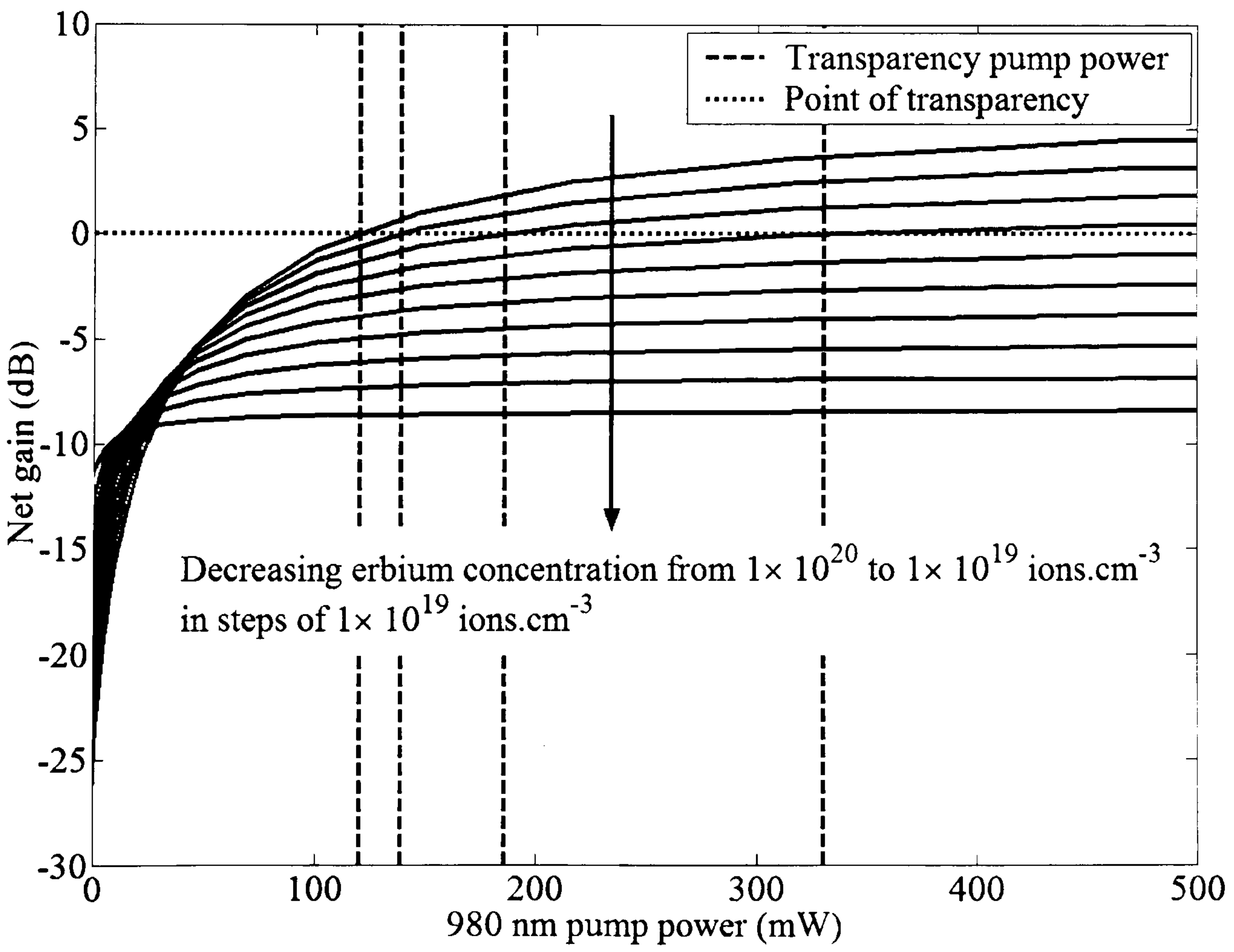

Figure 2-6 Modelled net gain vs. 980 nm pump power characteristics for the same waveguide with different erbium concentrations.

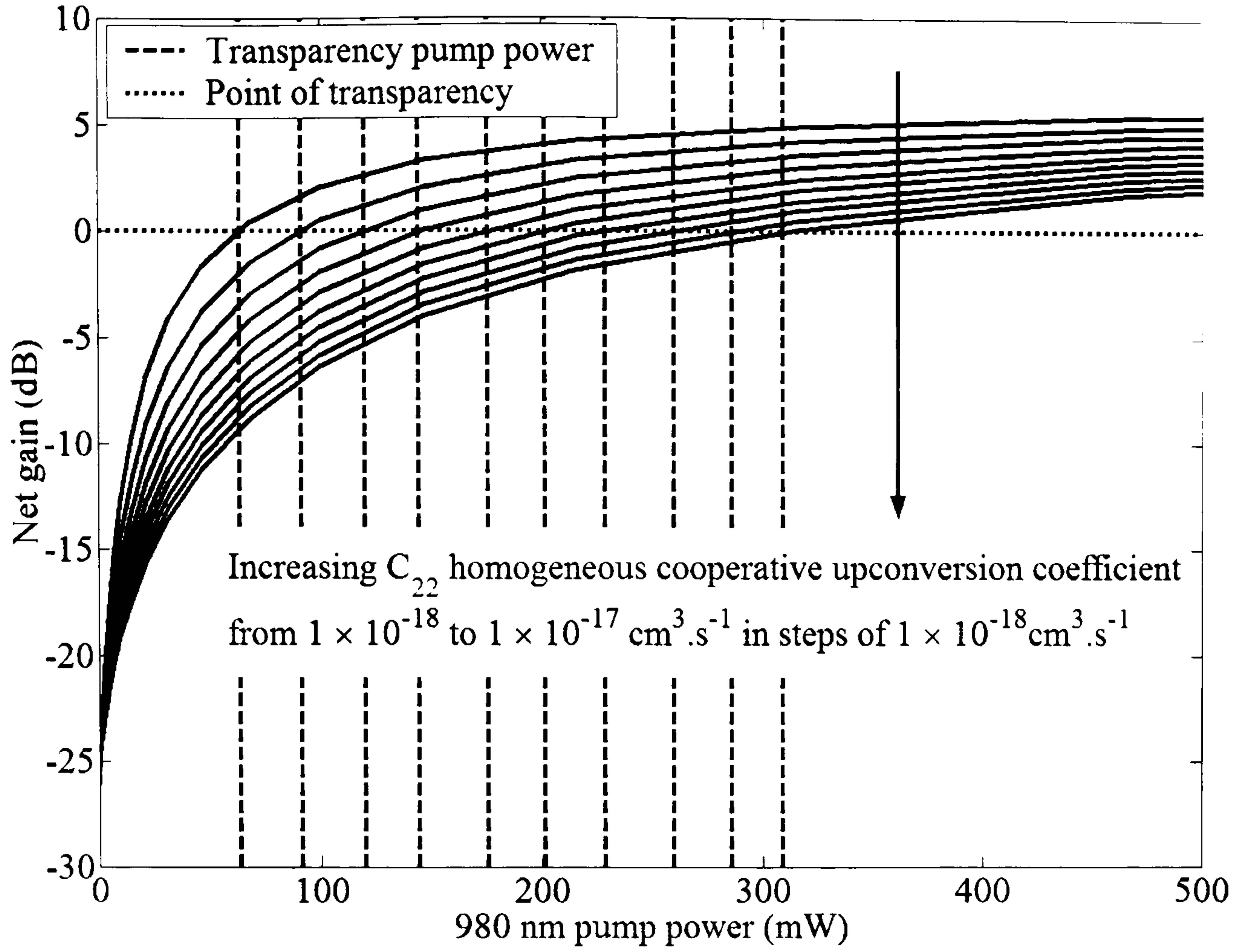

Figure 2-7 Modelled net gain vs. 980 nm pump power characteristics for the same waveguide with different homogeneous C_{22} cooperative upconversion coefficients.

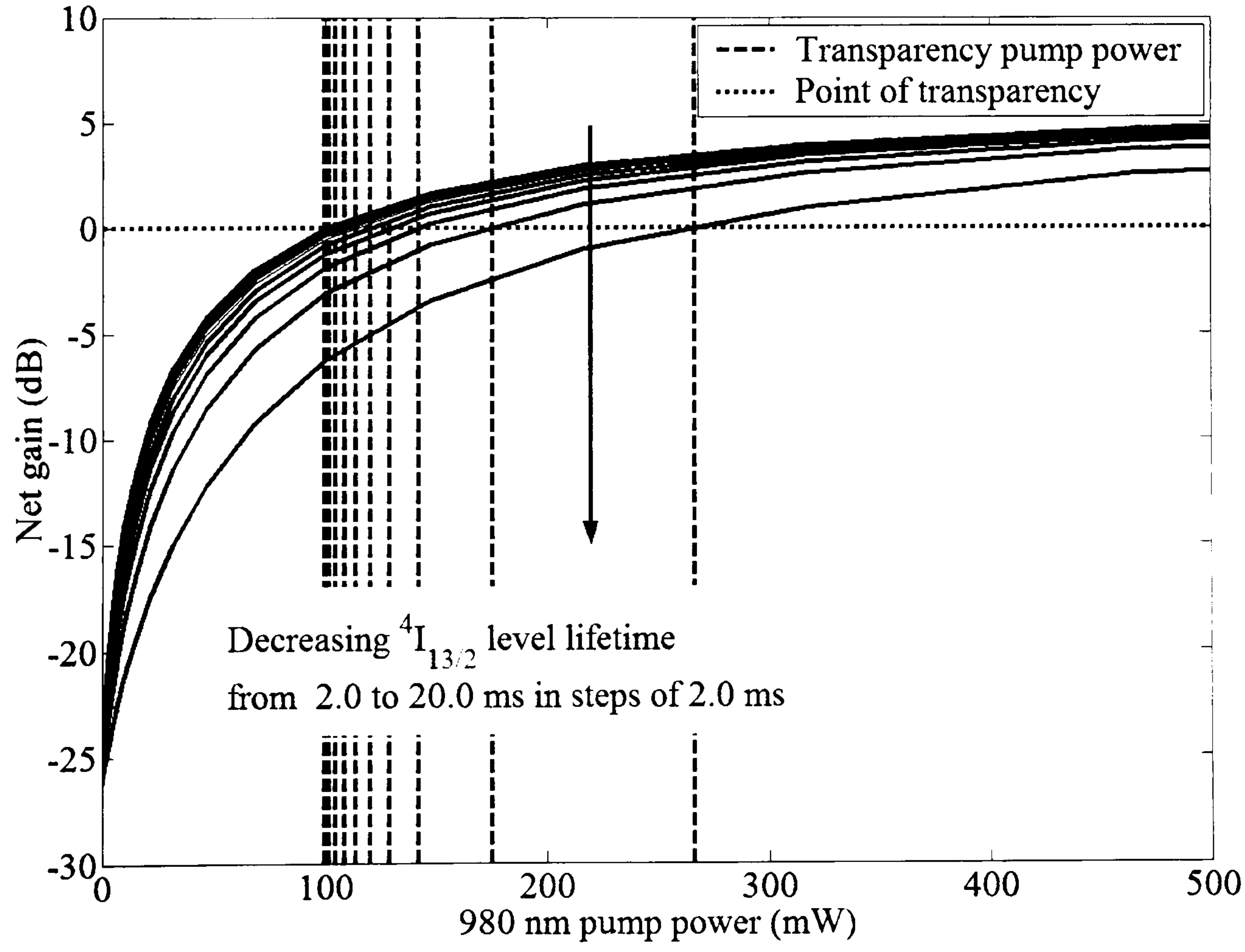

Figure 2-8 Modelled net gain vs. 980 nm pump power characteristics for the same waveguide with different $^4I_{13/2}$ level lifetimes.

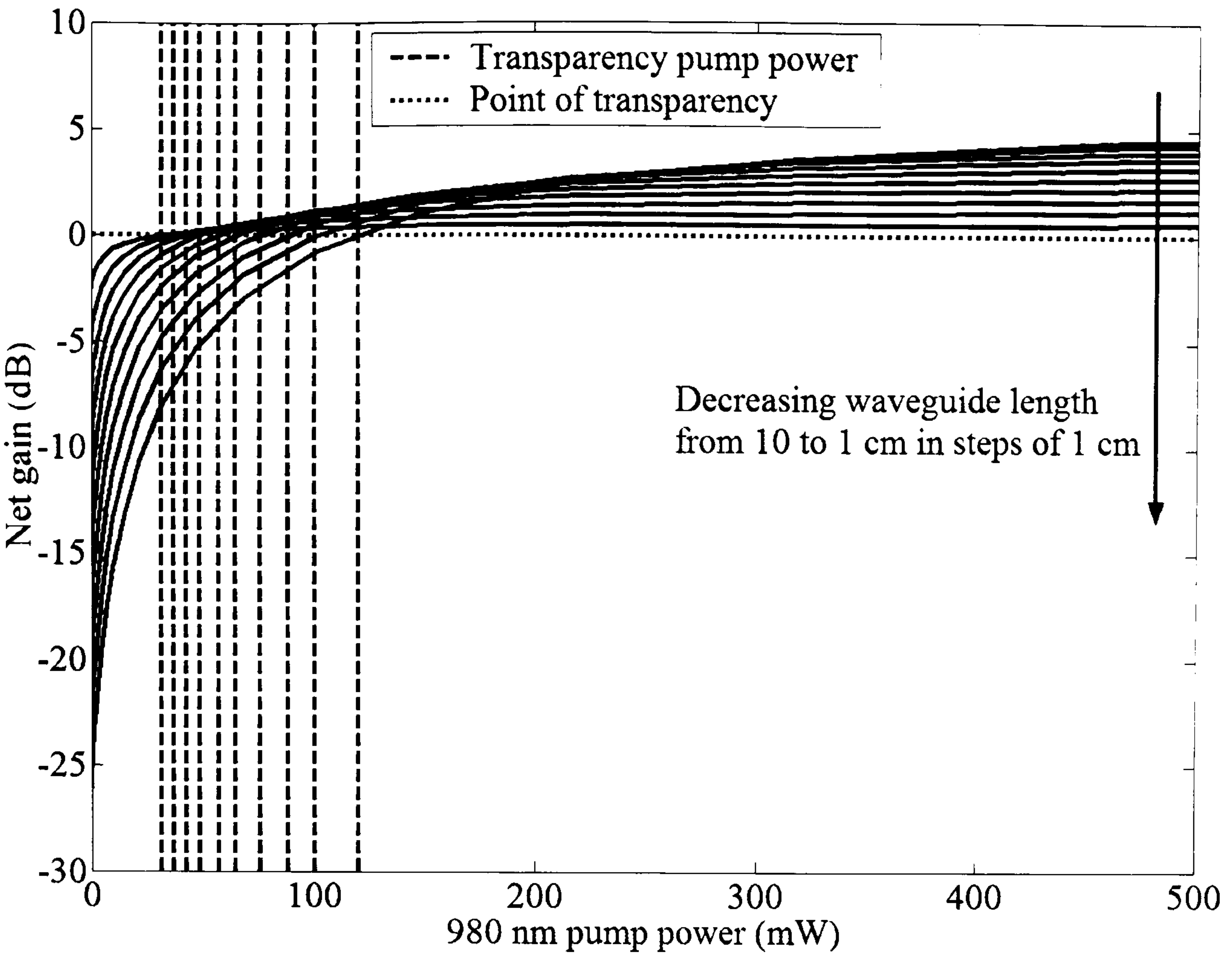

Figure 2-9 Modelled net gain vs. 980 nm pump power characteristics for the same waveguide of different lengths.

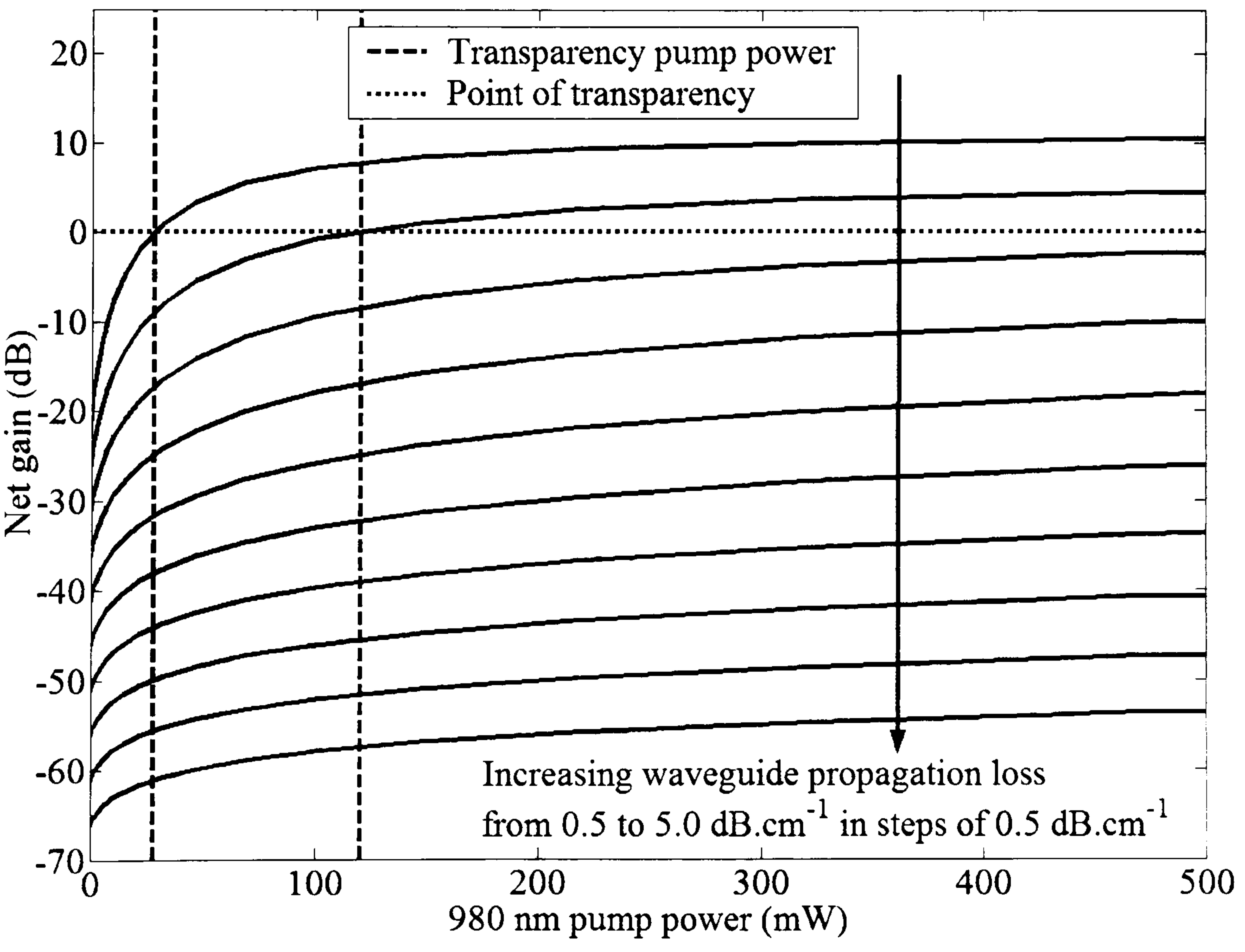

Figure 2-10 Modelled net gain vs. 980 nm pump power characteristics for the same waveguide with different propagation losses.

Since the pump intensity in this simple model is simply defined as the pump power divided by the waveguide core cross sectional area, the trends shown in Figure 2-5 are easily understood. Under this simplification, a linear increase in the waveguide cross section requires a linear increase in the pump power required to achieve the same pump intensity. Consequently, the pump power required to achieve transparency increases linearly with increasing waveguide core cross sectional area. These trends should be treated with caution however since, in reality, a reduction in the core area would also require an increase in the waveguide refractive index contrast to maintain the same pump-waveguide and signal-waveguide overlap factors.

The trends shown in Figure 2-6 are in agreement with the behaviour expected according to Equation 2-23. It is clear that in order to achieve transparency and hence net gain from an Er-doped waveguide of a certain length, the erbium concentration must be at least high enough for the stimulated emission processes to compensate for the propagation losses of the waveguide. As shown in Figure 2-6, net gain is impossible without this minimum concentration, even with a complete population inversion.

As shown in Figure 2-7, and as expected from Equation 2-10, the pumping efficiency is reduced as the cooperative upconversion coefficient is increased. The pump power required to achieve transparency appears to increase linearly with increasing homogeneous C_{22} cooperative upconversion coefficient. What is also apparent from Figure 2-7 however, is that even for very large values of C_{22}, large population inversions are still possible with only moderate pump powers.

As shown in Figure 2-8, the pumping efficiency decreases with decreasing $^4I_{13/2}$ lifetime (τ_{21}). This trend is in agreement with that expected from Equation 2-11. Although the pump power required for transparency increases nonlinearly with decreasing lifetime it is also clear from Figure 2-8 that this effect only becomes severe for lifetimes below ≈ 6 ms, with a decrease in the lifetime from 20 – 6 ms increasing the transparency pump power by only around 30 %.

As shown in Figure 2-9, the maximum net gain available from an EDWA is limited by its length, with longer devices giving the possibility for higher net gains. It is also apparent from Figure 2-9 however that shorter waveguides achieve transparency at lower pump powers and as a result are more efficient if a lower gain is required from the device. Consequently, practical EDWAs must be carefully designed to supply the necessary gain at the lowest pump power.

Finally, as shown in Figure 2-10, increased propagation losses reduce not only the net gain from the waveguide, but also the pumping efficiency. It can also be seen from Figure 2-10 that once the propagation losses exceed a certain value, the stimulated emission is no longer able to compensate for the losses and net gain is impossible, even with complete inversion.

2.5.1 *The optimum Er-doped silica waveguide*

From the presented analysis of Er-doped waveguide physics a number of conclusions can be made about what physical parameters the ideal Er-doped silica waveguide would exhibit. Under various assumptions, the three equations that define the operation of an Er-doped silica waveguide are Equation 2-10, Equation 2-22 and Equation 2-23, all given again below.

$$\frac{dn_2}{dt} = R.(1-n_2) - \frac{n_2}{\tau_{21}} - \rho_{Er}.C_{22}.n_2^2$$

Equation 2-10

$$\frac{dI_p(z)}{dz} = -\alpha_p.I_p(z) - I_p(z).(1-n_2).\sigma_p^a.\Gamma_p.\rho_{Er}$$

Equation 2-22

$$\frac{dI_s(z)}{dz} = -\alpha.I_s(z) - I_s(z).(1-n_2).\sigma_s^a.\Gamma_s.\rho_{Er} + I_s(z).n_2.\sigma_s^e.\Gamma_s.\rho_{Er}$$

Equation 2-23

From a materials point of view it is clear from Equation 2-10, Figure 2-7 and Figure 2-8 that to minimise the de-excitation rate from the $^4I_{13/2}$ level and maximise the population inversion, the $^4I_{13/2}$ level lifetime should be as large as possible while the cooperative upconversion coefficient should be as small as possible. The $^4I_{13/2}$ level lifetime is maximised by minimising impurities in the waveguide material such as hydroxyl (O-H) bonds which rapidly quench nearby excited Er^{3+} ions in the $^4I_{13/2}$ level [21]. The C_{22} cooperative upconversion coefficient is minimised by homogeneously doping the host material to maximise the average distance between ions. Energy transfer between clustered ions is extremely efficient resulting in high cooperative upconversion coefficients for those ions. Nilsson et al [22] have modelled the effect of pair-induced and cluster-induced quenching and have suggested that for a cluster of 'n' ions, rapid cross relaxation allows only one excited ion per cluster resulting in an unsaturable absorption.

From Equation 2-10 it is clear that to maximise the pumping efficiency, the pump absorption cross section and pump intensity should be as high as possible. Although the transition cross sections are generally speaking not an issue for the fabrication process, the pump intensity can be increased by using high index contrast waveguides with a small core size. The effect of increasing the modal confinement is clearly apparent in Figure 2-5. From Equation 2-23, Figure 2-6 and Figure 2-9 it is clear that the maximum possible gain available from an Er-doped waveguide is limited by the length of the device and the Er^{3+} ion doping concentration, with the stimulated emission cross section at the signal wavelength also being an extremely important factor. It is clear therefore that to minimise the device size the Er^{3+} doping concentration should be as high as possible, without inducing significant detrimental effects due to energy transfer mechanisms. Finally, from Equation 2-22, Equation 2-23 and Figure 2-10 it is clear that the propagation losses should also be minimised since they not only subtract from the gain of the device but also decrease the efficiency at which pump light is delivered to the Er^{3+} ions.

Although not discussed in the previous analysis, it is important to note the significance of coupling losses to and from the waveguide itself. Coupling losses increase the overall insertion loss of the device and therefore subtract from any gain exhibited by the Er-doped waveguide. EDWAs are used in fibre optic transmission lines, with coupling to and from the transmission line generally being conducted using direct fibre-waveguide butt-coupling without the use of free space optics. The magnitude of this coupling loss is minimised by matching the waveguide and fibre mode fields, with any deviation from the matched case resulting in an increased loss. In the ideal situation, the coupling losses would be zero, but this may counteract the advantages of fabricating EDWAs with high modal confinement as discussed previously.

In this chapter, the physical principles that underlie the operation of an EDWA have been described. In addition, the various properties of an Er-doped waveguide that affect the operation of an EDWA have been identified and the effect of each on its operation discussed. In the following three chapters, a number of studies on Er-doped waveguide fabrication are presented and discussed. The theory outlined in this chapter gives a good theoretical foundation upon which the characterisation of these waveguides is based.

2.6 References

[1] E. Desurvire, "Characteristics of erbium-doped fibers," in *Erbium-doped fiber amplifiers: Principles and applications,* John Wiley & Sons, 2002, pp. 215

[2] E. Desurvire, "Characteristics of erbium-doped fibers," in *Erbium-doped fiber amplifiers: Principles and applications,* John Wiley & Sons, 2002, pp. 225

[3] P. Myslinski, D. Nguyen, and J. Chrostowski, "Effects of concentration on the performance of erbium doped fibre amplifiers," *J. Lightwave Technol.*, vol. 15, no. 1, pp. 112-120, Jan. 1997.

[4] M. P. Hehlen, N. J. Cockroft, T. R. Gosnell, A. J. Bruce, G. Nykolak, and J. Shmulovich, "Uniform upconversion in high-concentration Er^{3+}-doped soda lime silicate and aluminosilicate glasses," *Opt. Lett.*, vol. 22, no. 11, pp. 772-774, Jun. 1997.

[5] M. V. D. Vermelho, U. Peschel, and J. S. Aitchison, "Simple and accurate procedure for modeling erbium-doped waveguide amplifiers with high concentration," *J. Lightwave Technol.*, vol. 18, no. 3, pp. 401-408, Mar. 2000.

[6] A. Polman and F. C. J. M. Van Veggel, "Broadband sensitizers for erbium-doped planar optical amplifiers: review," *J. Opt. Soc. Am. B*, vol. 21, no. 5, pp. 871-892, May 2004.

[7] E. Desurvire, "Characteristics of erbium-doped fibers," in *Erbium-doped fiber amplifiers: Principles and applications,* John Wiley & Sons, 2002, pp. 277

[8] W. J. Miniscalco, "Erbium-Doped Glasses for Fiber Amplifiers at 1500 nm," *J. Lightwave Technol.*, vol. 9, no. 2, pp. 234-250, Feb. 1991.

[9] E. Desurvire, "Fundamentals of noise in optical fiber amplifiers," in *Erbium-doped fiber amplifiers: Principles and applications,* John Wiley & Sons, 2002, pp. 101

[10] M. Dejneka and B. Samson, "Rare-Earth-Doped Fibres for Telecommunications Applications," *MRS Bulletin*, vol 24, no. 9 pp. 39-45, Sep. 2005.

[11] E. Snoeks, G. N. van den Hoven, A. Polman, B. Hendriksen, M. B. J. Diemeer, F . Priolo, "Cooperative upconversion in erbium-implanted soda-lime silicate glass optical waveguides," *J. Opt. Soc. Am. B*, vol. 12, no. 8, pp. 1468-1474, Aug. 1995.

[12] E. Snoeks, G. N. van den Hoven, and A. Polman, "Optimization of an Er-doped silica glass optical waveguide amplifier," *IEEE J. Quantum Electron.*, vol. 32, no. 9, pp. 1680-1684, Sep. 1996.

[13] J. Wilson and J. Hawkes, "Fiber optical waveguides," in *Optoelectronics: An introduction*, 3rd ed., Prentice Hall, 1998, pp. 359-373.

[14] A. Yariv, "The propagation of optical beams in homogeneous and lenslike media," in *Quantum Electronics*, 3rd ed., John Wiley & Sons, 1988, pp. 115.

[15] E. R. Dobbs, "Electromagnetic waves in space," in *Basic Electromagnetism,* Chapman and Hall, 1993, pp. 135-136.

[16] R. G. Hunsperger, "Losses in optical waveguides," in *Integrated optics: Theory and Technology,* Springer-Verlag, 1982, pp. 71.

[17] A. Siegman, "Basic Laser Physics," in *Lasers*, University Science Books, 1986, pp. 287.

[18] These are typical values for the sol-gel fabricated Er^{3+}-doped waveguides that are the subject of Chapter 4 of this thesis.

[19] W. B. Huang and R. R. A. Syms, "Analysis of folded erbium-doped planar waveguide amplifiers by the method of lines," *J. Lightwave Technol.*, vol. 17, no. 12, pp. 2658-2664, Dec. 1999.

[20] E. Desurvire and J. R. Simpson, "Amplification of spontaneous emission in erbium-doped single mode fibers," *J. Lightwave Technol.*, vol. 7, no. 5, pp. 835-845, May 1989.

[21] E. Snoeks, P. G. Kik, and A. Polman, "Concentration quenching in erbium implanted alkali silicate glasses," *Opt. Mater.*, vol. 5, no. 3, pp. 159-167, Mar. 1996.

[22] J. Nilsson, B. Jaskorzynska, and P. Blixt, "Performance reduction and design modification of erbium-doped fibre amplifiers resulting from pair-induced quenching," *IEEE Photon. Technol. Lett.*, vol. 5, no. 12, pp. 1427-1429, Dec. 1993.

Chapter 3 - Erbium-doped waveguide fabrication using a single sol-gel deposition technique

3.1 Introduction

The following chapter describes a study on the development of Er-doped channel waveguides for EDWA applications using a novel single deposition sol-gel route. Due to the chemical based nature of the sol-gel process, it is a low cost route for fabricating planar lightwave circuits (PLCs). As such, the sol-gel process is of high interest for fabricating devices for LAN / MAN applications.

All samples discussed in this chapter were fabricated by Navin Suyal and co-workers at Exxelis Ltd. My role within this work was to investigate the optical properties of these samples in order to understand and optimise the device operation.

The outline of this chapter is as follows. In section 3.2, the basic chemistry of the sol-gel process and sol-gel planar waveguide fabrication are presented. In section 3.3, the fabrication of the sol-gel samples discussed in this chapter is described. In section 3.4, various studies of the optical properties of the sol-gel samples are presented. The results of these studies are then used in section 3.5 to model the gain operation of selected samples. Finally, in section 3.6 conclusions are drawn from this work and suggestions for future work in this area are made.

3.2 The sol-gel route for waveguide fabrication

3.2.1 Basics of sol-gel processing

Sol-gel processing is an extremely versatile technique for fabricating ceramic materials of many different compositions. The chemical basis of sol-gel processing is the hydrolysis and subsequent condensation of metal alkoxides [1]. One such hydrolysis reaction is Equation 3-1.

$$Si(OR)_4 + H_2O \rightarrow HO - Si(OR)_3 + ROH$$

Equation 3-1

where, R represents either a proton or ligand structure.

As shown in Equation 3-1, reacting a silicon alkoxide molecule with a water molecule replaces one of the OR groups with an OH group from the water molecule. Such an hydrolysis reaction can then be followed by a condensation reaction such as Equation 3-2 or Equation 3-3.

$$(OR)_3 Si - OH + HO - Si(OR)_3 \rightarrow (OR)_3 Si - O - Si(OR)_3 + H_2O$$

Equation 3-2

$$(OR)_3 Si - OR + HO - Si(OR)_3 \rightarrow (OR)_3 Si - O - Si(OR)_3 + ROH$$

Equation 3-3

The result of these hydrolysis and condensation reactions is the formation of a colloidal suspension of particles in a liquid solution; the sol. If allowed to continue, these reactions will result in the creation of larger and larger polymeric molecules, which, after some time, will extend throughout the liquid in some random way to form a gel.

To form a ceramic material from the gel, the liquid solvents must be removed. This is done by using a combination of evaporation and drying. By carefully controlling the pressure and temperature during drying and sintering, crack free ceramic monoliths and thin films can be fabricated.

Although Equation 3-1, Equation 3-2 and Equation 3-3 show the hydrolysis and condensation reactions for silicon alkoxides, similar reactions exist for many different alkoxides. As such, a major advantage of the sol-gel process is the ability to incorporate co-dopants into the final material at the sol stage.

3.2.2 Sol-gel fabrication of thin glass films

One of the most significant advantages of the sol-gel process over other glass fabrication techniques is the ease with which thin films can be fabricated. Using either spin-, dip- or spray-coating techniques, thin films of a sol can be deposited onto the desired substrate. Due to the large surface area of these films, the solvent rapidly evaporates from the sol to form a gel layer. By carefully controlling the drying and sintering rate of these gel films, optical quality glass films can easily be fabricated on many different substrates.

Although thin glass films < 1 μm thick are relatively easy to fabricate in a single step, the deposition of thicker crack-free films in a single step is substantially harder due to the build up of residual stress in the film during solvent removal. To fabricate the thicker glass films necessary for integrated optics applications, a repetitive cycle spin-coating and rapid-thermal-anneal (SC-RTA) process has been developed, in which the desired film thickness is constructed from multiple depositions of thinner films [2,3]. Although this iterative SC-RTA process is a proven route for fabricating thick films of up to 10 μm thick, the thickness of each individual deposition may only be of the order of 2000 Å [4]. Consequently, many depositions may be required to construct the required film thickness, a process that would be time consuming and costly in any commercial environment. In contrast to this process, the samples discussed in this chapter were fabricated using a novel sol-gel technique that allows fully densified glass films of up to 10 μm thick to be fabricated in a single deposition. To overcome problems of stress induced cracking in thick sol-gel films, proprietary organic additives are added to the sol that restrict agglomeration during sol-synthesis, storage and solvent evaporation [5]. By using these additives, the residual stress in the film and the likelihood of cracking is greatly reduced. Since only a single sol-gel deposition is required to fabricate thick glass films using this route, it could provide an extremely quick and low cost route to fabricating PLC devices for LAN / MAN applications.

3.3 Fabricating Er-doped waveguides using a single sol-gel deposition technique

The starting point for the production of sol-gel layers was the synthesis of a colloidal silica sol consisting of well-dispersed oxide units (containing over 80 mol % SiO_2 with various refractive index modifying elements) with tailored size distribution using controlled chemistry. For this, 1 mole of tetraethoxysilane (TEOS) was taken and a mixture of 11.24 moles of absolute ethanol and 19.4 moles of NH_3 water (containing 1×10^{-3} moles of NH_4OH per mole of water) was added to it and stirred. This mixture was reacted at 80 °C for 72 hours under reflux condition. After this, the sol was concentrated to 30 % silica content and filtered using 0.8 µm Teflon filters. A key point is to restrict these oxide units from agglomeration during sol synthesis, storage and the evaporation of solvents during drying. This is done using proprietary organic additives to control their surface properties [5]. Additional sol components were either high refractive index components such as GeO_2 that enhance the refractive index of resulting glass layers, or components like Al_2O_3, B_2O_3 and P_2O_5, which modify the thermal expansion and flow properties of the layers. Using a combination of these dopants, the refractive index contrast between the core and cladding was engineered to be ≈ 0.75 %.

Er-doped core layers, were fabricated by dissolving $Er(NO_3)_3$ and aluminum (III) diisopropoxide ethylacetoacetate precursors in ethyl alcohol (20 wt.%), and suitable amounts of this solution (as required from the sol formulations listed in Table I) were added to the above sol before the addition of organic additives and stirred well. Such sols were filtered using 0.8 µm Teflon filters before they were spun onto the substrate. The viscosity of a finished sol could be controlled in a wide range by additives [5]. 6 µm thick waveguide core glass layers were fabricated by dispensing 4 ml of the sol onto 6 inch oxidized silicon wafers with a 20 µm buffer layer and spinning at 350 rpm for 90 seconds. Wafers were dried at 20 °C for 30 minutes and at 100 °C for 20 minutes under air. Subsequently, these films were densified at temperatures ranging from 1000 to 1200 °C for 1 to 2 hours under oxygen during ramping and dry air during soaking periods. Figure 3-1 is a block diagram of the synthesis route for the sol-gel layers.

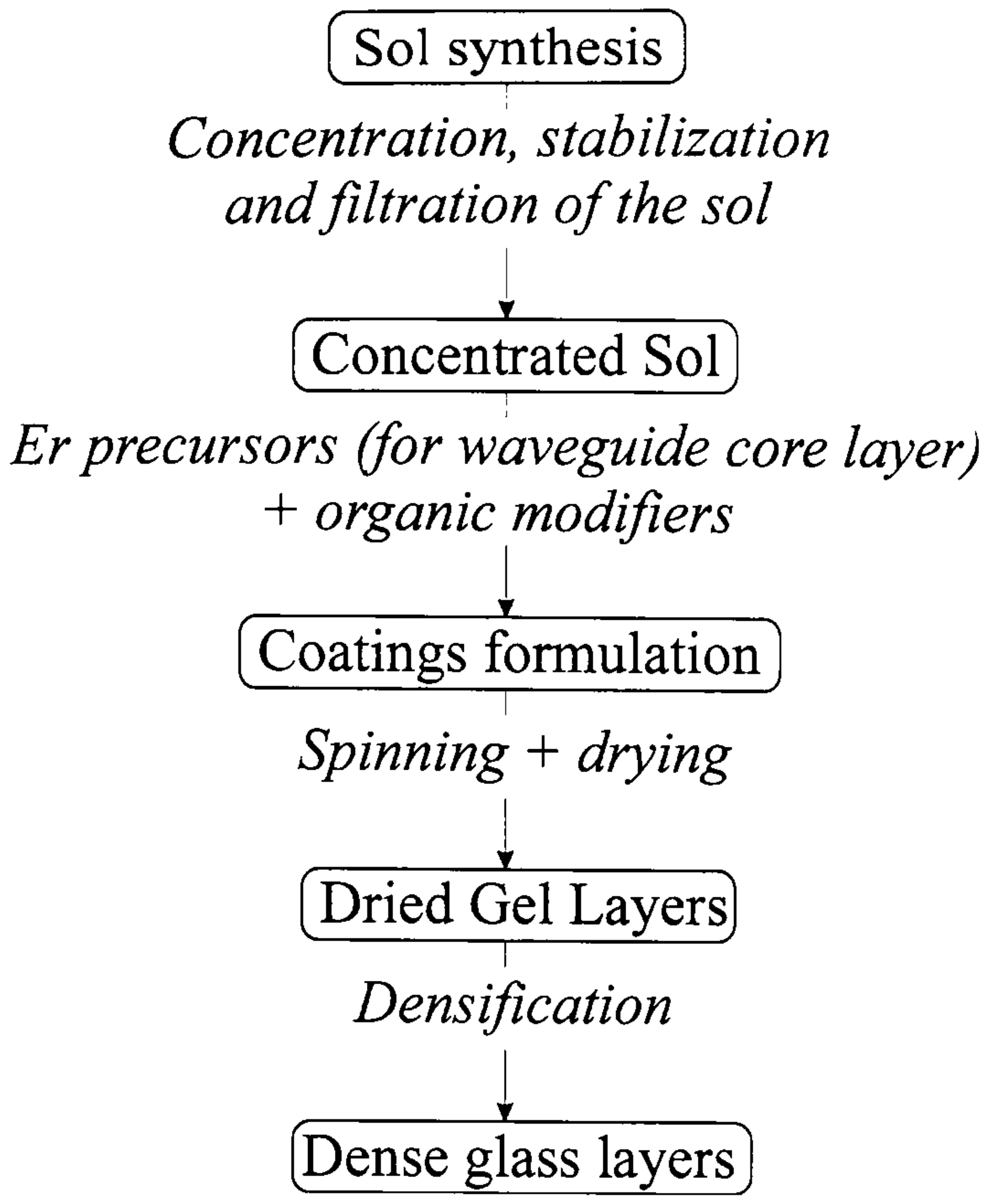

Figure 3-1 Block diagram of the sol-gel layer synthesis route.

To understand the densification behaviour of the films, He-Ne laser light was coupled into the films using a commercially available prism coupler (Metricon 2010) and the relative behaviour of the scattered "streak" was observed. It was found that core films sintered at temperatures below 1150 °C showed significant scattering. After 1150 °C the refractive index assumed a constant value and the scattered streak was found to be sharp with significant light throughput. Thus, fully densified optical quality glass layers were produced using such single spinning and drying operations after densification at 1150 °C.

Six different core sol compositions were chosen in an attempt to compare the effect of the glass composition on the operation of each device. Samples B, C and D were chosen to investigate the effect of aluminium concentration, the other samples were chosen to investigate the effect of erbium concentration. Table 3-1 summarises the sol compositions used to make the various samples. Also shown in Table 3-1 are the calculated Er^{3+} ion doping concentrations for each of the core glasses. To calculate these concentrations it was assumed that the density of the final core material was the same as that of fused silica, i.e. 2.2 $g.cm^{-3}$, an assumption that was felt to be valid due to the high silica content of the initial sol, the close similarity of the glass film refractive index compared to that of pure silica, and the fully densified nature of these films. It should be noted however that the composition of the final glass film may be significantly different from that indicated by the sol composition, and the calculated Er^{3+} concentration is intended only as an estimate.

Sample	Er_2O_3 (mol%)	Al_2O_3 (mol%)	GeO_2 (mol%)	P_2O_5 (mol%)	B_2O_3 (mol%)	SiO_2 (mol%)	Calculated Er^{3+} ion doping concentration (ions.cm^{-3})
Cladding	0	0	0	2.5	10	87.5	-
A	0.08	0.08	10	0.75	4.5	84.67	3.2×10^{19}
B	0.25	0	7.5	0.5	3.5	88.25	1.0×10^{20}
C	0.25	1.1	6.0	0.75	4.8	87.1	1.0×10^{20}
D	0.25	1.5	6.0	0.9	3.1	88.25	1.0×10^{20}
E	0.35	1.85	6.0	0.75	5.0	86.05	1.4×10^{20}
F	0.9	2.5	6.0	0.75	4.5	85.35	3.5×10^{20}

Table 3-1 Sol compositions and calculated Er^{3+} ion doping concentrations for the various samples.

To fabricate channel waveguides from the Er-doped films, a commercial photoresist (Shipley, SU1818) was spun on top of the core glass layers. I-line photolithography using an Electron Vision EV 620 mask aligner and an e-beam written silica mask were used for defining waveguides. An optimised etching process was developed for obtaining waveguides with desired cross section and minimal sidewall roughness using an Oxford Plasmalab RIE 80 and CHF_3 and Ar gases. Waveguide cross sections were of the order of 6 μm x 6 μm. For a comparison of the sidewalls of the etched waveguides, etching was also performed on thermally grown oxide layers. The resulting sidewalls are shown in Figure 3-2.

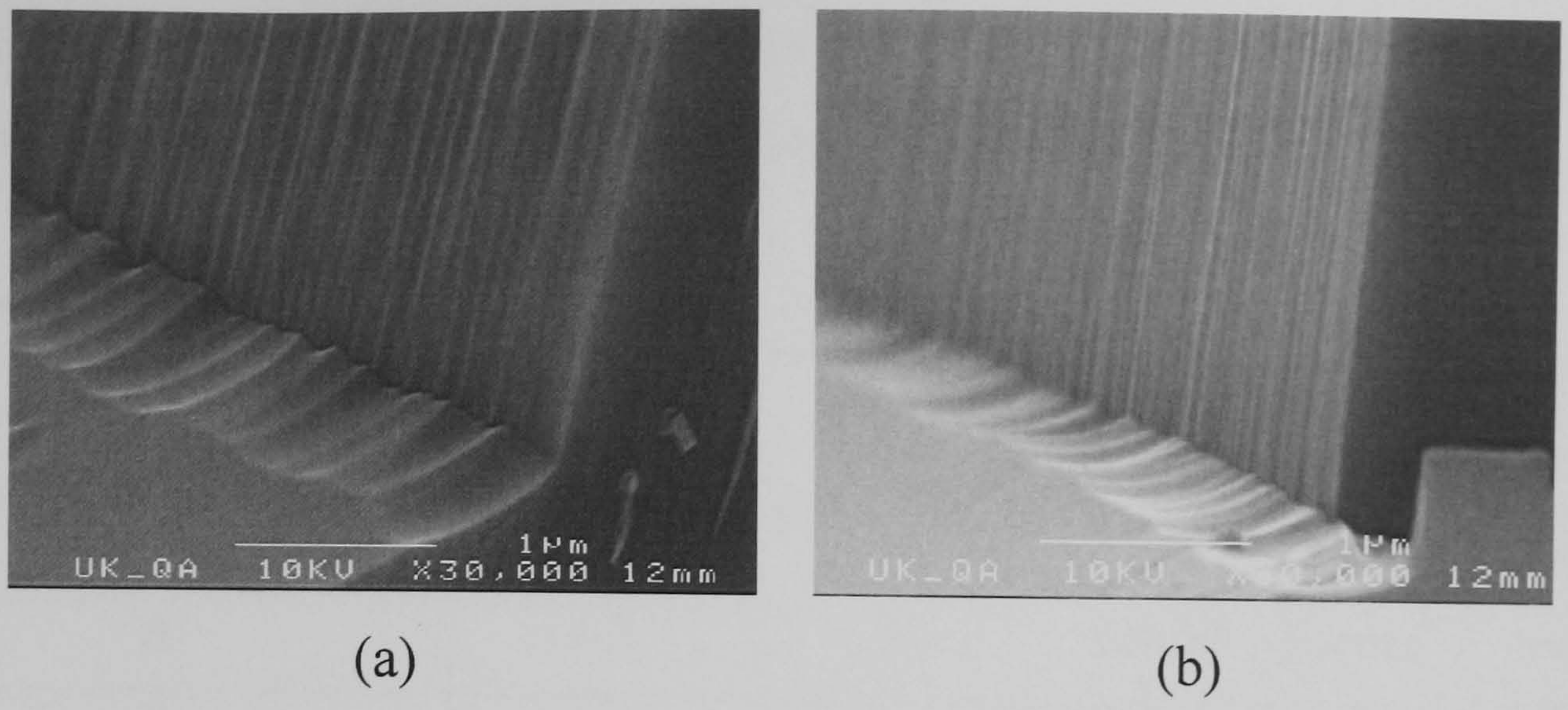

(a) (b)

Figure 3-2 Scanning electron microscope images of the side walls after etching either (a) sol-gel layers or (b) thermal oxide layer. The field of view of each picture is approximately 2.9 µm × 3.8 µm.

It can be seen from Figure 3-2 that the sidewalls of etched sol-gel and thermally oxidized films show a similar roughness, of order of 10's of nanometers. It can be concluded therefore that the sol-gel glass synthesized in this work is quite homogeneous.

To obtain a cladding formulation showing conformal coverage of the guides, significant concentration of boron and phosphorous is needed. High concentration of boron is needed to adjust the refractive index down to that of SiO_2 level (i.e., 1.445 at 1550 nm). Tuning in the cladding composition and densification process has resulted in an optimised cladding formulation containing 10 mol % B_2O_3, 2.5 mol % P_2O_5 and 87.5 mol % SiO_2 with a refractive index of 1.446 at 1550 nm (the same as that of thermally oxidized SiO_2) showing high flowability at around 1000 °C. As a result, the cladding shows conformal filling of narrow gaps without any deformation of the core geometry.

Prior to waveguide etching and cladding deposition, the refractive index and thickness of the core material was measured at 633 nm using a Metricon 2010 prism coupler, these measurements were conducted by the group at Exxelis Ltd. In order to evaluate the refractive index of the core material at other wavelengths, the refractive index of a separate sol-gel planar waveguide supplied by Exxelis was measured at 633, 980 and 1550 nm by me using a separate Metricon 2010 prism coupler located at the University of Leeds. The dispersion characteristics of this material were then used to infer the refractive index of the other samples at 980 and 1550 nm. The results of the refractive index measurements and calculations are summarised in Table 3-2.

Sample	Waveguide core size (μm)		Refractive index (n)		
	x-axis	y-axis	633 nm	980 nm	1550 nm
Cladding				1.4485*	1.4460
A	6.2	5.5	1.4695	1.4610*	1.4569*
B	8.0	6.1	1.4465	1.4580*	1.4540*
C	6.9	5.3	1.4666	1.4581*	1.4541*
D	8.3	5.3	1.4660	1.4575*	1.4535*
E	6.1	5.1	-	-	-
F	8.1	4.8	1.4725	1.4639*	1.4599*
Sol-gel planar waveguide			1.4633	1.4523	1.4508
* indicates that this value has been inferred from the dispersion characteristics of the sol-gel planar waveguide sample					

Table 3-2 Waveguide core cross sections and refractive indices.

The refractive index data for sample E is not reported in Table 3-2 because the refractive index data supplied for this sample was unreliable. For the mode modelling described in the following sections, the refractive index data for sample C was used for sample E since the composition of sample E is most similar to that of sample C.

Although many waveguides were available for characterisation on each sample, only one waveguide was chosen from each sample and used consistently throughout all characterisation experiments. The cross sectional size of this waveguide was measured using a calibrated optical microscope as shown in Figure 3-3. The results of these measurements are also summarised in Table 3-2. The brightness and contrast of Figure 3-3 has been adjusted to increase the visibility of the core area.

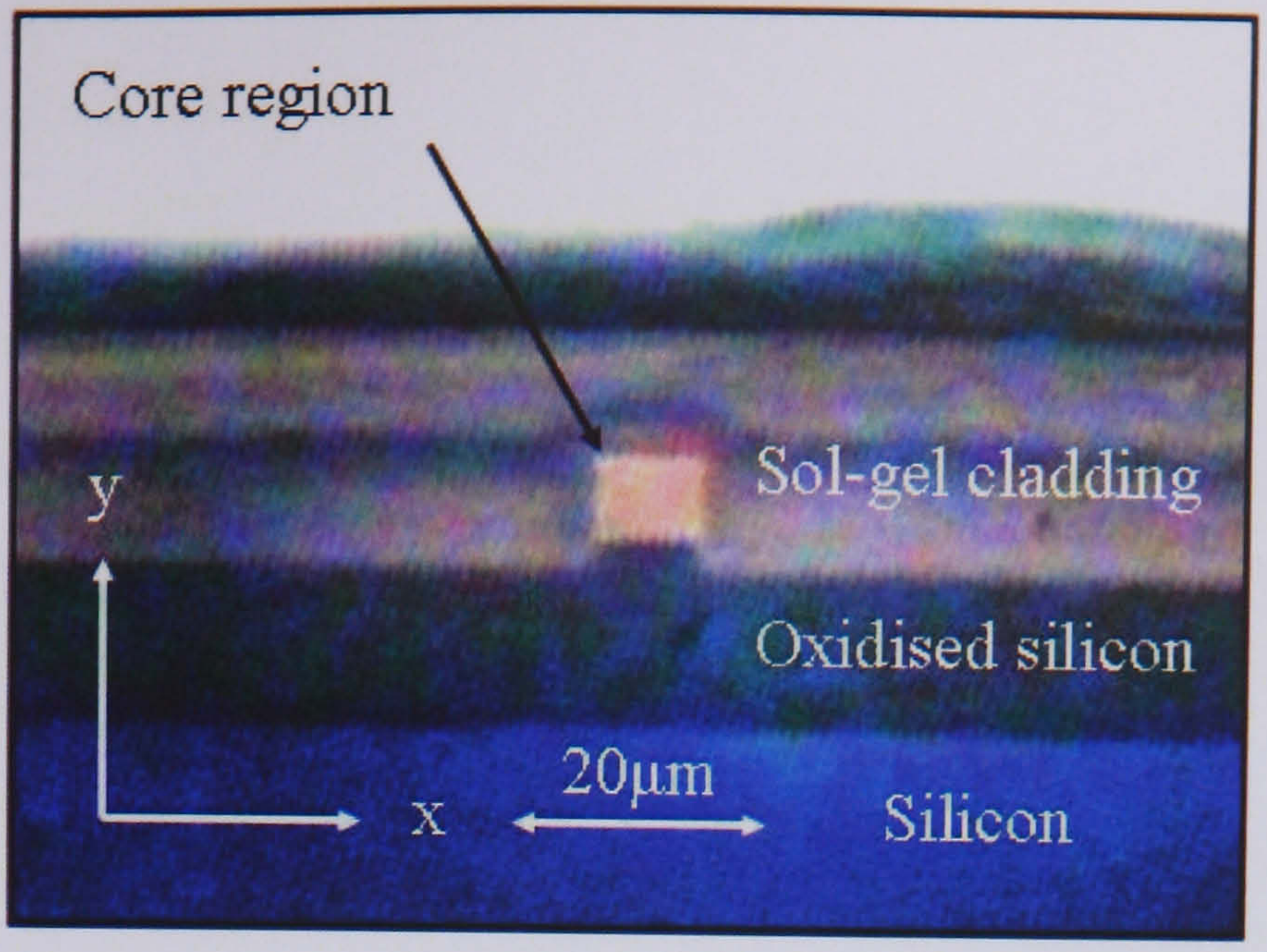

Figure 3-3 Transmission mode optical microscope image of the waveguide characterised on sample B.

In this section, the fabrication of the sol-gel samples has been described together with some of the basic properties of the channel waveguides of interest. In the following section, the experimental techniques used to characterise the sol-gel waveguides will be presented, together with the results of these investigations.

3.4 Sol-gel fabricated Er-doped waveguide characterisation

In Chapter 2, the physical principles that underlie the operation of an EDWA were presented and discussed, and a number of physical parameters that affect the operation of an EDWA were identified. At the end of the Chapter 2, the effect of these parameters on the gain vs. 980 nm pump power characteristics of a theoretical EDWA were investigated using the Snoeks model. Consequently, it is clear that in order to understand and improve the gain operation of Er-doped waveguides, these parameters must be experimentally measured or evaluated in some way. This section of the thesis describes a number of studies conducted to evaluate these parameters in the sol-gel waveguides.

3.4.1 Signal-waveguide and pump-waveguide overlap factors

As discussed in the Chapter 2, the overlap of the pump and signal fields with the Er-doped core region is a significant factor in the operation of an EDWA. The degree of this overlap is represented by the overlap factor (Γ). As discussed in Chapter 2, the overlap factor is defined by Equation 2.20

$$\Gamma = \int_{-x}^{+x} \int_{-y}^{+y} p_0(x,y)\,dxdy$$

Equation 2.20

where, $+x$, $-x$, $+y$, $-y$ are the dimensions of the Er-doped core region and $p_o(x,y)$ is the intensity distribution of the optical mode, normalised such that $\int_{-\infty}^{+\infty}\int_{-\infty}^{+\infty} p_0(x,y)\,dxdy = 1$.

To determine the Γ factor for the sol-gel samples, the experimentally measured refractive index and waveguide cross sectional data presented in Table 3-2 was used to model the pump and signal fields in the waveguide. The modelling was conducted using a commercially available finite element modelling package (Femlab^{TM}). As an example, Figure 3-4 shows the modelled time averaged total energy density distribution for the 1550 nm TE fundamental mode for sample C.

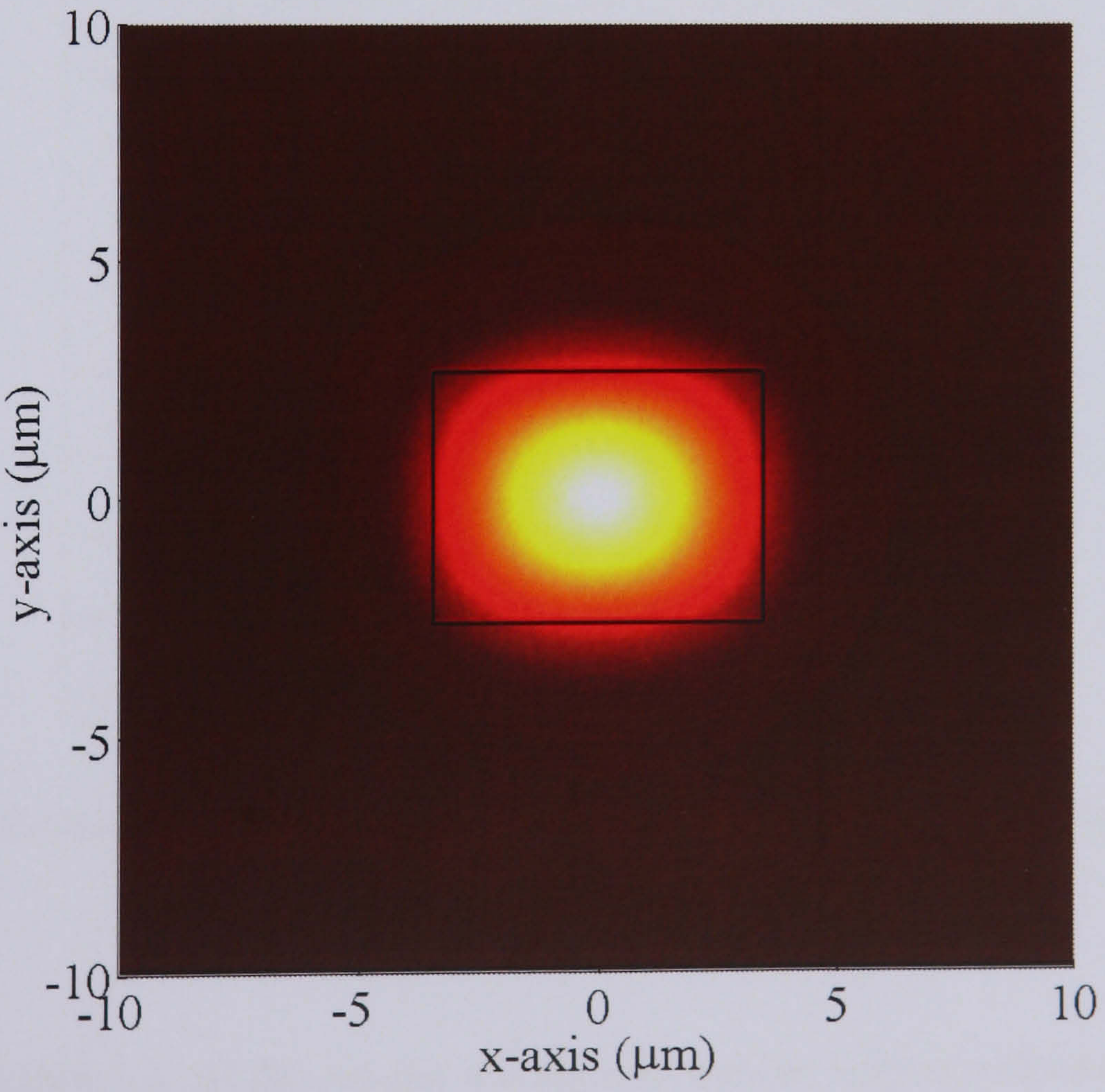

Figure 3-4 Modelled time averaged total energy density distribution for the 1550 nm fundamental mode using data for sample C. The black rectangle in the middle of the figure represents the boundary of the waveguide core.

Modelling results indicated that all sol-gel waveguides should support higher order modes than the fundamental TE and TM modes at both the 980 nm pump and 1550 nm signal wavelengths. To investigate this result the output facet of each waveguide was imaged onto an IR Vidicon camera while coupling a signal at the correct wavelength into the waveguide at the other end. In contrast to the modelling results, all waveguides were observed to be single mode at 1550 nm, indicating that the higher order modes were lossy. In agreement with the modelling results however, all waveguides were observed to be multimode at 980 nm, both in the x-axis and the y-axis. It was also observed however that under the condition of maximum throughput, the 980 nm waveguide mode closely resembled that of the TEM (0,0) mode.

Using the mode field modelling results and the core size data presented in Table 3-2, the Γ factors for both the fundamental 980 nm pump and fundamental 1550 nm signal fields were evaluated numerically according to Equation 2.20. The calculated Γ factors are summarised in Table 3-3.

Sample	Signal – waveguide overlap factor (Γ_s)	Pump – waveguide overlap factor (Γ_p)
A	0.81	0.94
B	0.78	0.9
C	0.73	0.9
D	0.7	0.82
E	0.7	0.9
F	0.73	0.8

Table 3-3 Calculated signal-waveguide and pump-waveguide overlap factors for the various sol-gel samples

As shown in Table 3-3, all the sol-gel waveguides exhibit similar values of Γ_s and Γ_p. It is also apparent from Table 3-3 that since the pump wavelength is always shorter than the signal wavelength, Γ_p is consistently higher than Γ_s.

3.4.2 Absorption losses

In the simplest model, the Er^{3+} ion $^4I_{13/2} \rightarrow {}^4I_{15/2}$ transition emission and $^4I_{15/2} \rightarrow {}^4I_{13/2}$ transition absorption cross sections are close to equal at around 1550 nm. When pump light is applied to the device, Er^{3+} ions are excited to the $^4I_{13/2}$ energy level, with each excited ion not only providing the possibility for stimulated emission, but also removing the possibility for a similar amount of absorption. It is clear therefore that if all ions are excited to the $^4I_{13/2}$ energy level, a change in signal transmission (excluding the effect of ASE) of approximately twice the absorption would be expected [6]. Consequently, it is essential to know the amount of absorption present in the waveguide so that the degree of population inversion obtained through pumping can be calculated.

The total insertion loss of an un-pumped Er doped waveguide when placed in an optical fibre transmission line is the sum of coupling losses to and from the waveguide and all propagation losses along the waveguide. The total propagation losses are the result of absorption by the Er^{3+} ions, scattering and radiation losses. By assuming that the amount of absorption at 1625 nm due to Er^{3+} ions is negligible [7], the loss due to absorption by Er^{3+} ions throughout the $^4I_{15/2} \rightarrow {}^4I_{13/2}$ transition can be calculated by subtracting the insertion loss at 1625 nm from the insertion loss measured inside the absorption band.

The insertion losses of the sol-gel samples were measured using the experimental setup shown in Figure 3-5.

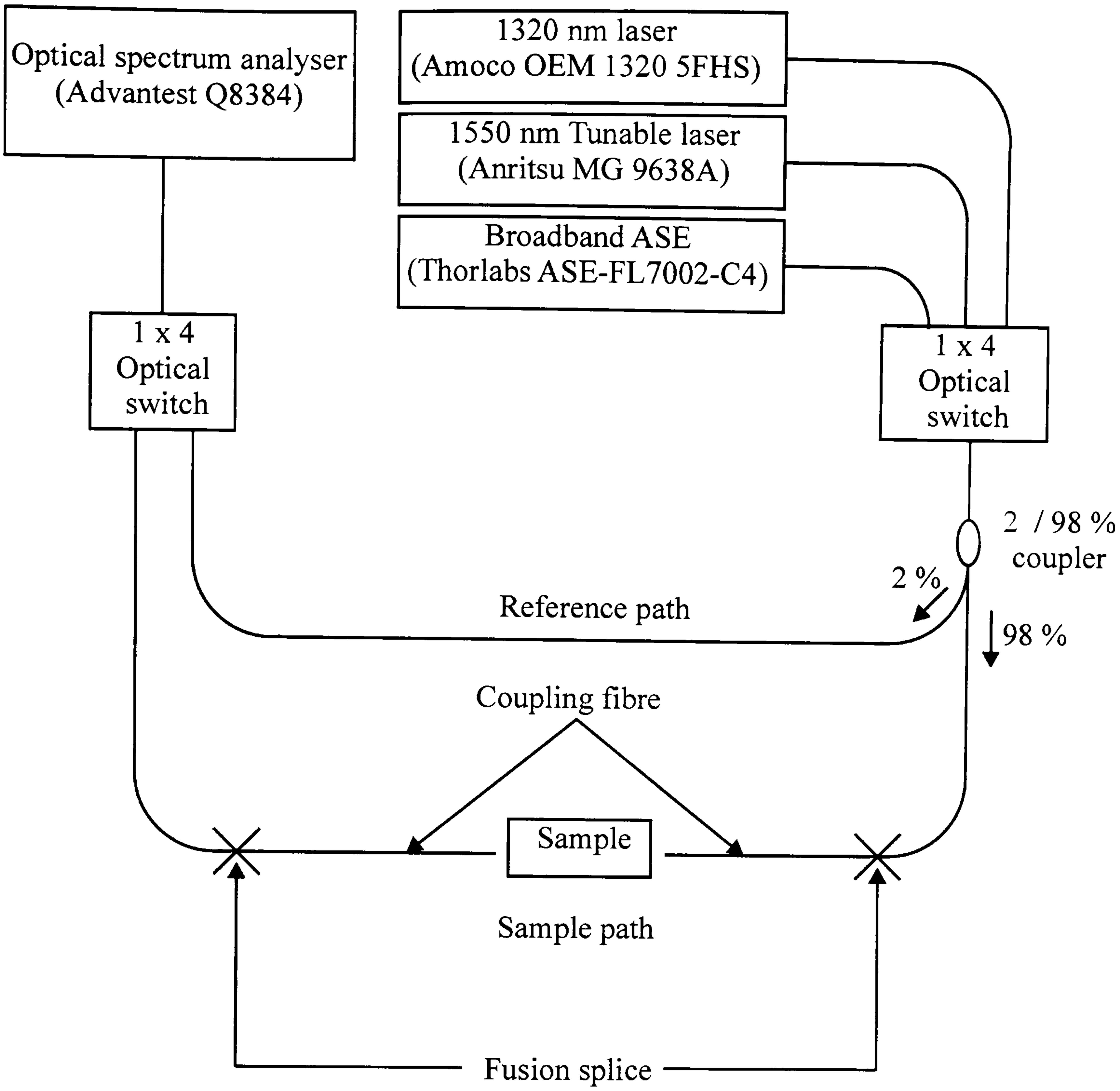

Figure 3-5 Schematic diagram of the experimental setup used to measure the insertion loss of the sol-gel waveguides.

As shown in Figure 3-5, light from three different signal sources could be coupled one at a time into the 2 / 98 % directional coupler using a 1 × 4 optical switch. By coupling the signal from the 2 % arm of the coupler into the OSA via a second 1 × 4 optical switch, a reference signal was obtained that could be used to check the stability of the signal sources during the measurements. The signal from the 98 % arm of the coupler was used as the signal to be coupled to the waveguide under test. This signal was coupled into the waveguide under test using direct fibre-waveguide butt coupling. All fibre-waveguide alignment was conducted using x-y-z flexure stages with pitch and yaw angular adjustment. The transmitted signal was collected at the opposite end of the waveguide and connected to a second 1 × 4 optical switch. Index matching gel was used between the cleaved coupling fibres and the waveguide facets to minimise the loss due to reflection. Using the experimental setup shown in Figure 3-5, the insertion loss was defined as the difference in signal transmission through the sample arm of the setup with the sample in place, and with the two coupling fibres fusion spliced together. The repeatability of the switching of the optical switches was < 0.1 dB. Using this experimental setup, the possible error in the measured insertion loss is estimated to be approximately 0.3 dB and is due to alignment accuracy. Due to the nature of the insertion loss measurement, the insertion loss cannot be greater than measured.

As a typical example, Figure 3-6 shows the insertion loss spectrum from 1520-1625 nm measured for sample C when coupled to SMF-28 fibres. The insertion loss spectrum was measured using the broadband ASE light source.

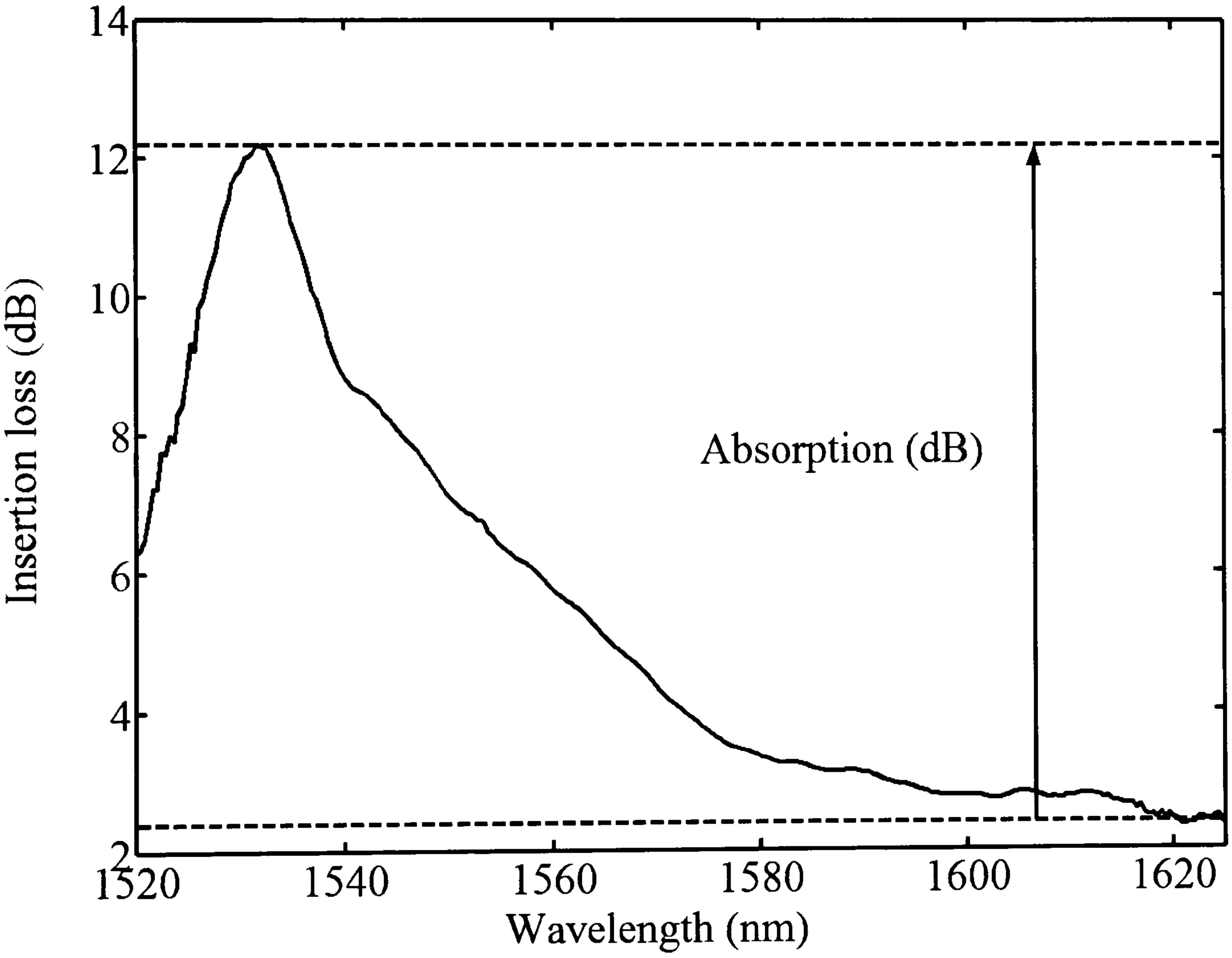

Figure 3-6 Insertion loss spectra for sample C when coupled to SMF-28 fibres.

Using the technique described, the loss due to absorption in all the sol-gel samples was measured. Figure 3-7 is a plot of the measured peak erbium absorption coefficient vs. the Er_2O_3 concentration in the sol.

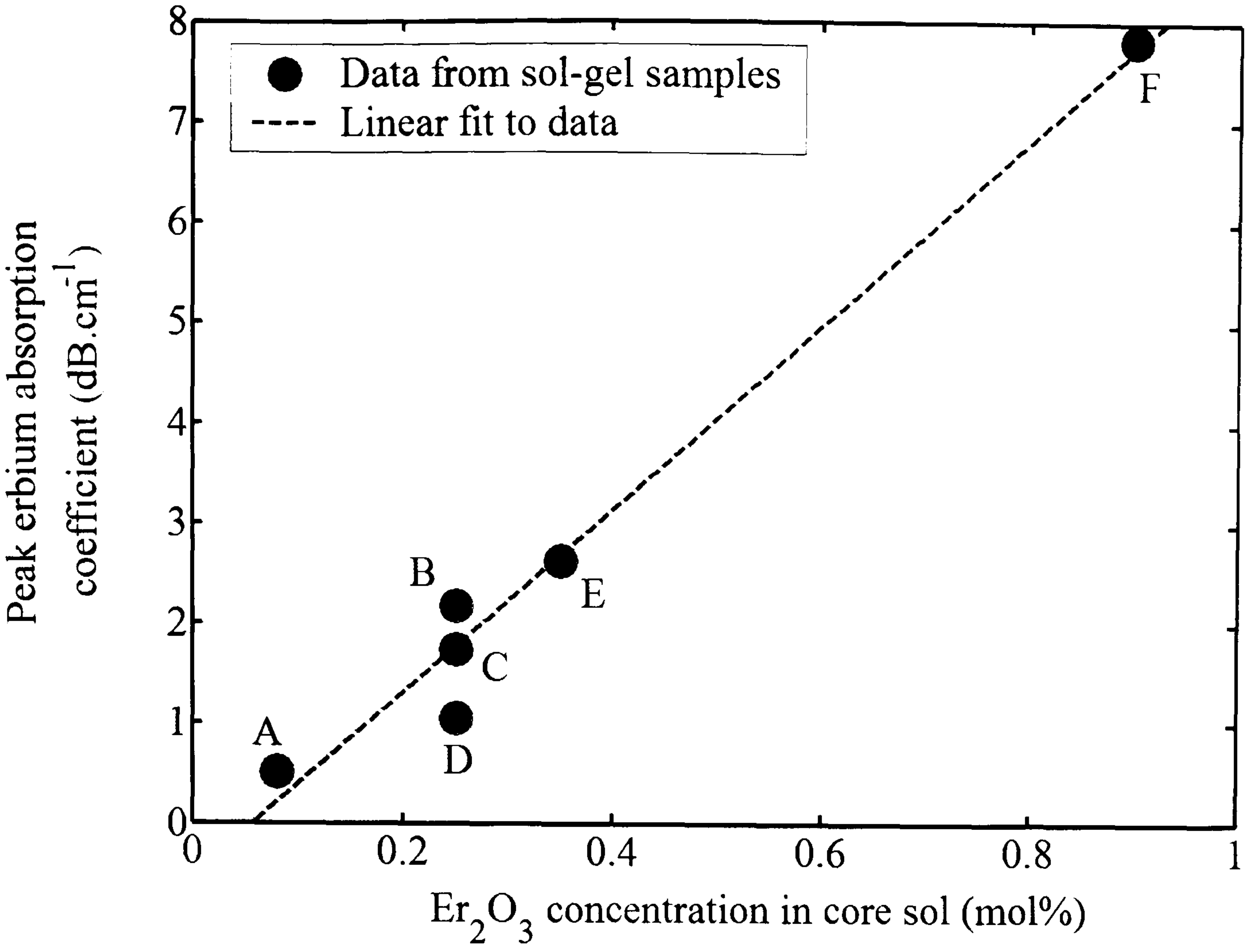

Figure 3-7 Peak erbium absorption coefficient vs. the Er_2O_3 concentration in the sol

As can be seen in Figure 3-7, the peak absorption coefficient generally increases linearly with Er_2O_3 concentration in the sol. However, for samples B, C and D that use the same Er_2O_3 concentration in the sol, there is a range of measured peak absorption coefficients from 2.18 → 1.06 dB.cm^{-1}. Because the difference in the calculated signal-waveguide overlap factors given in Table 3-3 is small, the variation in measured absorption coefficient may indicate that the final glass composition is significantly different from that indicated by the sol composition.

3.4.3 Propagation and coupling losses

A number of techniques have previously been successfully applied to measuring the propagation losses of channel waveguides, these include the cutback method [8], Fabry-Perot method [9] and streak method [10]. For our purposes however, we used the multimode fibre method [11], since it is non-destructive and accurate for single mode waveguides. To do this, the coupling losses to and from the sol-gel samples using SMF-28 fibres were first measured using the experimental setup shown in Figure 3-8.

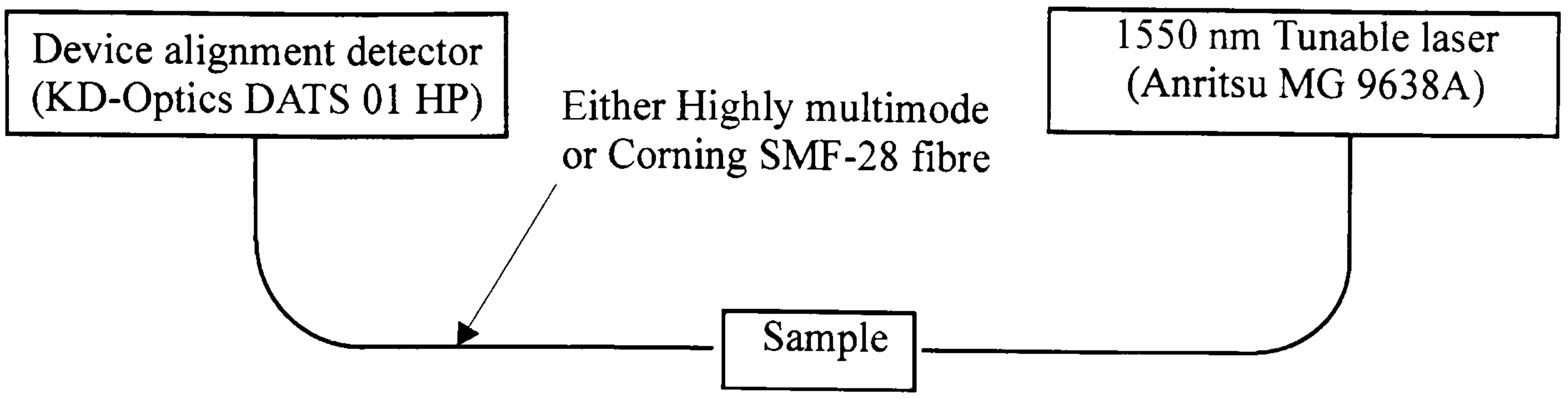

Figure 3-8 Schematic diagram of the experimental setup used to measure the coupling losses between the waveguide under test and Corning SMF-28.

As shown in Figure 3-8, light at 1550 nm is coupled into the waveguide under test at one end using direct fibre-waveguide butt-coupling. The transmitted light is then collected at the opposite end of the waveguide using either a highly multimode or Corning SMF-28 fibre. Assuming the coupling loss from the waveguide to the highly multimode fibre is zero, the coupling loss is the difference in signal throughput when using the single mode fibre compared to using the highly multimode fibre to collect the light from the waveguide. Alignment to the waveguide was performed in the usual manner. Index matching gel was used between the fibres and the sample facets.

Once the coupling losses had been established, the background propagation loss due to non-absorption mechanisms were calculated by subtracting the total coupling losses from the measured insertion loss at 1625 nm. The results of the coupling loss and background propagation loss measurements are summarised in Table 3-4.

Sample	Coupling loss to SMF-28 (dB)	Insertion loss at 1625 nm (dB)	Sample length (cm)	Average propagation loss ($dB.cm^{-1}$)	Polarisation dependent loss (dB)
A	0.4	2.6	5.2	0.35	0.17
B	0.7	4.1	7.7	0.35	0.26
C	0.6	2.4	5.6	0.21	0.2
D	0.4	3.5	7.1	0.38	0.18
E	0.6	2.1	7.1	0.13	0.29
F	1.1	3.1	3.75	0.24	0.72

Table 3-4 Summary of coupling loss, waveguide loss and polarisation dependent loss measurements for the sol-gel samples

As shown in Table 3-4, channel waveguides with low propagation, coupling and insertion losses have been fabricated. As discussed in Chapter 2, low propagation and coupling losses are critical for maximising the EDWA device gain and pumping efficiency. The demonstration of propagation losses as low as 0.13 $dB.cm^{-1}$ and coupling losses as low as 0.4 dB/facet to SMF-28 are a significant demonstration for the development of efficient EDWA devices using the single sol-gel deposition route.

3.4.4 Waveguide polarisation dependent loss (PDL)

For single mode optical waveguides, including single mode optical fibres, the propagating light can be thought to be composed of two orthogonal modes; the transverse electric (TE) and the transverse magnetic (TM). If the waveguide exhibits any degree of birefringence, each polarisation experiences a slightly different waveguide refractive index contrast resulting in different TE and TM mode fields and a polarisation dependent insertion loss (PDL). When this effect is combined with stress induced polarisation scrambling in real fibre-optic transmission lines, the S/N ratio becomes degraded, reducing the maximum BL product of the connection. It is clear therefore that useful PLC devices must exhibit low PDL.

To measure the PDL of the sol-gel samples, the well known all states method was used. Figure 3-9 shows a schematic diagram of the experimental setup used to measure the PDL at 1550 nm of the sol-gel samples.

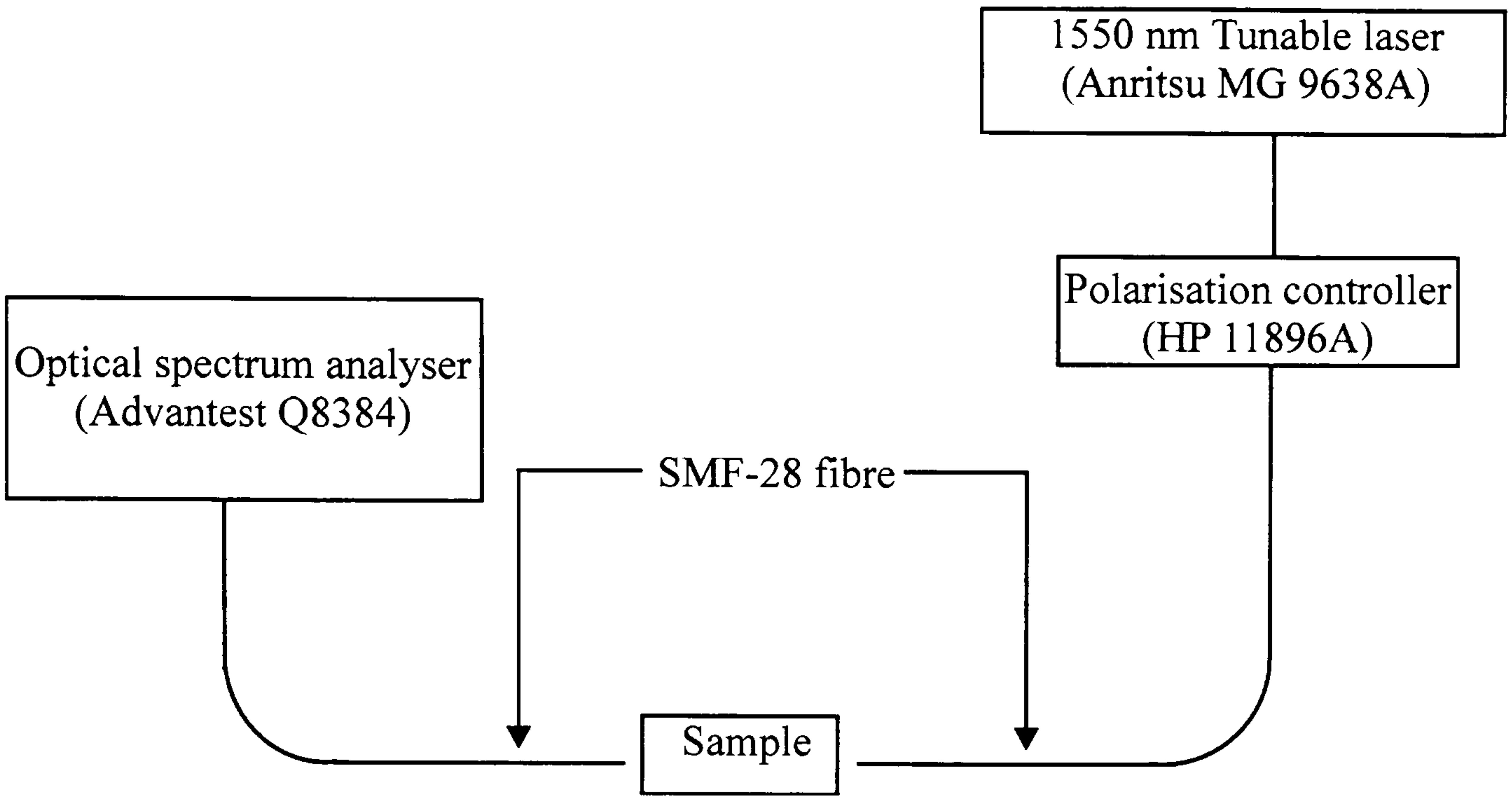

Figure 3-9 Schematic diagram of the experimental setup used to measured the PDL at 1550 nm for the various waveguide samples

As shown in Figure 3-9, a linearly polarised signal from a tuneable laser at 1550 nm is coupled into an automated polarisation controller. This signal is subsequently coupled into and out of the waveguide under test using direct fibre-waveguide butt-coupling. The signal from the waveguide under test is finally coupled into an OSA. To measure the PDL, the polarisation controller is set to scan all polarisation states while the OSA is used to measure the maximum and minimum signal power. Prior to measuring the PDL of any samples, the PDL of the measurement system with the two waveguide coupling fibres fusion spliced together was measured and found to be < 0.05 dB. The error in the PDL measurement is therefore ± 0.1 and is due to the PDL of the measurement setup itself.

The results of the PDL measurements are also summarised in Table 3-4. As shown in Table 3-4, PDL values of as low as 0.17 dB for a 5.2 cm long sample indicate that waveguides with low birefringence have been fabricated, an important demonstration for sol-gel fabricated waveguide devices.

3.4.5 Waveguide gain studies

Clearly, one of the most important characteristics of any Er-doped waveguide intended for EDWA applications is the ease with which a population inversion may be induced through pumping. Three definitions are generally used for the gain of an optical amplifier; the relative gain, the net gain and the internal gain [12]. The relative gain is defined as the change in transmission of a signal due to pumping as shown by Equation 3-4.

$$G_{Rel}\ (dB) = 10Log\left(\frac{P_{out(Pump)} - ASE}{P_{out(No\ pump)}}\right)$$

Equation 3-4

where, G_{Rel} is the measured relative gain, $P_{out(Pump)}$ is the signal power measured after the device while pumping, ASE is the power of the amplified spontaneous emission at the signal wavelength and $P_{out(No\ Pump)}$ is the signal power measured after the device without pumping.

The net gain is defined as the change in signal power due to propagation through the device as shown by Equation 3-5.

$$Net\ gain\ (dB) = 10Log\left(\frac{P_{out(Pump)} - ASE}{P_{in}}\right)$$

Equation 3-5

where, P_{in} = the signal power measured before the device.

Finally, the internal gain is defined as the net gain that the device would have exhibited under pumping if all the background losses were zero.

The gain operation of the sol-gel samples was characterised using the experimental setup shown in Figure 3-10.

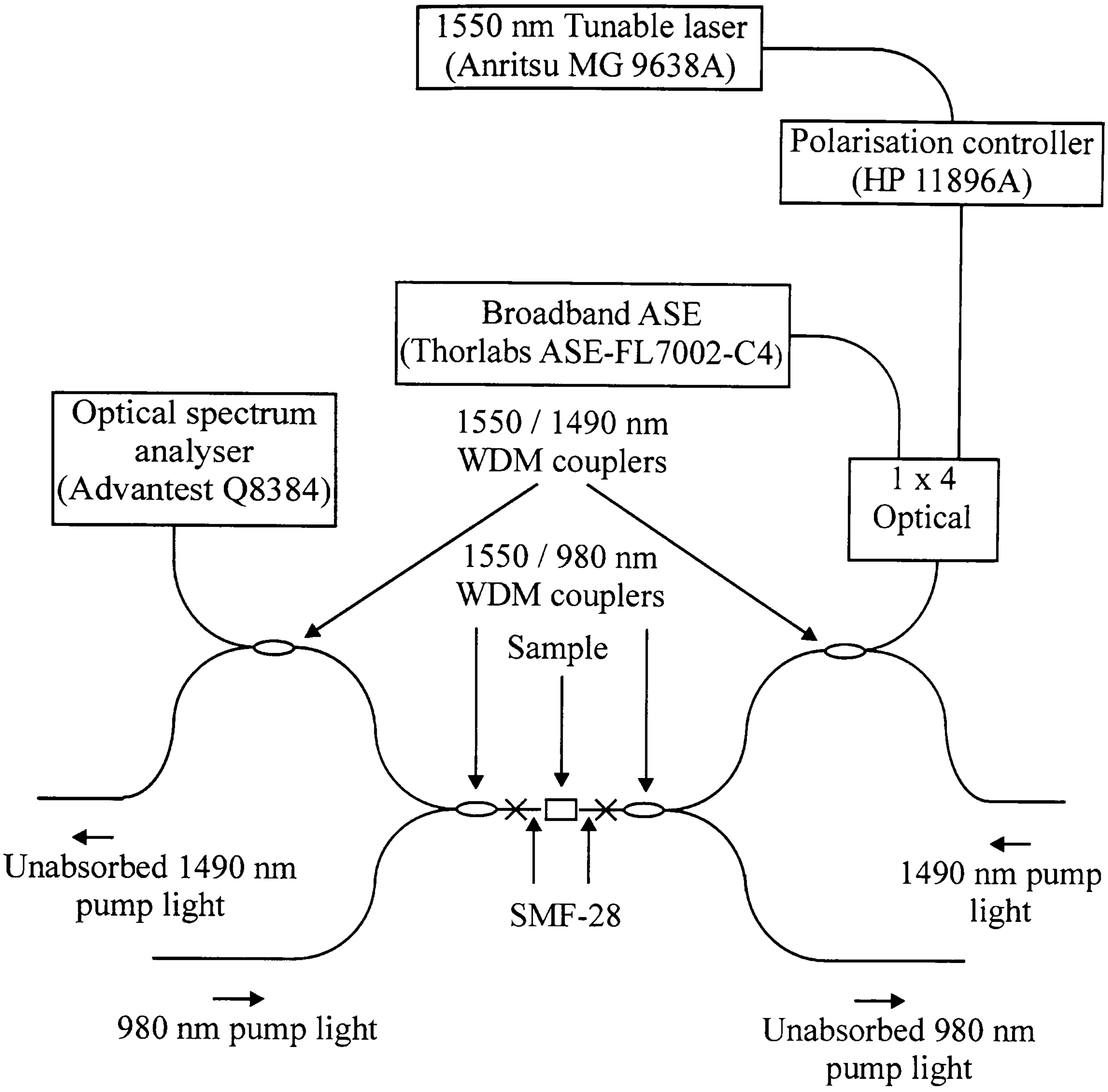

Figure 3-10 Schematic diagram of the experimental setup used to characterise the gain operation of the sol-gel waveguides.

As shown in Figure 3-10, pumping could be conducted at either 980 or 1490 nm. By polarisation combining two 980 nm diode lasers, up to 500 mW of 980 nm pump light was available for pumping. By polarisation combining two 1490 nm diode lasers, up to 220 mW of 1490 nm pump light was available for pumping. For each pump wavelength, the gain operation was characterised in the following manner. A probe signal from a broadband ASE source was first used to measure the relative gain spectrum across the 1550 nm region. In order to avoid any spectral hole burning effects, a signal from a tuneable laser set to the peak of the gain spectrum was then used to measure the relative gain vs. pump power and relative gain vs. signal power characteristics. To investigate if polarisation dependent gain (PDG) effects were significant, the PDL of the waveguide under test was measured under maximum pumping. Due to a lack of laser power supplies at the time of testing, pumping was either conducted using either 980 or 1490 nm pumping, but not at the same time. Coupling to the waveguide was performed using direct fibre-waveguide butt-coupling. Errors in the gain characteristics measured using this setup shown in Figure 3-10 are negligible. As a typical example, Figure 3-11 shows the relative gain spectrum recorded for sample C using 500 mW of 980 nm pump power.

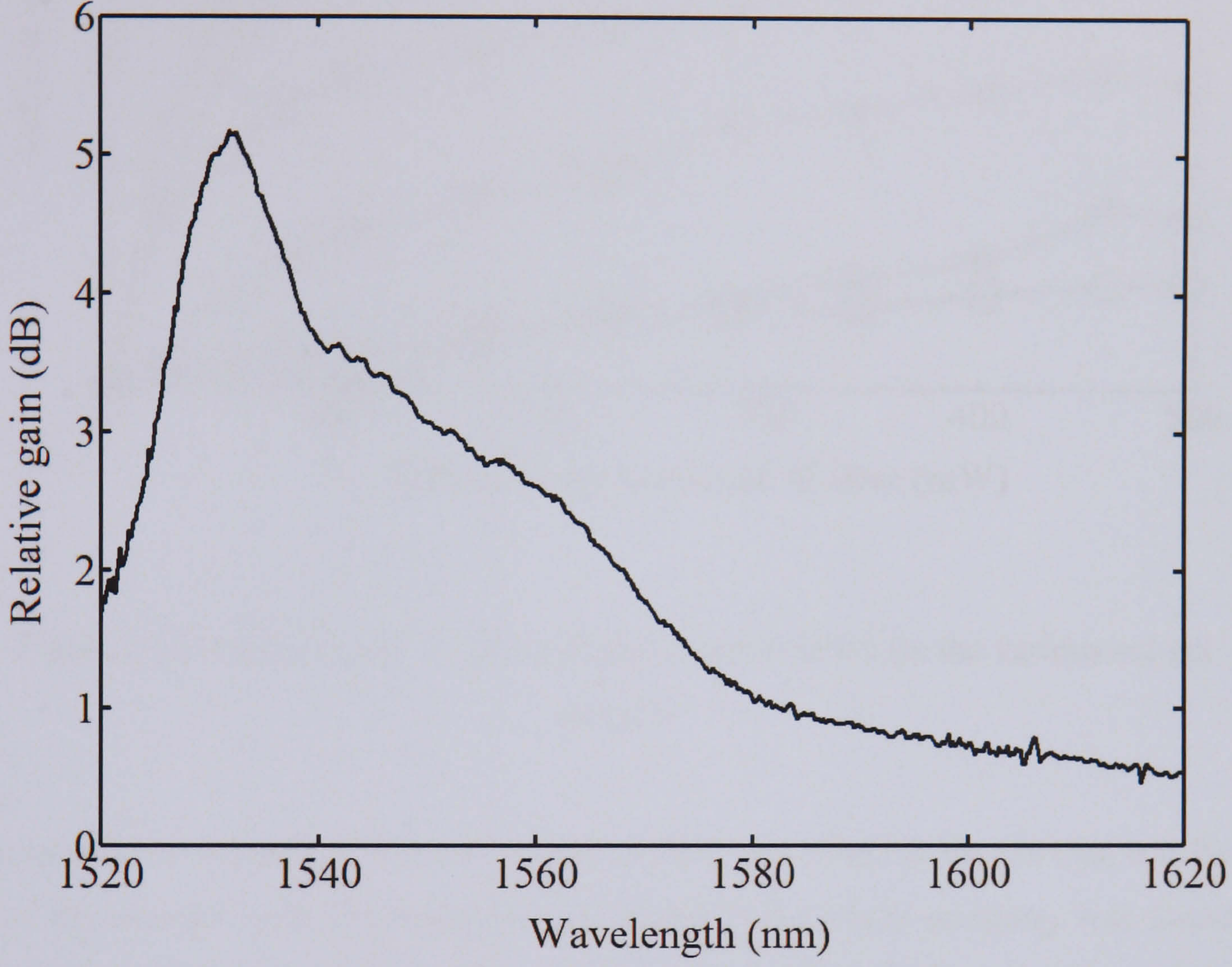

Figure 3-11 Relative gain vs. wavelength spectrum for sample C using 500 mW of 980 nm pump.

As expected, the relative gain spectrum shown in Figure 3-11 closely resembles the absorption and fluorescence lineshapes of the $^4I_{15/2} \rightarrow {}^4I_{13/2}$ and $^4I_{13/2} \rightarrow {}^4I_{15/2}$ transitions respectively.

Figure 3-12 shows the relative gain vs. 980 nm pump power characteristics measured for the various sol-gel samples. Measuring the relative gain vs. signal power up to a maximum signal power of 6 dBm using maximum pump power revealed little change in the relative gain indicating that all measurements were conducted in the small signal regime. Pumping at 1490 nm showed no increase in the relative gain.

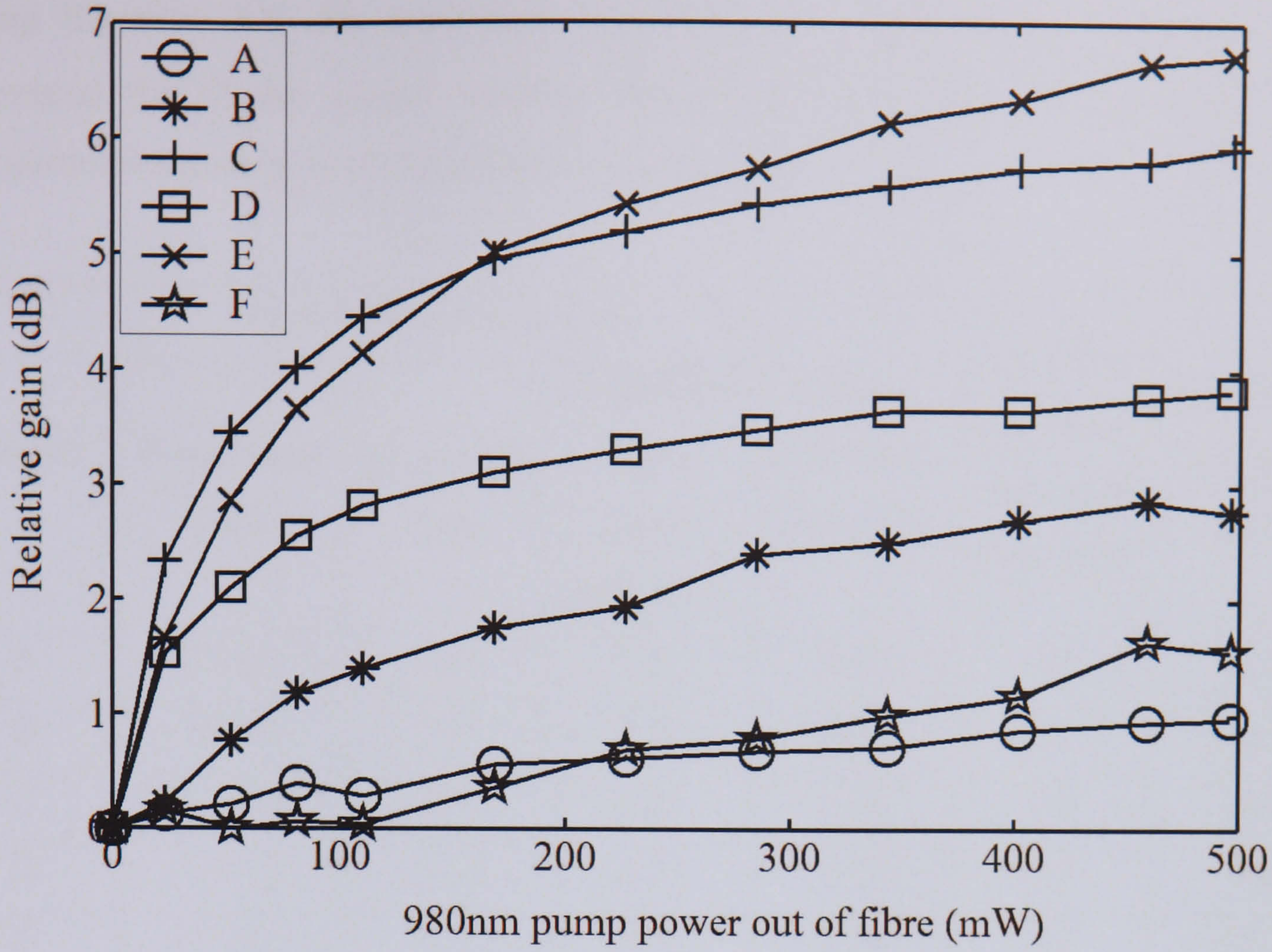

Figure 3-12 Relative gain vs. pump power characteristics for the various sol-gel samples.

The increase or decrease in PDL as a result of PDG was found to be less than 0.1 dB for all of the samples with the exception of sample F for which pumping was found to decrease the PDL by 0.3 dB. These results indicate that PDG is not a significant problem for devices fabricated using this route.

As mentioned previously, the degree of population inversion obtained through pumping can be calculated from the magnitude of the relative gain. Assuming the emission and absorption cross sections are the same at the signal wavelength, Equation 3-6 relates the average fractional population of the $^4I_{13/2}$ level (n_2) along the waveguide, to the magnitude of the relative gain (G_{Rel}) and the absorption in the waveguide (Abs) (both at the signal wavelength). The derivation of Equation 3-6 is given in Appendix B.

$$n_2 = \frac{G_{Rel}\,(dB)}{2 \times Abs\,(dB)}$$

Equation 3-6

Using Equation 3-6, the maximum value of n_2 obtained through pumping was calculated for all the sol-gel samples. Table 3-5 summarises the results of these calculations and the gain characterisation experiments.

Sample	Maximum relative gain			Erbium absorption (dB.cm^{-1})	Estimated fraction of ions in the $^4I_{13/2}$ state	Maximum Net gain (dB)
	Wavelength (nm)	Magnitude (dB)	Magnitude / unit length (dB.cm^{-1})			
A	1536.6	1.0	0.19	0.51	0.2	-4.3
B	1533.2	2.9	0.38	2.02	0.1	-16.8
C	1531.8	5.9	1.05	1.75	0.3	-6.3
D	1533.2	3.8	0.54	1.05	0.3	-7.2
E	1534.4	6.7	0.94	2.51	0.2	-13.2
F	1538.0	1.6	0.43	6.87	0.0	-27.3

Table 3-5 Summary of relative gain and net gain measurements, together with the estimated maximum fractional population of the $^4I_{13/2}$ metastable state obtained through pumping.

As can be seen in Table 3-5 the maximum value of n_2 obtained through pumping was 0.3, thus indicating that a population inversion had not been obtained in the sol-gel samples. In addition, it is also clear from Figure 3-12 that the relative gain vs. 980 nm pump power characteristics are heavily saturated under maximum pumping and that increased pumping would not significantly increase the magnitude of the relative gain. Consequently, it is concluded that there is a substantial amount of unsaturable absorption present in the sol-gel samples, which, after consulting the literature, is most likely to be due to clustering of the rare earth ions. It has been proposed by a number of groups that due to efficient ion-ion interactions between clustered ions, it is only possible to excite one ion per cluster resulting in an unsaturable loss [13,14].

3.4.6 *Time resolved erbium $^4I_{13/2} \rightarrow {}^4I_{15/2}$ transition fluorescence studies*

Under the assumptions discussed in Chapter 2, the rate of change of the $^4I_{13/2}$ level population can be described by Equation 2.10 given again below.

$$\frac{dn_2}{dt} = R.(1-n_2) - \frac{n_2}{\tau_{21}} - \rho_{Er}.C_{22}.n_2^2$$

Equation 2.10

It is clear therefore that the $^4I_{13/2} \rightarrow {}^4I_{15/2}$ transition lifetime (τ_{21}), and the C_{22} homogeneous cooperative upconversion (HCU) coefficient play an important role in determining how easily a population inversion can be induced. In this section, time resolved fluorescence studies are conducted to determine these parameters in the sol-gel samples.

Under zero pump conditions, R in Equation 2.10 is zero and Equation 3-7 is a solution to Equation 2.10 [15].

$$N_2(t) = \frac{1}{\tau_{21}}\left[\left(\frac{1}{\tau_{21}\,N_2(0)} + C_{22}\right)\exp\left(\frac{t}{\tau_{21}}\right) - C_{22}\right]^{-1}$$

Equation 3-7

Equation 3-7 predicts the decay of N_2 after excitation by a pump source, the evolution of which is dependent on only N_2 at t = 0 ($N_2(0)$), the $^4I_{13/2} \rightarrow {}^4I_{15/2}$ lifetime excluding the effect of HCU (τ_{21}) and the C_{22} HCU coefficient. By measuring the time-resolved fluorescence emission from the $^4I_{13/2}$ level, the magnitude of which is proportional to the $^4I_{13/2}$ population density, a fit can be made to the data using Equation 3-7 to extrapolate the magnitudes of C_{22} and τ_{21}, assuming $N_2(0)$ is known.

Time resolved studies of the $^4I_{13/2} \rightarrow {}^4I_{15/2}$ transition fluorescence emission were conducted using the experimental setup shown in Figure 3-13.

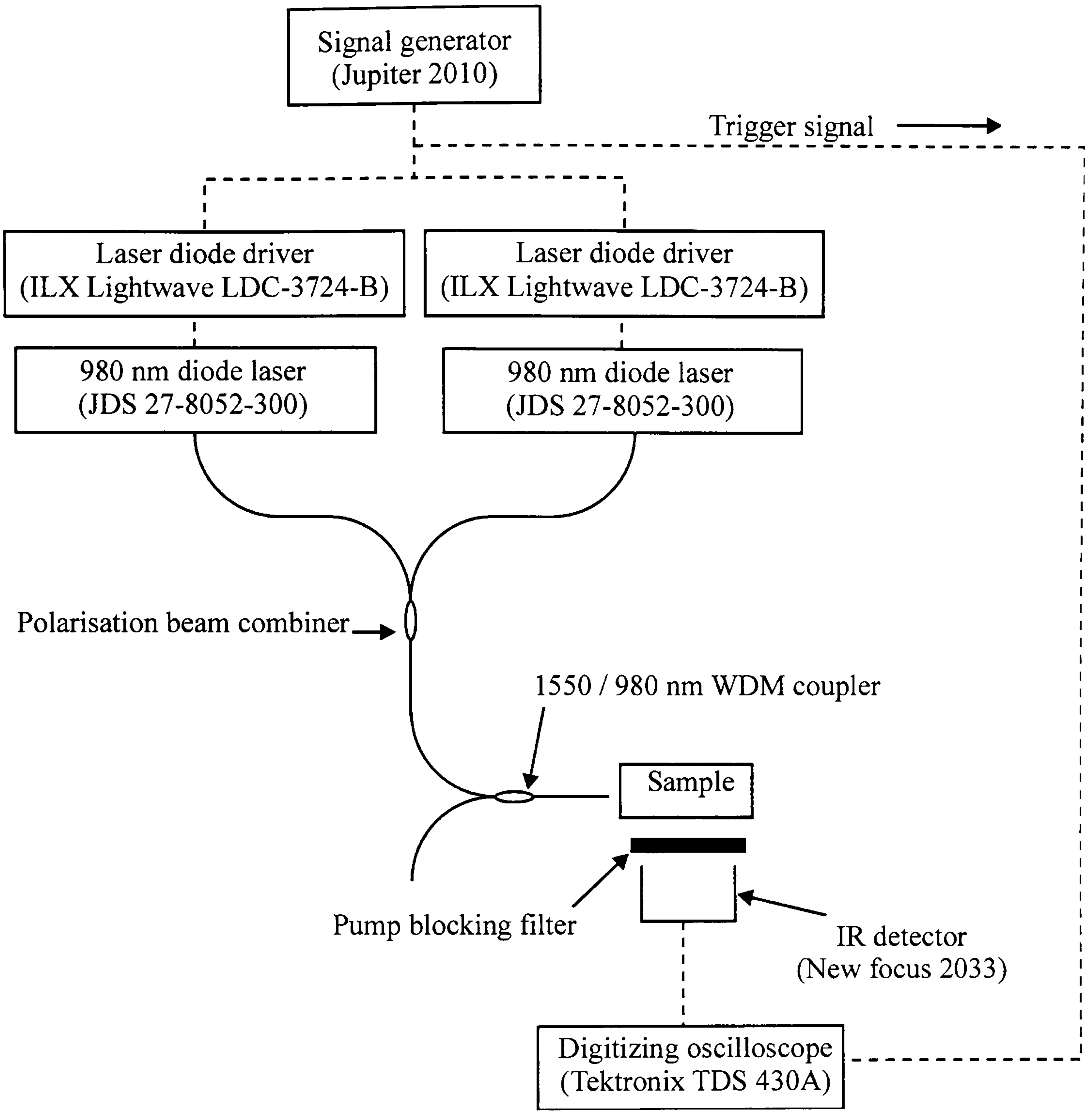

Figure 3-13 Schematic diagram of the experimental setup used to measure the $^4I_{13/2} \rightarrow {}^4I_{15/2}$ transition fluorescence lifetime.

As shown in Figure 3-13, a signal generator was used to provide a square wave electrical signal. This signal was used to modulate the 980 nm pump laser diodes via the laser diode driver units and also to trigger the digitising oscilloscope. The modulation frequency, switch off and switch on times and laser diode driver current could all be controlled independently in this manner. By applying a square wave modulation signal, the pump switch off time was measured to be approximately 0.02 ms. To excite the Er^{3+} ions, the modulated pump light was coupled into the waveguide under test via a 1550 / 980 nm WDM coupler using direct fibre-waveguide butt-coupling. Alignment to the waveguide was performed in the usual manner. The fluorescence decay from the waveguide under test was detected perpendicular to the waveguide surface to avoid any absorption and reemission effects [16]. By using high pass optical filters with a cut-off wavelength of 1.0 µm, and a detector with a responsivity that dropped off quickly at about 1.8 µm, only fluorescence emission in the 1.0-1.8 µm region was detected. The error in the measured shape of the fluorescence decay is negligible due to the fast switch off of the pump source. It is important to note that prior to pump switch-off, the duration of the pump-on state was long enough to allow the fluorescence to reach a steady level, thus indicating the population of the $^4I_{13/2}$ level had reached a steady state equilibrium. This is a critical point since the following calculations of $N_2(0)$ in Equation 3-7 are based on relative gain measurements obtained using a CW pump source. It is therefore necessary to re-create this equilibrium situation prior to pump switch off for the fitting of the model results to the experimental data to be valid.

In agreement with the behaviour expected from Equation 3-7, all sol-gel samples exhibited pump power dependent fluorescence lifetimes, decreasing with increasing pump power. Figure 3-14 shows the $^4I_{13/2} \rightarrow {}^4I_{15/2}$ transition fluorescence lifetime (1/e) vs. pump power characteristics for the various sol-gel samples.

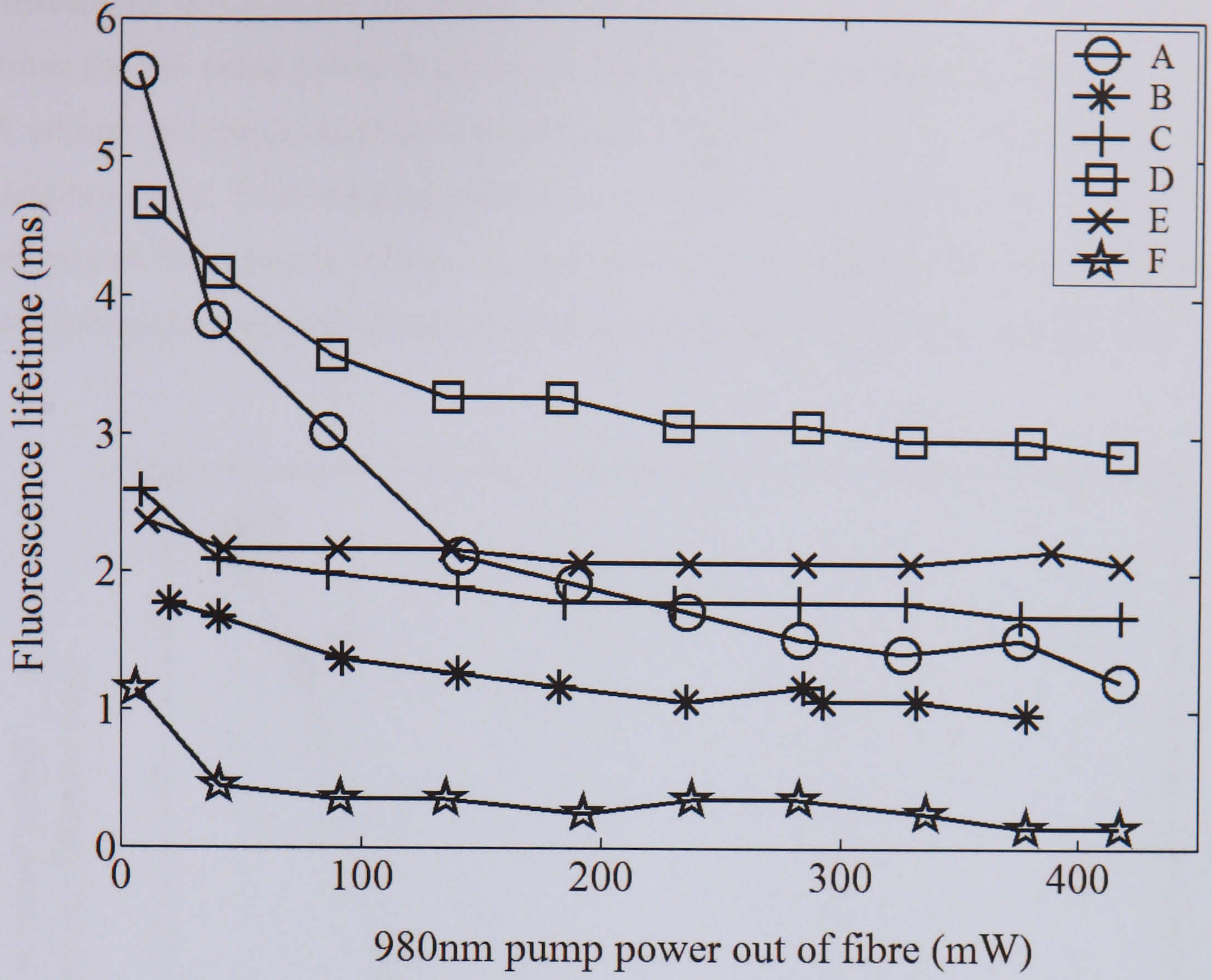

Figure 3-14 $^4I_{13/2} \rightarrow {}^4I_{15/2}$ transition fluorescence lifetime (1/e) vs. pump power characteristics for the various samples.

The results of the fluorescence lifetime experiments are summarised in Table 3-6.

Sample	Absorption peak (nm)	Erbium absorption (dB.cm^{-1})	$^4I_{13/2} \rightarrow {}^4I_{15/2}$ transition fluorescence lifetime (ms)	
			Low pump	High pump
A	1536.4	0.51	5.6	1.2
B	1532.4	2.18	1.8	1.0
C	1532.0	1.75	2.6	1.7
D	1532.8	1.06	4.7	2.9
E	1532.4	2.64	2.4	2.1
F	1540.0	7.83	1.2	0.2

Table 3-6 Summary of erbium absorption and fluorescence lifetime measurements

To investigate qualitatively the effect of the erbium concentration on the fluorescence lifetime, the low pump power fluorescence lifetime (1/e) was plotted as a function of the peak erbium absorption coefficient as shown in Figure 3-15. This was done to avoid any uncertainty in the final glass composition. As can be seen from Figure 3-15, the low pump power fluorescence lifetime is seen to decrease substantially for higher erbium absorption coefficients and is indicative of concentration induced quenching [17].

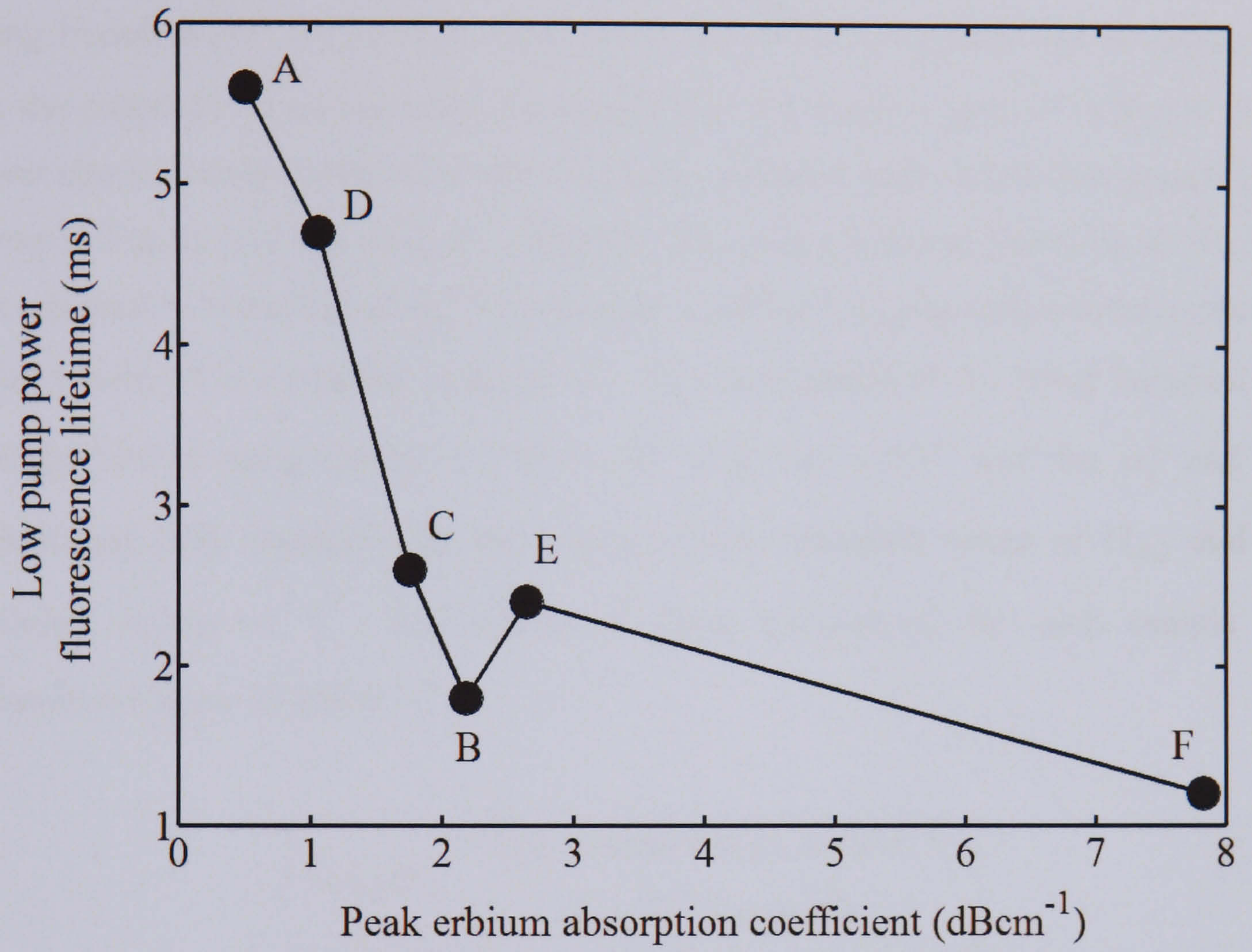

Figure 3-15 Low pump power $^4I_{13/2} \rightarrow {}^4I_{15/2}$ transition fluorescence lifetime (1/e) vs. peak erbium absorption coefficient for each sample.

In order to calculate C_{22} and τ_{21} from the fluorescence decays using Equation 3-7, it was necessary to first establish the magnitude of $N_2(0)$. For our purposes, $N_2(0)$ was calculated using a method similar to that proposed in [18]. When an Er-doped material is pumped, a probe signal experiences a relative gain due to the presence of stimulated emission and a reduction in the ground state absorption. As shown in Appendix B, the magnitude of the relative gain can be expressed as Equation 3-8.

$$G_{Rel}\ (dB) = 10Log_{10}\Big(\exp\Big(\Gamma_s L(\sigma_s^a N_2 + \sigma_s^e N_2\Big)\Big)$$

Equation 3-8

where, G_{Rel}, Γ_s, N_2, σ_s^a and σ_s^e all have their usual meanings, and L is the length of the waveguide.

Using Equation 3-8, the average value of N_2 along the waveguide can be calculated. For the purposes of the samples discussed here, the relative gain vs. 980 nm pump power characteristics exhibited a high degree of saturation under maximum pumping, as shown in Figure 3-12. As such, it is assumed that under maximum pumping, all the ions that can readily be excited to the $^4I_{13/2}$ level are, and the $^4I_{13/2}$ population directly prior to pump switch off is a constant equal to N_2. The calculations of N_2 using Equation 3-8 were performed using values of 5.36×10^{-21} and 5.41×10^{-21} cm^2 for σ_s^a and σ_s^e respectively [19], together with the experimentally evaluated values of G_{Rel} and the modelled values of Γ_s. The results of these calculations for each sample are summarised below in Table 3-7.

Sample	Maximum calculated value of N_2 (1×10^{19} ions.cm^3)
A	0.5
B	1.0
C	3.1
D	1.6
E	2.9
F	1.3

Table 3-7 Maximum calculated average value of N_2 along the waveguide for each sol-gel sample

Prior to fitting the modelled population decay to the measured fluorescence decay, the fluorescence signal was normalised such that at t = 0, the fluorescence signal represented the calculated value of $N_2(0)$. Fitting was conducted using a χ^2 fitting procedure in two dimensions (C_{22} and τ_{21}).

Figure 3-16 shows a comparison of the experimentally measured and modelled decay of N_2 for sample C using the fitted parameters. Also shown in Figure 3-16 is the decay of N_2 that would be expected if no HCU effects were present.

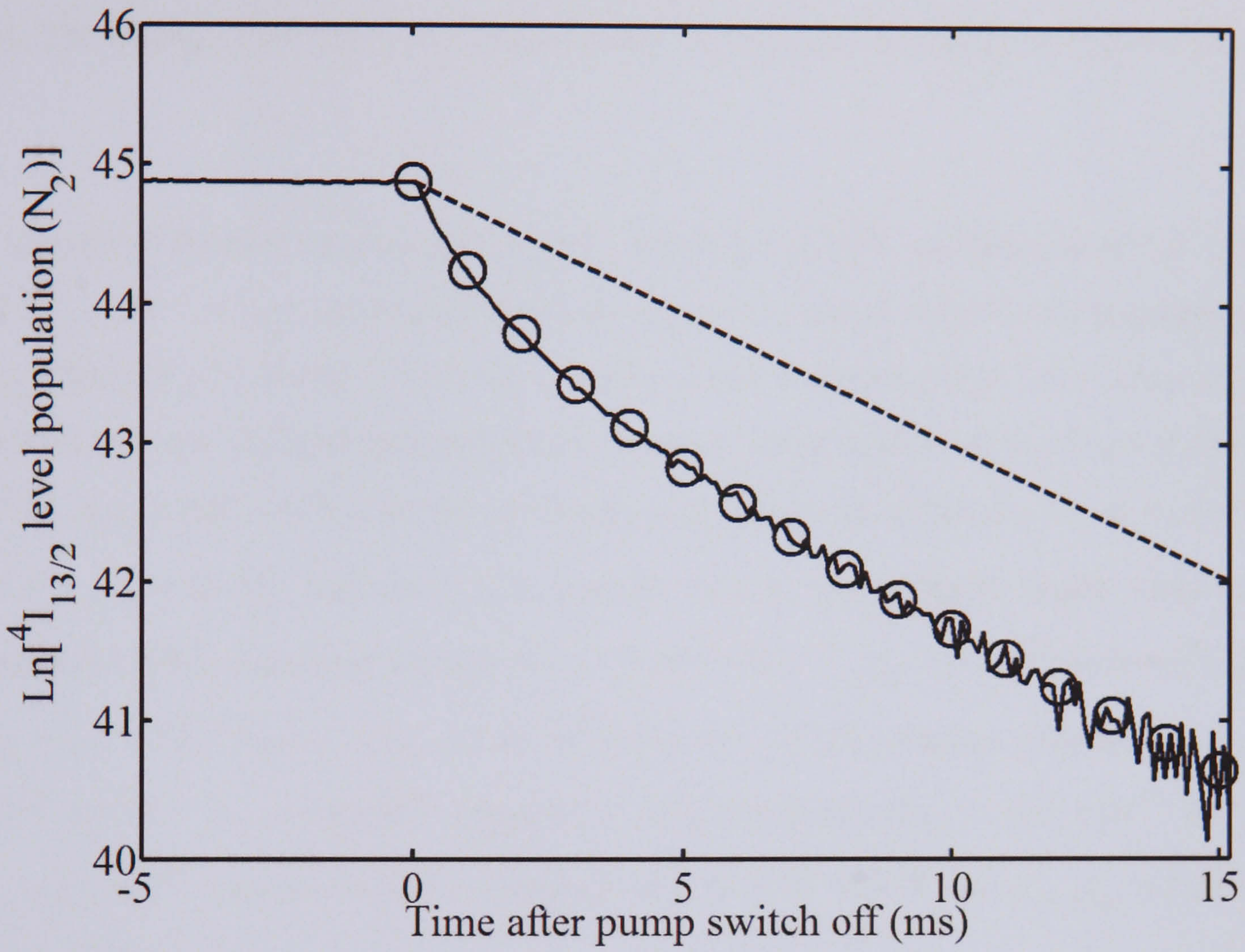

Figure 3-16 Modelled (circles) and experimentally measured decay (solid line) of N_2 for sample C. The modelled decay was calculated using the experimentally determined value of $N_2(0) = 3.1\times 10^{19}$ ions.cm^{-3} and the fitted values of $C_{22} = 2.0 \times 10^{-17}$ cm^3.s^{-1} and $\tau_{21} = 5.3$ ms. Also shown is the single exponential decay of N_2 that would be expected if no HCU effects were present (dashed line).

Although six sol-gel samples were available, only samples C and E exhibited both sufficiently saturated relative gain vs. 980 nm pump power characteristics (so that it may be assumed that a constant value of N_2 is present along the waveguide) *and* fluorescence decays that could be satisfactorily explained by the model. In the cases where the fluorescence decays could not be satisfactorily explained by the model, very fast components of the order of 100 μs on the fluorescence decay characteristics were detected. Such features indicate higher order effects that cannot be explained by the HUC model and are thought to be the result of rare earth clustering [20].

As can be seen from Figure 3-16, a good fit of the modelled data to the experimental data has been obtained. As such, this is strong evidence that the optically active ions in samples C and E decay in accordance with the model of HCU proposed by Snoeks et al [21]. The fitting of the data for sample E was very similar in quality to that for sample C.

As a result of the time resolve fluorescence analysis, C_{22} HCU coefficients of 2.0×10^{-17} and 1.7×10^{-17} $cm^3.s^{-1}$ were determined for samples C and E respectively together with $^4I_{13/2}$ lifetimes of 5.3 and 5.8 ms for samples C and E respectively. The values of C_{22} reported here are in broad agreement with those reported in other silica ($C_{22} \approx 0.7\times10^{-17}$ $cm^3.s^{-1}$, $\rho_{Er} = 3.41\times10^{20}$ ions.cm^{-3}) [18] and sol-gel derived silica ($C_{22} \approx 1.0 \rightarrow 5\times10^{-17}$ $cm^3.s^{-1}$, $\rho_{Er} = 1\times10^{20}$ ions.cm^{-3}) [11] glasses, but are substantially higher than those reported in either soda-lime silicate ($C_{22} \approx 5\times10^{-19}$ $cm^3.s^{-1}$, $\rho_{Er} = 1\times10^{20}$ ions.cm^{-3}) [22], ($C_{22} = 3.2 \times10^{-18}$ $cm^3.s^{-1}$, $\rho_{Er} = 1.4\times10^{20}$ ions.cm^{-3}) [21], alumino-silicate ($C_{22} \approx 7.7 \times10^{-19}$ $cm^3.s^{-1}$, $\rho_{Er} = 0.8\times10^{20}$ ions.cm^{-3}) [22], phosphate ($C_{22} \approx 8.0 \times10^{-19}$ $cm^3.s^{-1}$, $\rho_{Er} = 2.0\times10^{20}$ ions.cm^{-3}) [23] or tellurite ($C_{22} \approx 2.74 \times10^{-18}$ $cm^3.s^{-1}$, $\rho_{Er} = 3.4\times10^{20}$ ions.cm^{-3}) [24] glasses.

The most apparent source of error in the analysis presented here is the assumption that N_2 is a constant along the waveguide. As outlined previously however, this source of error is thought to be small since both samples discussed here exhibited strong gain saturation.

In the following section, the gain operation of samples C and E will be modelled using the experimentally measured parameters. The aim of this modelling is to understand what factors have been significant in limiting the performance of the sol-gel waveguides.

3.5 Modelling the gain operation of the sol-gel samples

In the previous chapter, the Snoeks model was used to investigate how the various properties of an Er-doped waveguide affect the gain vs. 980 nm pump power characteristics of a theoretical EDWA. In this section, the experimentally determined magnitudes of these parameters are used together with the Snoeks model to investigate what factors limit the gain operation of the sol-gel samples. Since it was only possible to determine the C_{22} HCU constant for samples C and E, only the gain operation of these samples will be modelled. The model parameters for samples C and E are summarised in Table 3-8 below.

Parameter	Unit	Sample C	Sample E
Doped waveguide core dimensions	μm	6.9 × 5.3	6.1 ×5.1
Pump light wavelength	nm	980	
Signal light wavelength	nm	1531.8	1534.4
Erbium concentration	ions.cm^{-3}	1×10^{20}	1.4×10^{20}
Pump light $^4I_{15/2} \rightarrow {}^4I_{11/2}$ transition cross section	cm^2	2.58×10^{-21}	
Signal light $^4I_{15/2} \rightarrow {}^4I_{13/2}$ transition cross section	cm^2	5.36×10^{-21}	
Signal light $^4I_{13/2} \rightarrow {}^4I_{15/2}$ transition cross section	cm^2	5.41×10^{-21}	
Homogeneous cooperative upconversion coefficient (C_{22})	cm^3.s^{-1}	2.0×10^{-17}	1.7×10^{-17}
$^4I_{13/2}$ level lifetime (τ_{21})	ms	5.3	5.8
Waveguide length	cm	5.6	7.1
Pump-waveguide overlap factor (Γ_p)	Arb.U	0.9	0.9
Signal-waveguide overlap factor (Γ_s)	Arb.U	0.73	0.7
Waveguide propagation loss at both the pump and signal wavelengths	dB.cm^{-1}	0.21	0.13

Table 3-8 Parameters used for modelling the gain operation of samples C and E.

Using the parameters detailed in Table 3-8, the gain vs. 980 nm pump power characteristics for samples C and E were modelled using the Snoeks model described in

Chapter 2. Figure 3-17 and Figure 3-18 show a comparison of the experimental and modelling results for samples C and E respectively.

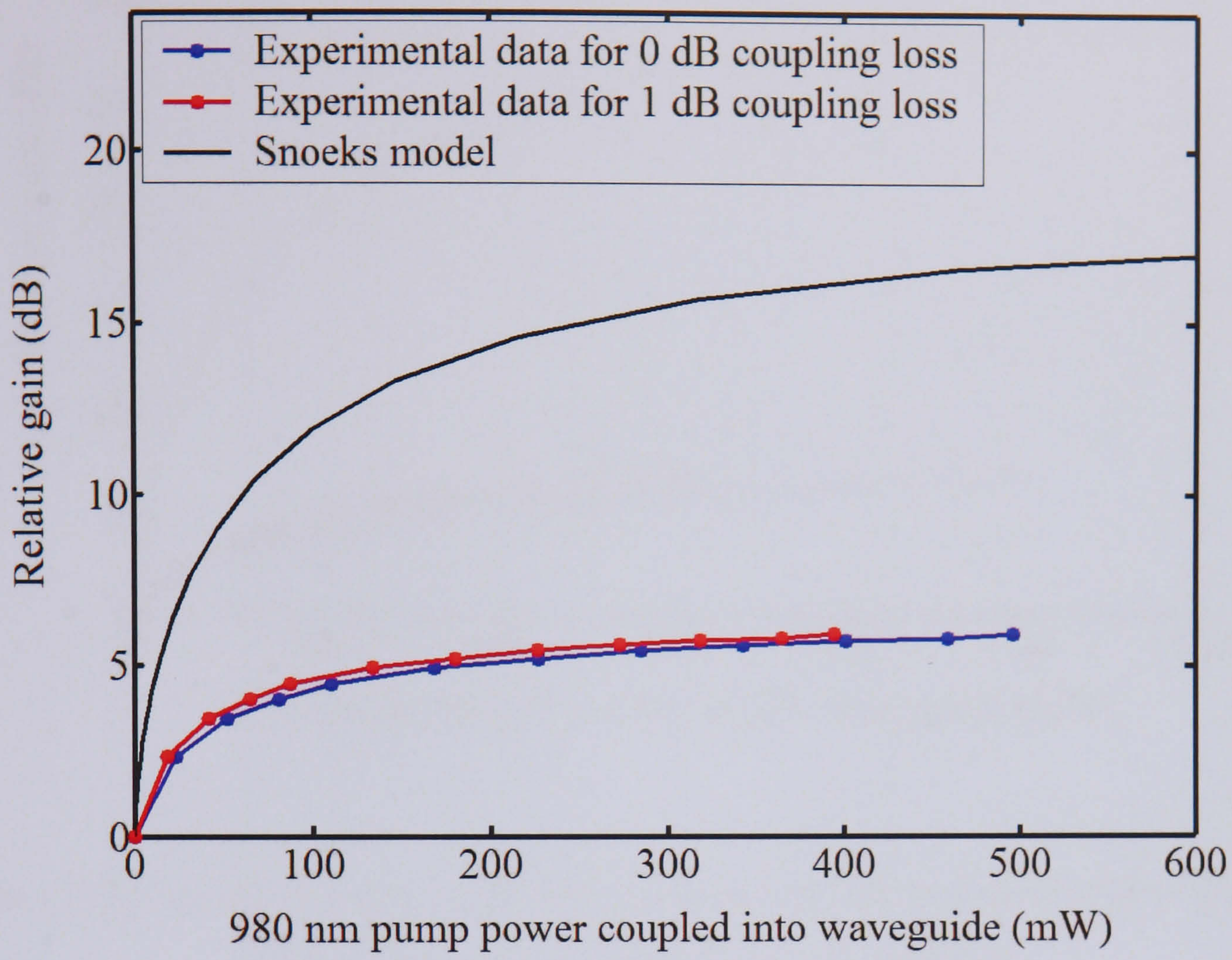

Figure 3-17 Comparison of the modelled and experimentally measured relative gain vs. 980 nm pump power characteristics for sample C.

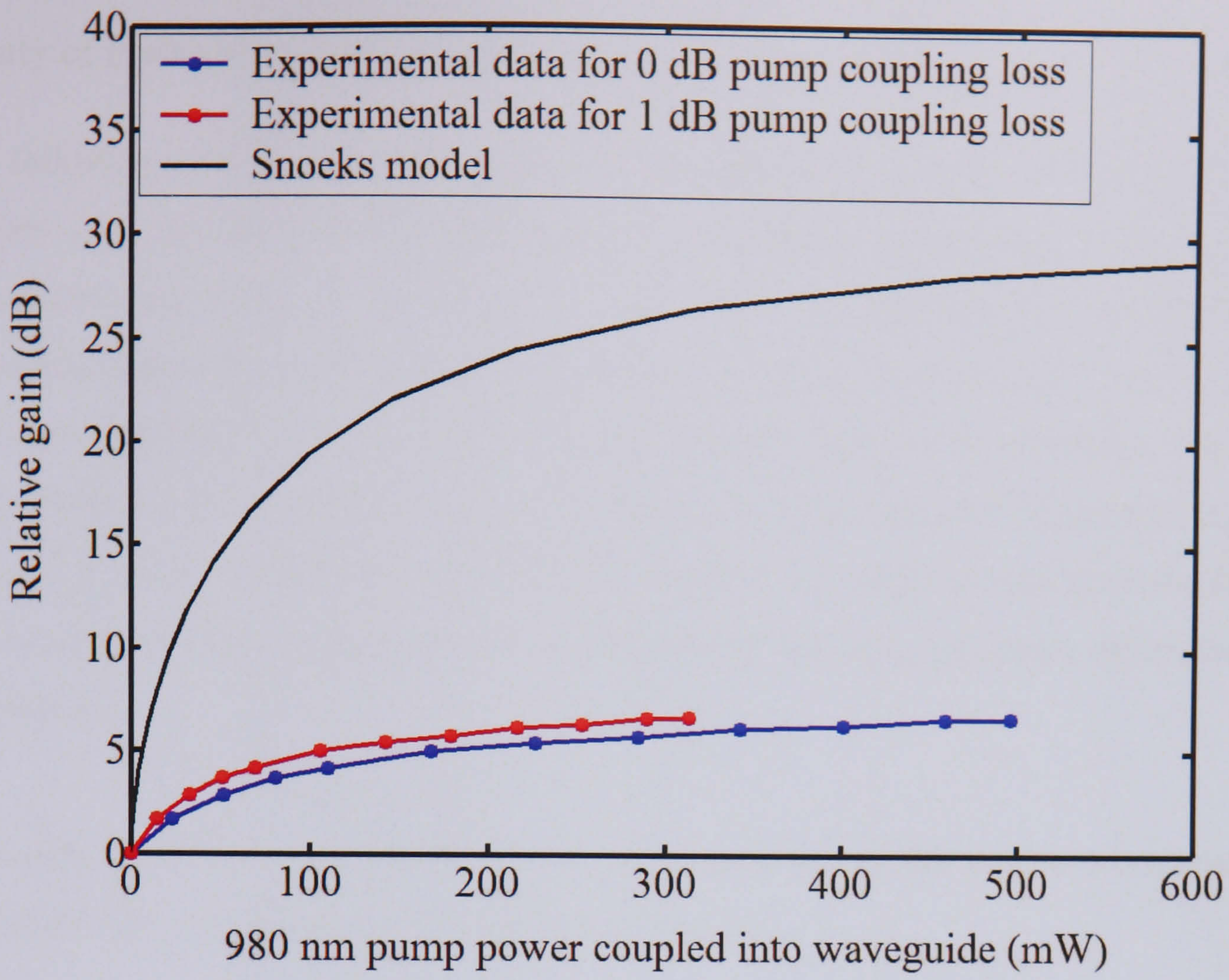

Figure 3-18 Comparison of the modelled and experimentally measured relative gain vs. 980 nm pump power characteristics for sample E.

As shown in Figure 3-17 and Figure 3-18, the Snoeks model is unable to predict the experimentally measured gain vs. 980 nm pump power characteristics for either sample C or sample E. From the characterisation results presented in this chapter, it is clear that the passive performance of the sol-gel samples is excellent, with all samples exhibiting low propagation, coupling and insertion losses. As such, it is concluded that the passive properties do not play a significant role in limiting the amplification properties of the sol-gel samples. In addition, it is also clear from the modelling results shown in Figure 3-17 and Figure 3-18 that neither the magnitudes of the $^4I_{13/2}$ level or the C_{22} HCU constant can explain on their own the poor amplifier performance.

As discussed in section 3.4.5 there is a large amount of unsaturable absorption present in these samples, and it was concluded that the most probable reason for this is clustering of the Er-ions. In an attempt to take into account the effect of clustered ions in the Snoeks model, a clustering parameter, "k" was introduced that expresses the density of clustered ions as a fraction of the total ion density i.e. $k = \frac{\rho_{Er}(Clustered)}{\rho_{Er}(Total)}$.

The following alterations to the Snoek's model were based on the assumption that the erbium ions are divided into two entirely segregated populations, a clustered ion population that does not participate in gain and a homogeneously distributed ion population that does. Although this may be a over simplification of the true situation, it has been suggested by direct observation of rare earth cluster sizes in neodynium doped silica fibre that the number ions in each cluster may be of the order of several hundreds [25]. As a result, it can be assumed that the effect of the single ions in each cluster that can be excited can be neglected when compared to the homogeneously distributed ion population.

Following on from this assumption, the gain dynamics of the device were modelled using the following alterations to the Snoek's model:

1. The gain dynamics of the device were modelled using an unclustered ion population of: $\rho_{Er}(unclustered) = \rho_{Er}.(1-k)$.

2. The waveguide loss at the pump wavelength was adjusted to include the effect of the absorption due to the clustered ions, i.e. $\alpha_p = \alpha_{Background} + \alpha_{clustered\,ions}$, where $\alpha_{clustered\,ions} = \sigma_p^a.\rho_{Er}(clustered).\Gamma_p$

3. The waveguide loss at the signal wavelength was adjusted to include the effect of the absorption due to the clustered ions, i.e. $\alpha_p = \alpha_{Background} + \alpha_{clustered\,ions}$, where $\alpha_{clustered\,ions} = \sigma_s^a.\rho_{Er}(clustered).\Gamma_s$

Using this modified Snoeks model, the gain vs. 980 nm pump power characteristics were again modelled using the parameters defined in Table 3-8 while varying the magnitude of the clustering parameter, k. Figure 3-19 and Figure 3-20 show a comparison of the experimental and modelling results using the modified Snoeks model for samples C and E respectively.

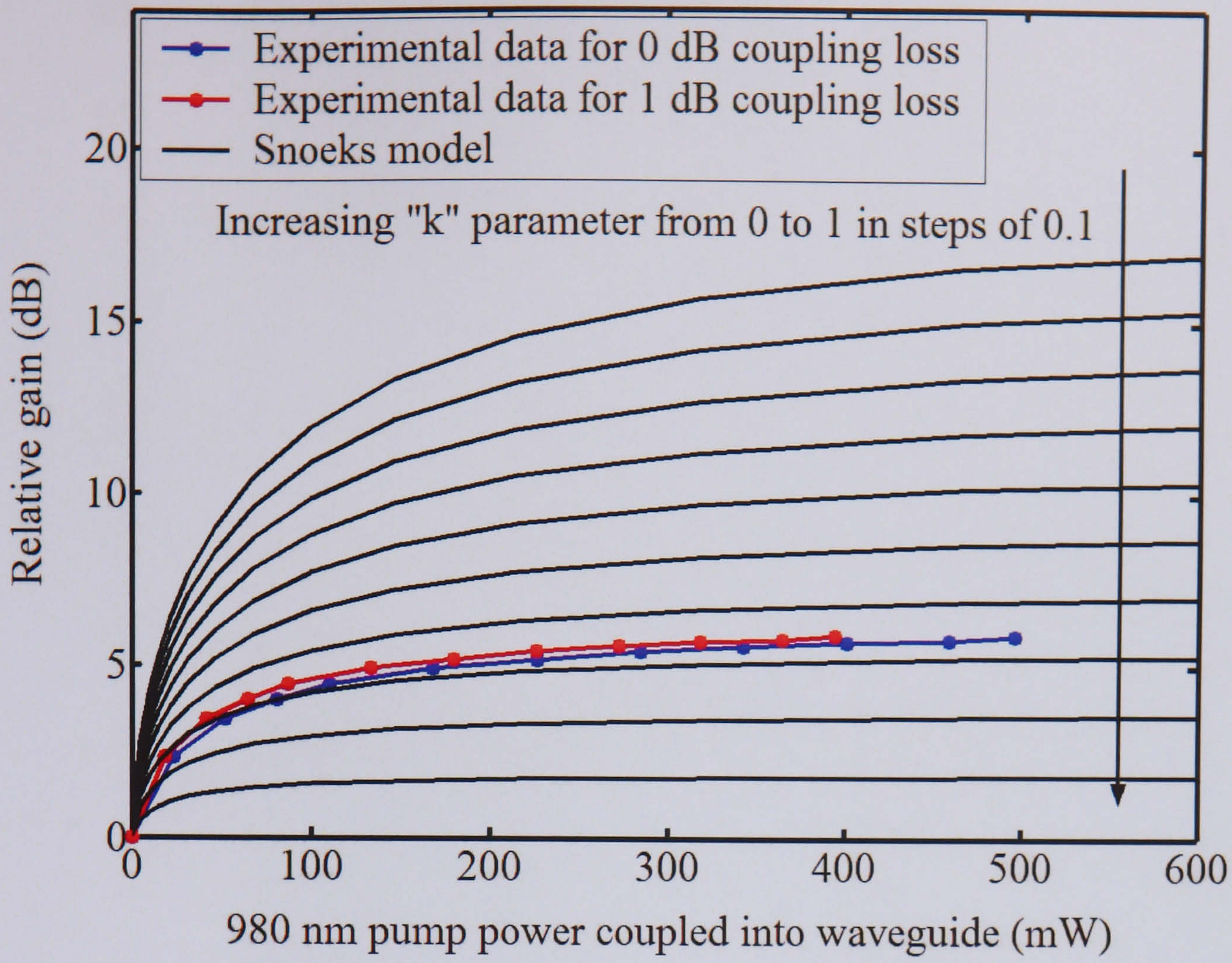

Figure 3-19 Comparison of the modelled and experimentally measured relative gain vs. 980 nm pump power characteristics for sample C. The modelled characteristics were calculated using the modified Snoeks model.

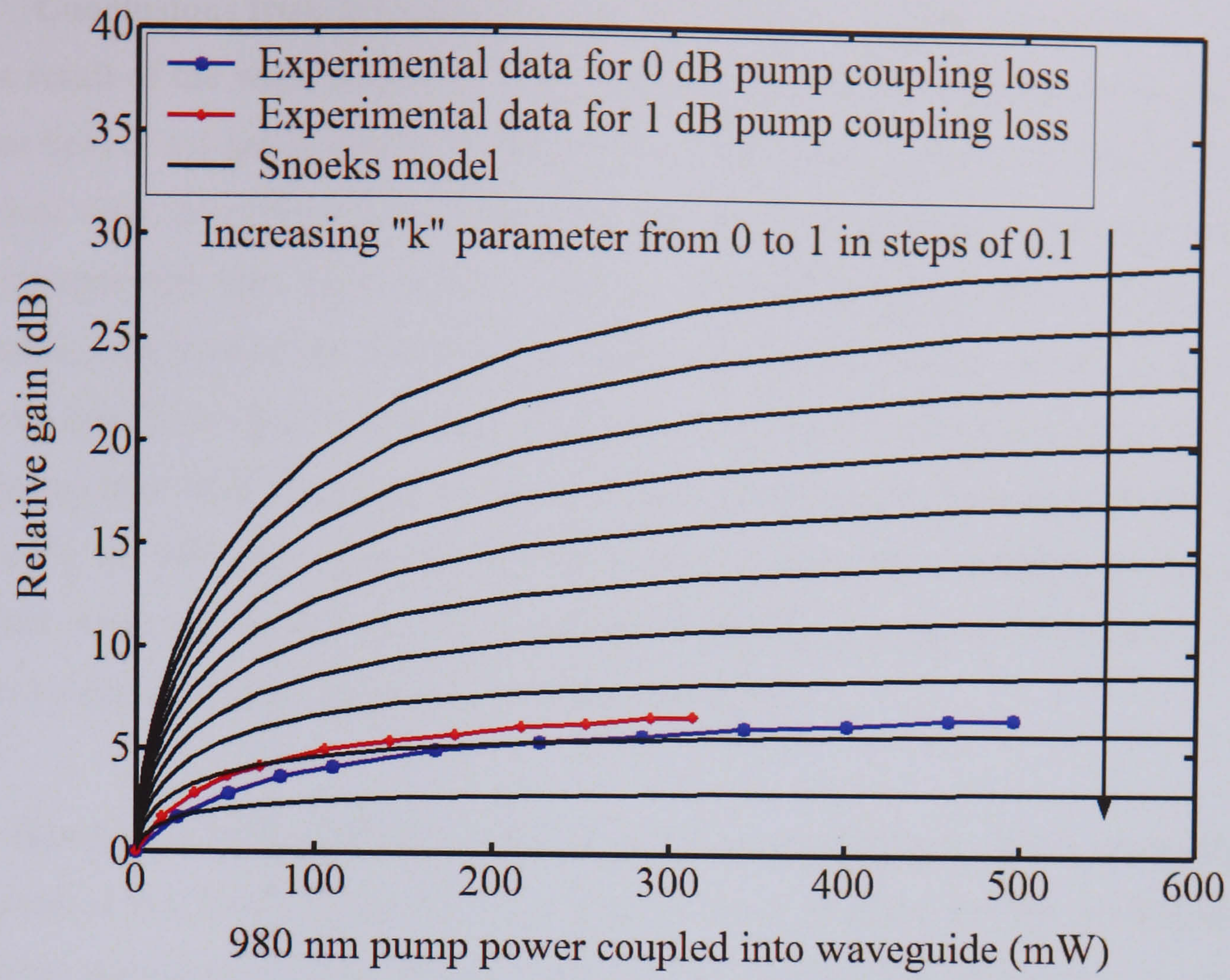

Figure 3-20 Comparison of the modelled and experimentally measured relative gain vs. 980 nm pump power characteristics for sample E. The modelled characteristics were calculated using the modified Snoeks model.

As can be seen in Figure 3-19 and Figure 3-20, the introduction of the k parameter into the model does allow the modified Snoeks model to predict gain vs. 980 nm pump power characteristics that are similar in shape to those measured experimentally. For sample C, the best comparison of the modelled to theoretical gain characteristics were observed using values of k between 0.6 and 0.7, whereas for sample E, the best fit was observed using values of k between 0.7 and 0.9. These modelling results indicate that ≈ 35 % of ions for sample C and ≈ 20 % of ions for sample E can be excited to the $^4I_{13/2}$ level under pumping, figures that are in close agreement with those quoted in Table 3-5. The observation that the modelled and experimental gain characteristics are similar in shape is convincing evidence that the ions participating in the gain mechanisms interact, at least to a first order approximation, in accordance with the theory of HCU.

3.6 Conclusions from studies of sol-gel fabricated Er-doped waveguides

As a result of the work described in this chapter, a number of significant contributions to the field of sol-gel fabricated Er-doped waveguides have been made. From a practical point of view, it has been shown that a significant amount of optically active erbium can be incorporated into high quality channel waveguides using only a single sol-gel deposition for each of the cladding and core layers. Previous work on sol-gel fabricated erbium doped waveguides indicates that there is no fundamental reason why the issues regarding rare-earth clustering cannot be overcome in sol-gel fabricated devices [4,26]. As such, the fabrication process described here, if optimised to reduce the amount of erbium clustering would provide significant benefits over the conventional SC-RTA route by significantly reducing device fabrication time.

The observation of fluorescence lifetimes as high as 5.6 ms have clearly shown that the removal of the O-H solvent from the glass is not a problem for the development of efficient high gain, low cost devices using a single sol-gel deposition route. In addition, PDL values as low as 0.17 dB for a 5.2 cm long waveguide indicate that waveguides exhibiting low stress have been fabricated, an important demonstration if useful telecommunications devices are to be fabricated.

From a theoretical point of view it has been shown that the original Snoeks model is unable to predict the gain vs. 980 nm pump power characteristics of heavily clustered materials. To model the effect of rare earth clustering, the original Snoeks model was modified to take into account the unsaturable absorption of the clustered ions. By doing so, it was found that varying the fraction of total ions that reside in clusters allowed the Snoeks model to predict gain characteristics similar in shape to those measured experimentally. As discussed in section 3.5, the modelling results are convincing evidence that the total Er^{3+} ion population may be considered as two entirely segregated populations, a clustered ion population that does not participate in gain mechanism, and a homogeneously distributed ion population that does and interacts in accordance with the theory of HCU.

Future fabrication work should clearly focus on reducing the amount of rare earth clustering through a more thorough investigation of the effect of varying the fabrication parameters and sol composition on the level of population inversion obtained through pumping. Laliotis et al [11] have recently shown that a reduction in the annealing time increases the internal gain for a given sample, possibly by reducing the amount of erbium clustering.

From a theoretical point of view, a more detailed model such as those proposed by Vermelho et al [27] or Huang et al [19] should be used to model the gain operation of these devices. These models include higher order upconversion, energy transfer and ESA effects not included in the Snoeks model, and as such will give greater insight into how the operation of sol-gel fabricated Er-doped waveguides can be optimised. Such theoretical work will in turn require extensive additional experimental investigations to measure the constants that govern these higher order interactions.

To conclude, the results described in this chapter have clearly added to the body of work that demonstrate the potential of the sol-gel route for fabricating low cost EDWA devices for LAN / MAN applications. Although much work is clearly still required to achieve the quality of operation necessary for practical applications, there appears to be no reason why the practical issues limiting the performance of the devices discussed here cannot be overcome.

3.7 References

[1] C. J. Brinker and G. W .Scherer, "Introduction-Sol-Gel processing," in *Sol-Gel Science - The Physics and Chemistry of Sol-Gel Processing*, Academic Press, 1990, pp. 3-4.

[2] R. R. A. Syms and A. S. Holmes, "Deposition of thick silica-titania sol-gel films on Si substrates," *J. Non-Cryst. Solids*, vol. 170, no. 3, pp. 223-233, Jul. 1994.

[3] R. R. A. Syms, "Stress in thick sol-gel phosphosilicate glass films formed on Si substrates," *J. Non-Cryst. Solids*, vol. 167, no. 1-2, pp. 16-20, Jan. 1994.

[4] W. Huang and R. R. A. Syms, "Sol-gel silica-on-silicon buried-channel EDWAs," *J. Lightwave Technol.*, vol. 21, no. 5, pp. 1339-1349, May 2003.

[5] N. Suyal and H. Ur-Rehman, "Improved binders for coatings" G.B. Patent 2375107, Jul 9, 2003.

[6] E. M. Yeatman, M. M. Ahmad, O. McCarthy, A. Vannucci, P. Gastaldo, D. Barbier, D. Mongardien, and C. Moronvalle, "Optical gain in Er-doped SiO2-TiO2 waveguides fabricated by the sol-gel technique," *Opt. Commun.*, vol 164, pp. 19-25, Jun 1999.

[7] E. Desurvire, "Characteristics of erbium-doped fibers," *Erbium doped fiber amplifiers : principles and applications,* John Wiley & Sons, 2002, pp. 249.

[8] R. G. Hunsperger, "Losses in optical waveguides," in *Integrated optics: Theory and Technology,* Springer-Verlag, 1982, pp. 71.

[9] R. Regener and W. Sohler, "Loss in low-finesse Ti:LiNbO$_3$ optical waveguide resonators," *Appl. Phys. B-Lasers O*, vol. 36, no. 3, pp. 143-147, Mar. 1985.

[10] Y. Okamura, S. Yoshinaka, and S. Yamamoto, "Measuring mode propagation losses of integrated optical-waveguides: a simple method," *Appl. Optics*, vol. 22, no. 23, pp. 3892-3894, Dec. 1983.

[11] A. Laliotis, E. M. Yeatman, M. M. Ahmad, and W. Huang, "Molecular homogeneity in erbium-doped sol-gel waveguide amplifiers," *IEEE J. Quantum Electron.*, vol 40, pp. 805-814, Jun 2004.

[12] E. M. Yeatman, M. M. Ahmad, O. McCarthy, A. Martucci, and M. Guglielmi, "Sol-gel fabrication of rare-earth doped photonic components," *J. Sol-Gel Sci. Techn.* vol 19, pp. 231-236, Dec 2000.

[13] P. Myslinski, D. Nguyen, and J. Chrostowski, "Effects of concentration on the performance of erbium-doped fiber amplifiers," *J. Lightwave Technol.*, vol. 15, no. 1, pp. 112-120, Jan. 1997.

[14] J. Nilsson, B. Jaskorzynska, and P. Blixt, "Performance reduction and design modification of erbium doped fiber amplifiers resulting from pair induced quenching," *IEEE Photon. Technol. Lett.*, vol. 5, no. 12, pp. 1427-1429, Dec 1993.

[15] T. Ohtsuki, S. Honkanen, S. I. Najafi, and N. Peyghambarian, "Cooperative upconversion effects on the performance of Er^{3+}-doped phosphate glass waveguide amplifiers," *J. Opt. Soc. Am. B*, vol. 14, no. 7, pp. 1838-1845, Jul. 1997.

[16] J. R. Bonar, M. V. D. Vermelho, P. V. S. Marques, A. J. McLaughlin, and J. S. Aitchison, "Fluorescence lifetime measurements of aerosol doped erbium in phosphosilicate planar waveguides," *Opt. Commun.*, vol. 149, no. 1-3, pp. 27-32, Apr. 1998.

[17] X. Orignac, D. Barbier, X. M. Du, R. M. Almeida, O. McCarthy, and E. Yeatman, "Sol-gel silica/titania-on-silicon Er/Yb-doped waveguides for optical amplification at 1.5 μm," *Opt. Mater.*, vol 12, pp. 1-18, May 1999.

[18] N. Nikonorov, A. Przhevuskii, M. Prassas, and D. Jacob, "Experimental determination of the upconversion rate in erbium-doped silicate glasses," *Appl. Optics,* vol. 38, no. 30, pp. 6284-6291, Oct. 1999.

[19] W. B. Huang and R. R. A. Syms, "Analysis of folded erbium-doped planar waveguide amplifiers by the method of lines," *J. Lightwave Technol.*, vol. 17, no. 12, pp. 2658-2664, Dec. 1999.

[20] E. Desurvire, "Characteristics of erbium-doped fibers," *Erbium doped fiber amplifiers : principles and applications,* John Wiley & Sons, 2002, pp. 277.

[21] E. Snoeks, G. N. van den Hoven, A. Polman, and B. Hendriksen, M. B. J. Diemeer, F. Priolo, "Cooperative upconversion in erbium-implanted soda-lime silicate glass optical waveguides," *J. Opt. Soc. Am. B*, vol. 12, no. 8, pp. 1468-1474, Aug.1995.

[22] M. P. Hehlen, N. J. Cockroft, T. R. Gosnell, A. J. Bruce, G. Nykolak, and J. Shmulovich, "Uniform upconversion in high-concentration Er^{3+}-doped soda lime silicate and aluminosilicate glasses," *Opt. Lett.*, vol. 22, no. 11, pp. 772-774, Jun. 1997.

[23] B. C. Hwang, S. Jiang, T. Luo, J. Watson, G. Sorbello, and N. Peyghambarian, "Cooperative upconversion and energy transfer of new high Er^{3+}- and Yb^{3+}-Er^{3+}-doped phosphate glasses," *J. Opt. Soc. Am. B*, vol. 17, no. 5, pp. 833-839, May 2000.

[24] Y. Hu, S. Jiang, G. Sorbello, T. Luo, Y. Ding, B. C. Hwang, J. H. Kim, H. J. Seo, and N. Peyghambarian, "Numerical analyses of the population dynamics and determination of the upconversion coefficients in a new high erbium-doped tellurite glass," *J. Opt. Soc. Am. B*, vol. 18, no. 12, pp. 1928-1934, Dec. 2001.

[25] B. J. Ainslie, S. P. Craig, R. Wyatt and K. Moulding, "Optical and structural analysis of neodynium-doped silica-based optical fibre," *Mater. Lett.*, vol. 8, no. 6-7, pp. 204-208, Jul. 1989.

[26] W. Huang, R. R. A.Syms, E. M. Yeatman, M. M. Ahmad, V. T. Clapp., and S. M. Ojha, "Fiber-device-fiber gain from a sol-gel erbium-doped waveguide amplifier," *IEEE Photon. Technol. Lett.*, vol 14, pp. 959-961, Jul. 2002.

[27] M. V. D. Vermelho, U. Peschel, and J. S. Aitchison, "Simple and accurate procedure for modeling erbium-doped waveguide amplifiers with high concentration," *J. Lightwave Technol.*, vol. 18, no. 3, pp. 401-408, Mar. 2000.

Chapter 4- Erbium-doped oxyfluoride-silicate glass waveguide fabrication using pulsed laser deposition (PLD)

4.1 Introduction

Pulse laser deposition (PLD) is an attractive route for the fabrication of planar waveguides since it allows the stoichiometric transfer of material from a bulk target to a thin film [1,2]. As such PLD should be well suited to fabricating planar waveguide films from complex multi-component Er-doped glasses. This chapter describes work conducted on the fabrication of Er-doped rib waveguides using pulsed laser deposited thin films.

All thin films discussed in this chapter were fabricated by Professor Maurizio Martino and co-workers at the University of Lecce in Italy. It is also necessary however to acknowledge the role of samples fabricated at the Ultraviolet Laser Facility at the Foundation for Research and Technology Hellas (ULF-FORTH) in Crete. Over the course of a three week stay at this facility myself, Professor Costos Fotakis and co-workers fabricated a number of thin films using PLD that proved to be invaluable for preliminary investigations not discussed in the thesis. All photolithography and etching was performed by Mr Neil Ross at Heriot-Watt University. My primary role within the PLD work was to investigate the optical properties and evaluate the performance of the PLD samples.

The layout of this chapter is as follows. Firstly, in section 4.2 the basic PLD process for fabricating planar waveguide thin films is described. In section 4.3 the Er-doped target material used in these investigations is described and the results of a number of spectroscopic investigations presented. In section 4.4, the fabrication and characterisation of Er-doped planar waveguides using PLD and the oxyfluoride-silicate target material is described and discussed. In section 4.5, the fabrication and characterisation of rib waveguides using a PLD fabricated thin film is described. Finally, in section 4.6, conclusions from the PLD work are drawn and suggestions for future work in the area are made.

4.2 Pulsed laser deposition of planar waveguide thin films

PLD is an extremely versatile route for fabricating planar waveguide thin films. Thin films of almost any material can be fabricated by ablating a target material / materials using a pulsed laser, and collecting the plume of ablated material onto a substrate. Although the fabrication of thin films using PLD is well researched, its application to the fabrication of integrated optical devices is much less so due to the mature nature of other thin film fabrication techniques.

Conceptually and experimentally, PLD is very simple to perform. Figure 4-1 below is a sketch of a typical PLD experimental setup.

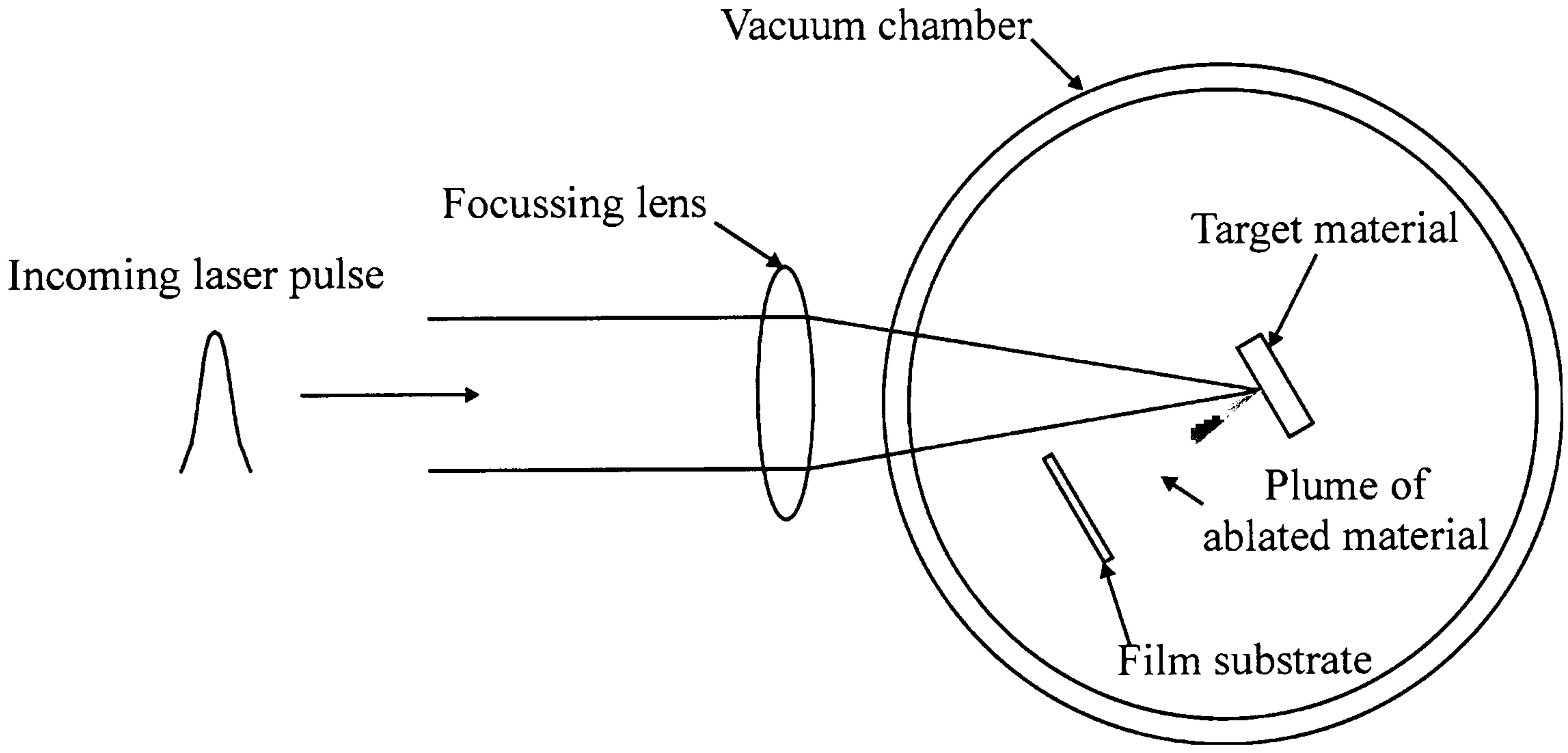

Figure 4-1 Sketch of PLD experimental setup.

As shown in Figure 4-1, optical pulses from a laser source are focussed onto the surface of a target material. The target material is contained inside a vacuum chamber that may or may not be filled with gas. If the vacuum chamber is filled with gas, the process is known as reactive PLD. When the laser pulse is incident on the target material, optical energy is absorbed by the target, either linearly or non-linearly. This optical energy is converted to electronic excitation and then thermal, chemical and mechanical energy. If the absorbed laser power density is high enough, a plume of the target material is produced due to evaporation, ablation, excitation, plasma formation and exfoliation mechanisms. The plume itself may consist of a mixture of atoms, molecules, electrons, ions, clusters, micron-sized solid particles and molten globules [3]. By collecting the plume from the target onto the desired substrate, thin films of almost any material can be fabricated.

In reality the physical mechanisms involved in PLD are extremely complex and multidisciplinary. Consequently, most of the theoretical studies do not provide insights into improving the PLD experimental conditions with most of the film optimisation relying on phenomenological studies using analytical techniques to study the effect of the plume characteristics on the film quality [4]. Generally speaking however, the quality of PLD fabricated films can be improved by using lasers with short pulse durations and wavelengths that are strongly absorbed by the target material [5].

For the studies discussed in this chapter, an Er-doped oxyfluoride-silicate glass was used as the target material in the PLD process. Due to the complex multi-component composition of this glass, PLD should be well suited to fabricating thin films from this material. In the following section, the Er-doped oxyfluoride-silicate glass material is introduced and some basic spectroscopic characterisation results presented.

4.3 The Er-doped oxyfluoride-silicate target material

As discussed in chapter 2, the host composition and structure has a small but significant effect on the spectroscopic properties of the $4f \rightarrow 4f$ lasing transitions of the Er^{3+} ion. In previous research, it has been shown that heavy metal fluoride glasses (ZBLAN) provide much larger emission bandwidths (65 nm) when compared to pure silica fibres [6]. Unfortunately, non-silica fibres pose problems in terms of compatibility with standard silica fibres such as Corning SMF-28, and as a result none have been widely accepted for use in industry.

With the advantages and disadvantages posed by fluoride glasses in mind, a series of Er-doped oxyfluoride-silicate glasses have been developed by Professor Animesh Jha and co-workers at the Institute of Materials Research at the University of Leeds. By using both fluoride and silicate network formers, these glasses aim to maintain both the structural properties of a silicate glass as well as the spectroscopic properties of fluoride glasses. The fabrication and spectroscopic optimisation of these glasses is described extensively in [6].

The thin film samples discussed in this chapter were fabricated using Er-doped oxyfluoride-silicate glass targets fabricated at the University of Leeds. The precursor composition of these target glasses was 65 SiO_2 – 12 Na_2O – 3 Al_2O_3 -10 LaF_3 – 10 PbF_2 (mol %) with 1 wt. % ErO_3 added. The Er^{3+} ion concentration is therefore estimated to be 1.1×10^{20} ions.cm^{-3}.

4.3.1 $^4I_{15/2} \leftrightarrow {}^4I_{13/2}$ *transition lineshape measurements*

As described in section 4.1, a major advantage of the PLD process is the ability to maintain the stoichiometry of the target material between bulk and film. With this advantage in mind, the $^4I_{15/2} \leftrightarrow {}^4I_{13/2}$ transition lineshapes provide a convenient and useful method by which to probe stoichiometric and structural changes between the target and film. The following section will describe the techniques used to measure these lineshapes in the target material.

The $^4I_{13/2} \rightarrow {}^4I_{15/2}$ transition lineshape was measured in the target material using the experimental setup shown in Figure 4-2.

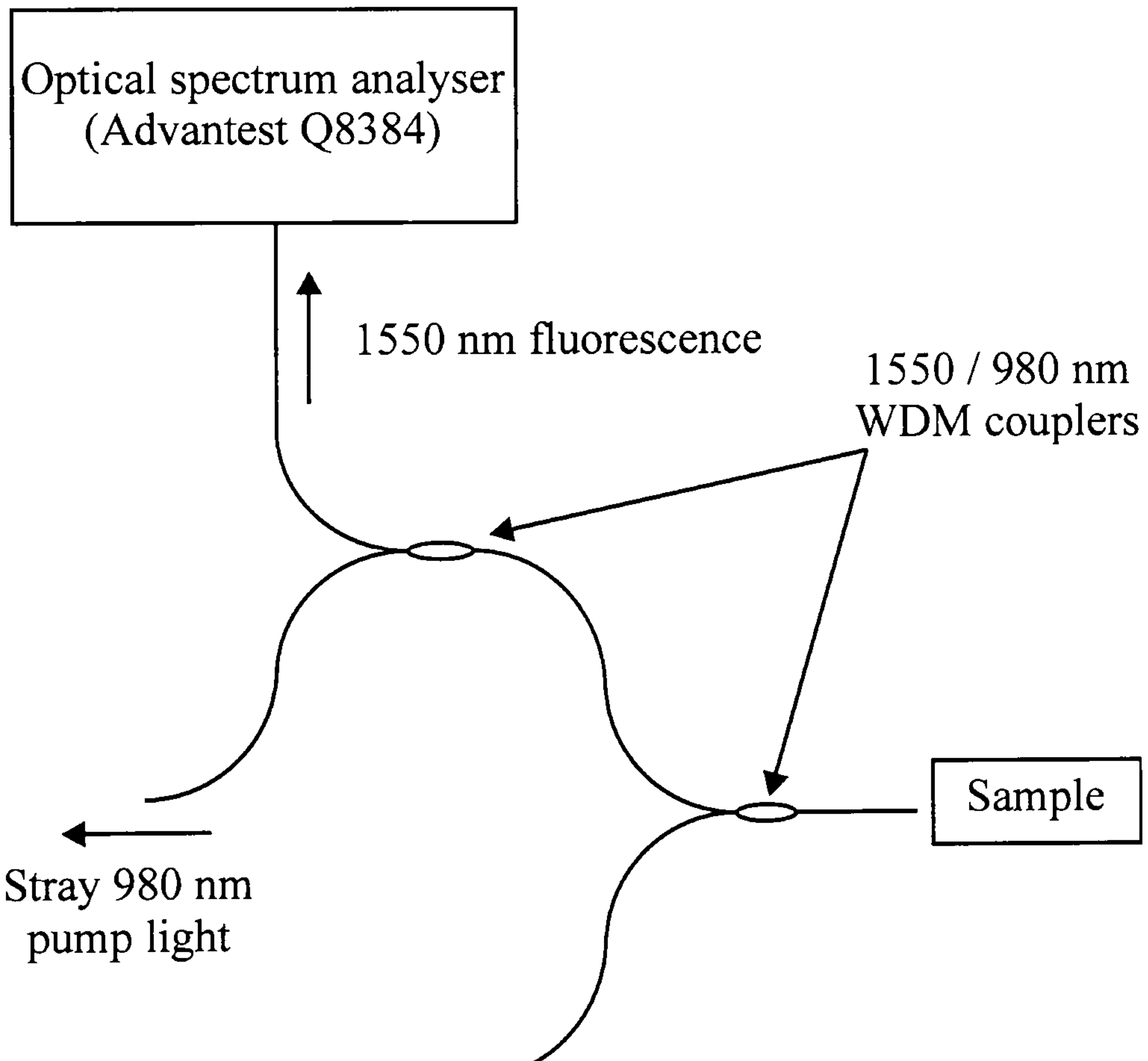

Figure 4-2 Schematic diagram of the experimental setup used to measure the $^4I_{13/2} \rightarrow {}^4I_{15/2}$ transition emission lineshape in the PLD target material

As shown in Figure 4-2, 980 nm pump light from a 980 nm laser diode is coupled into the bulk sample via a 1550 / 980 nm fused fibre WDM coupler. Fluorescence emission at 1550 nm is then collected by the same fibre and directed towards the OSA by the first WDM coupler. Index matching gel is used between the collection fibre and the target material to avoid any etalon effects. Any remaining pump light after the first WDM is separated from the fluorescence emission by a second WDM coupler. The fluorescence emission is then analysed using the OSA.

To investigate the effect of the WDM couplers on the fluorescence lineshape, the WDM coupler insertion loss from 1450 – 1650 nm was measured using a white light source. As a result, it was observed that the insertion loss was flat to within ≈ 0.3 dB for signals in the 1500 - 1625 nm range and to within ≈ 0.7 dB for signals in the 1450 – 1650 nm range. As such, the insertion loss of the two WDM couplers has a negligible effect on the lineshape of the measured fluorescence spectrum.

The $^4I_{15/2} \rightarrow {}^4I_{13/2}$ transition lineshape was measured in the target material using a Bruker IFS 66V/S FT-IR fourier transform infrared spectrometer. The results of the PLD target $^4I_{15/2} \leftrightarrow {}^4I_{13/2}$ transition lineshape characterisation experiments are presented in Figure 4-3.

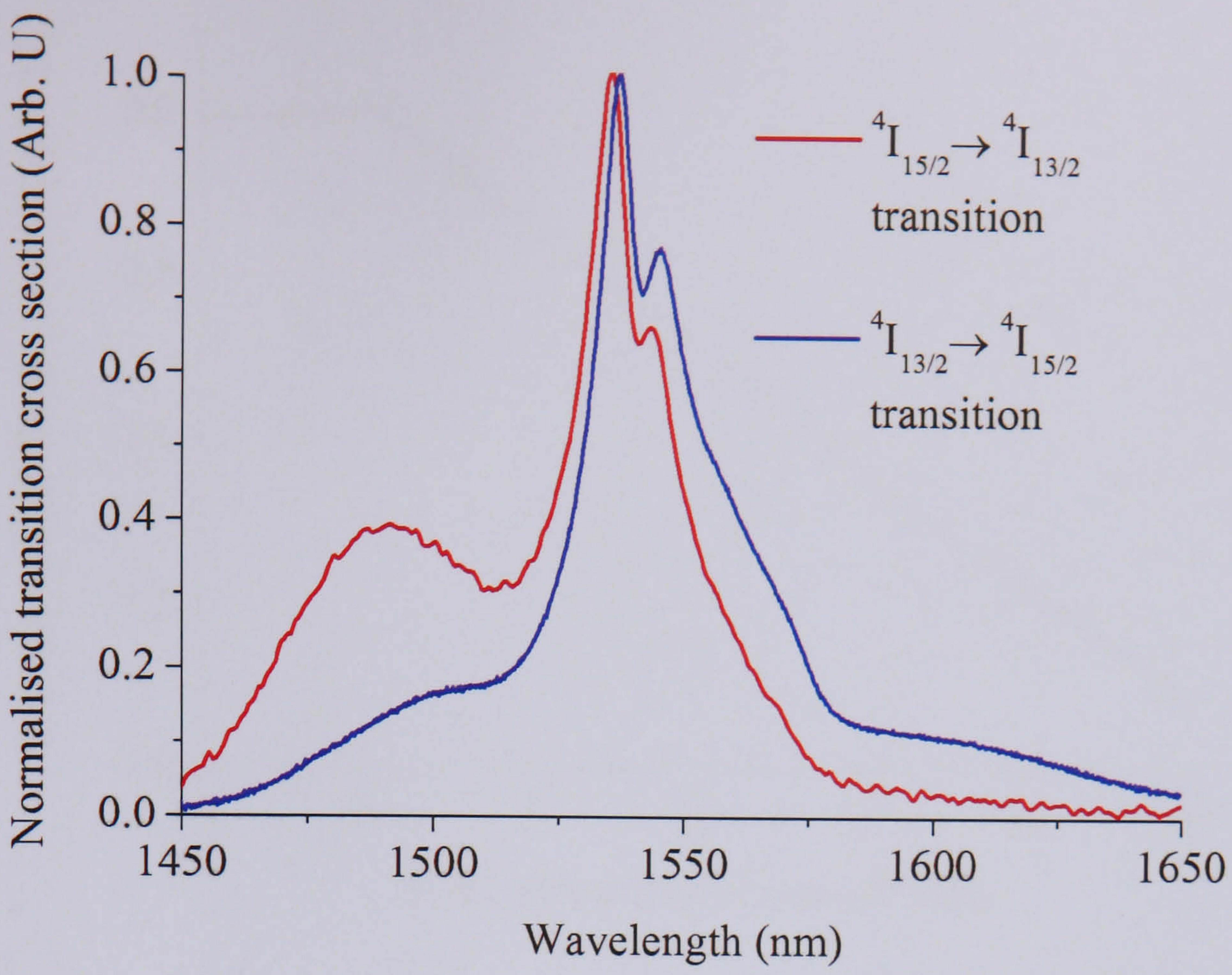

Figure 4-3 Normalised $^4I_{15/2} \leftrightarrow {}^4I_{13/2}$ transition lineshapes measured in the PLD target material.

As shown in Figure 4-3, the oxyfluoride-silicate target material exhibits broad absorption and emission spectra, each with a bandwidth of 20.9 and 24.4 nm (FWHM) respectively.

4.3.2 Time resolved $^4I_{13/2} \rightarrow {}^4I_{15/2}$ transition fluorescence studies

As with the transition lineshapes, the transition lifetimes also give insight into the host environment of the Er^{3+} ion. The $^4I_{13/2} \rightarrow {}^4I_{15/2}$ transition lifetime therefore also provides a useful method by which to probe stoichiometric and structural changes between the target and film as a result of the PLD process.

Time resolved $^4I_{13/2} \rightarrow {}^4I_{15/2}$ transition fluorescence studies of the target material were conducted using the experimental setup shown in Figure 3.13 in Chapter 3. Figure 4-4 shows the time resolved $^4I_{13/2} \rightarrow {}^4I_{15/2}$ transition fluorescence emission from the PLD target glass.

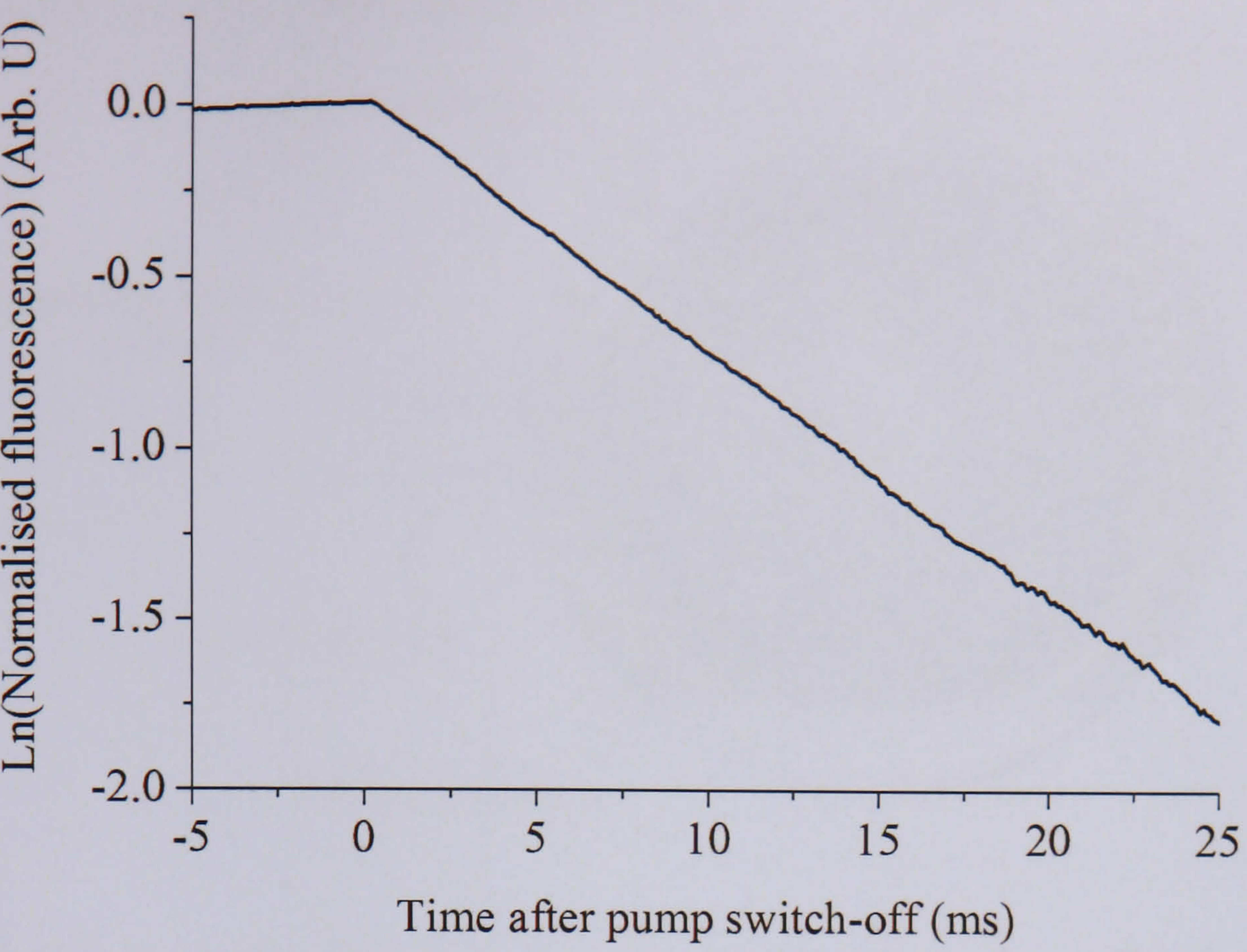

Figure 4-4 Time resolved $^4I_{13/2} \rightarrow {}^4I_{15/2}$ transition fluorescence emission from the PLD target glass

As shown in Figure 4-4, the fluorescence decay is characterised by a single exponential. The 1/e lifetime of this decay was measured to be 13.9 ms. Although the measured fluorescence decay was observed to be a single exponential, it is important to note that due to the fact that the pump light is not confined in a waveguide structure, the likelihood of observing the upconversion effects analysed in Chapter 3 is low.

4.4 Er-doped planar waveguide fabrication and characterisation

4.4.1 Planar waveguide fabrication using PLD

Thin films were deposited on fused silica substrates using reactive PLD. Depositions were performed in a stainless-steel high-vacuum chamber. Figure 4-5 is a photograph of PLD deposition chamber taken from above. Sketched on top of the photograph are the approximate paths of the focused pulsed laser beam and ablation plume.

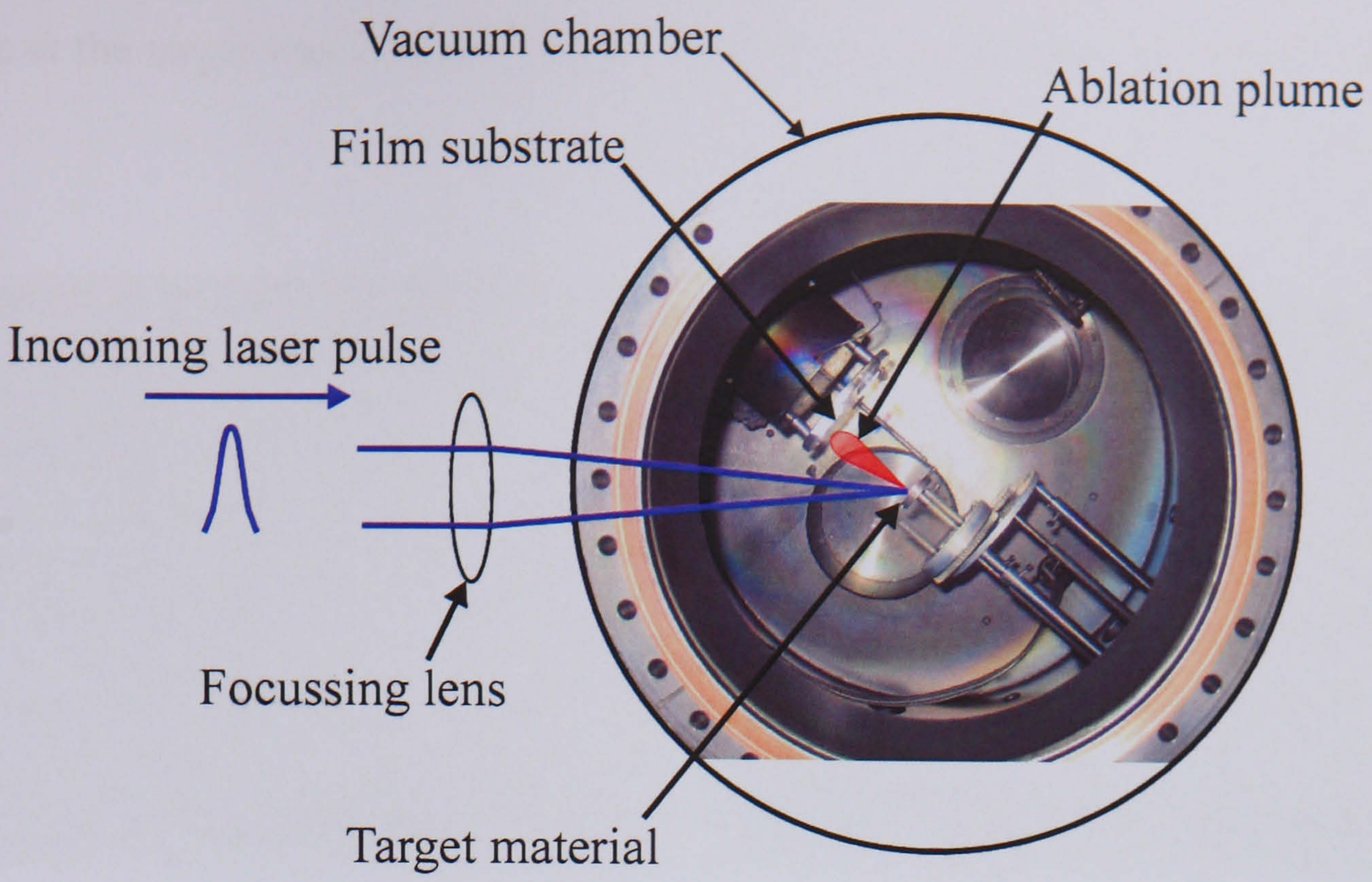

Figure 4-5 Photograph of PLD deposition chamber taken from above. Sketched on top of the photograph are the approximate paths of the pulsed laser and ablation plume.

Prior to depositions, the chamber was evacuated to 2×10^{-5} Pa, after which the residual water vapour content measured by mass spectrometer was 5×10^{-7} Pa. During the deposition process, a dynamic flow of oxygen at a pressure of 5 Pa was maintained in the chamber to compensate for the loss of oxygen during the deposition process. Ablation of the target material was performed using an ArF ($\lambda = 193$ nm) excimer laser. The repetition rate of the laser was 10 Hz and the pulse duration was 30 ns (FWHM). Due to the high absorption coefficient of 193 nm radiation in the oxyfluoride-silicate target material [6], the ArF excimer laser is well suited for the PLD process. The distance from the target to the substrate was set to either 45 or 55 mm and the fluence of the laser beam was either 2 or 4 J.cm^{-2}. To increase the film thickness homogeneity to ≈ 7 cm^2, the substrate was mounted on an automated x-y translation stage which was rastered during the deposition process. All films were fabricated using $1\text{x}10^5$ laser pulses. Thin films were deposited on substrates at either 200 °C or room temperature.

4.4.2 PLD film characterisation

To investigate the effect of the substrate temperature on the film morphology, SEM analysis was performed on two films. Film A was deposited using a target-substrate distance of 55 mm and room temperature substrate, Film B was deposited using a target-substrate distance of 45 mm and substrate at 200 °C. In both cases, the laser fluence at the target was 2 J.cm^{-2}. The SEM images of these films are shown in Figure 4-6.

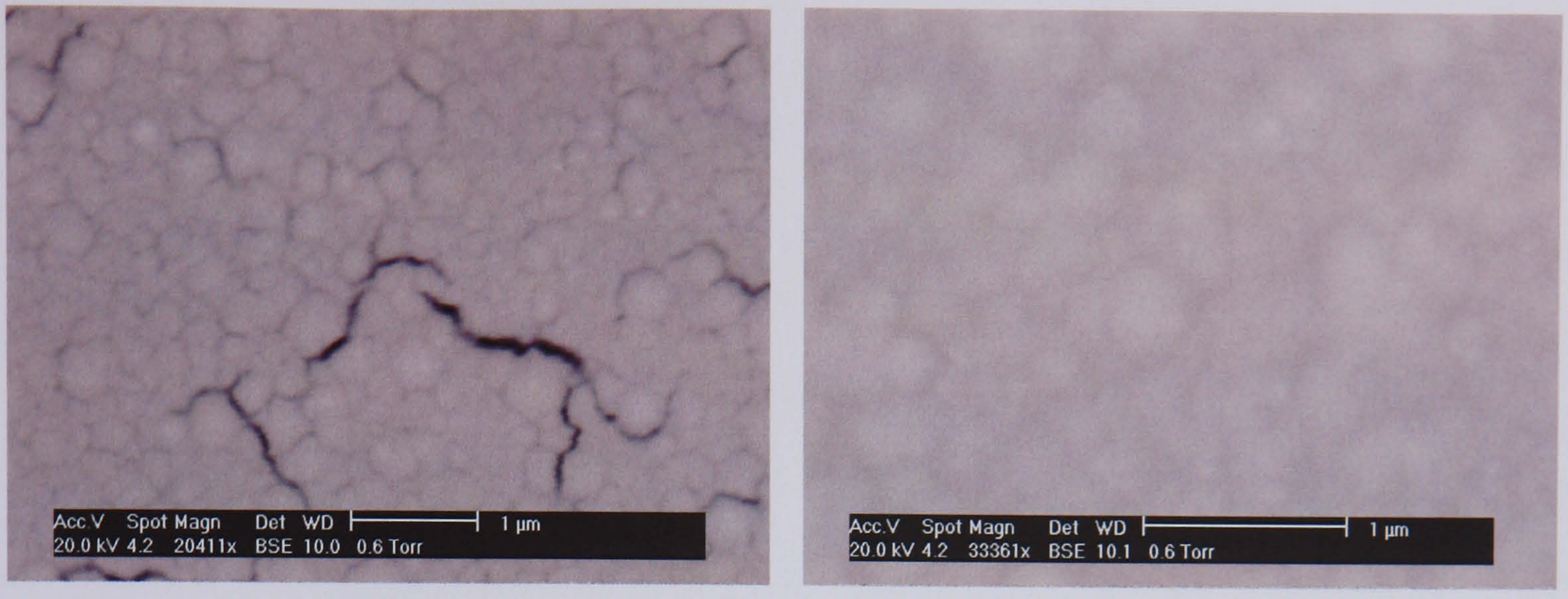

(a) (b)

Figure 4-6 SEM images of (a) film A and (b) film B.

As shown in Figure 4-6, both films were found to be granular in structure with a grain size of the order of ≈ 100 - 200 nm. It is also apparent from the SEM inspection that the contrast between the grains in film A is higher than that in film B, possibly indicating less cohesion between the grains in film A and a lower film packing density.

Although films deposited using a 200 °C substrate temperature were found to be crack free after both SEM inspection and reactive ion etching (RIE), films deposited on room temperature substrates were found to consistently crack under both SEM inspection and RIE. As a result, the following characterisation experiments will focus on film C used to fabricate rib waveguides. Film C was fabricated using very similar deposition conditions as film B, however the laser fluence at the target was 4 J.cm^{-2}.

The thickness, refractive index and propagation losses of film C were measured using a Metricon$^{\text{TM}}$ 2010 prism coupler. As a result, the thickness of film C was measured to be 1.8 µm. The refractive index data for the target material and film C are summarised in Table 4-1 and Figure 4-7. The possible error in the film thickness and refractive index data are thought to be 0.5 % and 0.001 respectively [7].

Sample	633 nm	1321 nm	1550 nm
Target	1.5753	1.5612	1.5608
Film C	1.6142	1.5970	1.5948

Table 4-1 Refractive index data for the target and PLD film materials

To calculate the refractive indices at other wavelengths not available for prism coupling experiments, a Cauchy fit was made to the refractive index data [8]. The resultant Cauchy fit for film C and target material data are Equation 4-1 and Equation 4-2 respectively given below.

$$n_{PLD\,film}(\lambda) = 1.5884 + \left(\frac{1.6447\times10^{4}}{\lambda^{2}}\right) - \left(\frac{2.4443\times10^{9}}{\lambda^{4}}\right)$$

Equation 4-1

$$n_{Target}(\lambda) = 1.5603 + \left(\frac{2.7528\times10^{2}}{\lambda^{2}}\right) + \left(\frac{2.3001\times10^{9}}{\lambda^{4}}\right)$$

Equation 4-2

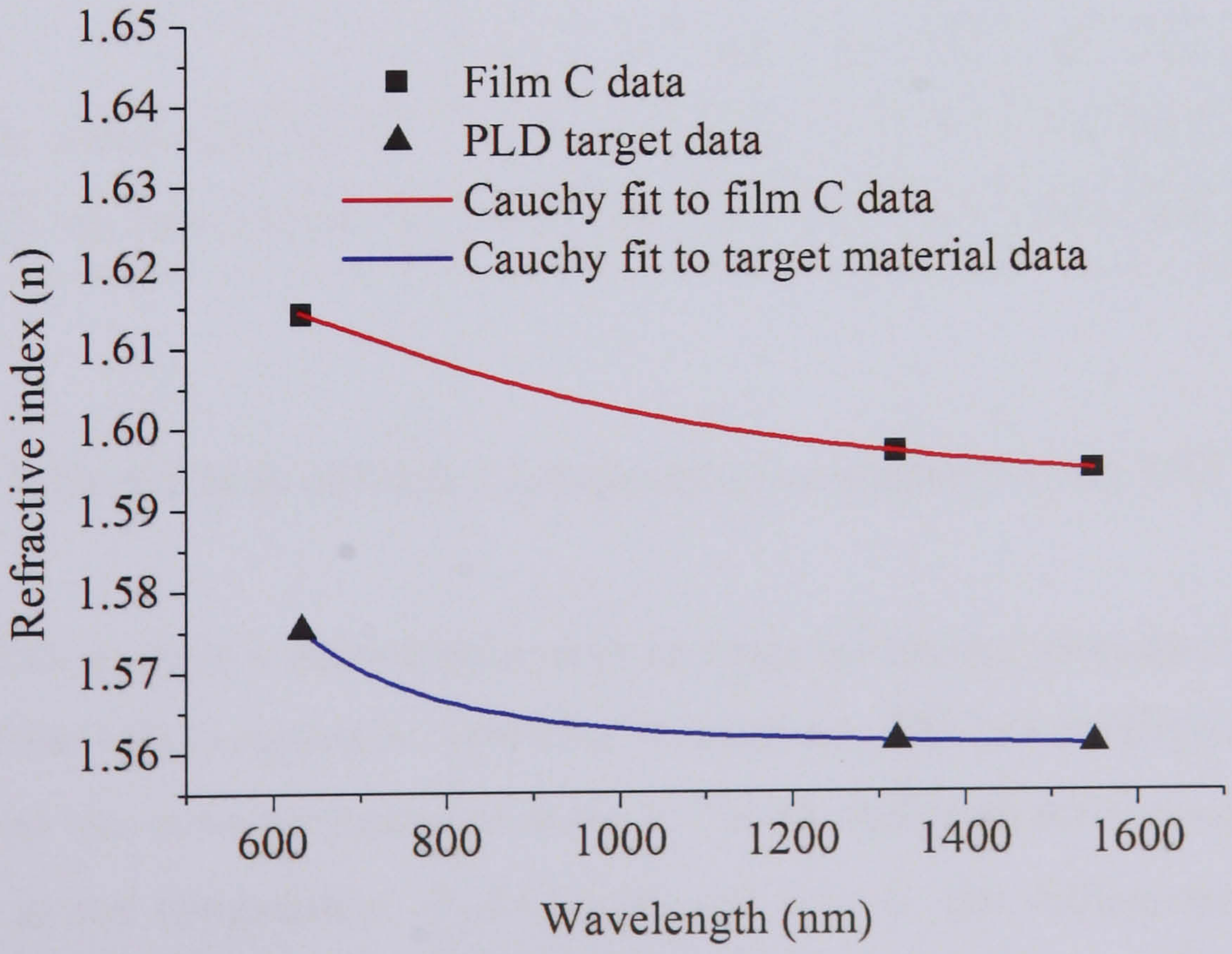

Figure 4-7 Comparison of refractive index vs. wavelength data for film C and the target material. Also shown in red and blue are the Cauchy fits to the refractive index data.

As can be seen in Figure 4-7, the refractive index of film C is consistently higher than that of the target material by approximately 2 %, possibly indicating a denser film material on average than the target material. Although not shown, the refractive index of films deposited using room temperature substrates were measured to be consistently lower than that of the target material.

Propagation losses in the planar waveguide film C were measured to be in the region of 1 dB.cm^{-1} at 633 nm using the well know streak method [9]. All prism coupling experiments were conducted by Dr Shaoxiong. Shen at the University of Leeds. To investigate the surface roughness of film C, Atomic Force Microscope (AFM) analysis was performed on the film surface. This analysis revealed a peak-peak surface roughness of the order of 100 nm, a value that is in rough agreement with that expected from the propagation loss measurements [10].

To investigate stoichiometric changes between the target and film due to the PLD process, the compositions of the target material and film C were measured using Energy Dispersive X-ray analysis (EDX). The results of these measurements are presented in Table 4-2.

Sample	Element							
	O	F	Na	Er	Al	Si	La	Pb
Bulk composition (at. %)	45.5	3.4	10.0	0.7	3.7	28.0	6.0	2.7
Film C composition (at. %)	49.8	2.9	8.1	0.7	3.3	26.4	6.4	2.4

Table 4-2 Bulk and film C compositions as measured using EDX

Although EDX analysis is known to be more accurate for heavier elements, the absolute accuracy of the values quoted in Table 4-2 is unknown. The repeatability in the EDX measurements was however measured to be $\approx$ 1 at. %. Although there are clearly some differences in the composition of the target and film C, the differences are small. Consequently, the data shown in Table 4-2 is strong evidence that the transfer of material from target to film is close to stoichiometric, a key advantage of the PLD process.

In this section, the deposited PLD films have been shown to be granular in structure. The refractive index of films deposited using 200 °C substrates have been shown to be consistently slightly higher than that of the target material, possibly indicating a denser material on average than the target material. Although the stoichiometry of film C has been shown to be very similar to that of the target material, no information regarding the structural similarity between the target and film C has been reported. In the following section, rib waveguides are fabricated from the film C, and various investigations performed to investigate the Er^{3+}-ion environment in the film compared to the target material.

4.5 Er-doped rib waveguide fabrication and characterisation

4.5.1 Er-doped rib waveguide fabrication

To fabricate rib waveguides from film C, a 1.5 μm thick layer of Shipley 1813 UV sensitive photoresist was spun onto the film surface and baked for 30 minutes at 90 °C. Rib structures of widths 2 → 15 μm were defined onto the resist by UV illumination for 15 seconds through a chrome-on-silica mask. The resist was developed using the resist developer and the resultant resist mask baked for 2 hours at 95 °C. Finally, the sample surface was etched for 105 minutes in an Oxford Plasma Technology RIE80 reactive ion etcher using CHF_3 gas. The final etch depth was measured to be 0.9 μm by AFM analysis. Figure 4-8 shows an AFM image of one of the fabricated rib waveguides.

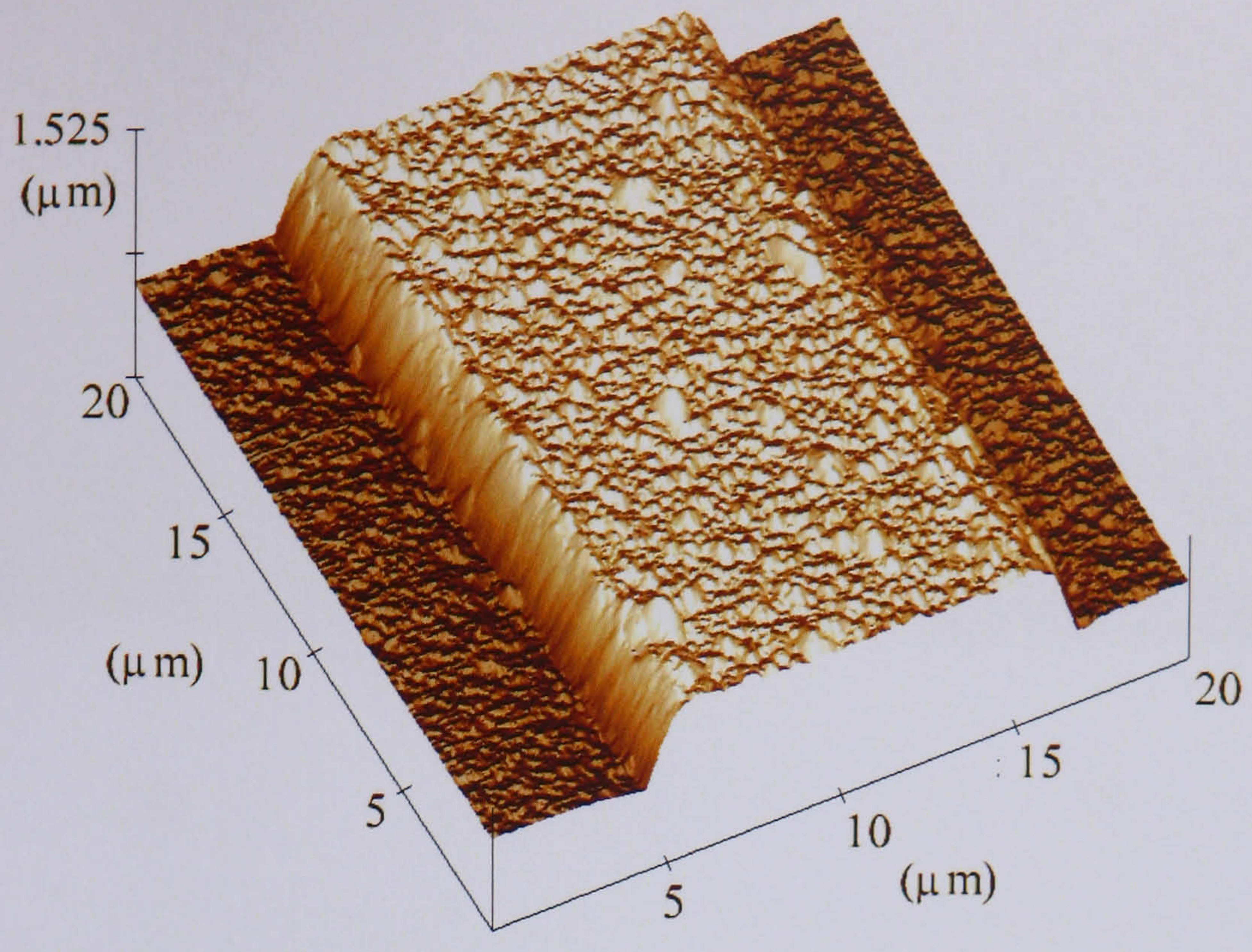

Figure 4-8 AFM image of one of the fabricated ridge waveguides

Waveguide facets for coupling light to and from the waveguides were obtained by dicing with a diamond dicing saw (Disco DAD321). Extensive effort was made to optimise the waveguide facet quality by varying the dicing parameters and using different cladding materials for protection during dicing, Through these investigations it was found that although it was possible to dice the fused silica substrate material precisely with minimal chipping, the film itself consistently chipped away from the substrate edge leaving an essentially random quality waveguide facet for coupling. It was concluded therefore that the dicing quality of the film was limited by either or both the structural integrity of the film itself or the adhesion of the film to the substrate surface. As an example, Figure 4-9 shows SEM images of the film and substrate edge, and the waveguide end facet after dicing with the optimum dicing parameters (100 $\mu m.s^{-1}$ cut speed and an SU8 resist protective cladding layer).

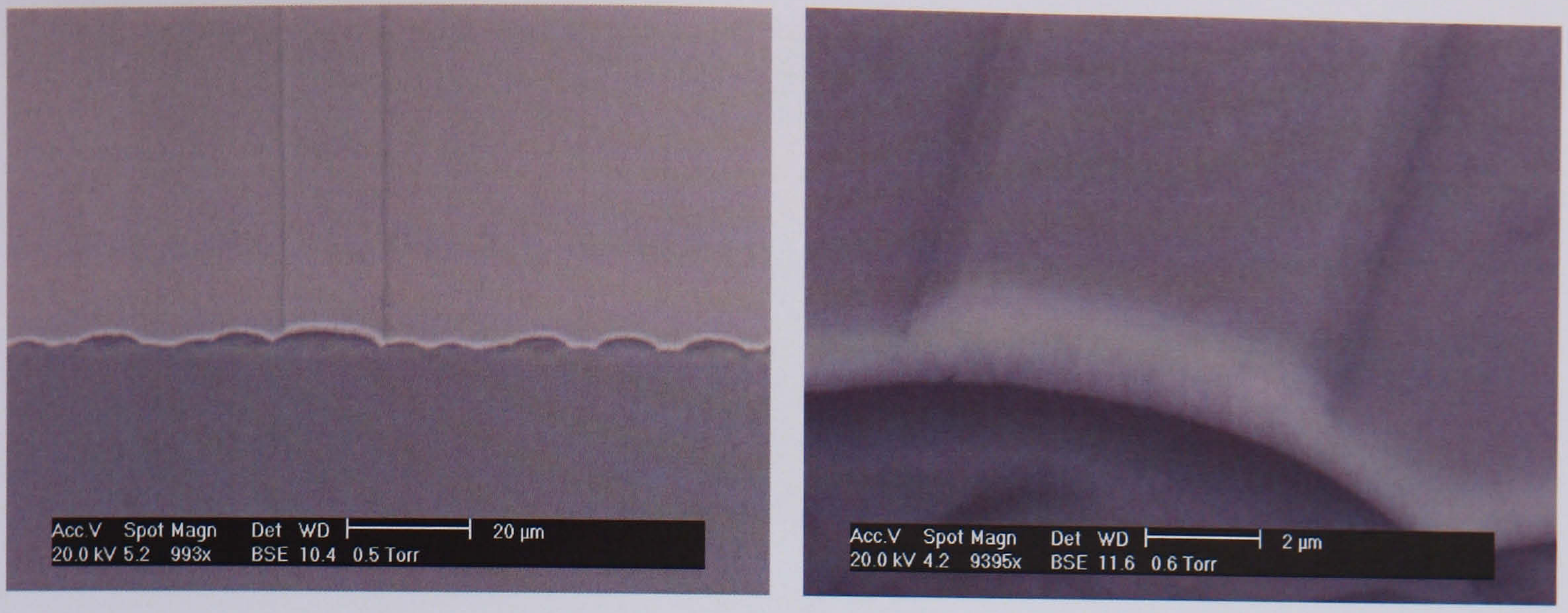

(a) (b)

Figure 4-9 SEM images of (a) the film and substrate edge and (b) the waveguide end facet after dicing with the optimum parameters.

Although the quality of the waveguide facet shown in Figure 4-9 is clearly not ideal, the use of index matching gel when coupling fibres to the waveguide facets should address much of the coupling losses induced by the poor facet quality. As discussed in the following section, the mode field of these waveguides are extremely different from that of conventional SMF-28 fibre. As such, the majority of the fibre-waveguide and waveguide-fibre coupling losses are expected to originate from the fibre-waveguide mode-mismatch, not from the waveguide facet quality.

4.5.2 Investigating the guiding properties of the fabricated waveguides.

Prior to investigating the guiding properties of the fabricated rib waveguides experimentally, the 1550 nm waveguide modes were modelled using the Femlab^{TM} modelling package together with the experimentally measured film thickness, refractive index and etch distance data. Consequently, it was found that film C and also the remaining film after etching were able to support only one mode at 1550 nm (both TE and TM polarisations). It was also found that only 2 µm wide rib waveguides were single mode in the x-axis, all other wider rib waveguides were multimode in the x-axis. As an example of the modelling results, Figure 4-10 shows the modelled energy distribution of the TE (0,0) and TE (1,0) modes for a 4 µm wide rib waveguide.

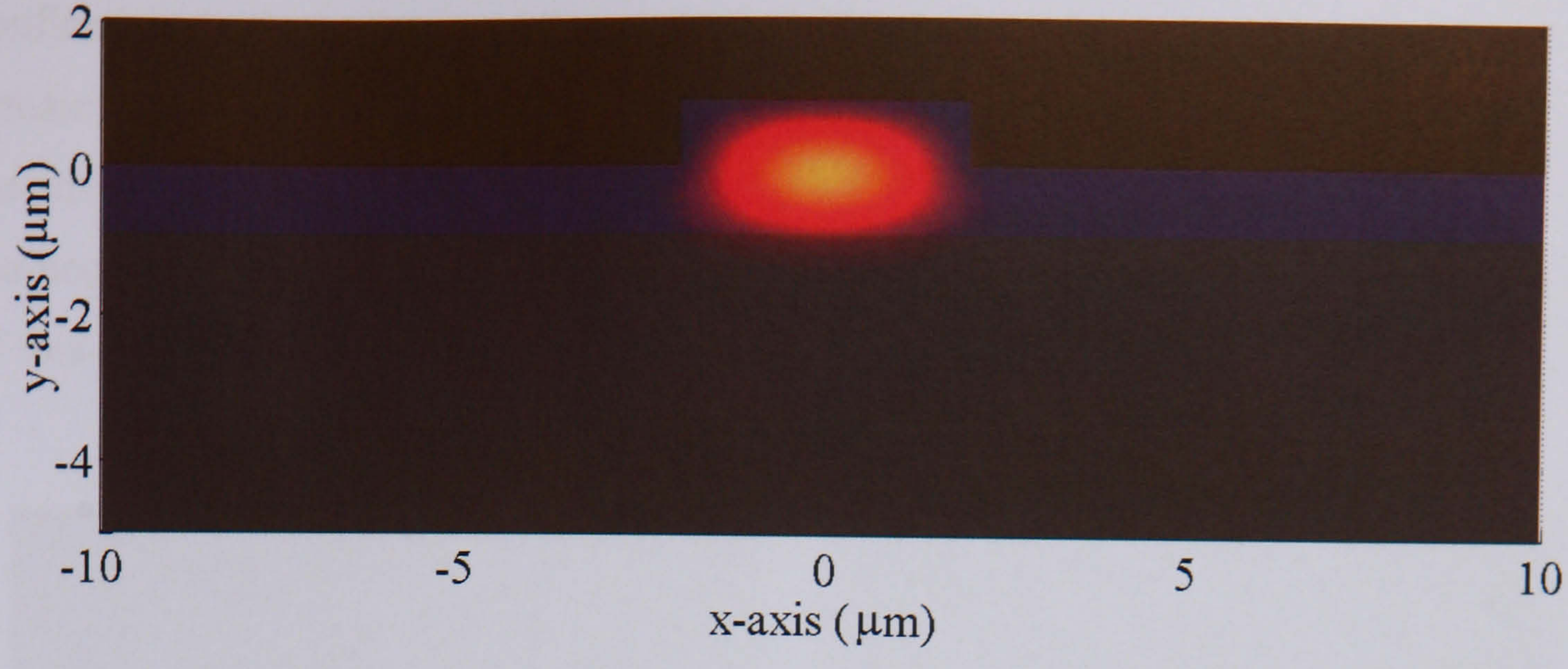

(a)

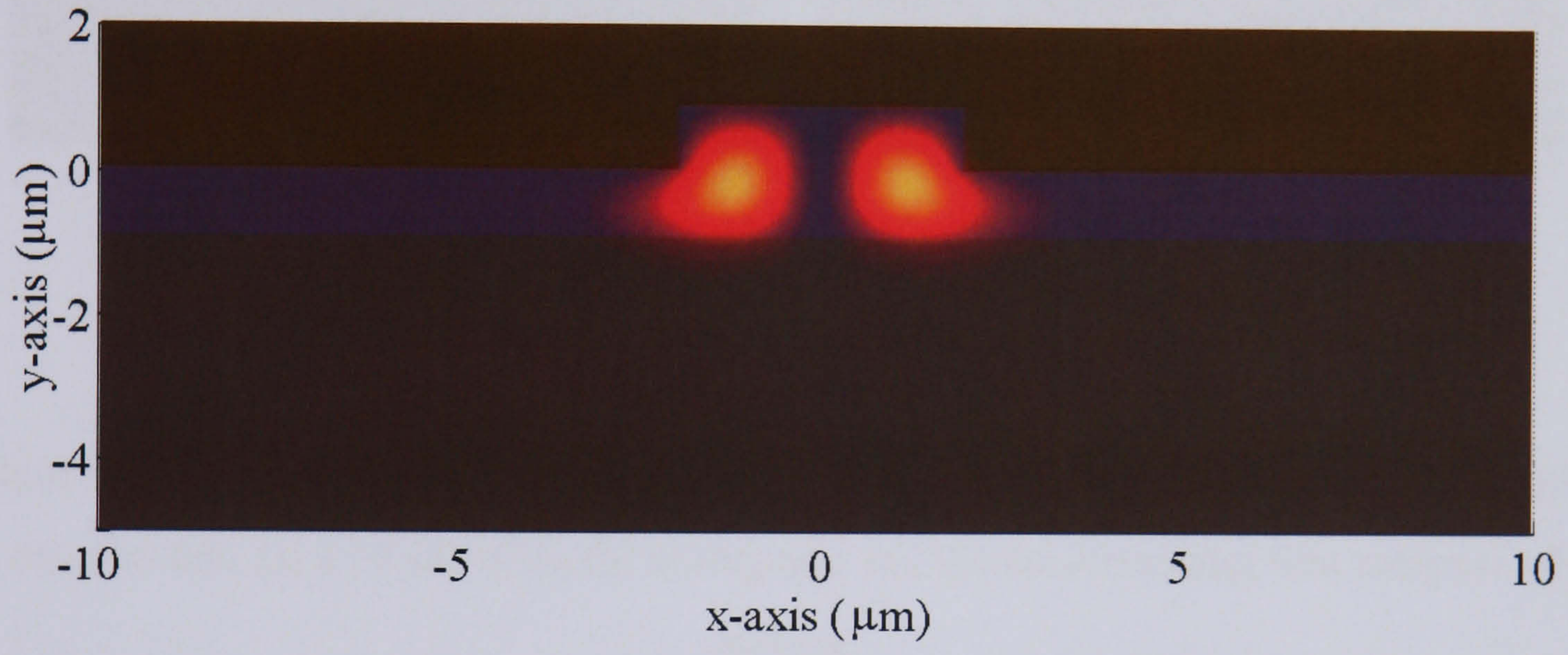

(b)

Figure 4-10 Normalised total energy distribution of the (a) TE (0,0) and (b) TE (1,0) mode for a 4 μm wide rib waveguide. Three areas are shown in each figure; the lower area is the fused silica substrate, the middle area is the PLD film, the upper area is air.

Once guiding of light in the waveguide structures had been theoretically confirmed, the guiding properties of the waveguides were investigated experimentally. To do this, the waveguide end facet was imaged onto an IR Vidicon camera while coupling light into the waveguide at the opposite end using direct fibre-waveguide butt-coupling. As an example, Figure 4-11 (a) shows the captured near field image of the output facet of a 15 μm wide rib waveguide when 1550 nm light is coupled into the waveguide at the opposite end. Figure 4-11 (b) shows the captured near field image of the same output facet shown in (a) when 1550 nm light is coupled into the remaining film material after etching. As shown in Figure 4-11, light coupled into the rib waveguide is strongly confined in both the horizontal and vertical directions, whereas light coupled into the remaining planar waveguide film is only confined in the vertical direction. We attribute the irregular spatial distribution of the emitted light shown in Figure 4-11 primarily to the poor film facet quality evident in Figure 4-9. It should be noted however that some of this structure may be due to high order modes and modal interference.

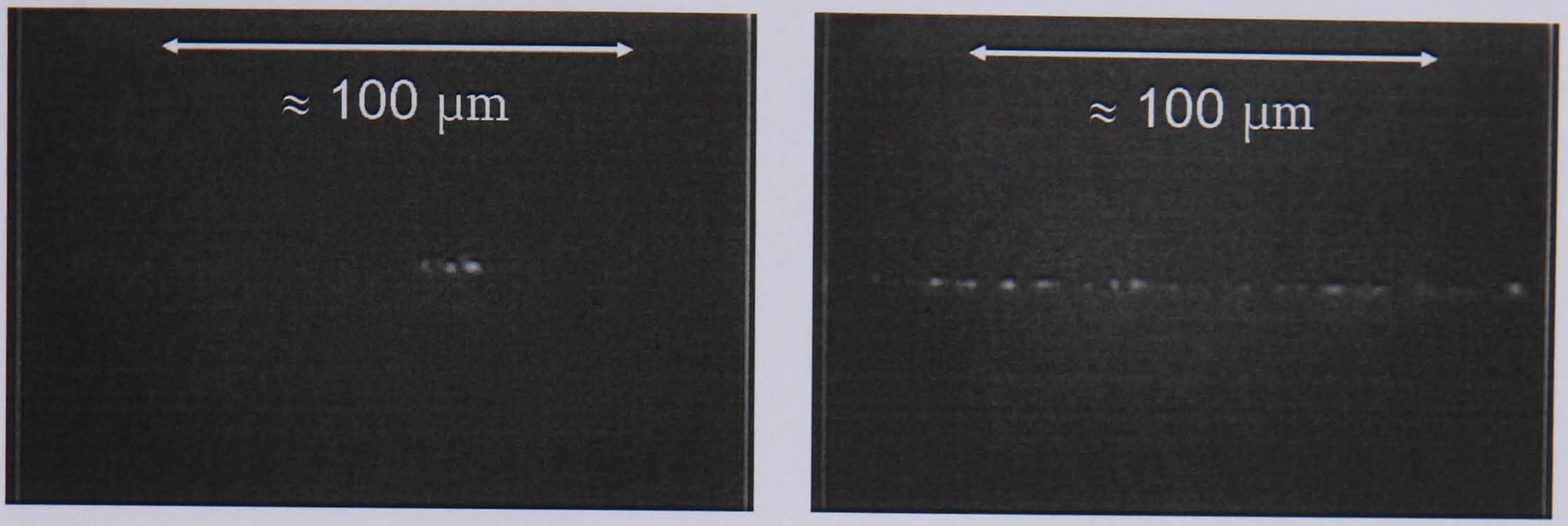

(a) (b)

Figure 4-11 Captured near field images of sample output facet when TM polarised light is coupled into (a) a 15 μm wide rib waveguide and (b) the remaining film material after etching.

As predicted by finite element modelling of the waveguide structure, well confined guiding of both 980 nm and 1550 nm light polarised in both TE and TM directions was observed for all waveguides. The degree to which these waveguides were or were not multimode could not be investigated due to the poor waveguide facet quality, the effect of which is clearly visible in Figure 4-11.

4.5.3 $^4I_{15/2} \leftrightarrow {}^4I_{13/2}$ transition lineshape measurements.

As outlined previously, the $^4I_{15/2} \leftrightarrow {}^4I_{13/2}$ transition lineshapes provide a convenient method by which to investigate stoichiometric and structural changes in the material between bulk and film. To compare the $^4I_{13/2} \rightarrow {}^4I_{15/2}$ transition lineshape in the film with that of the target material, the fluorescence emission from Er^{3+} ions in the waveguide core material was measured using the experimental setup shown in Figure 4-2. Figure 4-12 below is a comparison of the normalised $^4I_{13/2} \rightarrow {}^4I_{15/2}$ transition emission cross sections measured in one of the fabricated rib waveguides and the PLD target glass.

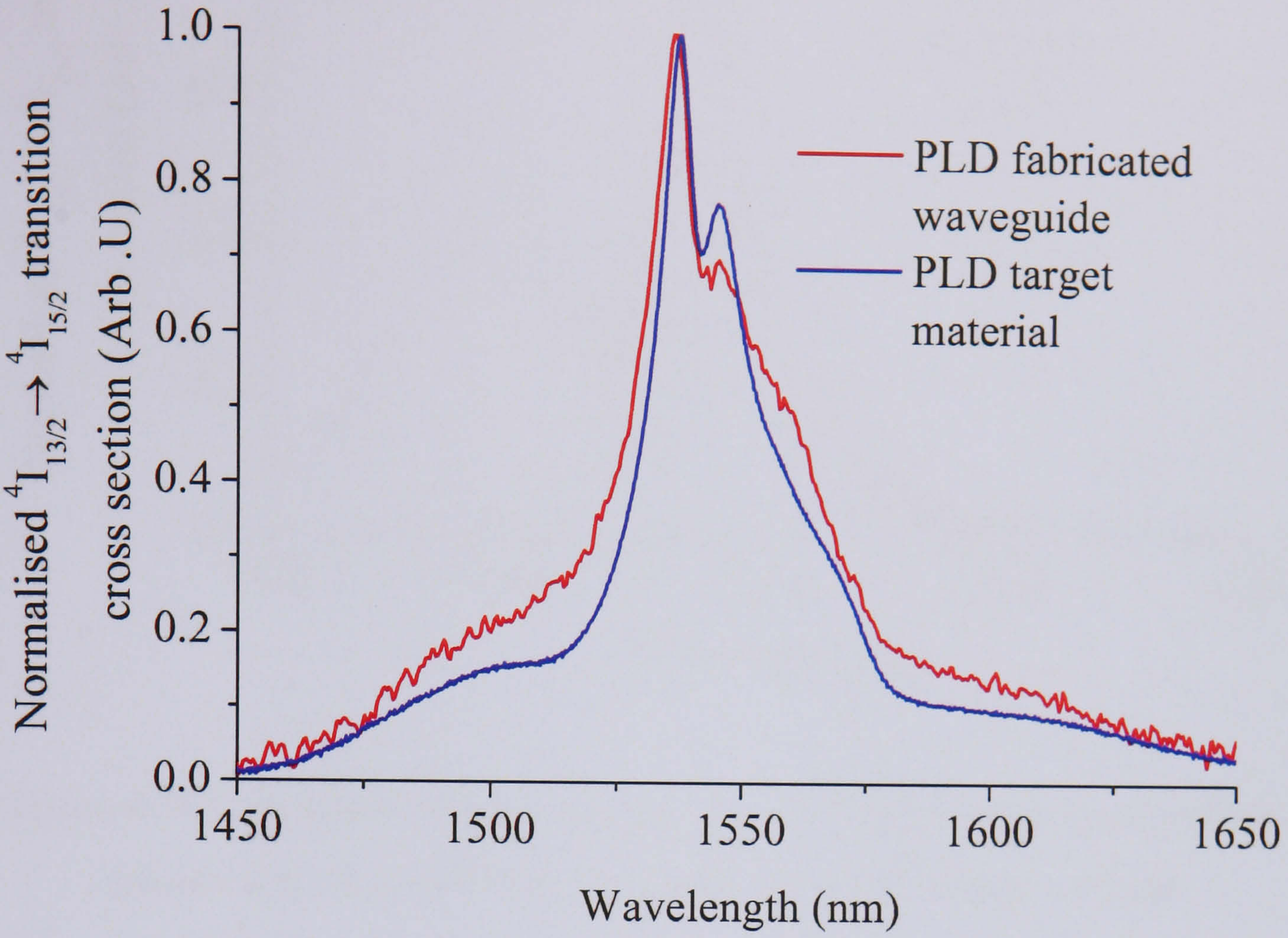

Figure 4-12 Comparison of the normalised $^4I_{13/2} \rightarrow {}^4I_{15/2}$ transition cross sections measured in the PLD fabricated waveguide and PLD target material

To measure the $^4I_{15/2} \rightarrow {}^4I_{13/2}$ transition lineshape in the film material, the insertion loss of one of the smaller width waveguides was measured using the experimental setup shown in Figure 3.5. Although the minimum background insertion loss was measured to be ≈ 20 dB for a 0.76 cm long, 4 μm wide rib waveguide, the effect of absorption by Er^{3+} ions was clearly observable in the insertion loss spectrum. By measuring the loss due to absorption in this manner, the peak erbium absorption coefficient through the 4 μm wide rib waveguide was measured to be 4.6 dB.cm^{-1}, slightly higher than the 3.4 dB.cm^{-1} value measured in the bulk material. Figure 4-13 shows a comparison of the normalised $^4I_{15/2} \rightarrow {}^4I_{13/2}$ transition cross sections measured in the PLD fabricated waveguide and PLD target material.

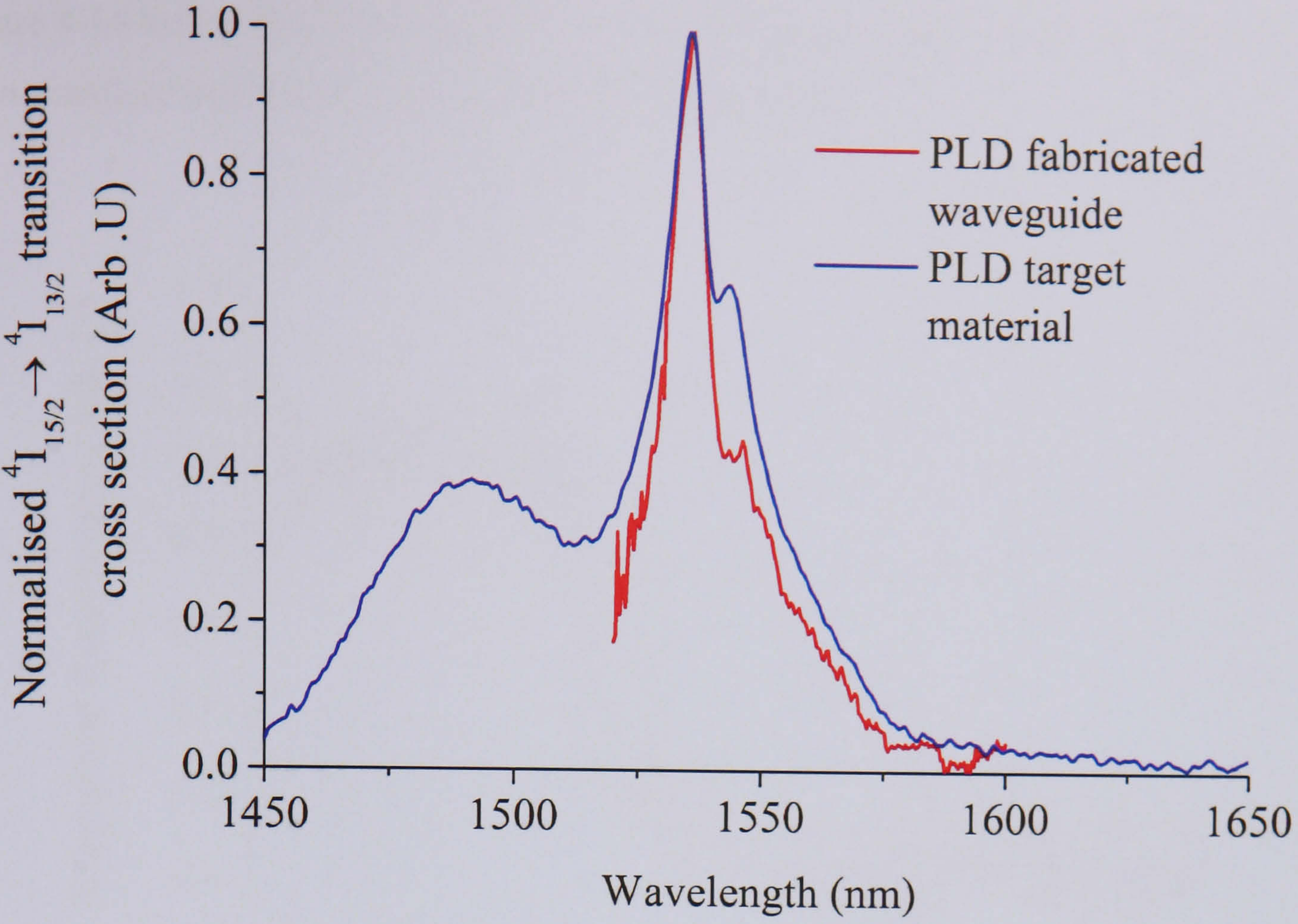

Figure 4-13 Comparison of the normalised $^4I_{15/2} \rightarrow ^4I_{13/2}$ transition cross sections measured in a 4 μm wide rib waveguide and the PLD target material

As shown in Figure 4-12 and Figure 4-13, the $^4I_{15/2} \leftrightarrow ^4I_{13/2}$ transition lineshapes measured in film C are significantly different from those measured in the target material. Such differences must in turn imply significant differences in the Er^{3+}-ion host environment. To investigate if these structural changes were detrimental or beneficial to the amplification properties of the material, time resolved fluorescence studies were conducted. The following section describes these studies.

4.5.4 Time resolved $^4I_{13/2} \rightarrow ^4I_{15/2}$ transition fluorescence studies

The EDX and Er^{3+}-ion absorption coefficient measurements strongly indicate close to stoichiometric transfer of material from target to film, whereas differences in the target and film $^4I_{15/2} \leftrightarrow ^4I_{13/2}$ transition lineshapes clearly indicate changes in the Er^{3+}-ion host environment. To assess whether these changes were beneficial or detrimental to the amplification properties of the film material, the $^4I_{13/2} \rightarrow ^4I_{15/2}$ transition fluorescence lifetime of Er^{3+} ions in the rib waveguides was measured using the experimental setup shown in Figure 3.13.

Figure 4-14 below shows the recorded fluorescence decay. Also shown in Figure 4-14 is the normalised pump modulation signal for comparison.

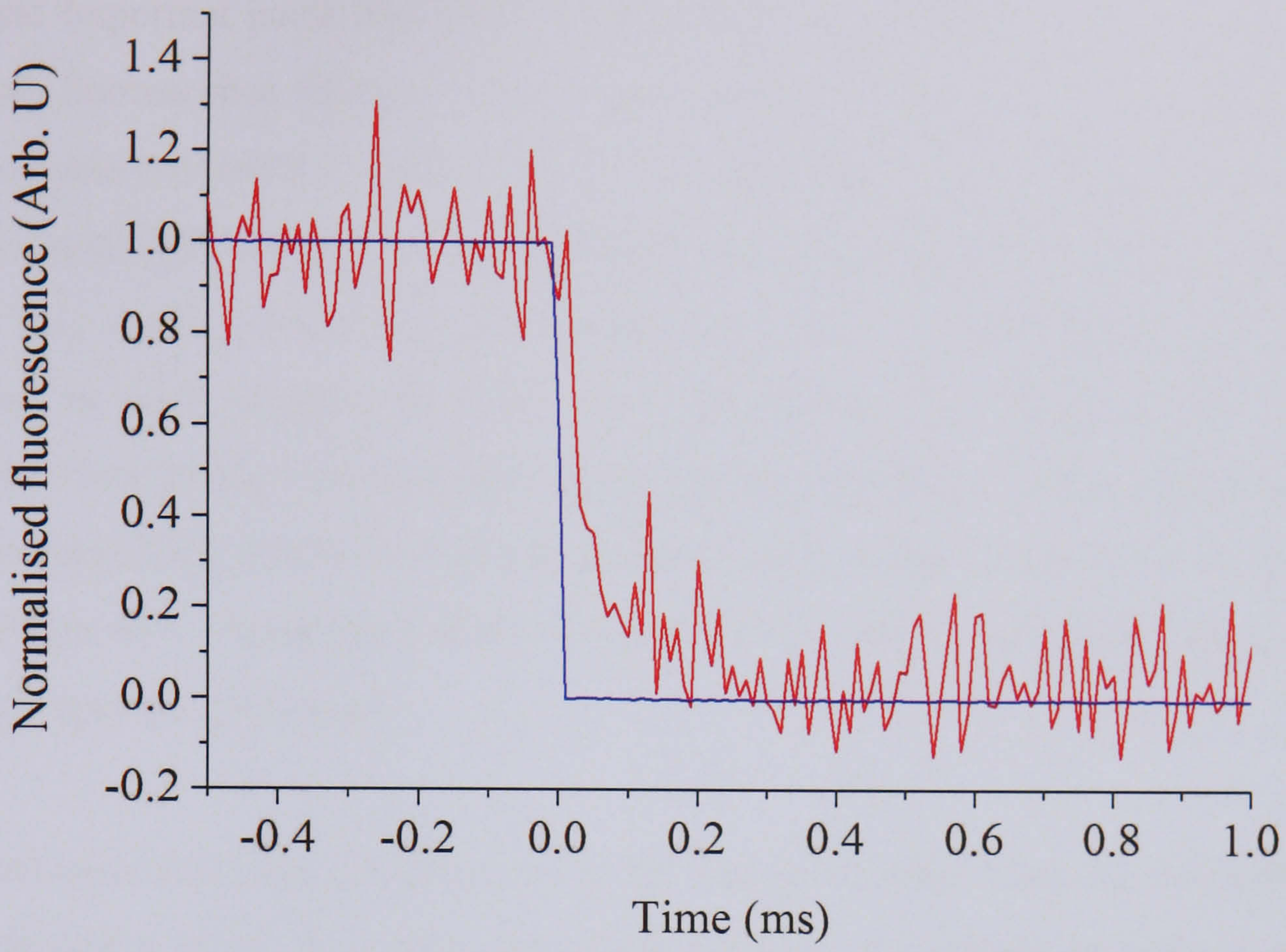

Figure 4-14 Time resolved $^4I_{13/2} \rightarrow {}^4I_{15/2}$ transition fluorescence emission from Er^{3+} ions in one of the rib waveguides (Red). Also shown in blue is the normalised pump signal for comparison.

As shown in Figure 4-14, the $^4I_{13/2} \rightarrow {}^4I_{15/2}$ transition fluorescence lifetime in the PLD film material is in the region of ≈ 0.05 ms, substantially lower than the 13.9 ms value measured in the bulk material. This reduction in the fluorescence lifetime clearly indicates the presence of significant quenching mechanisms such as hydroxyl (O-H) impurities [11] or strong energy transfer / cooperative upconversion mechanisms [12]. Insertion loss measurements of one of the rib waveguides did reveal an unexpected increase in the insertion loss at 1426 nm (close to the first vibrational overtone of the hydroxyl group centred at 1380 nm), a strong indication of a significant presence of O-H impurities [13].

4.6 Conclusions and future work

As a result of the work presented in this chapter, it has been shown that broadband EDWA fabrication could be possible using reactive PLD and oxyfluoride-silicate glass targets. There are however significant issues that must be addressed if useful devices are to be fabricated.

The most important point that must be addressed is the reduction in the $^4I_{13/2} \rightarrow {}^4I_{15/2}$ transition fluorescence lifetime of Er^{3+}-ions in the PLD film. From the results of the SEM analysis presented in section 4.4.2, it is clear that the PLD films are granular in structure, possibly leaving the films susceptible to water absorption and O-H quenching of the $^4I_{13/2} \rightarrow {}^4I_{15/2}$ transition. To address this problem, future films must be fully densified in some manner to stop water absorption. Film densification could be achieved either during the deposition process by increasing the substrate temperature or after the deposition process by annealing the samples either thermally or using a CO_2 laser. Either way, a systematic study of how the $^4I_{13/2} \rightarrow {}^4I_{15/2}$ transition lifetime can be increased must be performed.

A second issue that must be addressed is the waveguide-fibre coupling efficiency. Due to the thickness of the PLD film, the coupling losses will always be high when using direct fibre-waveguide butt-coupling, even with a perfect waveguide facet quality. As discussed in Chapter 2, coupling losses not only decrease the overall device gain, but also reduce the pumping efficiency. Possible approaches to improve this situation include fabricating thicker PLD films, using free space optics to couple into and out of the waveguide or possibly even the use of tapered fibres for evanescent coupling to the waveguide [14].

Although gain operation was not observed in the PLD fabricated waveguides, a number of significant contributions to the field of PLD have been made. Firstly, the fabrication of planar waveguide films with propagation losses in the region of 1 $dB.cm^{-1}$ at 633 nm is highly significant, and certainly confirms the possibility for fabricating low loss planar lightwave circuits using PLD. In addition, the similarity in the EDX and Er^{3+}-ion absorption coefficient measurements in the target and film materials strongly indicate close to stoichiometric transfer of the material from bulk to film, a major advantage of the PLD process. As a result of these key findings, it is concluded that PLD could provide a reliable route for fabricating broadband EDWA devices if the issues discussed above can be addressed.

4.7 References

[1] A. P. Caricato, M. Fernández, M. Ferrari, G. Leggieri, M. Martino, M. Mattarelli, M. Montagna, V. Resta, L. Zampedri, and R. M. Almeida. "Er^{3-} doped tellurite waveguides deposited by excimer laser ablation," *Mat. Sci. Eng. B-Solid*, vol. 105, no. 1-3, pp. 65-69, Dec. 2003.

[2] M. Martino, A. P. Caricato, M. Fernández, G. Leggieri, A. Jha, M. Ferrari, and M. Mattarelli, "Pulsed laser deposition of active waveguides," *Thin Solid Films* vol. 433, no. 1-2, pp. 39-44, Jun. 2003.

[3] D. B. Chrisey and G. K. Hubler, "History and fundamentals of pulsed laser deposition," *Pulsed Laser Deposition of Thin Films,* John Wiley & Sons, 1994, pp. 3-4.

[4] D. B. Chrisey and G. K. Hubler, "History and fundamentals of pulsed laser deposition," *Pulsed Laser Deposition of Thin Films,* John Wiley & Sons, 1994, pp. 12-13.

[5] D. B. Chrisey and G. K. Hubler, "History and fundamentals of pulsed laser deposition," *Pulsed Laser Deposition of Thin Films,* John Wiley & Sons, 1994, pp. 7.

[6] S. X. Shen and A. Jha, "The influence of F^--ion doping on the fluorescence ($^4I_{13/2} \rightarrow {}^4I_{15/2}$) line shape broadening in Er^{3+}-doped oxyfluoride silicate glasses," *Opt. Mater.*, vol. 25, no. 3, pp. 321-333, Apr. 2004.

[7] Metricon corporation. (2006, Jul.). Model 2010 prism coupler features and specifications [Online]. Available http://www.metricon.com/feature.htm.

[8] E. Hecht, "Electromagnetic theory, photons and light," *Optics*, 3rd edition, Addison Wesley Longman, 1998, pp. 84.

[9] Y. Okamura, S. Yoshinaka, and S. Yamamoto, "Measuring mode propagation losses of integrated optical waveguides: a simple method," *Appl. Optics*, vol. 22, no. 23, pp. 3892-3894, Dec. 1983.

[10] R. G. Hunsperger, "Losses in optical waveguides," in *Integrated optics: Theory and Technology,* Springer-Verlag, 1982, pp. 71.

[11] L.H.Slooff, M.J.A.de Dood, A.van Blaaderen, and A.Polman, "Effects of heat treatment and concentration on the luminescence properties of erbium-doped silica sol-gel films," *J Non-Cryst. Solids*, vol 296, pp. 158-164, 2001.

[12] E. Desurvire, "Characteristics of erbium-doped fibers," *Erbium doped fiber amplifiers : principles and applications,* John Wiley & Sons, 2002, pp. 273.

[13] R. R. Thomson, H. T. Bookey, A. K. Kar, M. R. Taghizadeh, A. Klini, C. Fotakis, F. Romano, A. P. Caricato, M. Martino, S. Shen, and A. Jha, "Erbium-doped waveguide fabrication via reactive pulsed laser deposition of erbium-doped oxyfluoride-silicate glass," *Electron. Lett.*, vol. 41, no. 25, pp. 1376-1377, Dec. 2005.

[14] M. Cai, O. Painter, and K. J. Vahala, "Observation of critical coupling in a fiber taper to a silica-microsphere whispering-gallery mode system," *Phys. Rev. Lett.*, vol. 85, no. 1, pp. 74-77, Jul. 2000.

Chapter 5– Femtosecond waveguide inscription in Erbium-doped oxyfluoride-silicate glass and crystalline $LiNbO_3$

5.1 Introduction

The following chapter describes work conducted on the fabrication of embedded waveguide structures in Er-doped oxyfluoride-silicate glass and crystalline $LiNbO_3$ using femtosecond waveguide inscription (FWI). FWI is a relatively new fabrication technique that allows three dimensional waveguide structures to be directly written inside transparent dielectric materials. As such, FWI is of high interest for fabricating novel photonic devices not possible using standard photolithography based techniques.

The structure of this chapter is as follows. Firstly, in section 5.2, the basic principles and physics of FWI are described and discussed. After this description, sections 5.3 and 5.4, describe two studies of FWI in Er-doped oxyfluoride-silicate glass. Finally, in section 5.5, a preliminary study of FWI in z-cut crystalline $LiNbO_3$ is presented.

5.2 Femtosecond waveguide inscription

When a photon is incident on a dielectric material, the photon may either be absorbed, scattered or transmitted. If the frequency of the photon is high enough, its energy may exceed the material band gap, or energy necessary to break or create new bonds. These processes can, in turn, result in a modification of the material refractive index through changes in either or both the material absorption spectrum [1] or density [2]. One particularly important application of this phenomena is the inscription of fibre Bragg gratings (FBGs) using UV light [3].

The photo-induced refractive index modification of dielectric materials by UV light has been well studied over the last 30 years. In contrast however, the refractive index modification of dielectric materials using radiation well below the material bandgap is a much less studied phenomenon. Although the exact mechanisms involved in the refractive index modification are still unclear, it is clear that multi-photon absorption plays an important role. Since the energy of individual visible and near-IR photons is low, optical energy can only be deposited in the material by means of multi-photon ionisation, tunnelling ionisation and avalanche ionisation [4,5]. It is currently believed that once optical energy is deposited in the material in the form of free electrons, energy is then rapidly transferred to the ions in the form of heat. It is postulated that the high temperatures and pressures generated can readily change the material structure, resulting in a refractive index modification [6]. Due to the highly nonlinear nature of the light-matter interaction, the refractive index modification can only be induced by focussing ultrashort pulses inside the material. One particularly exciting application of this phenomenon is the ability to directly inscribe subsurface optical waveguides in many transparent dielectric materials by translating the material through the focus [7]. The rest of this section will describe the FWI process in more detail.

5.2.1 Waveguide inscription geometries

As described previously, nonlinear absorption of sub band-gap photons can induce a highly localised refractive index modification of a dielectric material. This modification can be used to fabricate optical waveguides by translating the material through the focus. As shown in Figure 5-1, the sample can either be translated along the direction of propagation of the laser beam (z-axis), this is known as the longitudinal writing (LW) geometry, or perpendicular to the direction of propagation of the laser beam (x-y plane), this is known as the transverse writing (TW) geometry [8].

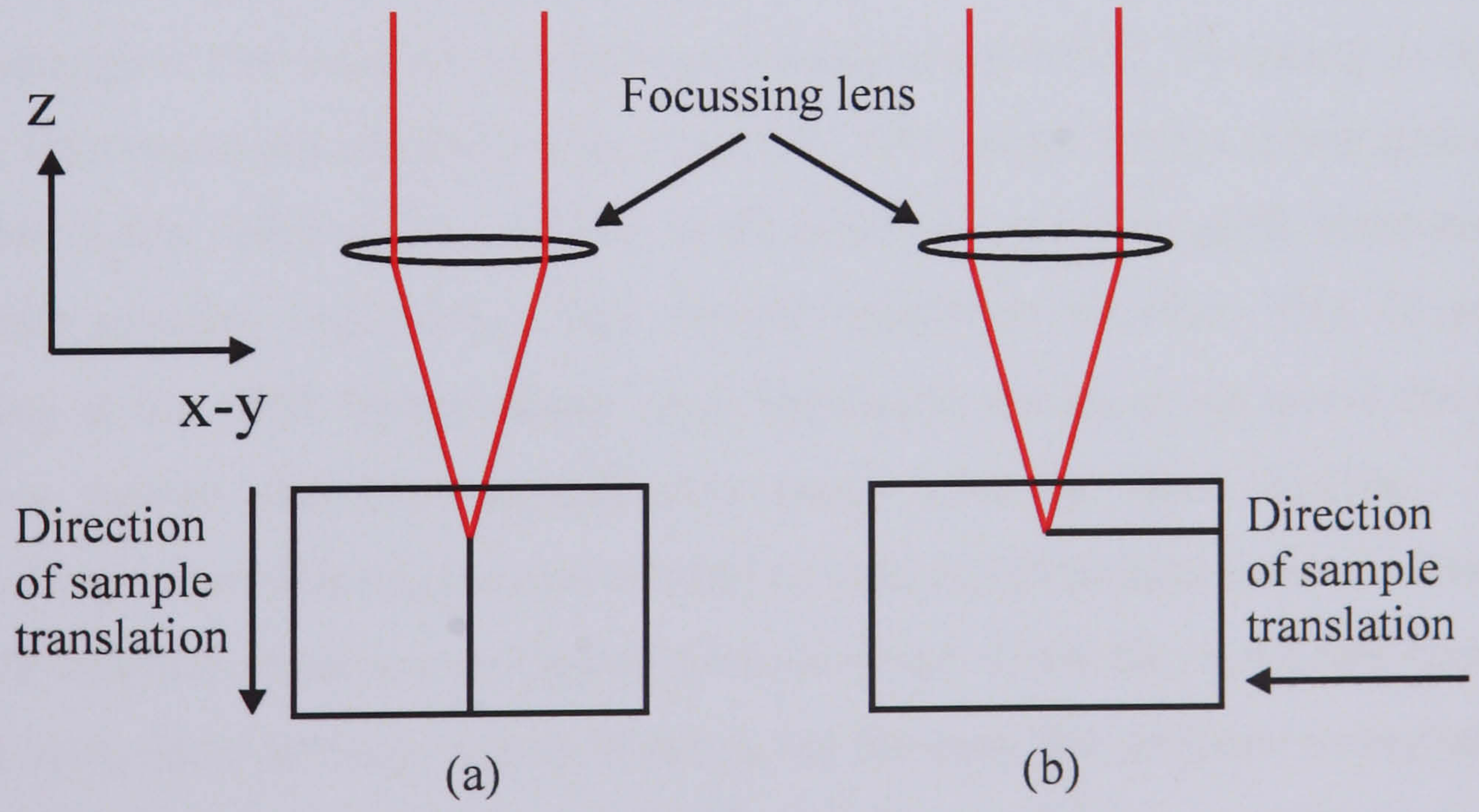

Figure 5-1 Diagram showing (a) the longitudinal writing (LW) geometry and (b) the transverse writing (TW) geometry.

Although the LW geometry has the advantage that the waveguide cross section is inherently circular due to the rotational symmetry of the laser beam, the maximum waveguide length is limited by the working distance of the lens. Consequently, the vast majority of current research is centred on the TW geometry since it allows waveguides of arbitrary length and path to be fabricated.

5.2.2 Fabrication regimes

The exact mechanisms involved in the femtosecond refractive index modification are not yet fully understood. The present consensus is that there are two distinct fabrication regimes; the high repetition rate (HRR) regime using lasers with repetition rates greater than ≈ 1 MHz, and the low repetition rate (LRR) regime using lasers with repetition rates less than ≈ 1 MHz [8-10]. In the following section, brief descriptions of the physical processes that underlie each of these regimes will be given, together with the advantages and disadvantages of each.

Since the amount of time required for heat to diffuse away from the focal region is ≈1 μs [11], using lasers operating in the HRR regime allows the significant build up of heat in the focal region. It is currently thought that this heating results in highly localised thermal annealing of the substrate material at the focus and that the induced refractive index change is the result of non-uniform resolidification [12]. Operating in the HRR regime has several process advantages over the LRR regime. Since the heat generated at the focal region diffuses away equally in all directions, the waveguide cross section is inherently circular, regardless of the sample translation direction [11]. In addition, operating in the HRR regime allows rapid translation speeds of up to ≈ 1 $cm.s^{-1}$, and does not require expensive amplification stages after the laser oscillator. Writing waveguides in the HRR regime also exhibits several disadvantages however. Firstly, the possible substrate materials are limited to those which allow the significant conduction of heat away from the focal region. If this is not the case, the resultant waveguide cross section is too small for fabricating telecommunications devices operating at 1550 nm. Further, the low pulse energies (nJ) available from laser oscillators require tight focussing using immersion lenses to initiate the nonlinear absorption process. Due to the small working distances of these lenses (≈ 100 μm), operating in the HRR regime does not allow the full three dimensional writing capability of FWI to be utilised.

By fabricating waveguides in the LRR regime the time between pulses is too long to allow the build up of heat in the focal region. Consequently, thermal accumulation and diffusion does not play a significant role in the refractive index modification. Because it is the electric field strength and not thermal effects that dominate in the LRR regime, the cross sectional shape of the waveguide is directly related to the distribution of the electric field in and around the focus. For waveguides written in the LRR regime using a LW geometry, the waveguide cross section is inherently circular due to the rotational symmetry of the laser beam. In this case, the cross sectional size of the waveguide is closely related to the focussed beam waist. For waveguides written in the LRR regime using a TW geometry however, the shape of the waveguide cross section is determined by the distribution of the electric field in either the z-x plane for waveguides written along the y-axis, or the z-y plane for waveguides written along the x-axis. Consequently, the size of the waveguide along the z-axis is closely related to the confocal parameter of the focussed beam, whereas the size of the waveguide along either the x or y-axis is closely related to the focussed beam waist.

To investigate how the cross sectional symmetry of a waveguide fabricated in the LRR regime using a TW geometry is affected by its size, Equation 5-1 can be used which relates the confocal parameter to the beam waist for a focussed Gaussian beam [13].

$$b = 2z_R = \frac{2\pi\omega_0{}^2}{\lambda}$$

Equation 5-1

where, ω_0 is the focussed beam waist, λ is the wavelength of the light in the medium, z_R is the Rayleigh range and b is the confocal parameter.

Given that the maximum refractive index change for femtosecond inscribed waveguides is ≈ 1 % [10,14], close to that of standard Corning SMF-28 fibre, it is reasonable to conclude that waveguides ≈ 5 μm in width are required for telecommunications device applications operating at 1550 nm. For a typical FWI experimental setup where 800 nm femtosecond pulses from a Ti: Sapphire laser are focussed into a glass material of refractive index 1.5, Equation 5-1 indicates that the waveguide cross section will exhibit an asymmetry ratio of approximately 60 to 1, resulting in a highly asymmetric mode shape and high coupling losses to and from the waveguide. To correct this asymmetry, a number of approaches have been proposed. These include multi-scan waveguide writing [14,15], astigmatic beam focussing [9] and the slit aperture method [16]. All of these techniques have been used successfully to write symmetric waveguides in the LRR regime. Significantly however, only the multi-scan technique allows waveguides of arbitrary cross section and path to be fabricated.

To summarise, each combination of writing geometry with fabrication regime has its advantages and disadvantages. Using lasers operating in the HRR regime together with a TW geometry has the advantage that the waveguide cross section is inherently circular and that the waveguide fabrication time can be very short, but has the disadvantages that only materials with relatively high thermal conductivity can be used, and that immersion lenses must be used to focus the low energy pulses. Using lasers operating in the LRR regime together with a LW geometry has the advantage that the waveguide cross section is inherently circular due to the rotational symmetry of the laser beam, but has the disadvantage that the waveguide length is limited to the working distance of the focussing lens. Using lasers operating in the LRR regime together with a TW geometry is the most flexible combination, allowing waveguides of truly arbitrary path to be fabricated in many different materials. As discussed previously however, this combination does have the disadvantage that the waveguides are highly asymmetric unless corrective steps are taken.

In the following sections, a number of investigations into FWI in Er-doped oxyfluoride-silicate glass and crystalline $LiNbO_3$ are presented.

5.3 Single-scan femtosecond waveguide inscription in Er-doped oxyfluoride silicate glass

Although EDWAs exhibiting impressive performance have recently been fabricated using FWI [17], almost all the work in this area has been conducted using Er-doped phosphate glass substrates. Even though phosphate glasses are excellent hosts for the Er^{3+}-ion, exhibiting high Er^{3+}-ion solubility and broad $^4I_{13/2} \rightarrow {}^4I_{15/2}$ transition lineshapes, other glasses may offer other significant features such as broader and flatter gain spectra or increased structural stability and compatibility. As discussed in Chapter 4, oxyfluoride-silicate glass is a particularly promising host material for future EDWA applications since it combines the attractive spectroscopic properties of a fluoride glass with the structural stability and compatibility of silica [18]. The current and following section of the thesis describes work conducted on FWI in Er-doped oxyfluoride-silicate glass.

As discussed in section 5.2.2, waveguides fabricated in the LRR regime using a TW geometry exhibit a high degree of asymmetry unless corrective steps are taken. Although this was known to be the case, a preliminary study was conducted, firstly to ascertain if oxyfluoride-silicate glass is suitable for FWI, and secondly to investigate how the various fabrication parameters affect the guiding properties of the waveguides. This preliminary study involved the fabrication of a number of waveguides, each using only a single translational scan of the sample through the focus. This section of the thesis describes this *single-scan* waveguide fabrication study.

5.3.1 Single-scan waveguide fabrication - experimental setup and procedure

All waveguides discussed in this chapter were fabricated using a commercially available regeneratively amplified Ti: Sapphire laser system (Spectra Physics-Hurricane) emitting 200 μJ pulses at a repetition rate of 5 kHz. The centre wavelength of the laser was 800 nm. For the single-scan investigations the pulse duration was 250 fs (FWHM). The diameter of the beam at the output of the laser was 5.6 mm at the 1/e point, and the M^2 of the beam was 1.3. As outlined previously, using this laser system places our fabrication setup firmly in the LRR regime. To fabricate the single-scan waveguides, the pulse train was focussed to a depth of ≈ 300 μm below the sample surface using a 0.4 NA, × 20 microscope objective. The sample was mounted on automated Newport ILS linear travel x-y-z translation stages which were controlled using a Newport ESP 300 control module. Figure 5-2 shows a schematic diagram of the FWI experimental setup.

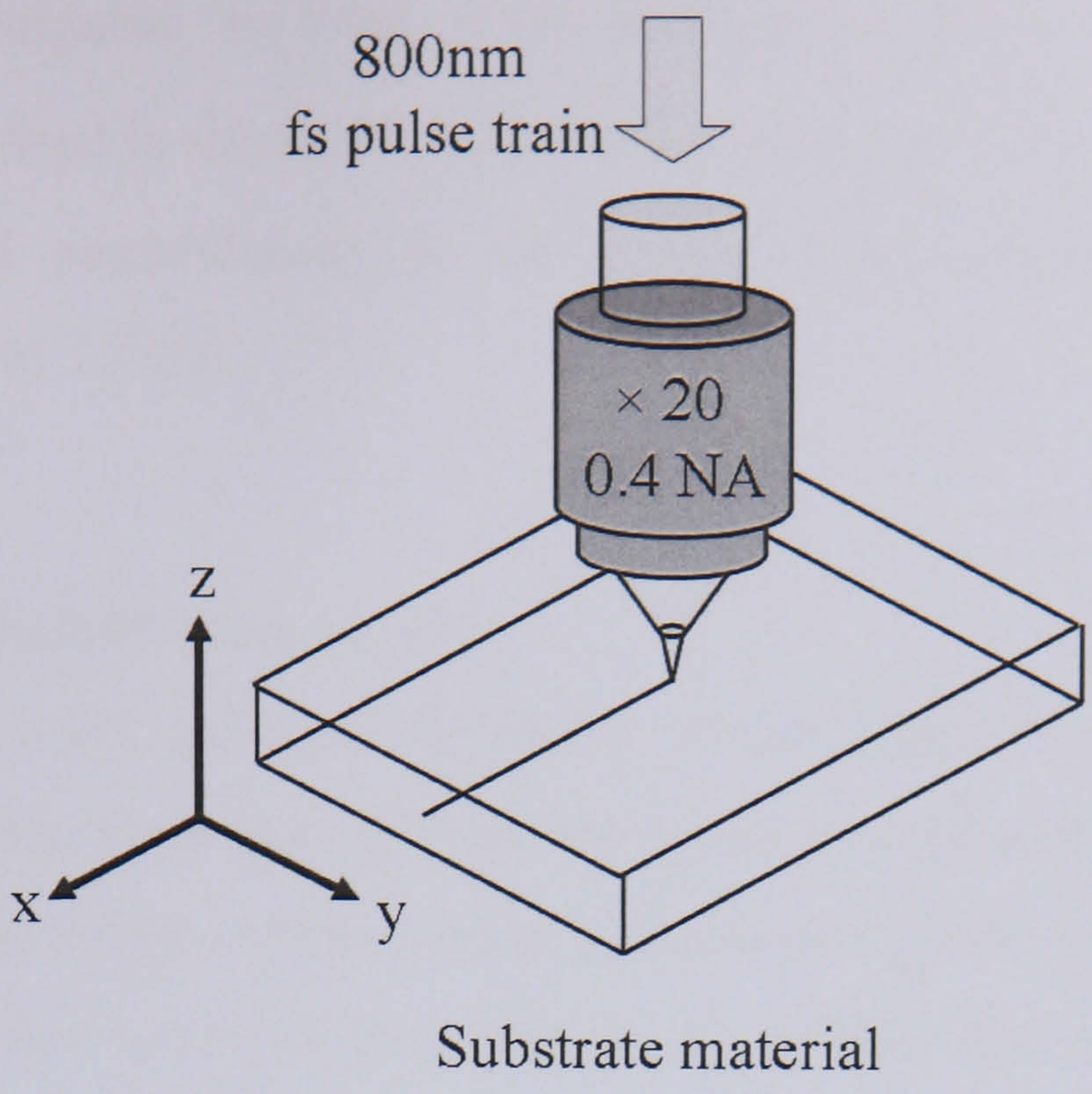

Figure 5-2 Schematic diagram of the FWI experimental setup

The axis shown in Figure 5-2 are consistent throughout this chapter. All waveguides described in this chapter were fabricated by scanning the vertical linear motion stage (which will be referred to as the x-axis). The other stages (z and y) were used only for positioning prior to each x-axis scan. The fabrication laser beam was linearly polarised along the y-axis.

The precursor composition of the substrate glass used in the single-scan investigation was 61 SiO_2-12 Na_2O-3 Al_2O_3-12 LaF_3-12 PbF_2 (mol %) + 1 wt % Er_2O_3. The glass has a density of 3.6 $g.cm^{-3}$ resulting in an erbium concentration of 1.1×10^{20} $ions.cm^{-3}$ [19]. The fabrication and spectroscopic optimisation of this glass is described extensively in [18].

Prior to fabricating the single-scan waveguides discussed in this section, a preliminary investigation was conducted to assess the approximate range of translation speeds and pulse energies that would be most suited to fabricating waveguides that guide 1550 nm light. From these investigations it was found that the confinement of the light in the waveguide increased with decreasing translation speed, and that only waveguides fabricated with pulse energies below 1 μJ showed promise of guiding at 1550 nm. As a result, the single-scan waveguides discussed here were fabricated with the lowest sensible translation speed (2 $\mu m.s^{-1}$), while still allowing a range of pulse energies (0.3 -

0.9 μJ) to be investigated. In total, seven waveguides were fabricated using pulse energies of 0.3 → 0.9 μJ in steps of 0.1 μJ. After waveguide fabrication, the sample was diced and polished perpendicular to the x-axis. After dicing and polishing, the waveguide length was 1.9 cm.

5.3.2 Passive characterisation results

To investigate the cross sectional symmetry of the modified regions, the polished waveguide facets were inspected using an optical microscope operating in transmission mode. Figure 5-3 shows the captured images of the waveguide end facets. The contrast and brightness of Figure 5-3 has been adjusted to increase the clarity of the modified regions.

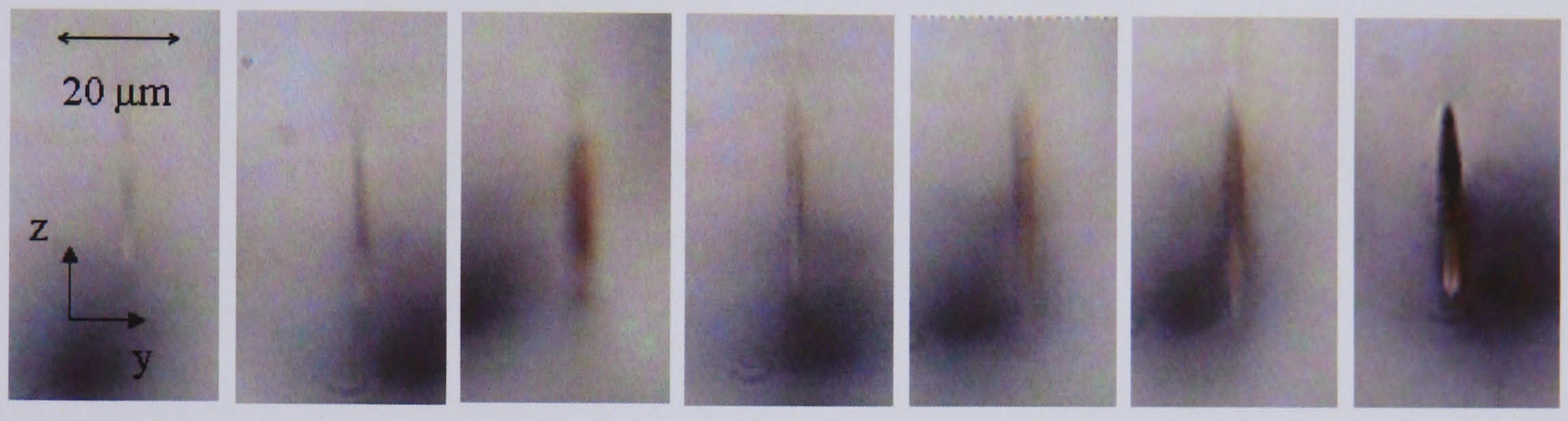

0.3 μJ 0.4 μJ 0.5 μJ 0.6 μJ 0.7 μJ 0.8 μJ 0.9 μJ

Figure 5-3 Transmission mode optical microscope images of the single-scan waveguide end-facets. Below each image is the pulse energy used to fabricate the waveguide.

As can be seen from Figure 5-3, the cross sectional shape of the modified region is highly asymmetric as expected, exhibiting an asymmetry ratio of approximately 1:10. In addition, all waveguides fabricated using pulse energies of 0.5 μJ or higher exhibit some degree of optical damage, as indicated by the darker colour of parts of the modified area.

To investigate the transmission properties of the fabricated waveguides, the waveguide output facet was imaged onto an Electrophysics Micron Viewer 7290-A IR-Vidicon camera while coupling a signal into the waveguide at the other end. Figure 5-4 shows a diagram of the experimental setup used to capture near field images of the waveguide mode.

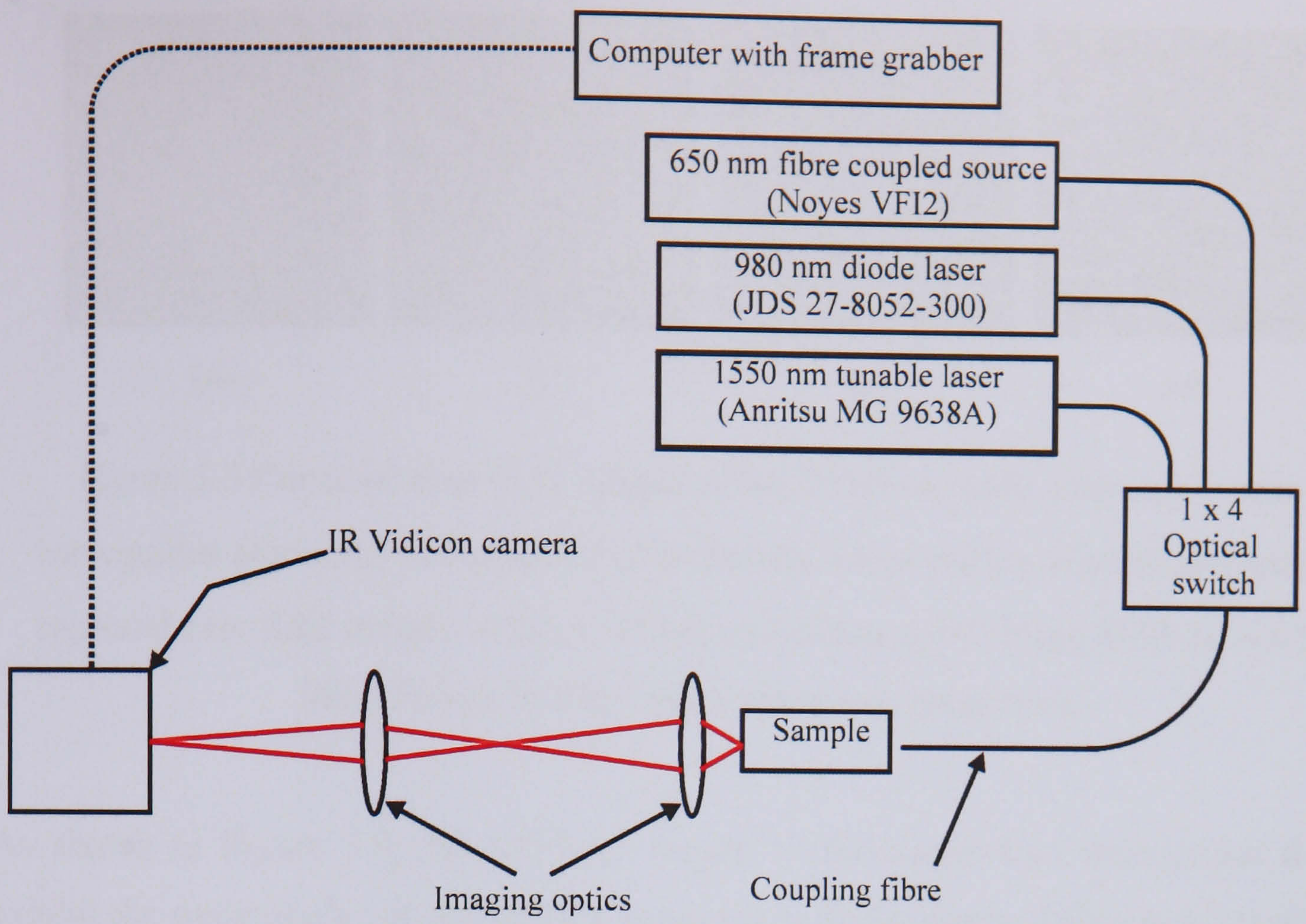

Figure 5-4 Diagram of the experimental setup used to capture near field images of the waveguide mode.

As a result of this investigation, waveguides fabricated using pulse energies of 0.8 and 0.9 μJ were found to only to support a single mode at 1550 nm. Waveguides fabricated with pulse energies of 0.4 → 0.7 μJ were found only to support a single mode at 980 nm. The waveguide fabricated using 0.3 μJ pulses was found to support only a single mode at 980 nm but was multimode at 650 nm. The lack of either a 980 nm mode for waveguides fabricated with 0.8 and 0.9 μJ pulses or a 650 nm mode for waveguides fabricated with 0.4 to 0.9 μJ pulses suggested strong scattering of these wavelengths in these waveguides. Figure 5-5 shows the captured near field images of the 1550 nm mode for the waveguides fabricated using 0.8 and 0.9 μJ pulses. Also shown in Figure 5-5 are the captured near field images of the 1550 nm mode from Corning SMF-28 and 980/1550 nm WDM coupler fibre for comparison.

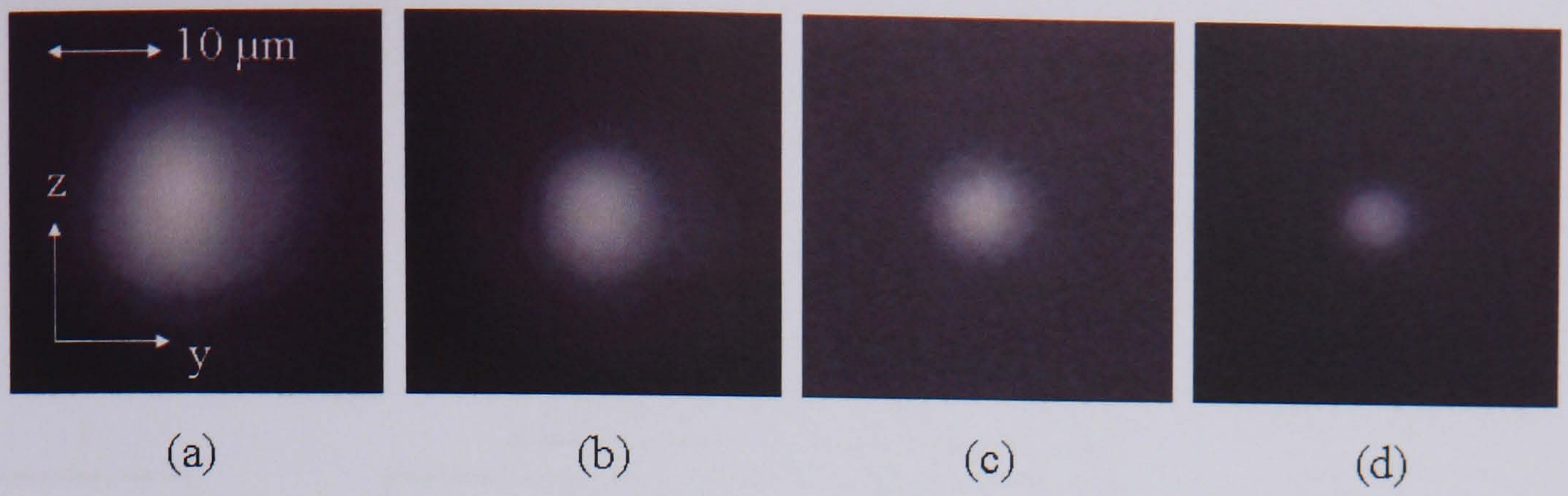

(a) (b) (c) (d)

Figure 5-5 Captured near field images of the 1550 nm mode from single-scan waveguides fabricated using (a) 0.8 μJ pulses (b) 0.9 μJ pulses. Also shown are the captured near field images of the 1550 nm mode from (c) Corning SMF-28 and (d) 980/1550nm WDM coupler fibre for comparison.

As shown in Figure 5-5, the 1550 nm modes of the single-scan waveguides do not exhibit the same degree of asymmetric expected from the shape of the modified regions shown in Figure 5-3. From the image of the facet of the waveguide fabricated using 0.9 μJ pulses shown in Figure 5-3, it can be seen that there is a significant degree of optical damage in the upper region of the modified area. It is possible that the high loss of this region may explain the more symmetric shape of the mode profiles shown in Figure 5-5.

To investigate how the waveguide propagation losses were affected by the fabrication pulse energy, the propagation losses at 650, 980 and 1426 nm were measured using the "streak" technique [20]. As light propagates along a waveguide, some fraction of the light is scattered out of the waveguide in the form of a detectable "streak". Since the intensity of the streak at any point along the waveguide is proportional to the amount of light in the waveguide at that point, the propagation loss of the waveguide can be inferred by measuring the decay of the streak. Figure 5-6 shows a schematic diagram of the experimental setup used to capture images of the streak.

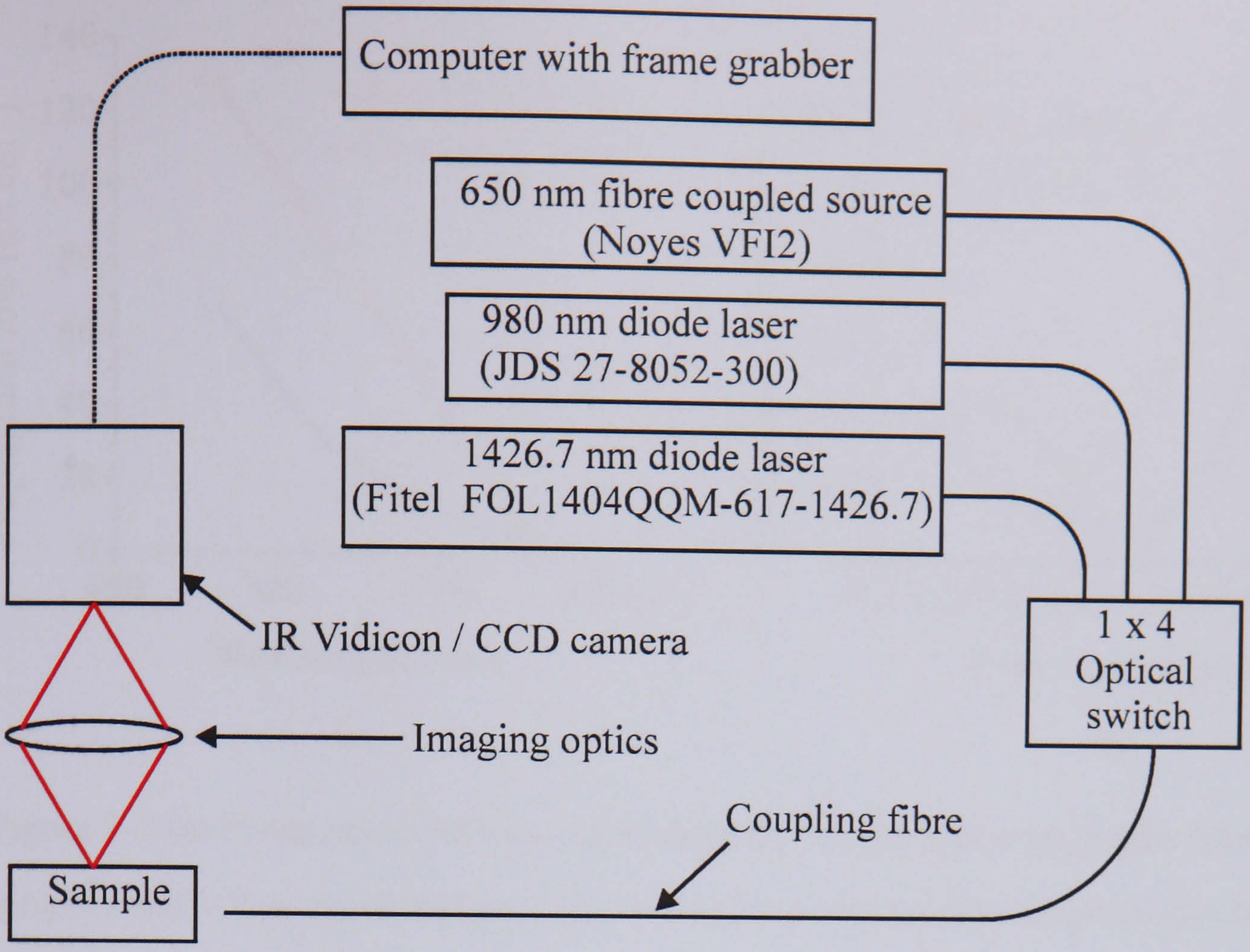

Figure 5-6 Schematic diagram of the experimental setup used to capture images of the scattered streak for propagation loss measurements.

Prior to capturing any streak data, fibre-waveguide coupling of the light was first established and optimised using 1426 nm light for waveguides fabricated using 0.8 μJ and 0.9 μJ pulses, and 980 nm light for all other waveguides. Once coupling had been achieved, streak data at the other wavelengths was obtained without altering the coupling. It was not possible to obtain streak data for the waveguide fabricated using 0.3 μJ pulses because the streak intensity was not high enough due to low scattering.

Figure 5-7 (a) is a plot of propagation loss vs. wavelength for waveguides fabricated using pulse energies of 0.8 and 0.9 μJ. The increase in propagation loss for shorter wavelengths in both waveguides indicates that the propagation loss is dominated by Rayleigh scattering. Figure 5-7 (b) is a plot of propagation loss vs. fabrication pulse energy for all the fabricated waveguides (with the exception of the waveguide fabricated using 0.3 μJ pulses) at both 980 and 650 nm.

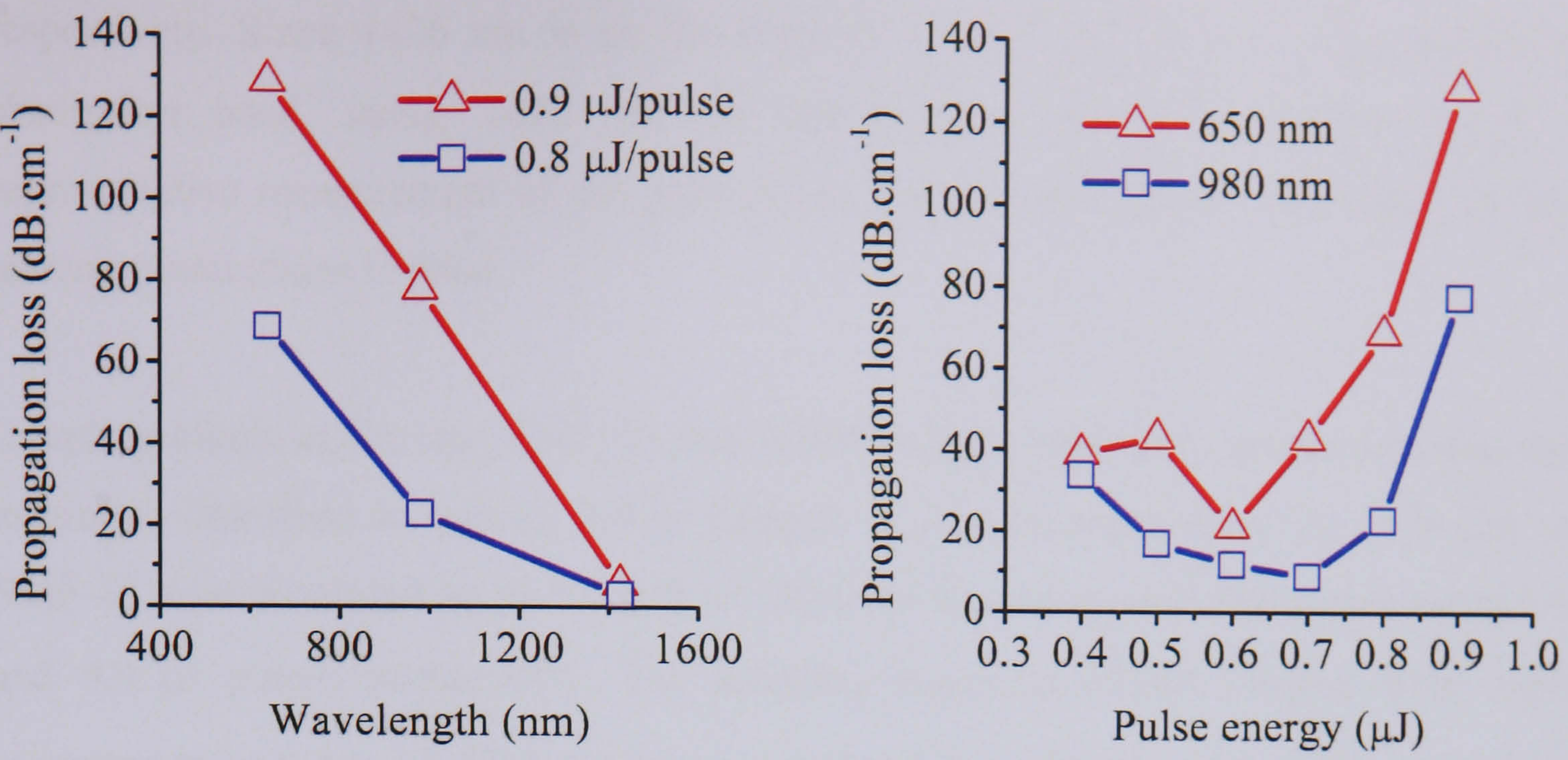

(a) (b)

Figure 5-7 (a) Propagation loss vs. wavelength for single-scan waveguides fabricated using 0.8 and 0.9 µJ pulse energies. (b) Propagation loss vs. fabrication pulse energy at 650 nm and 980 nm. The individual data points in both graphs are connected to increase the clarity of the trends.

From Figure 5-7 (b) it is clear that the loss at 650 nm is consistently higher than the loss at 980 nm, again due to Rayleigh scattering. In Figure 5-7 (b), the loss is observed to increase dramatically for pulse energies greater than 0.7 µJ, possibly due to increased scattering from more pronounced micro-fractures as a result of the increased fabrication pulse energy. It can also be seen that the propagation loss again increases for pulse energies of less than 0.7 µJ, we attribute this to higher radiation losses as result of the smaller refractive index change and lower mode confinement. Error bars have not been included in Figure 5-7 for clarity but are estimated at ≈ ± 40 % for data measured at 650 and 980 nm, and ≈ ± 20 % for data measured at 1426 nm. The high error values are due to noise in the streak data. It is noted that throughout the propagation loss measurements, no consideration was given to the fact that some of the waveguides may have been multimode at 650 nm. This source of error was considered to be insignificant when compared to the magnitude and errors of the measured values. It should also be noted that although both 980 and 650 nm are in Er^{3+}-ion absorption bands and that some of the propagation loss measured at these wavelengths will be due to absorption, again, the magnitude of this absorption is considered to be insignificant when compared to the magnitude and errors of the measured propagation losses. Propagation losses at 1426 nm for waveguides fabricated using 0.8 and 0.9 µJ were 3.2 and 5.6 dB.cm^{-1}

respectively. Since 1426 nm is on the edge of the Er^{3+} ion $^4I_{13/2} \rightarrow {}^4I_{15/2}$ transition absorption band, using 1426 nm for propagation loss measurements gives a representative measurement of the propagation loss as experienced by a signal in the telecommunications C-band.

Coupling losses to Corning SMF-28 and WDM coupler fibre were measured using the technique described in section 3.4 of Chapter 3. The coupling losses at 1550 nm to SMF-28 were measured to be 3.6 and 1.6 dB/facet for waveguides fabricated using 0.8 and 0.9 μJ pulses respectively. The coupling losses to WDM coupler fibre were measured to be 5.4 and 3 dB/facet for waveguides fabricated using 0.8 and 0.9 μJ pulses respectively. The possible error in these values is estimated at ± 0.2 dB due to errors in the alignment of the fibres. From these measurements, it is evident that the coupling losses to and from the waveguide fabricated using 0.8 μJ pulses are consistently higher than for the waveguide fabricated using 0.9 μJ, we believe this to be do to the higher fibre-waveguide mode mismatch evident in Figure 5-5.

Insertion loss measurements for butt-coupling WDM coupler fibres to the waveguides were conducted using the experimental technique described in section 3.4 of Chapter 3. The background insertion loss, measured at 1610 nm, was found to be 15.0 and 18.4 dB for the waveguides fabricated using 0.8 and 0.9 μJ pulses respectively.

The $^4I_{13/2} \rightarrow {}^4I_{15/2}$ transition absorption coefficient in the bulk material was measured throughout the 1550 nm region using a Bruker IFS 66V/S FT-IR spectrometer. The loss due to absorption that a signal experiences after propagation along the un-pumped waveguide was evaluated using this absorption coefficient.

5.3.3 Active characterisation results

Gain characterisation experiments were conducted in the manner described in section 3.4 of Chapter 3. Figure 5-8 (a) shows relative gain spectra measured using either 140 mW of 1490 nm pump or 420 mW of 980 nm pump for the waveguide fabricated using 0.9 μJ pulses. Figure 5-8 (b) shows relative gain vs. pump power characteristics for the same waveguide using either 1490 or 980 nm pumping. The waveguide fabricated using

0.9 μJ pulses displayed a slightly higher level of relative gain compared to the waveguide fabricated using 0.8 μJ pulses.

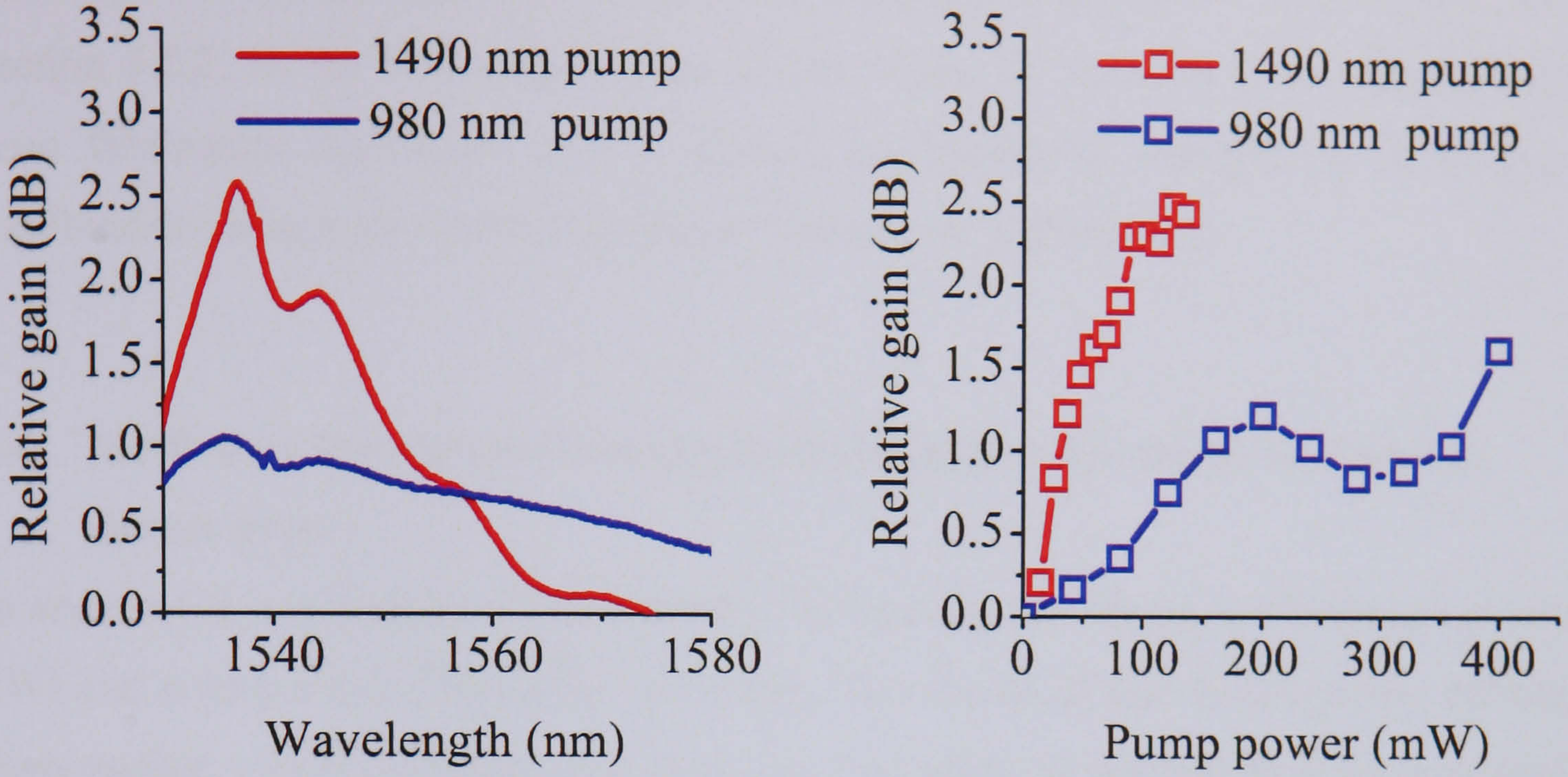

Figure 5-8 (a) Relative gain spectra obtained using either 140 mW of 1490 nm pump or 420 mW of 980 nm pump. (b) Relative gain vs. pump power characteristics (measured at the peak of the relative gain spectrum) using either 1490 or 980 nm pumping. Both (a) and (b) were obtained from the same single-scan waveguide fabricated using 0.9 μJ pulses

As discussed in Chapter 3, a saturated peak relative gain of approximately twice the peak absorption would be expected for a complete population inversion. According to the FT-IR measurements, the peak absorption coefficient for the $^4I_{15/2} \rightarrow {}^4I_{13/2}$ transition was 3.73 dB.cm^{-1}. Consequently, it is concluded that a peak absorption of 7 dB is present in these waveguides and as a result, a saturated peak relative gain of ≈ 14 dB would be expected if a complete population inversion were obtained. As shown in Figure 5-8, it has not been possible to induce a population inversion in the single-scan waveguides. It is concluded that the most probable reasons for this are the high waveguide-fibre coupling losses and high propagation losses.

5.3.4 Conclusions from single-scan investigations

From the results of the single-scan waveguide investigations it is clear that in terms of minimising the waveguide insertion loss, there is a trade off between achieving low coupling and radiation losses by using higher pulse energies, and achieving low scattering losses by using low pulse energies. We conclude therefore that to fabricate higher quality waveguides, exhibiting lower propagation losses *and* lower coupling losses, it is necessary to use a fabrication technique that allows the cross sectional size and shape of the waveguide to be controlled independently of the limits discussed in section 5.2.2. In the following section of the thesis, the recently demonstrated *multi-scan* fabrication technique [14] is applied to fabricating waveguides in Er-doped oxyfluoride-silicate glass with significantly improved performance.

5.4 Multi-scan femtosecond waveguide inscription in Er-doped oxyfluoride silicate glass

In section 5.3, waveguides were fabricated in Er-doped oxyfluoride-silicate glass using FWI and a single-scan fabrication technique. The results of this investigation, although encouraging, clearly indicated that steps must be taken to address both the waveguide cross section asymmetry and high propagation losses. In this section of the thesis, the recently demonstrated *multi-scan* fabrication technique proposed by Nasu et al [14] is applied to fabricating waveguides in Er-doped oxyfluoride-silicate glass.

In the multi-scan technique, the waveguide cross section is not directly determined by the distribution of the electric field in the focal region. Instead, the desired waveguide cross section is constructed by creating many lines of modified material shifted slightly relative to each other, as shown in Figure 5-9.

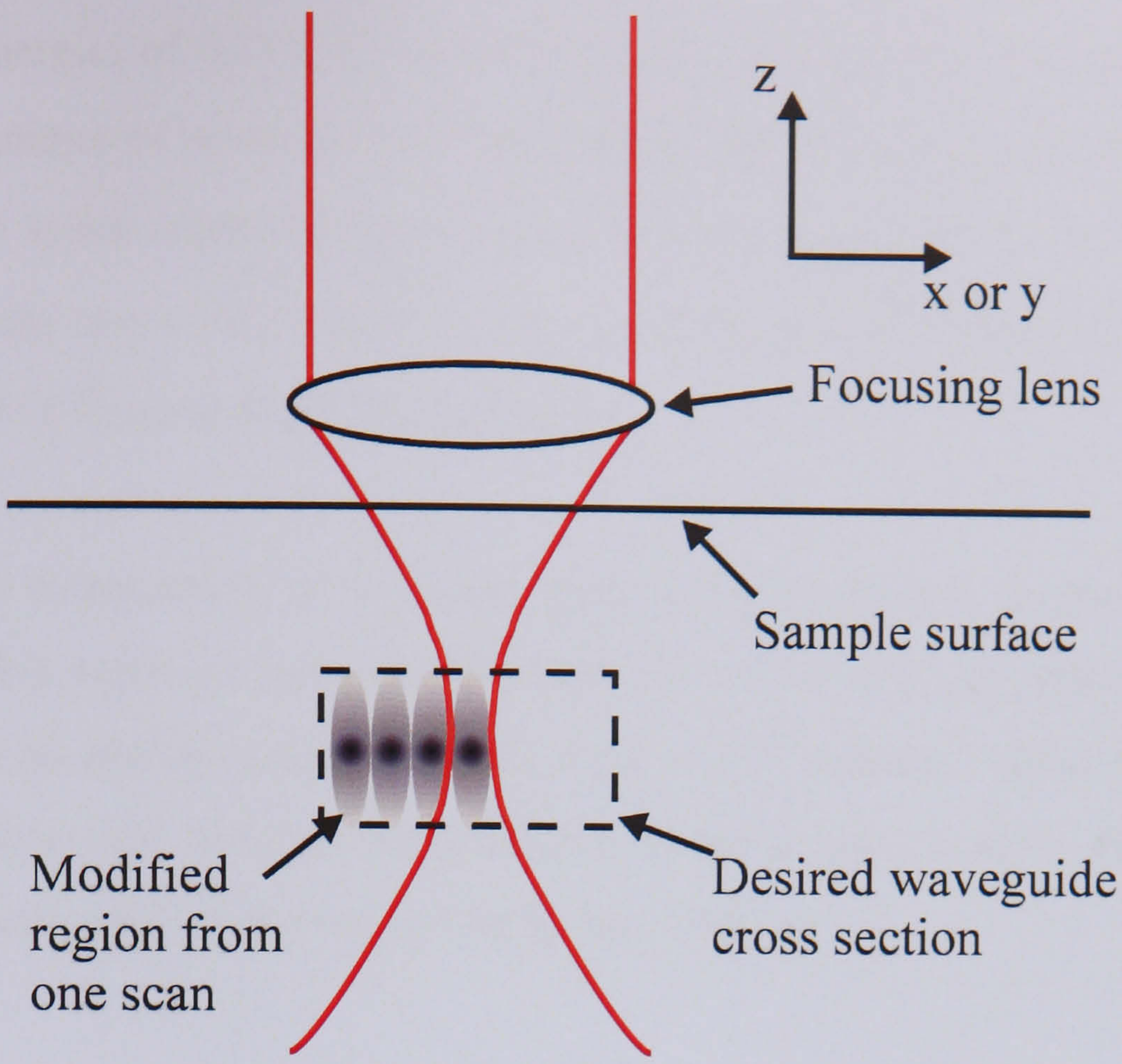

Figure 5-9 Diagram showing how the desired waveguide cross section can be constructed using the multi-scan fabrication technique.

As discussed by Nasu et al [14], the height of the waveguide along the z-axis can be controlled by varying the pulse energy, whereas the width of the waveguide along either the x or y-axis and refractive index contrast can be controlled by varying the number of and distance between individual scans. Consequently, the desired waveguide cross section can be controlled independently of the shape of the focal region.

5.4.1 Multi-scan waveguide fabrication - experimental setup and procedure

Multi-scan waveguides were fabricated using the same experimental setup described in section 5.3.1. For the multi-scan study however, the pulse duration was 130 fs (FWHM). All multi-scan waveguides were fabricated using a translation speed of 50 $\mu m.s^{-1}$.

Prior to fabricating the waveguides discussed in this section, a preliminary investigation was conducted to assess what range of pulse energies would be most suited to fabricating multi-scan waveguides using our experimental setup. As a result of this investigation, it was found that the threshold energy for optical damage lay between 0.4 and 0.53 μJ. Consequently, the waveguides discussed in this section were fabricated using pulse energies of 0.225, 0.3, 0.4 and 0.5 μJ. In order to investigate the effect of varying the number of scans on the waveguide properties, waveguides were fabricated using both 40 scans separated by 0.21 μm and 20 scans separated by 0.43 μm. The distance between scans was chosen in order to fabricate a waveguide 8.2 μm wide, the same diameter as Corning SMF-28 fibre core.

The precursor composition of the glass used in the multi-scan investigation was 61 SiO_2-12 Na_2O-3 Al_2O_3-12 LaF_3-12 PbF_2 (mol %) + 1 wt % Er_2O_3, resulting in a glass substrate with an erbium concentration of $\approx 1.1 \times 10^{20}$ ions.cm^{-3}. After fabrication, the sample was diced and polished perpendicular to the x-axis shown in Figure 5-2. The waveguide length after dicing and polishing was 1.85 cm.

5.4.2 Passive characterisation results

To investigate the cross sectional shape of the multi-scan waveguides, the polished facets of the waveguides were inspected using an optical microscope operating in transmission mode. Figure 5-10 shows the captured images of the multi-scan waveguide end facets. The contrast and brightness of Figure 5-10 has been adjusted to increase the clarity of the modified regions.

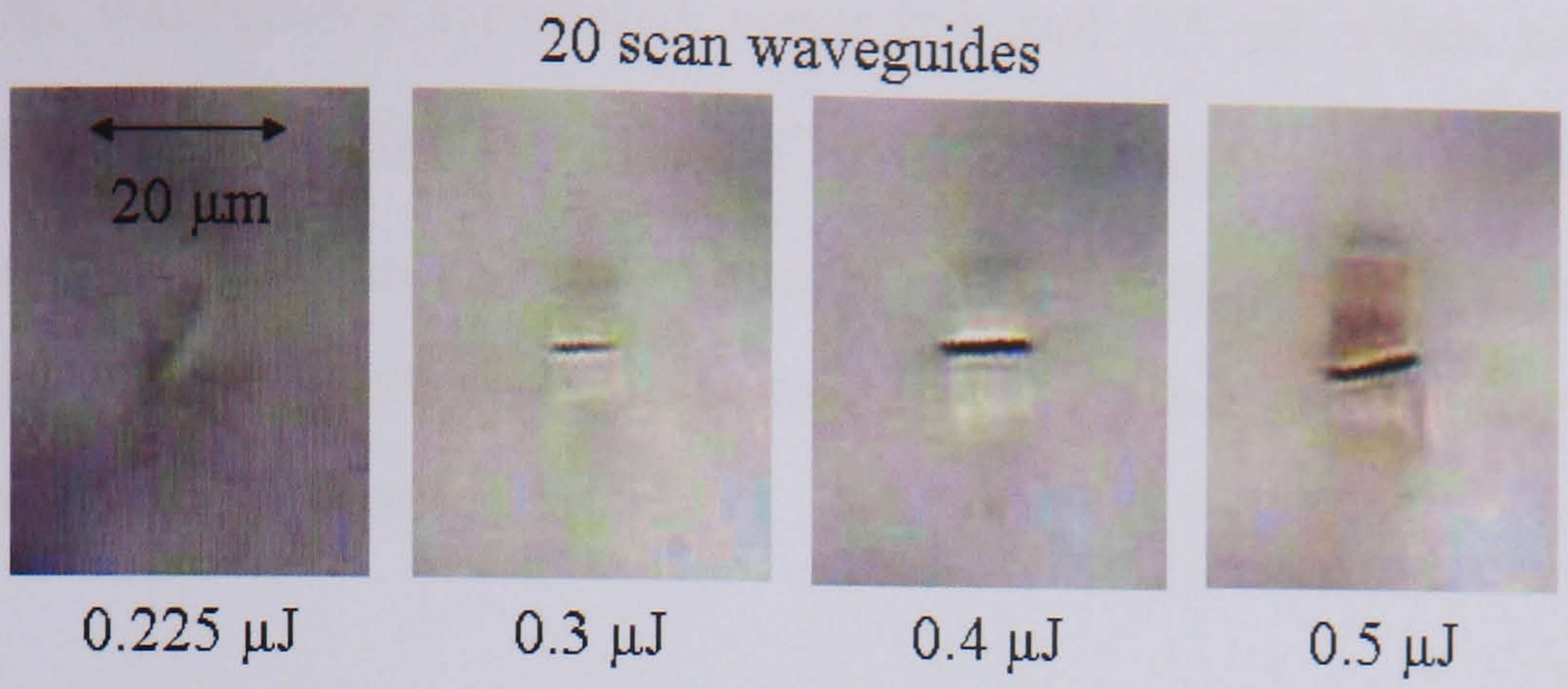

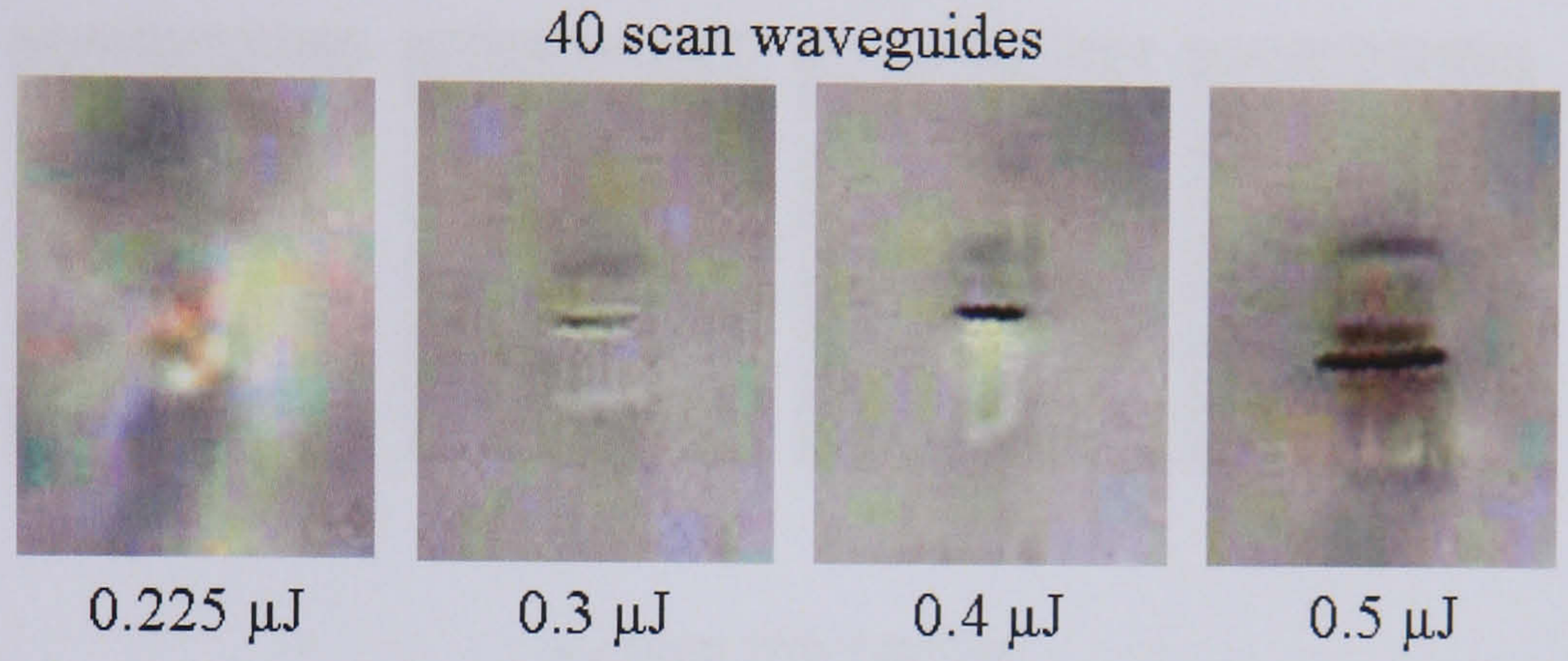

Figure 5-10 Transmission mode optical microscope images of the polished end facets of the multi-scan waveguides. Below each image is the pulse energy used to fabricate the waveguide.

As shown in Figure 5-10, the multi-scan waveguides exhibit a significantly more symmetric cross section than the single-scan waveguides described in section 5.3. As expected from the preliminary multi-scan investigations, a threshold pulse energy between 0.4 and 0.5 µJ exists, above which optical damage is evident throughout the modified region. Currently, the origin of the dark horizontal line apparent in all waveguides fabricated using pulse energies of 0.3 µJ or greater is unknown. It is possible that it could be optical damage but as will be outlined shortly, low propagation losses were measured in some of these waveguides, suggesting the degree of optical damage is low.

The guiding properties of the multi-scan waveguides were investigated in the same manner as for the single-scan waveguides. Consequently, all multi-scan waveguides were observed to guide 1550 nm light to some degree, with waveguides fabricated using higher pulse energies either confining the light more tightly or exhibiting multimode confinement. Figure 5-11 shows the captured near field images of the 1550 nm mode for the multi-scan waveguides. It was not possible to excite only the fundamental mode for the 40 scan waveguides fabricated using 0.4 and 0.5 μJ pulses or the 20 scan waveguide fabricated using 0.5 μJ pulses. The fact that multimode confinement occurs in waveguides fabricated using lower energy pulses for the 40 scan waveguides compared to the 20 scan waveguides indicates that a larger refractive index change has been induced for 40 scan waveguides.

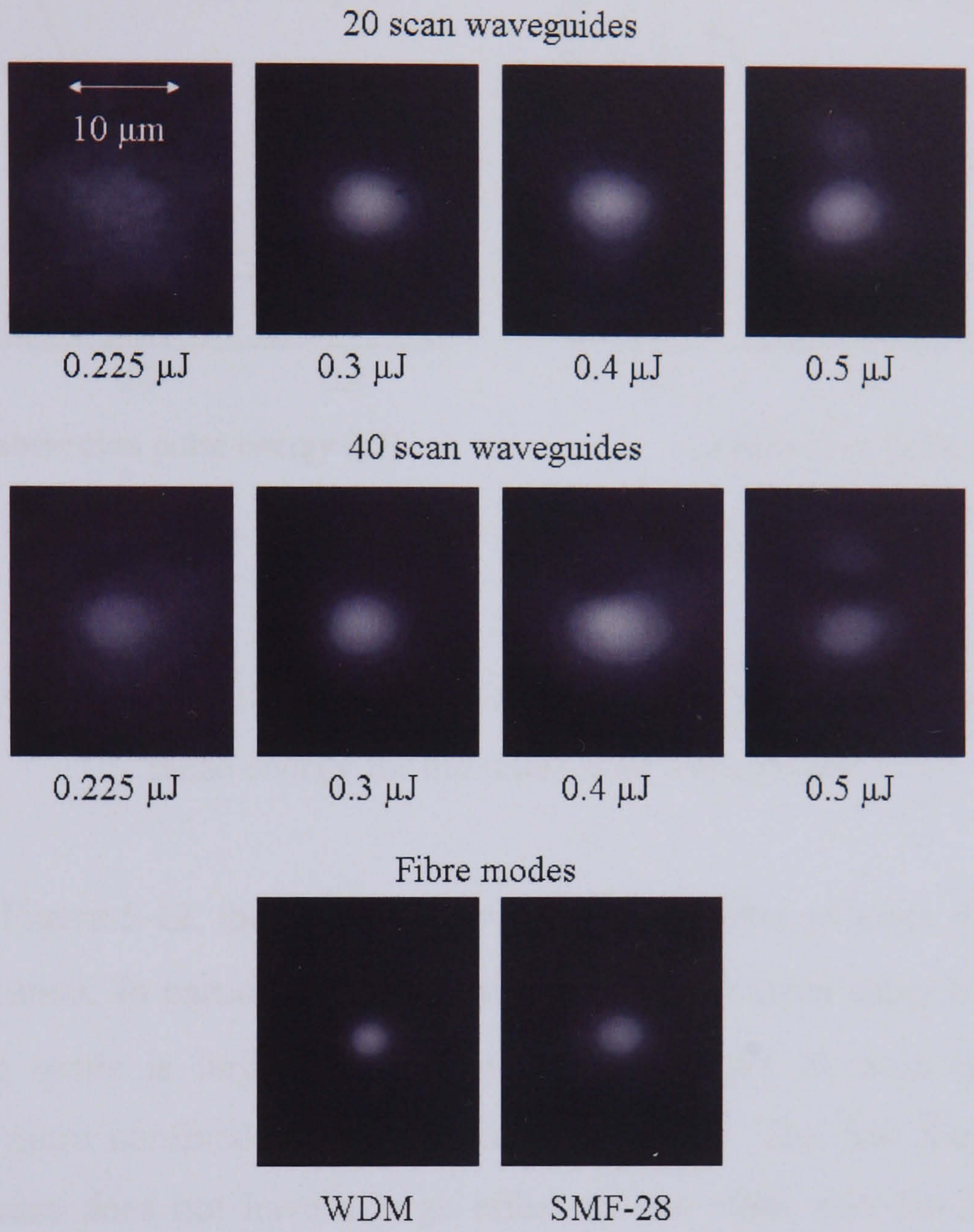
20 scan waveguides

0.225 μJ 0.3 μJ 0.4 μJ 0.5 μJ

40 scan waveguides

0.225 μJ 0.3 μJ 0.4 μJ 0.5 μJ

Fibre modes

WDM SMF-28

Figure 5-11 Near field images of the 1550 nm mode from the multi-scan waveguides. Below each image is the pulse energy used to fabricate the waveguide. Also shown are the near field images of the 1550 nm mode from WDM coupler fibre and Corning SMF-28 for comparison.

As shown in Figure 5-11, both 20 and 40 scan waveguides fabricated using 0.3 μJ pulses exhibit 1550 nm modes that are close to circular and comparable in size to the 1550 nm mode of SMF-28. To investigate this further, the $1/e^2$ mode field diameter (MFD) was measured for each waveguide. Figure 5-12 is a plot of the $1/e^2$ MFD as a function of fabrication pulse energy for each of the multi-scan waveguides that exhibited single mode transmission.

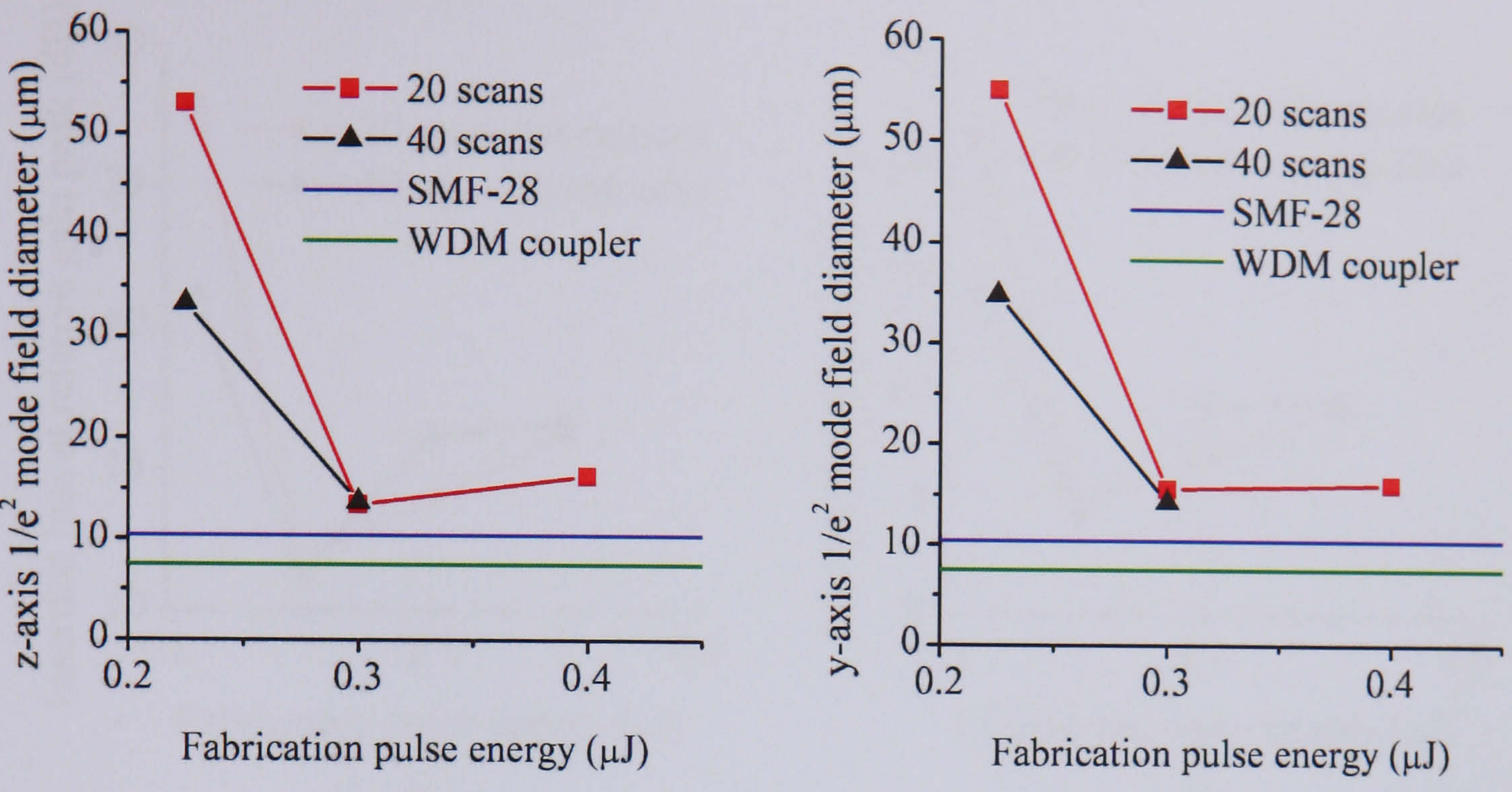

(a) (b)

Figure 5-12 (a) z-axis and (b) y-axis 1550 nm $1/e^2$ mode field diameter vs. fabrication pulse energy for the multi-scan waveguides

As shown in Figure 5-12, the effect of increasing the number of scans from 20 to 40 is small but apparent. In particular, for the waveguides fabricated using 0.225 μJ pulses, the 1550 nm mode is large and close to cut-off in the 20 scan waveguide, but significantly more confined in the 40 scan waveguide. The fact that doubling the number of scans does not have a large effect on the mode size for the waveguides fabricated using 0.3 μJ pulses indicates that the photo-induced refractive index change is close to saturation.

Insertion loss, coupling loss and propagation loss measurements were conducted in the same manner as for the sol-gel waveguides described in Chapter 3. All experiments were performed by butt-coupling SMF-28 fibres to the waveguide. The results of these experiments are shown in Figure 5-13. As with the single scan waveguides, the ${}^4I_{13/2} \rightarrow {}^4I_{15/2}$ transition absorption coefficient in the bulk material was measured using a Bruker IFS 66V/S FT-IR spectrometer. The loss due to absorption that a signal experiences after propagation along the unpumped waveguide was evaluated using this absorption coefficient. The loss due to absorption at the peak of the relative gain spectrum (1537 nm) was measured to be 6.9 dB for the 1.85 cm long sample (3.73 dB.cm^{-1})

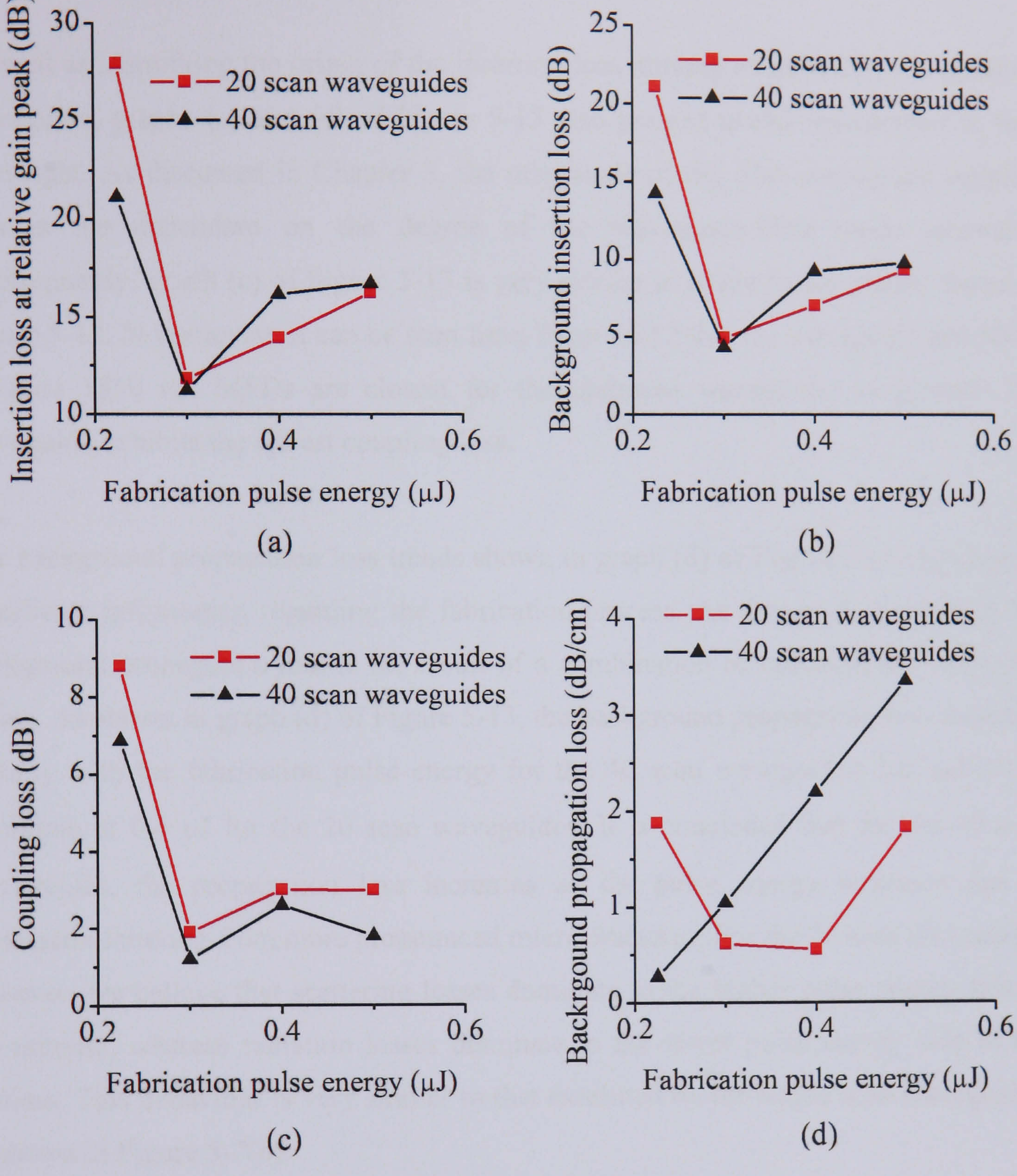

(a) (b)

(c) (d)

Figure 5-13. (a) Insertion loss at relative gain peak vs. fabrication pulse energy, (b) background insertion loss vs. fabrication pulse energy, (c) coupling loss vs. fabrication pulse energy (d) Background propagation loss vs. fabrication pulse energy. All graphs are for the multi-scan waveguides. All experiments were performed by butt-coupling SMF-28 fibres to the waveguide

From Figure 5-13 (b) it can be seen that the background insertion loss reaches a minimum value of 4.3 dB for the 40 scan waveguide fabricated using 0.3 μJ pulses. The origin of this minimum is apparent from graphs (c) and (d) in Figure 5-13, where it can be seen that the optimum waveguide exhibits not only the lowest coupling loss, but also one of the lowest propagation losses.

As well as identifying the origin of the insertion loss minima exhibited by the optimum waveguide, graphs (c) and (d) of Figure 5-13 also present useful information in their own right. As discussed in Chapter 3, the magnitude of the fibre-waveguide coupling loss is the dependent on the degree of the waveguide-fibre mode mismatch. Consequently, graph (c) of Figure 5-13 is very similar in shape to the graphs shown in Figure 5-12. In particular, it can be seen from Figure 5-12 that the waveguide and SMF-28 fibre 1550 nm MFDs are closest for the optimum waveguide, as a result this waveguide exhibits the lowest coupling loss.

The background propagation loss trends shown in graph (d) of Figure 5-13 also display significant information regarding the fabrication process. As discussed previously, the background propagation loss is the result of a combination of radiation and scattering losses. As shown in graph (d) of Figure 5-13, the background propagation loss increases linearly with the fabrication pulse energy for the 40 scan waveguides, but exhibits a minimum at 0.4 μJ for the 20 scan waveguides. It is concluded that for the 40 scan waveguides, the propagation loss increases as the pulse energy increases due to increased scattering from more pronounced micro-fractures. For the 20 scan waveguides however, we believe that scattering losses dominate to the higher pulse energy side of the minima, whereas radiation losses dominate to the lower pulse energy side of the minima. This behaviour is very similar to that exhibited by the single scan waveguides, as shown in Figure 5-7(b).

To investigate if waveguide birefringence was significant in the multi-scan waveguides, the PDL of optimum waveguide was measured in the same manner described in Chapter 4. The PDL was measured to be 0.4 dB at 1550 nm, thus indicating that waveguide birefringence is not a significant problem for waveguides fabricated using this material and fabrication technique.

5.4.3 Active characterisation results

Gain characterisation experiments were conducted using the experimental setup shown in Figure 5-14. Using this experimental setup, it was possible to pump the waveguide under test with up to 412 mW of 980 nm and up to 243 mW of 1480 nm, both in a bi-directional pumping scheme with a 50:50 directional splitting ratio.

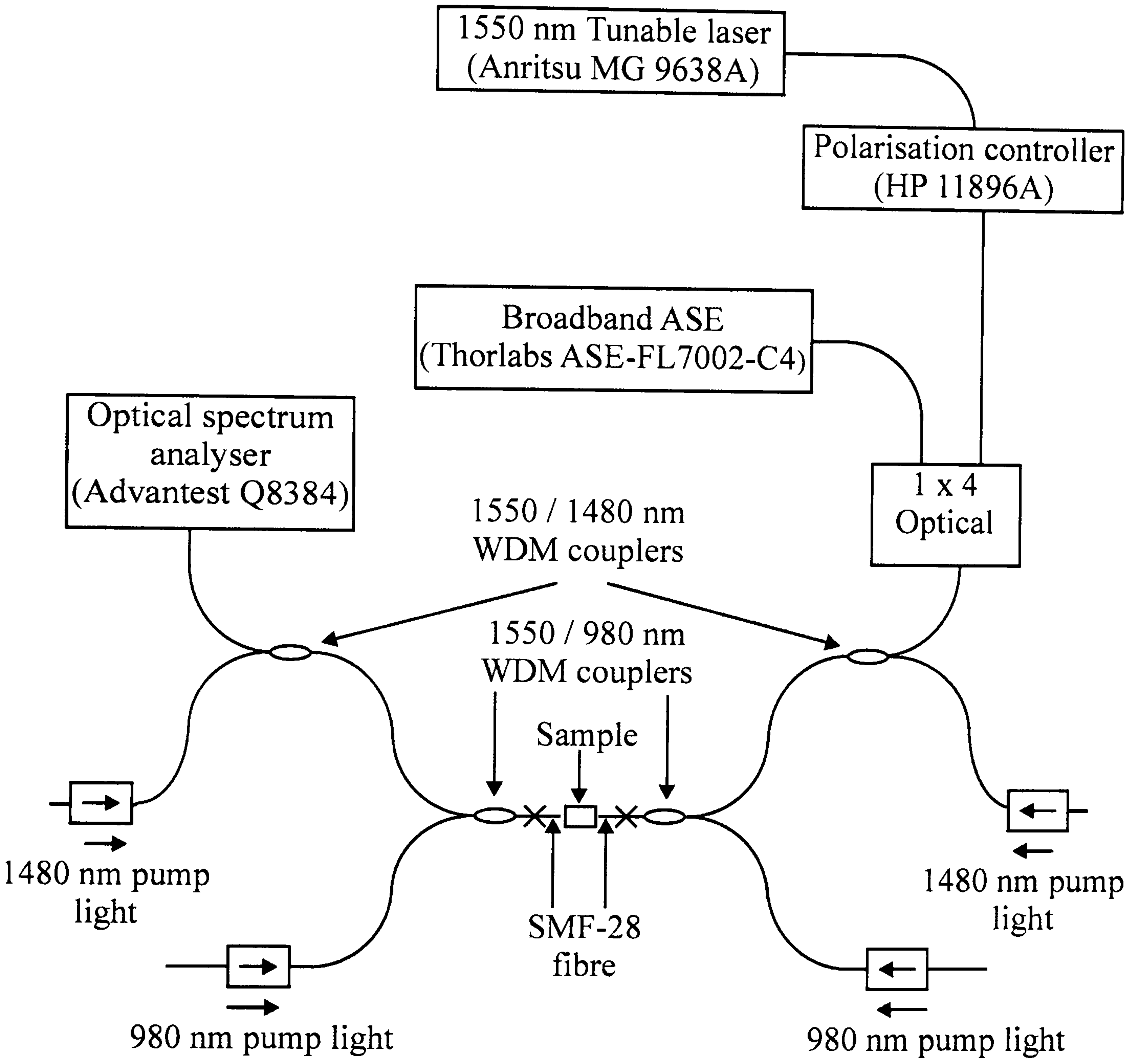

Figure 5-14 Experimental setup used to characterise the gain operation of the multi-scan waveguides.

When pumping all lower insertion loss multi-scan waveguides at 980 and 1480 nm, clear green upconversion emission was visible along the entire length of the waveguide. Figure 5-15 is a photograph of the optimum waveguide under maximum pumping at both wavelengths. The consistency and homogeneity of the green upconversion along the entire length of the waveguide confirms the quality of the fabricated waveguide.

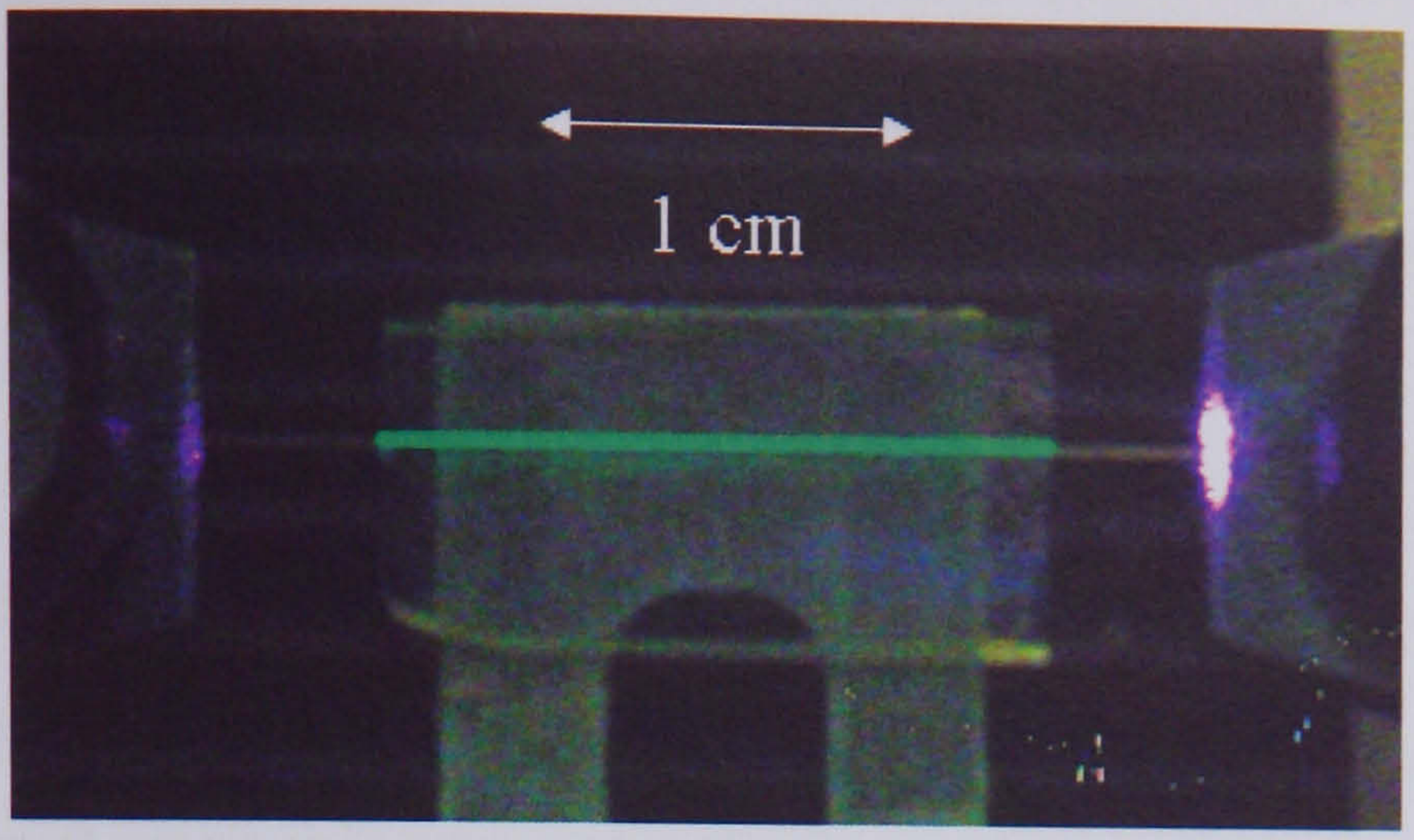

Figure 5-15 Green upconversion from the optimum multi-scan waveguide when bi-directionally pumped under maximum pump power at both 980 and 1480 nm.

Figure 5-16 shows the results of the relative gain spectrum and relative gain vs. pump power characterisation experiments.

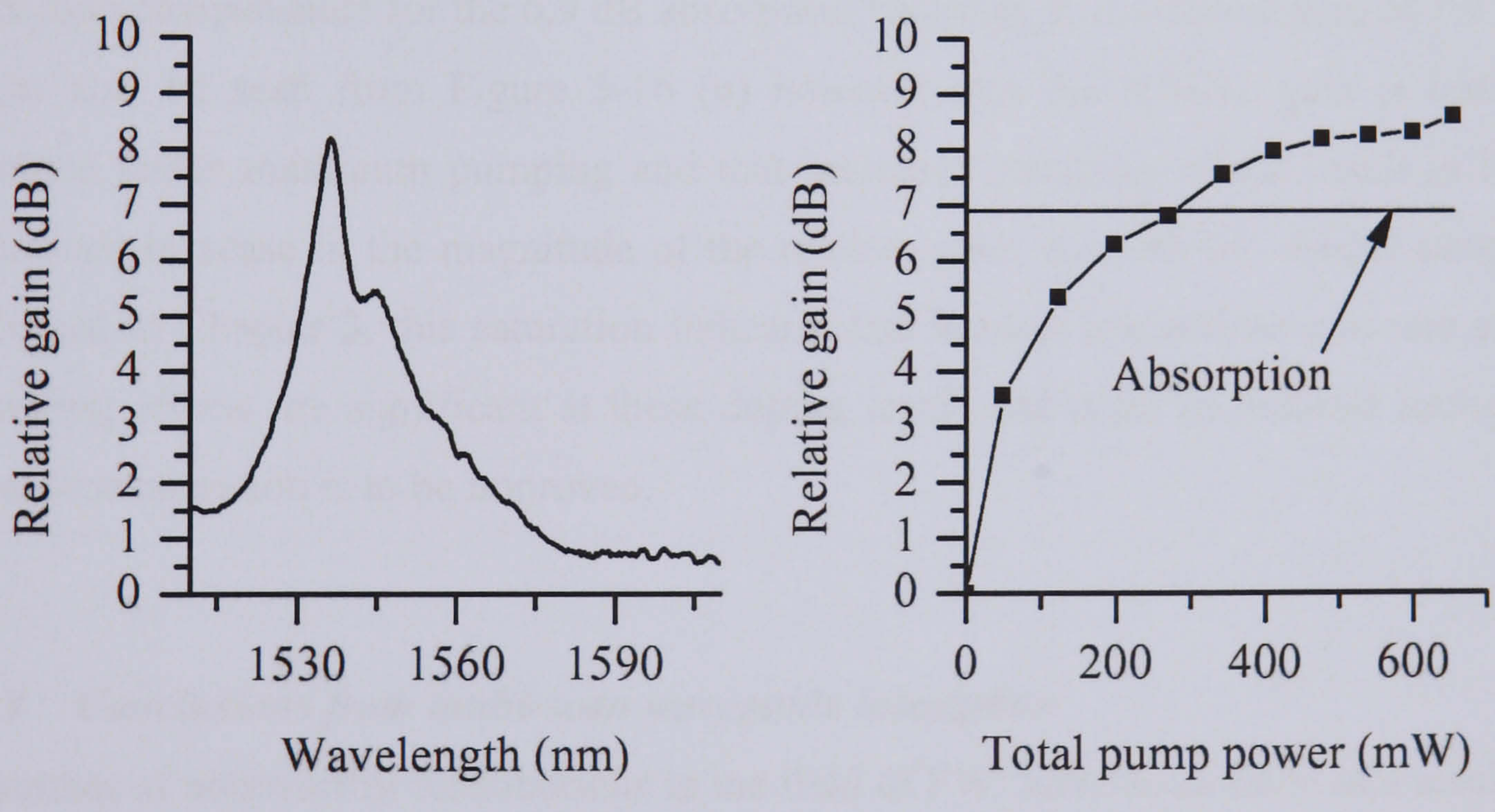

(a) (b)

Figure 5-16 (a) Relative gain spectrum for the optimum multi-scan waveguide under 412 mW of 980 nm and up to 243 mW of 1480 nm pumping, (b) Relative gain vs. total pump power characteristic measured at the peak of the relative gain spectrum. In (b), ≈ 65% of the total pump power is 980 nm, ≈ 35% is 1480 nm.

Relative gain vs. signal power measurements revealed little change in the relative gain using signal powers up to a maximum of ≈ 1 mW, thus indicating that all gain characterisation measurements were conducted in the small signal regime.

In order to assess if polarisation dependent gain (PDG) effects were significant, the PDL was measured under maximum pumping. The PDL under maximum pumping was measured to be 0.13 dB, thus indicating that PDG is not a significant issue for waveguides fabricated using this material and fabrication technique.

As outlined previously, a saturated peak relative gain of approximately twice the peak absorption in magnitude would be expected if a complete population inversion were obtained through pumping. As a result, a saturated peak relative gain of around 13.8 dB would be expected for the optimum waveguide if a complete population inversion were obtained. From Figure 5-16 (b) it can be seen that although a complete population inversion has not been obtained, the maximum measured relative gain of 8.6 dB has more than compensated for the 6.9 dB absorption resulting in an internal gain of 1.7 dB. It can also be seen from Figure 5-16 (b) however that the relative gain is heavily saturated under maximum pumping and that increased pumping would result in little significant increase in the magnitude of the relative gain. As with the sol-gel samples discussed in Chapter 3, this saturation indicates that ion-ion interactions and rare earth clustering effects are significant at these doping levels and must be reduced further if the device operation is to be improved.

5.4.4 Conclusions from multi-scan waveguide inscription

A number of noteworthy contributions to the field of FWI have been made as a result of the multi-scan investigations. Firstly, the demonstration of a 1.85 cm long waveguide exhibiting low PDL and a total background insertion loss of only 4.3 dB when directly butt-coupled to SMF-28 fibres clearly indicates that commercial devices should be possible using this fabrication route. Secondly, the demonstration of internal gain and low PDG from the optimum multi-scan waveguide clearly indicates that operational EDWA devices should be possible using FWI and oxyfluoride-silicate glass substrates [21].

Due to the low value of insertion loss exhibited by the optimum waveguide, it is concluded that the most probable reason for not achieving a complete population inversion is efficient energy transfer and upconversion effects between clustered Er^{3+}-ions. Consequently, it is concluded that although future work should involve improving the quality of the fabricated waveguides, the primarily focus of such work should be on optimising the substrate material composition to reduce the rare-earth clustering.

5.5 Single-scan femtosecond waveguide inscription in z-cut $LiNbO_3$

Lithium niobate ($LiNbO_3$) has excellent acousto-optic, electro-optic and non-linear optical properties. For these reasons, it has long been used for active optical applications such as free space acousto-optic and electro-optic modulators and parametric amplification [22]. In addition to these free space applications, integrated optical devices have also been fabricated using $LiNbO_3$. Examples of which include RF-spectrum analysers [23], electro-optic modulators [24], and wavelength converters [25]. Although the majority of the work described in this thesis concerns EDWA design and fabrication, the following section details the results of some preliminary studies into FWI in crystalline $LiNbO_3$.

Traditionally, $LiNbO_3$ waveguides are fabricated using either titanium in-diffusion or annealed proton exchange (APE) processes [24]. These processes may either be performed across the whole of the $LiNbO_3$ substrate to fabricate planar waveguides, or in selected regions only using masks defined through photolithography to create channel waveguides. The development of new fabrication techniques using $LiNbO_3$ is therefore of high interest since it may open up new areas of device design and fabrication. Although waveguide fabrication in $LiNbO_3$ using FWI has been demonstrated [26], no mention was made to their polarization dependent guiding properties. In addition, only guiding at 633 nm was demonstrated which is of little interest for telecommunications device applications. At present, FWI in $LiNbO_3$ is still a relatively unexplored area.

5.5.1 Femtosecond waveguide inscription in z-cut $LiNbO_3$ - experimental setup and procedure

Waveguide structures were fabricated in z-cut $LiNbO_3$ using the experimental setup described in section 5.3. For the $LiNbO_3$ work however, the pulse duration was 520 fs

(FWHM). To fabricate the waveguides, the pulse train was focussed to a distance of ≈ 250 μm below the surface of a 500 μm thick piece of z-cut $LiNbO_3$. All waveguides were fabricated using a single translational scan along the x-axis shown in Figure 5-2, perpendicular to the polarization fabrication laser. After fabrication, the sample was diced and polished perpendicular to the x-axis.

The primary aim of the work described here was to produce high confinement guiding at 1550 nm for telecommunications device applications. The first step in this investigation was to identify the fabrication pulse energy above which well confined guiding at either 1550 or 650 nm was not observed. To this end, a set of structures was fabricated using a range of translation speeds (20 → 100 $\mu m.s^{-1}$) and pulse energies (10 nJ → 10 μJ). Although some of the structures fabricated in this preliminary investigation were found to support guiding at 650 nm, none were found to support guiding at 1550 nm. In addition, it was also observed that structures fabricated using 0.46 μJ pulses or higher did not exhibit well confined guiding at 650 nm.

To fabricate waveguides supporting a mode at 1550 nm, it was concluded that waveguides with a higher refractive index contrast were required. Consequently, it was reasoned that slower translation speeds would result in a higher refractive index change since more pulses would overlap in a given distance. A second set of structures were thus fabricated using slower translation speeds of 2, 5, 10 and 20 $\mu m.s^{-1}$ together with pulse energies of 0.1, 0.2, 0.3 and 0.4 μJ (below the 0.46 μJ value above which well confined guiding at 650 nm was not observed in the preliminary investigation). The rest of this section describes the optical characterisation of this set of structures.

5.5.2 Waveguide characterisation

To investigate the cross sectional shape of the waveguide structure, the polished waveguide facet was inspected using an optical microscope operating in transmission mode. Figure 5-17 shows the captured images for waveguides fabricated using 0.3 and 0.4 μJ pulses and a translation speed of 2 $\mu m.s^{-1}$. No significant difference in the shape of the modified region as a result of varying the translation speed was apparent. No modified region could be observed for structures fabricated using either 0.1 or 0.2 μJ pulses.

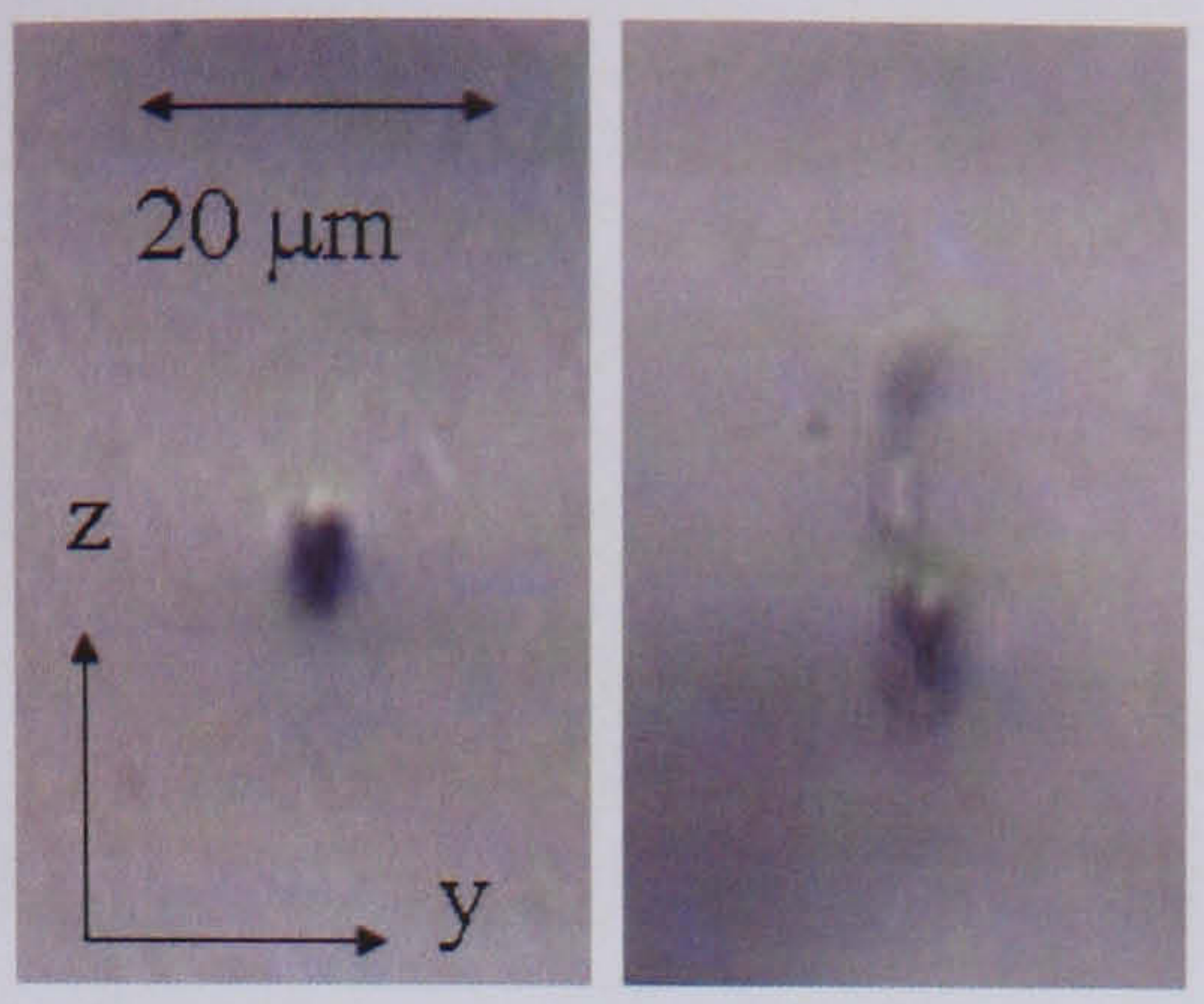

0.3 μJ 0.4 μJ

Figure 5-17 Transmission mode optical microscope images of the polished end facets of the $LiNbO_3$ waveguides fabricated using a translation speed of 2 μm.s^{-1}, and pulse energies of 0.3 and 0.4 μJ. Below each image is the pulse energy used to fabricate the waveguide.

The guiding properties of the second set of structures were investigated using the experimental setup shown in Figure 5-4. As a result of this investigation, 1550 nm guiding was observed in waveguides fabricated using pulse energies of 0.3 and 0.4 μJ. Figure 5-18 shows near field images of the 1550 nm mode for waveguides fabricated using 0.3 and 0.4 μJ pulses, and translation speeds from 2 to 20 μm.s^{-1}.

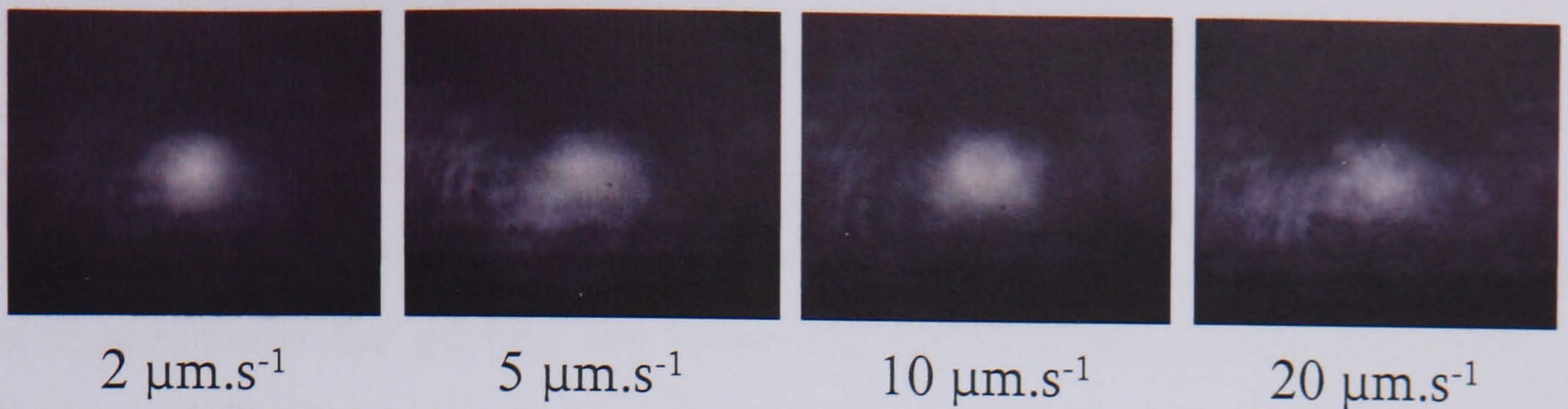

Waveguides fabricated using 0.4 μJ pulses

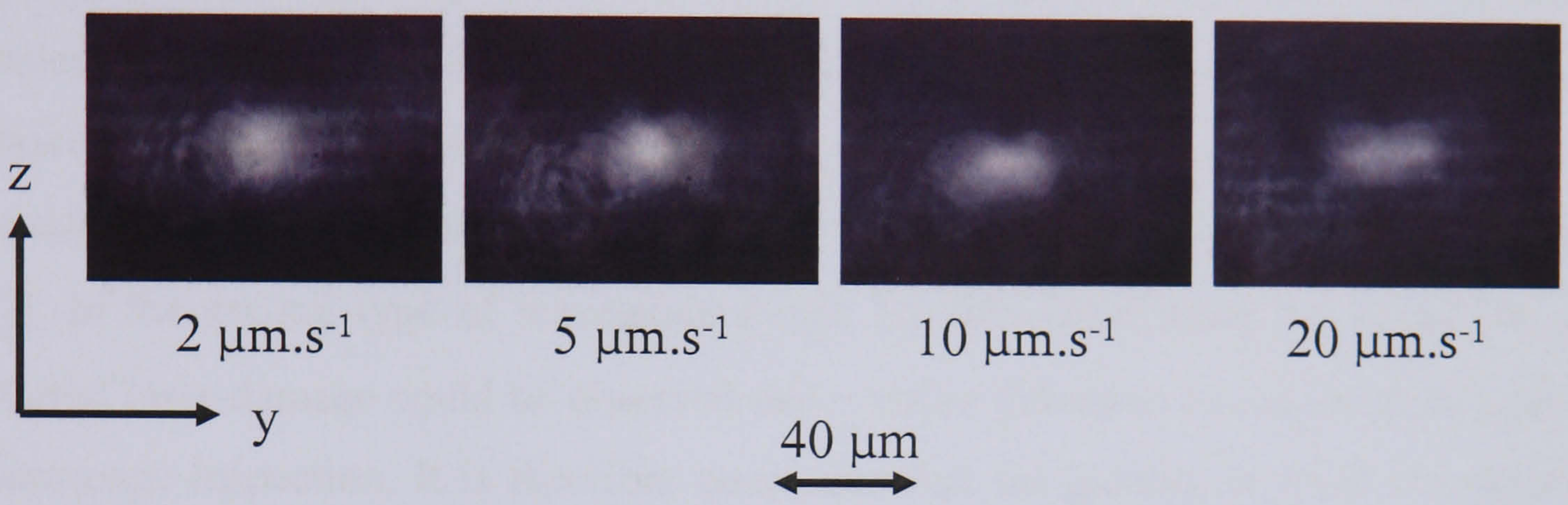

Waveguides fabricated using 0.3 μJ pulses

Figure 5-18 Near field images of the 1550 nm mode from waveguides fabricated in $LiNbO_3$ using 0.4 and 0.3 μJ pulses, and a translation speeds of 2, 5, 10 and 20 $\mu m.s^{-1}$. Below each image is the pulse energy used to fabricate the waveguide.

The horizontal periodic patterns visible in Figure 5-18 are believed to be the result of interference between non-guided light reflected from the upper and lower surfaces of the substrate and non-guided forward propagating light. These patterns were observed in regions where no structures had been fabricated. As seen in Figure 5-18, confinement of the 1550 nm guiding was found to improve with lower translation speeds, most probably due to a larger induced refractive index change.

Unfortunately, the high confinement guiding of 1550 nm light evident in Figure 5-18 was observed to deteriorate over time, and could no longer be observed after approximately 1 month. It is concluded therefore that at least part of the refractive index change in these structures is due to processes that are subject to relaxation e.g. stress. Although no guiding at 1550 nm was observed for structures created using pulse energies lower than 0.3 μJ, clear distortions in the transmission of the 1550 nm light were observed at the locations where these structures were expected, thus indicating some form of structural change had occurred.

Due to the temporary nature of the guiding at 1550 nm, further characterization experiments of these waveguides were conducted at 650 nm where the refractive index contrast requirements for guiding are lower than at 1550 nm. Consequently, it was found that two different types of waveguide structure had in fact been fabricated. In the first (Type I), fabricated using pulse energies of 0.3 and 0.4 μJ, it was found that the guiding at 650 nm actually occurred *around* a central laser-damage region, presumably created at the focus. This form of guiding is similar to that reported in other waveguides fabricated in crystalline materials using FWI, in which the refractive index change is thought to be primarily due to a stress field induced around the central damage region [27]. In the second type of waveguide (Type II), fabricated using 0.2 μJ pulses, no material laser-damage could be observed under either reflection or transmission optical microscope inspection. It is therefore concluded that the guiding in these waveguides occurs *in* a material modification region created at the focus. Figure 5-19 shows near field images of the 650 nm mode for waveguides fabricated using pulse energies of 0.3 μJ (Type I) and 0.2 μJ (Type II) and translation speeds from 2 to 20 $\mu m.s^{-1}$.

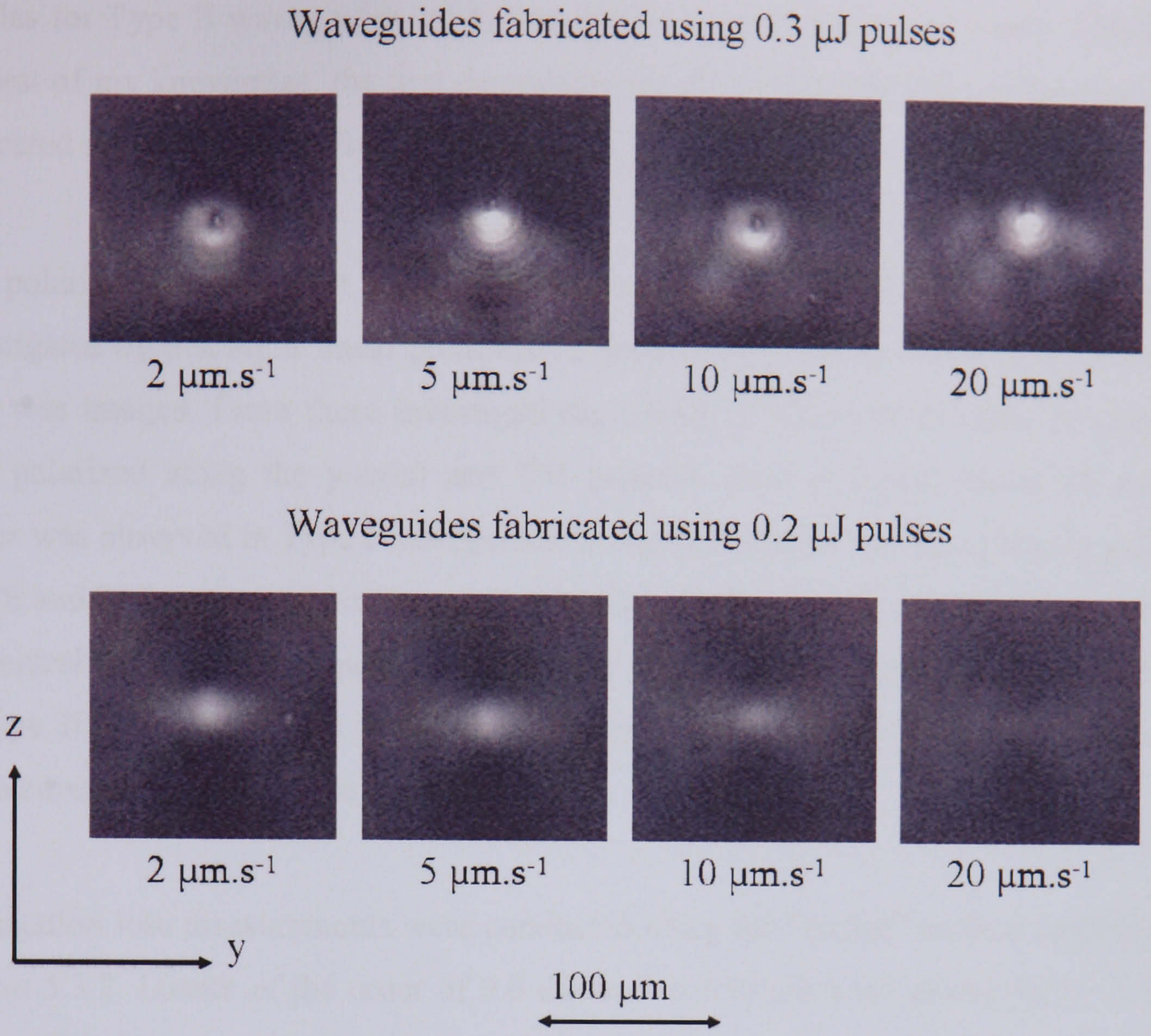

Figure 5-19 Near field images of the 650 nm mode from waveguides fabricated in $LiNbO_3$ using 0.3 and 0.2 μJ pulses, and a translation speeds of 2, 5, 10 and 20 μm.s^{-1}. Below each image is the pulse energy used to fabricate the waveguide.

The shape of the mode shown in Figure 5-19 is clearly related to the spatial distribution of the induced refractive index change. Although the exact distribution of the induced refractive index change is complex, all structural changes should be symmetric about the z-axis due to the symmetry of the fabrication laser beam. The symmetry of the refractive index distribution about the y-axis may be broken however due to the reduction in fabrication pulse energy (due to multi-photon absorption) as it travels through the material [28]. Clearly, for Type I waveguides, where guiding takes place around the damage region created at the centre of the focus, the damage region negates the possibility for a symmetric mode shape. As a result, the mode profiles shown in Figure 5-19 for Type I waveguides are not symmetric about the y-axis, but are symmetric about the z-axis. For Type II waveguides however, guiding occurs in a material modification region created at the focus. As a result, the observed mode profiles for Type II waveguides are symmetric about both the z- and y-axis. This is, to the best of my knowledge, the first demonstration of two separate forms of waveguides fabricated in $LiNbO_3$ using femtosecond pulses [29].

The polarization dependent guiding properties of the fabricated waveguides were investigated by placing a linear polarizer in front of the camera onto which the output facet was imaged. From these investigations, strong confinement of both TE (electric field polarized along the y-axis) and TM (electric field polarized along the z-axis) modes was observed in Type I waveguides. It was noted however that optimum guiding for TE and TM modes did not appear to take place in the exactly the same place around the central damage region, possibly indicating a high degree of birefringence. Guiding in Type II waveguides was found to be highly polarization selective, with only high confinement of the TM mode being observed.

Propagation loss measurements were conducted using the "streak" method described in section 5.3.2. Losses of the order of 9.0 $dB.cm^{-1}$ at 650 nm were measured for Type I waveguides. We directly attribute this high propagation loss value to the large amount of scattering expected due to the close proximity of the guiding and laser-damage regions. It was not possible to measure the losses of the Type II waveguides using the streak method since it requires a significant amount of scattered light from the waveguide, which was not detectable. This may indicate the possibility for low loss guiding in Type II waveguides fabricated using this technique.

5.5.3 Conclusions from waveguide inscription in $LiNbO_3$

It has been shown that two types of waveguide may be fabricated in z-cut $LiNbO_3$ using femtosecond pulses. In the first type (Type I), guiding was found to occur around a visible laser-damage region. The increase in refractive index in this region is thought to be primarily due to a stress field induced as a result of the expansion of the material at the focus of the writing laser beam. Analysis of the guiding properties of Type I waveguides showed that high confinement guiding at 1550 nm is possible. This was found to deteriorate with time however, indicating that at least part of the refractive index change is due to processes such as stress that may be subject to relaxation. Polarization investigations of Type I waveguides showed high confinement guiding of both TE and TM modes. Optimum guiding of TE and TM modes appeared to take place in different places around the damage region, possibly indicating a high degree of birefringence. Propagation loss measurements of Type I waveguides indicated high propagation losses in the region of 9.0 $dB.cm^{-1}$ at 650 nm, most probably due to the close proximity of the laser-damage and guiding regions. In the second type of waveguide (Type II), it is concluded that the guiding occurs in the region where the focus of the writing laser had been placed. The precise origin for the increase in refractive index is unknown at present but must somehow relate to a change in material structure at the focus. Previous investigations of femtosecond irradiation in other crystalline materials have suggested that the refractive index change is the result of strong and rapid heating inside the focal volume resulting in a local amorphization of the crystal structure. This amorphization is believed to result in a stress field, increasing the refractive index of the surrounding material which remains crystalline [28,30]. Analysis of the guiding properties at 650 nm revealed the guiding to be highly polarization dependent, with only high confinement of the TM mode being observed, this behaviour is in agreement with that reported in [30], where polarization selective guiding was observed in waveguides fabricated in crystalline silicon. Propagation loss measurements could not be conducted for Type II waveguides since the scattering of coupled light was not detectable. This may indicate low propagation losses for Type II waveguides.

Finally, it has been suggested that the refractive index change in Type II waveguides is the result of a local amorphization of the crystal structure. Amorphization would clearly result in the loss of the crystal properties. The degree to which this amorphization may affect the possible applications of Type II waveguides would depend on both the degree of amorphization and the overlap of effected region with the propagating mode. Future studies should focus on quantifying this.

5.6 References

[1] D. P. Hand and P. St. J. Russell, "Photoinduced refractive-index changes in germanosilicate fibers," *Opt. Lett.*, vol. 15, no. 2, pp. 102-104, Jan. 1990.

[2] N. F. Borrelli, C. Smith, D. C. Allan, and T. P. Seward III, "Densification of fused silica under 193-nm excitation," *J. Opt. Soc. Am. B,* vol. 14, no. 7, pp. 1606-1615, Jul. 1997.

[3] A. Othonos, "Fiber Bragg gratings," *Rev. Sci. Instrum.*, vol. 68, no. 12, pp. 4309-4341, Dec. 1997.

[4] D. Du, X. Liu, G. Korn, J. Squier, and G. Mourou, "Laser-induced breakdown by impact ionization in SiO_2 with pulse widths from 7 ns to 150 fs," *Appl. Phys. Lett.*, vol. 64, no. 23, pp. 3071-3073, Jun. 1994.

[5] C. B. Schaffer, A. Brodeur, and E. Mazur, "Laser-induced breakdown and damage in bulk transparent materials induced by tightly focused femtosecond laser pulses," *Meas. Sci. Technol.*, vol. 12, no. 11, pp. 1784-1794, Nov. 2001.

[6] M. E. Fermann, A. Galvanauskas, and G. Sucha, "Structural changes in transparent materials with ultrashort laser pulses," in *Ultrafast lasers: Technology and applications*, Marcel Dekker, 2003, pp. 396.

[7] K. M. Davis, K. Miura, N. Sugimoto, and K. Hirao, "Writing waveguides in glass with a femtosecond laser," *Opt. Lett.*, vol. 21, no. 21, pp. 1729-1731, Nov. 1996.

[8] C. Florea and K. A. Winick, "Fabrication and characterization of photonic devices directly written in glass using femtosecond laser pulses," *J. Lightwave Technol.*, vol. 21, no. 1, pp. 246-253, Jan. 2003.

[9] R. Osellame, S. Taccheo, M. Mariangoni, R. Ramponi, P. Laporta, D. Polli, S. De Silvestri, and G. Cerullo, "Femtosecond writing of active optical waveguides with astigmatically shaped beams," *J. Opt. Soc. Am. B*, vol. 20, no. 7, pp. 1559-1567, Jul. 2003.

[10] R. Osellame, N. Chiodo, V. Maselli, A. Yin, M. Zavelani-Rossi, G. Cerullo, P. Laporta, L. Aiello, S. De Nicola, P. Ferraro, A. Finizio, and G. Pierattini, "Optical properties of waveguides written by a 26 MHz stretched cavity Ti: Sapphire femtosecond oscillator," *Opt. Express*, vol. 13, no. 2, pp. 612-620, Jan. 2005.

[11] C. B. Schaffer, A. Brodeur, J. F. Garca, and E. Mazur, "Micromachining bulk glass by use of femtosecond laser pulses with nanojoule energy," *Opt. Lett.*, vol. 26, no. 2, pp. 93-95, Jan. 2001.

[12] M. E. Fermann, A. Galvanauskas, and G. Sucha, "Structural changes in transparent materials with ultrashort laser pulses," in *Ultrafast lasers: Technology and applications*, Marcel Dekker, 2003, pp. 410.

[13] A. Siegman, "Optical beams and resonators," in *Lasers*, University Science Books, 1986, pp. 669.

[14] Y. Nasu, M. Kohtoku, and Y. Hibino, "Low-loss waveguides written with a femtosecond laser for flexible interconnection in a planar light-wave circuit," *Opt. Lett.*, vol. 30, no. 7, pp. 723-725, Apr. 2005.

[15] J. Liu, Z. Zhang, C. Flueraru, X. Liu, S. Chang, and C. P. Grover, "Waveguide shaping and writing in fused silica using a femtosecond laser," *IEEE J. Sel. Top. Quant.*, vol. 10, no. 1, pp. 169-173, Jan. 2004.

[16] M. Ams, G. Marshall, D. Spence, and M. Withford, "Slit beam shaping method for femtosecond laser direct-write fabrication of symmetric waveguides in bulk glasses," *Opt. Express*, vol. 13, no. 15, pp. 5676-5681, Jul. 2005.

[17] G. Della Valle, R. Osellame, N. Chiodo, S. Taccheo, G. Cerullo, P. Laporta, A. Killi, U. Morgner, M. Lederer, and D. Kopf, "C-band waveguide amplifier produced by femtosecond laser writing," *Opt. Express*, vol. 13, no. 16, pp. 5976-5982, Aug. 2005.

[18] S. X. Shen and A. Jha, "The influence of F^--ion doping on the fluorescence ($^4I_{13/2} \rightarrow {}^4I_{15/2}$) line shape broadening in Er^{3+}-doped oxyfluoride silicate glasses," *Opt. Mater.*, vol. 25, no. 3, pp. 321-333, Apr. 2004.

[19] E. Desurvire, "Characteristics of erbium-doped fibers," in *Erbium-doped fiber amplifiers: Principles and applications,* John Wiley & Sons, 2002, pp. 277

[20] Y. Okamura, S. Yoshinaka, and S. Yamamoto, "Measuring mode propagation losses of integrated optical waveguides - A simple method," *Appl. Optics*, vol. 22, no. 23, pp. 3892-3894, Dec. 1983.

[21] R. R. Thomson, H. T. Bookey, N. Psaila, S. Campbell, D. T. Reid, S. Shen, A. Jha, and A. K. Kar, "Internal gain from an erbium-doped oxyfluoride-silicate glass waveguide fabricated using femtosecond waveguide inscription," *IEEE Photonic. Tech. L.,* vol. 18, no. 14, Jul. 2006.

[22] A. Yariv, "Electrooptic modulation of laser beams" in *Optical Electronics in modern Communications*, Oxford University Press, 1997, pp. 363.

[23] D. Mergerian, E. C. Malarkey, R. P. Pautienus, J. C. Bradley, A. L. Kellner and M. D. Mill, " Guided wave optical RF spectrum analyser," Microwave Symposium Digest, *MTT-S International*, vol. 81, no. 1, pp. 517 -519, Jun. 1981.

[24] E. L. Wooten, K. M. Kissa, A. Yi-Yan, E. J. Murphy, D. A. Lafaw, P. F. Hallemeier, D. Maack, D. V. Attanasio, D. J. Fritz, G. J. McBrien, and D. E. Bossi, "A review of lithium niobate modulators for fiber-optic communications systems," *IEEE J. Sel. Top. Quant.*, vol. 6, no. 1, pp. 69-82, Jan. / Feb. 2000.

[25] J. Webjörn, F. Laurell, and G. Arvidsson, "Fabrication of periodically domain-inverted channel waveguides in lithium-niobate for second harmonic-generation," *J. Lightwave Technol.*, vol. 7, no. 10, pp. 1597-1600, Oct. 1989.

[26] L. Gui, B. Xu, and T. C. Chong, "Microstructure in lithium niobate by use of focused femtosecond laser pulses," *IEEE Photonic. Tech. L.*, vol. 16, no. 5, pp. 1337-1339, May 2004.

[27] V. Apostolopoulos, L. Laversenne, T. Colomb, C. Depeursinge, R. P. Salathé, M. Pollnau, R. Osellame, G. Cerullo, and P. Laporta, "Femtosecond-irradiation-induced refractive-index changes and channel waveguiding in bulk Ti^{3+}: Sapphire," *Appl. Phys. Lett.*, vol. 85, no. 7, pp. 1122-1124, Aug. 2004.

[28] T. Gorelik, M. Will, S. Nolte, A. Tuennermann, and U. Glatzel, "Transmission electron microscopy studies of femtosecond laser induced modifications in quartz," *Appl. Phys. A-Mater.*, vol. 76, no. 3, pp. 309-311, Mar. 2003.

[29] R. R. Thomson, S. Campbell, I. J. Blewett, A. K. Kar, and D. T. Reid, "Optical waveguide fabrication in z-cut lithium niobate ($LiNbO_3$) using femtosecond pulses in the low repetition rate regime," *Appl. Phys. Lett.*, vol. 88, no. 11, Art. No. 111109, Mar. 2006.

[30] A. H. Nejadmalayeri, P. R. Herman, J. Burghoff, M. Will, S. Nolte, and A. Tünnermann, "Inscription of optical waveguides in crystalline silicon by mid-infrared femtosecond laser pulses," *Opt. Lett.*, vol. 30, no. 9, pp. 964-966, May 2005.

Chapter 6 - Conclusions and future work

6.1 Conclusions

The majority of the work described in this thesis is concerned with the development of Er-doped waveguides for EDWA applications. In the course of this work, the sol-gel, PLD and FWI techniques have all been used to fabricate Er-doped waveguides. In addition to the Er-doped waveguide work, a preliminary study on FWI in crystalline $LiNbO_3$ was also presented. The following will summarise the conclusions made from the work in each of these areas.

In Chapter 3, the development of Er-doped waveguides using a novel single sol-gel deposition technique was described. As a result of this work, channel waveguides exhibiting background propagation losses as low as ≈ 0.1 dB.cm^{-1}, coupling losses to SMF-28 as low as 0.4 dB/facet, and PDL values as low as 0.17 dB for a 5.2 cm long waveguide, all at 1550 nm, were demonstrated. It is concluded therefore that the passive performance of these waveguides is currently at the stage necessary for fabricating operational EDWA devices. It was also observed however that although the passive performance of the sol-gel waveguides was excellent, it was not possible to obtain a population inversion in these waveguides under optical pumping. As a consequence of the theoretical and experimental investigations described in Chapter 3, it is concluded that clustering of the Er^{3+} ions is the most probable reason for the poor amplifier performance. Although it was not possible to demonstrate either a population inversion or net gain in the sol-gel waveguides, the demonstration of high quality, optically active Er-doped waveguides fabricated using this sol-gel technique is, in itself, a noteworthy accomplishment [1].

In Chapter 4, the development of Er-doped oxyfluoride-silicate glass waveguides using PLD was described. From this work, it was shown that thin films of Er-doped oxyfluoride-silicate glass can be deposited onto fused silica substrates using PLD. Such films were found to be granular in structure, exhibiting reasonably low propagation losses in the region of ≈ 1 dB.cm^{-1} at 633 nm. As a result of the work described in Chapter 4, it is concluded that the stoichiometry of the film is extremely similar to that of the target material. Rib waveguides were subsequently fabricated from one of the PLD films deposited on a 200 °C substrate. The quality of these waveguides was high enough to allow the direct measurement of the $^4I_{15/2} \rightarrow {}^4I_{13/2}$ transition absorption lineshape. From the results of the spectroscopic and compositional analysis presented in Chapter 4, it is concluded that although the stoichiometry of the film and target are almost identical, there are significant differences in the Er^{3+} ion environment in the film and target materials. Significantly, it was found that the $^4I_{13/2} \rightarrow {}^4I_{15/2}$ transition fluorescence lifetime of Er^{3+} ions in the film material is three orders of magnitude less than that of Er^{3+} ions in the target material. It is concluded that the most probable reason for the reduction in fluorescence lifetime is O-H quenching of the $^4I_{13/2} \rightarrow {}^4I_{15/2}$ transition due to water absorption by the granular film [2].

In Chapter 5, two studies into FWI in Er-doped oxyfluoride-silicate glass were presented. In the first, waveguides were fabricated using a single-scan fabrication technique. In the second waveguides were fabricated using a multi-scan fabrication technique. As a result of the single-scan study, it is shown that oxyfluoride-silicate glass is a suitable substrate material for FWI and that there is a trade off between achieving low coupling losses and low propagation losses [3]. From the results of the single-scan study it was concluded that in order to fabricate high quality waveguides exhibiting low insertion losses, it is necessary to use the multi-scan fabrication technique. As a result of the multi-scan study, a high quality waveguide exhibiting a total background insertion loss of only 4.3 dB when coupled to SMF-28 fibres was fabricated. Under optical pumping, this optimum waveguide exhibited an internal gain of 1.7 dB at 1537 nm [4]. Due to the high quality passive performance of the optimum multi-scan waveguide, it is concluded that the most probable reason for not achieving net gain is clustering of the Er^{3+} ions in the substrate material.

In addition to the work on FWI in Er-doped oxyfluoride-silicate glass, Chapter 5 also describes a preliminary study of FWI in crystalline $LiNbO_3$. As a result of this study it was found that depending on the fabrication pulse energy, two forms of optical waveguide could be fabricated. In the first (Type I), fabricated using higher energy pulses, it was observed that guiding took place around a central laser damage region created at the focus. In the second (Type II), fabricated using lower energy pulses, it was observed that guiding took place in a material modification region created at the focus. For Type I waveguides it is concluded that the waveguide refractive index contrast is primarily due to a stress field induced as a result of the expansion of the material at the focus of the laser beam. High confinement guiding of 1550 nm light was demonstrated in Type I waveguides, but found to be temporary, thus indicating that at least part of the refractive index change is due to processes such as stress that are subject to relaxation. The high propagation losses measured in Type I waveguide are believed to be the direct result of scattering from the laser damage region. For Type II waveguides, the origin of the refractive index change is as yet unknown, but must somehow relate to a change in the material structure at the focus. Polarisation investigations revealed that guiding in Type II waveguides is highly polarisation sensitive, with only guiding of the TM polarisation being observed. It was not possible to measure the propagation losses of Type I waveguides due to the low degree of scattering, this may indicate the possibility for low loss guiding in type II waveguides [5].

6.2 Future work

The study presented in Chapter 3 has certainly demonstrated that although the passive performance of the sol-gel waveguides is excellent, the active performance requires significant improvement. With this in mind, recent work published by Huang et al [6] has shown that sol-gel glasses, similar in composition to those used in this study, can host large erbium concentrations without clustering. It is clear therefore that future work in this area should focus on improving the active performance of the sol-gel waveguides by reducing the degree of clustering. Once net gain has been demonstrated, subsequent work should focus on increasing the pumping efficiency and reducing the amplifier noise figure, possibly through the use of co-dopants such as Yb.

From the study presented in Chapter 4 it is clear that neither the passive or active performance of the PLD fabricated waveguides is at the stage necessary for operational devices. To improve the passive performance, future work should focus on increasing the fibre-waveguide coupling efficiency and reducing the waveguide propagation losses. To improve the fibre-waveguide coupling efficiency it is clear that the most challenging problem for direct fibre-waveguide butt-coupling is the degree of waveguide-fibre mode mismatch. To improve this situation, it may be possible to either, fabricate thicker PLD films, use free space optics or possibly even use tapered fibres for evanescent coupling. To decrease the waveguide propagation losses it is clear that the granular structure of the film must be addressed, possibly through either post deposition annealing or optimisation of the PLD process itself. To improve the active performance on the other hand, it is clear that future work must address the reduction in the $^4I_{13/2} \rightarrow {}^4I_{15/2}$ transition fluorescence lifetime of Er^{3+} ions in PLD film. As outlined previously, the granular structure of the PLD film is believed to play an important role in the observed lifetime reduction. As such, post deposition annealing or optimisation of the PLD process itself may result in an improvement of the situation.

The work described in Chapter 5 has demonstrated that there are many possibilities for future work in the area of FWI. From the viewpoint of fabricating high gain EDWAs using oxyfluoride-silicate glass substrates, future work must aim at improving the passive performance of the waveguides by reducing the propagation and coupling losses. More importantly however, future work in this area must focus primarily on improving the active performance by reducing the degree of rare-earth clustering in the substrate material. Outside the area of EDWA fabrication, the possibilities for future work are numerous. As yet, the physical mechanisms behind the refractive index modification are far from fully understood. Future work in this area is necessary to better understand these processes. Finally, from a device engineering point of view, the ability to fabricate three dimensional photonic devices is too attractive to be ignored. Future work in the area of FWI should focus on exploiting this capability to fabricate three dimensional photonic devices such as laser arrays, amplifier arrays, couplers and resonators.

6.3 References

[1] R. R. Thomson, H. T. Bookey, H. Ur-Rehman, S. Liu, N. Suyal, and A. K. Kar, "Optically active erbium-doped waveguides fabricated using a single-sol-gel deposition technique," *J. Lightwave Technol.*, vol. 23, no. 12, pp. 4249-4256, Dec. 2005.

[2] R. R. Thomson, H. T. Bookey, A. K. Kar, M. R. Taghizadeh, A. Klini, C. Fotakis, F. Romano, A. P. Caricato, M. Martino, S. Shen, and A. Jha, "Erbium-doped waveguide fabrication via reactive pulsed laser deposition of erbium-doped oxyfluoride-silicate glass," *Electron. Lett.*, vol. 41, no. 25, pp. 1376-1377, Dec. 2005.

[3] R. R. Thomson, S. Campbell, I. J. Blewett, A. K. Kar, D. T. Reid, S. Shen and A. Jha, "Active waveguide fabrication in erbium-doped oxyfluoride silicate glass using femtosecond pulses," *Appl. Phys. Lett.*, vol. 87, no. 12, Art. 121102, Sept.2005.

[4] R. R. Thomson, H. T. Bookey, N. Psaila, S. Campbell, D. T. Reid, S. Shen, A. Jha, and A. K. Kar, "Internal gain from an erbium-doped oxyfluoride-silicate glass waveguide fabricated using femtosecond waveguide inscription" *IEEE Photonic. Tech. L.* vol. 18, no. 14, pp. 1515-1517. Jul. 2006.

[5] R. R. Thomson, S. Campbell, I. J. Blewett, A. K. Kar, and D. T. Reid, "Optical waveguide fabrication in z-cut lithium niobate ($LiNbO_3$) using femtosecond pulses in the low repetition rate regime," *Appl. Phys. Lett.*, vol. 88, no. 11, Art. No. 111109, Mar. 2006.

[6] W. Huang, R. R. A.Syms, E. M. Yeatman, M. M. Ahmad, V. T. Clapp., and S. M. Ojha, "Fiber-device-fiber gain from a sol-gel erbium-doped waveguide amplifier," *IEEE Photon. Technol. Lett.*, vol 14, pp. 959-961, Jul. 2002.

Appendix A

A.1 Matlab code used for EDWA modelling.

The following are screen dumps of the Matlab code written to model the gain operation of a silica Er-doped waveguide under uni-directional 980 nm pumping. The code is used to model both the operation of the theoretical EDWAs in Chapter 2, and the operation of the two sol-gel Er-doped waveguides discussed in Chapter 3.

The program as a whole consists of two separate scripts. The control script shown in Figure A-1 defines all the necessary variables and performs the integration of Equation 2.24 to obtain the gain function of the waveguide. The second script, shown in Figure A-2, defines Equation 2.22 that represents the evolution of the pump light along the waveguide. This function is solved using the ode15s differential equation solver as detailed in line 73 of the control program.

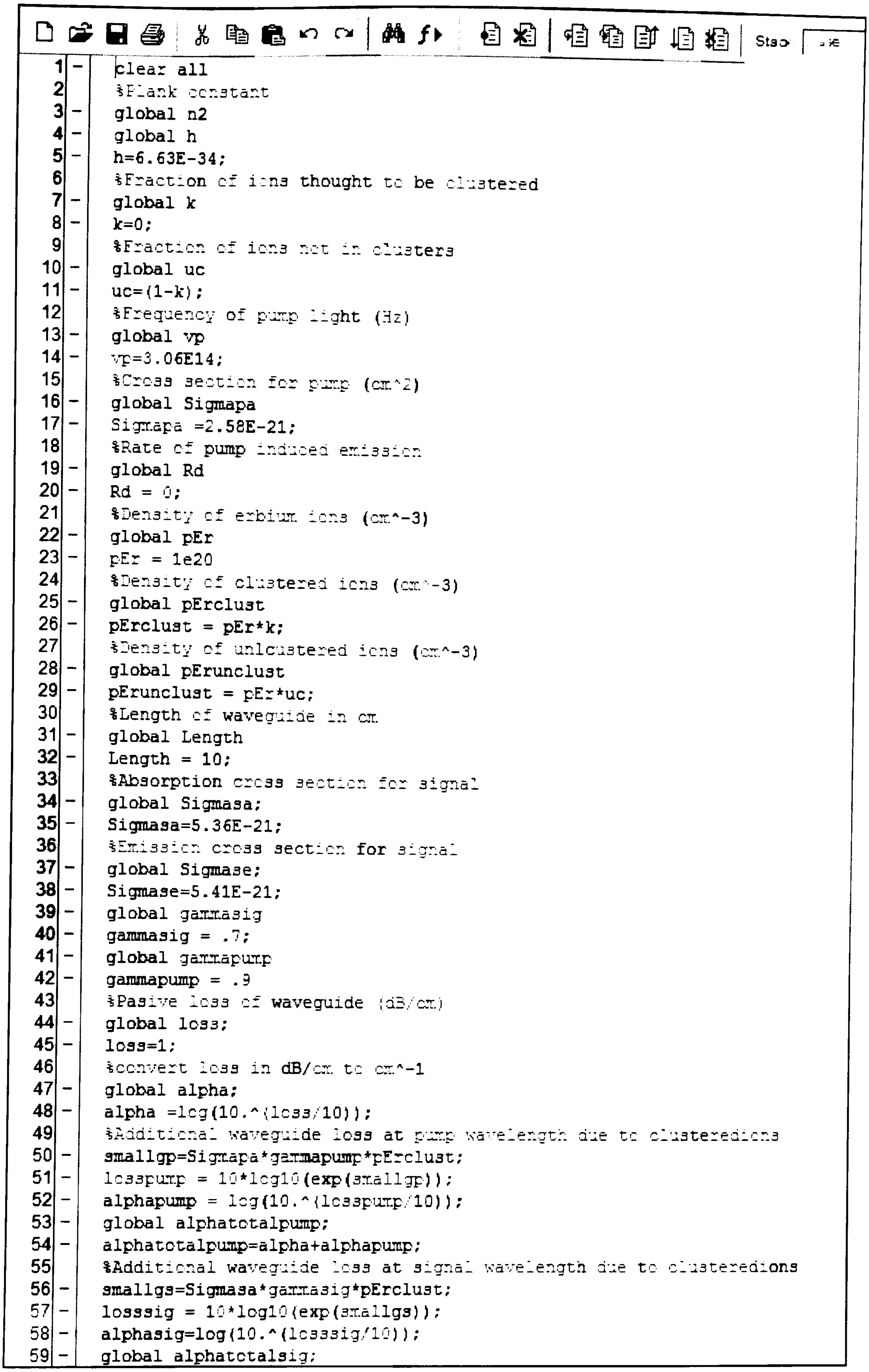

```
clear all
%Plank constant
global n2
global h
h=6.63E-34;
%Fraction of ions thought to be clustered
global k
k=0;
%Fraction of ions not in clusters
global uc
uc=(1-k);
%Frequency of pump light (Hz)
global vp
vp=3.06E14;
%Cross section for pump (cm^2)
global Sigmapa
Sigmapa =2.58E-21;
%Rate of pump induced emission
global Rd
Rd = 0;
%Density of erbium ions (cm^-3)
global pEr
pEr = 1e20
%Density of clustered ions (cm^-3)
global pErclust
pErclust = pEr*k;
%Density of unlcustered ions (cm^-3)
global pErunclust
pErunclust = pEr*uc;
%Length of waveguide in cm
global Length
Length = 10;
%Absorption cross section for signal
global Sigmasa;
Sigmasa=5.36E-21;
%Emission cross section for signal
global Sigmase;
Sigmase=5.41E-21;
global gammasig
gammasig = .7;
global gammapump
gammapump = .9
%Pasive loss of waveguide (dB/cm)
global loss;
loss=1;
%convert loss in dB/cm to cm^-1
global alpha;
alpha =log(10.^(loss/10));
%Additional waveguide loss at pump wavelength due to clusteredions
smallgp=Sigmapa*gammapump*pErclust;
losspump = 10*log10(exp(smallgp));
alphapump = log(10.^(losspump/10));
global alphatotalpump;
alphatotalpump=alpha+alphapump;
%Additional waveguide loss at signal wavelength due to clusteredions
smallgs=Sigmasa*gammasig*pErclust;
losssig = 10*log10(exp(smallgs));
alphasig=log(10.^(losssig/10));
global alphatotalsig;
```

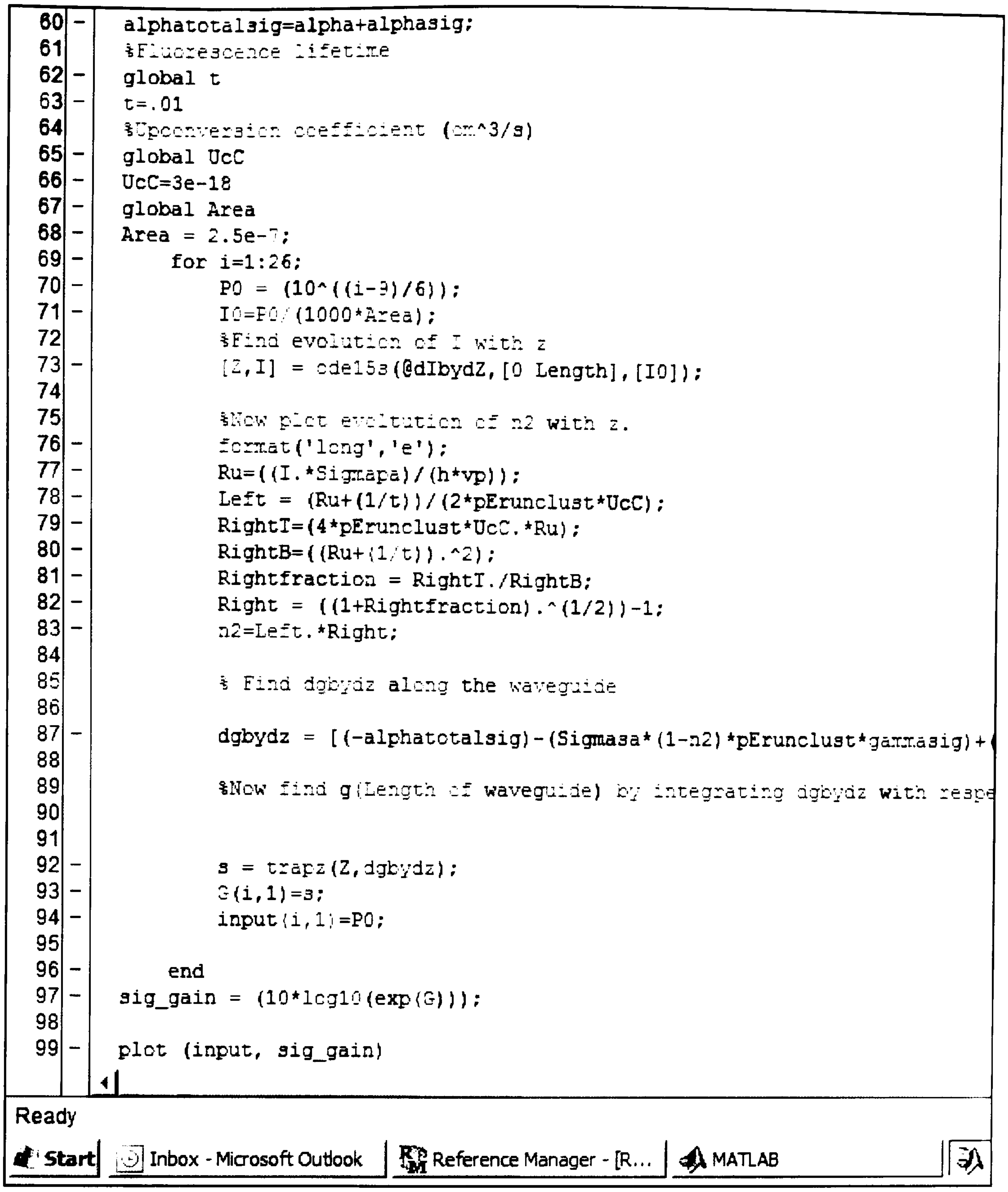

```
alphatotalsig=alpha+alphasig;
%Fluorescence lifetime
global t
t=.01
%Upconversion coefficient (cm^3/s)
global UcC
UcC=3e-18
global Area
Area = 2.5e-7;
    for i=1:26;
        P0 = (10^((i-9)/6));
        I0=P0/(1000*Area);
        %Find evolution of I with z
        [Z,I] = ode15s(@dIbydZ,[0 Length],[I0]);

        %Now plot evoltution of n2 with z.
        format('long','e');
        Ru=((I.*Sigmapa)/(h*vp));
        Left = (Ru+(1/t))/(2*pErunclust*UcC);
        RightT=(4*pErunclust*UcC.*Ru);
        RightB=((Ru+(1/t)).^2);
        Rightfraction = RightT./RightB;
        Right = ((1+Rightfraction).^(1/2))-1;
        n2=Left.*Right;

        % Find dgbydz along the waveguide

        dgbydz = [(-alphatotalsig)-(Sigmasa*(1-n2)*pErunclust*gammasig)+(

        %Now find g(Length of waveguide) by integrating dgbydz with respe


        s = trapz(Z,dgbydz);
        G(i,1)=s;
        input(i,1)=P0;

    end
sig_gain = (10*log10(exp(G)));

plot (input, sig_gain)
```

Figure A-1 Main control program

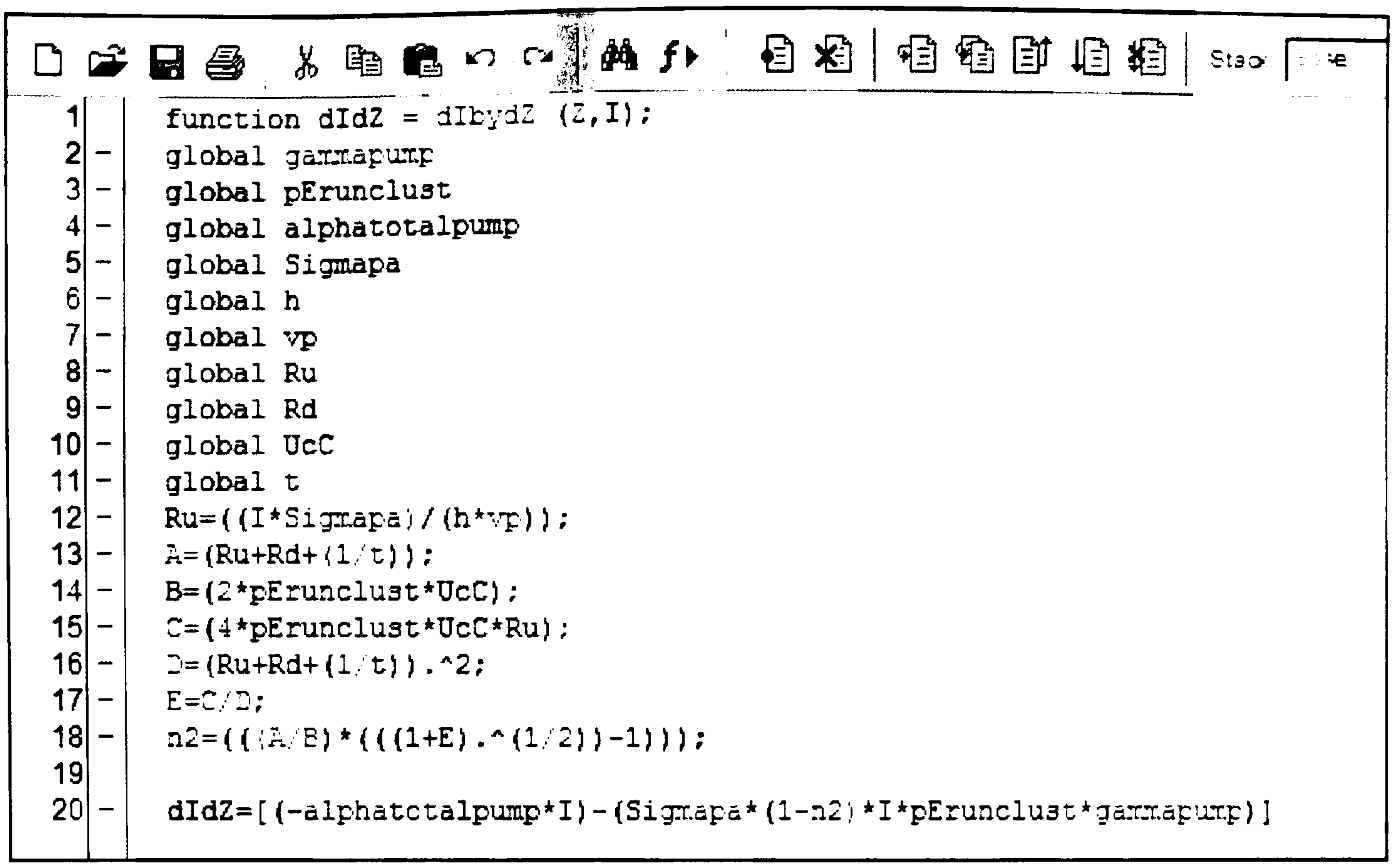

```
function dIdZ = dIbydZ (Z,I);
global gammapump
global pErunclust
global alphatotalpump
global Sigmapa
global h
global vp
global Ru
global Rd
global UcC
global t
Ru=((I*Sigmapa)/(h*vp));
A=(Ru+Rd+(1/t));
B=(2*pErunclust*UcC);
C=(4*pErunclust*UcC*Ru);
D=(Ru+Rd+(1/t)).^2;
E=C/D;
n2=(((A/B)*(((1+E).^(1/2))-1)));

dIdZ=[(-alphatotalpump*I)-(Sigmapa*(1-n2)*I*pErunclust*gammapump)]
```

Figure A-2 Function representing the pump intensity evolution along the waveguide.

Appendix B

This appendix gives the derivation of Equation 3.6 in Chapter 3.

The gain coefficient for any laser material can be expressed as Equation B-1 [1].

$$k = \Delta N_{12} . \sigma_{12}$$

Equation B-1

where k is the gain coefficient for the signal light (cm^{-1}), ΔN_{12} is the population difference between the first state (1) and the second state (2) of the transition (ions.cm^{-3}) and σ_{12} is the transition cross section for the signal light (cm^{2}).

For the case of Er-doped waveguides, Equation B-1 must be modified slightly to include the effect of the signal waveguide overlap to give Equation B-2.

$$k = \Gamma_s . \Delta N_{12} . \sigma_{12}$$

Equation B-2

where Γ_s is the signal-waveguide overlap factor as defined by Equation 2.20 in Chapter 2.

Under the condition of zero pump light, all ions are in the ground state, and the absorption coefficient for the waveguide is given by Equation B-3.

$$k_{Abs} = \Gamma_s . \rho_{Er} . \sigma_s^a$$

Equation B-3

where ρ_{Er} is the total Er^{3+} ion concentration (ions.cm^{-3}) and σ_s^a is the cross section for the $^4I_{15/2} \rightarrow {}^4I_{13/2}$ transition (cm^{2}).

Since k is in units of cm^{-1}, Equation B-4 must be used to calculate the loss due to absorption a signal would experience after propagation along an unpumped waveguide.

$$Absorption\,(dB) = 10Log_{10}(\exp(L.k_{Abs}) = 10Log_{10}(\exp(L.\Gamma_s.\rho_{Er}.\sigma_s^a)$$

Equation B-4

where L is the length of the waveguide (cm).

A similar expression relating the magnitude of the relative gain to the population inversion can be constructed. Again by using Equation B-2, the change in the gain coefficient (Δk_{pump}) of the waveguide under pumping can be expressed as Equation B-5.

$$\Delta k_{pump} = \Gamma_s(\sigma_s^a.\Delta N_1 + \sigma_s^e.N_2)$$

Equation B-5

where σ_s^e is the $^4I_{13/2} \rightarrow {}^4I_{15/2}$ transition cross section at the signal wavelength (cm^2) and N_2 is the population of the $^4I_{13/2}$ level (ions.cm^{-3}).

By assuming that $N_1 + N_2 = \rho_{Er}$ and $\sigma_s^a = \sigma_s^e = \sigma_s$, Equation B-5 can be expressed in terms of the fractional population of the $^4I_{13/2}$ level, n_2, where $n_2 = \dfrac{N_2}{\rho_{Er}}$ to give Equation B-6.

$$\Delta k_{pump} = 2.\Gamma_s.\sigma_s.\rho_{Er}.n_2$$

Equation B-6

Equation B-6 can then be used to calculate the change in transmission (or relative gain) of the waveguide after pumping to give Equation B-7

$$G_{Rel}(dB) = 10Log(\exp(L.\Delta k_{pump})) = 10Log(\exp(L.2.\Gamma_s.\sigma_s.\rho_{Er}.n_2))$$

Equation B-7

Finally, by dividing Equation B-7 by Equation B-4, we obtain Equation B-8 that relates the magnitude of the relative gain to the induced population inversion.

$$n_2 = \frac{G_{Rel}(dB)}{2 \times Absorption\,(dB)}$$

Equation B-8

B.1 References

[1] A. Siegman, "Basic Laser Physics," in Lasers, University Science Books, 1986, pp. 287.